

**Analytical and Experimental Investigation of Tidal  
Influence in Coastal Aquifers**

*Thesis submitted to the  
Indian Institute of Technology Kharagpur  
for Award of the Degree*

*of*

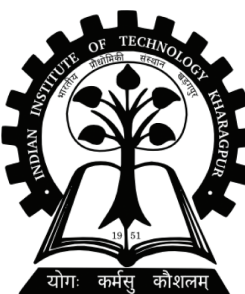
**Doctor of Philosophy**

*by*

**Selva Balaji. M**

Under the Guidance of

**Dr. Anirban Dhar**



**DEPARTMENT OF CIVIL ENGINEERING  
INDIAN INSTITUTE OF TECHNOLOGY KHARAGPUR**

**July 2019**

©2019 Selva Balaji M. All rights reserved.



## APPROVAL OF THE VIVA-VOCE BOARD

/ /2019

Certified that the thesis entitled **Analytical and Experimental Investigation of Tidal Influence in Coastal Aquifers** submitted by **Selva Balaji. M** to the Indian Institute of Technology Kharagpur, for the award of the degree Doctor of Philosophy has been accepted by the external examiners and that the student has successfully defended the thesis in the viva-voce examination held today.

**Prof. Subhasish Dey Prof. Venkappayya R Desai Dr. Mihir Kumar Dash**

Dept. of Civil Engg.

Dept. of Civil Engg.

CORAL

Member of the DSC

Member of the DSC

Member of the DSC

**Dr. Anirban Dhar**

Dept. of Civil Engg.

Supervisor

External Examiner

Chairman



## **CERTIFICATE**

This is to certify that the thesis entitled **Analytical and Experimental Investigation of Tidal Influence in Coastal Aquifers**, submitted by **Selva Balaji. M** to Indian Institute of Technology Kharagpur, is a record of bonafide research work under my supervision and I consider it worthy of consideration for the award of the degree of Doctor of Philosophy of the Institute.

**Dr. Anirban Dhar**

Associate Professor

Department of Civil Engineering

Indian Institute of Technology Kharagpur

Date : / /2019

Place: IIT Kharagpur



## Acknowledgment

I am overwhelmed with pleasure and pride to express my feelings and a sense of indebtedness, in gesture of acknowledgment to different persons for their valuable guidance and sensible direction during the course of my Ph.D. study that enabled me to successfully complete my study at IIT Kharagpur.

I am grateful and indebted to my parents, sister, brother-in-law and niece whose forbearance and emotional support helped this thesis a successful pursuit. I express my heartfelt deep sense of gratitude to Prof. Anirban Dhar, Department of Civil Engineering, Indian Institute of Technology Kharagpur for his helpful and inspiring guidance, effective discussions, persistent encouragements and meticulous effort during the study. Despite his busy academic schedule and other preoccupations, he has patiently guided me throughout the period of my research work and thesis preparation.

I convey my heartfelt thanks to Chitaranjan, Gourabananda, Satiprasad, Madhumita, and Manasa for their timely help and support. Especially, I would like to thank Chitaranjan for sharing the huge amount of work load in performing experiments. I would like to thank my Tamil friends and hall friends including, Marxim Rahula Bharathi, Rajarajan, Ramakrishna, Siva Ok, Ashok, Vasudevan, Elango, Anulekha, Kamaraj and Arunjunai, who were always supportive and took all my irritations with utmost care and always showed love. I also express my thanks to all my friends from Department of Civil Engineering for their help and encouragement during my research tenure and stay in IIT. I also express my thanks to my longterm friends Sivarajani, Banu, Kumaran, Kaarthik, Vidhyalakshmi, Revathi, Surendar, Siddharth and Aravendan who always supported by me like a pillar and always welcomed me and loved me from the first day I know them. I would like to thank Science Education Group friends for giving me opportunity to have interesting discussions as necessary diversions in the stressful moments. I would also like to thank Vigneshwari for her continuous care and support given to me. I express my gratitude for Sucheritha for her patience and care she gave for my wellbeing.

With deep sense of indebtedness, I express my sincere and heartfelt thanks to Prof. N. Dhang, Head of the Department and members of my Doctoral Scrutiny Committee - Prof. VR Desai, Prof. Mihir Kumar Dash and Prof. Subhasish Dey, for their guidance, constructive criticisms, advice and providing me with requisite facilities to carry out my research work. I am grateful to all the faculty members of the School for their encouragement and kind cooperation. Finally, I would like to thank Periyar and Ambedkar for their fights for persons like me to dream and

achieve things which were not possible a century ago.

பிறப்பொக்கும் எல்லா உயிர்க்கும் சிறப்பொவ்வா  
செய்தொழில் வேற்றுமை யான்.

I would like to conclude with thanking Thiruvalluvar for his Thirukkural and people who imbibed the thought of the above kural (couplet) in me: "By birth everybodys nature is the same none can be branded as good or bad. Regardless of family status one born into, and the opportunities one is bestowed with, depending how they fulfill their duties well or not, the greatness or glory will be theirs."

**Selva Balaji. M**

## DECLARATION

I certify that

- a. The work contained in the thesis is original and has been done by myself under the general supervision of my supervisor.
- b. The work has not been submitted to any other Institute for any degree or diploma.
- c. I have followed the guidelines provided by the Institute in writing the thesis.
- d. I have conformed to the norms and guidelines given in the Ethical Code of Conduct of the Institute.
- e. Whenever I have used materials (data, theoretical analysis, and text) from other sources, I have given due credit to them by citing them in the text of the thesis and giving their details in the references.
- f. Whenever I have quoted written materials from other sources, I have put them under quotation marks and given due credit to the sources by citing them and giving required details in the references.

Selva Balaji. M



## List of Journal Publications

1. **Munusamy, S.B.**, Dhar, A. ( 2016) "Homotopy Perturbation Method-Based Analytical Solution for Tide-Induced Groundwater Fluctuations", *Groundwater*,54(3), 440-447.
2. **Munusamy, S.B.**, Dhar, A. (2017) "Analytical Solution of Groundwater Waves in Unconned Aquifers with Sloping Boundary", *Sadhana*, 42 (9), 1571-1578.
3. **Munusamy, S.B.**, Dhar, A. (2019) "On Use of Expanding Parameters and Auxiliary Term in Homotopy Perturbation Method for Boussinesq Equation with Tidal Condition", *Environmental Modeling and Assessment*,24 (1), pp. 109-120.



## Abstract

Coastal aquifers play an important role in supporting the freshwater needs of the highly populated coastal areas. More than half of the world's population lives within 60 km of the shoreline (UNCED, 1992), and more than 17 million people live in coastal districts of India (MOEFCC, 2017). Groundwater abstraction will increase 39% by 2050 compared to 2010 (Burek et al., 2016). The understanding of the processes in coastal aquifers are important for optimal planning of pumping rates, selection of pumping well locations without contaminating the production wells with saltwater, and to identify the nutrient or contaminant pathways. Quantification of tidal influence on the groundwater table is important. Traditional perturbation approaches require pre-defined, non-dimensional perturbation parameters to get an analytical solution of higher-order accuracy. The present work proposes a homotopy perturbation based new framework for solution for tide-induced groundwater fluctuations. A homotopy perturbation based new analytical solution framework was utilized for tide-induced groundwater waves in isotropic/anisotropic unconfined aquifers with sloping/vertical beach face. The solutions are derived for Boussinesq equation and higher-order Boussinesq equation for coastal aquifers with vertical beach face/sloping beach face. The solution process results in the identification of non-dimensional parameters. The solution of higher-order Boussinesq equation is more accurate, and the solutions are not applicable for flatter beach slopes. Tidal fluctuations changes the salinity pattern in the intertidal zone and influences the rate and zone of freshwater discharge towards the sea. Tidal effects create separate saltwater circulation zone in the intertidal zone with inverse saline concentration with depth from beach face. Experimental works in sand-box setup were performed to study the groundwater waves under tidal boundary conditions for two different sands and two different slopes. The pressure data are recorded using pressure transducers at multiple points to observe the groundwater wave propagation. The amplitudes of the waves were attenuating exponentially with increasing distance from the seaside boundary. Similarly, phase differences from the tides were also increasing with distance from the seaside boundary. The amplitudes and time-averaged water table height data were used to calibrate the hydraulic conductivity of the sands. Experimental works completed to understand the influence of tidal fluctuations on coastal aquifers on density-dependent flow. Similarly, there is a scope to improve the understanding of contaminant transport pathways in the coastal aquifer environment. A simple image processing technique is used to analyse the saltwater wedge. The image processing technique adopted captures the interface of the dyed saltwater and freshwater interface well. Exper-

iments were done for two slopes  $\pi/12$  and  $\pi/6$  for coarse river sand and IS sand (Indian Standard sand). Upper saline plumes were developed in all four experimental cases of density-dependent flow. The extent of the upper saline plume was dependent on the freshwater flux. Time-averaged water table heights recorded at the inland boundary shows as an outlier in comparison with the numerically simulated time-averaged water table heights. This is due to freshwater flux injected at the inland boundary. Density neutral contaminant flow pathways were observed by injecting density neutral tracers/contaminants inside saltwater wedge and freshwater zone. The contaminant inside the saltwater wedge closer to the interface travels along the interface region to discharge in the saltwater boundary. Both freshwater and saltwater contaminants oscillates within tidal cycles in their movement.

# Contents

|  |             |
|--|-------------|
| <b>Title Page</b>                        | <b>i</b>    |
| <b>Certificate of Approval</b>           | <b>iii</b>  |
| <b>Certificate</b>                       | <b>v</b>    |
| <b>Acknowledgment</b>                    | <b>vii</b>  |
| <b>Declaration</b>                       | <b>ix</b>   |
| <b>List of Journal Publications</b>      | <b>xi</b>   |
| <b>Abstract</b>                          | <b>xiii</b> |
| <b>1 Introduction</b>                    | <b>1</b>    |
| 1.1 Overview . . . . .                   | 1           |
| 1.2 Objectives of the Thesis . . . . .   | 3           |
| 1.3 Organization of the Thesis . . . . . | 4           |
| 1.4 Summary . . . . .                    | 4           |
| <b>2 Literature Review</b>               | <b>5</b>    |
| 2.1 Overview . . . . .                   | 5           |

|          |  |           |
|----------|--|-----------|
| 2.2      | Tidal Influence without Density Effects . . . . .  | 5         |
| 2.2.1    | Analytical Solutions for Groundwater Waves in Response to Tidal Oscillations without Considering Density Effects . . . . . | 6         |
| 2.2.2    | Experimental Studies for Groundwater Waves in Response to Tidal Oscillations without Considering Density Effects . . . . . | 12        |
| 2.3      | Tidal Influence with Density Effects . . . . .   | 12        |
| 2.3.1    | Analytical and Semi-analytical Approach . . . . .  | 13        |
| 2.3.2    | Numerical Modeling Approach . . . . .  | 15        |
| 2.3.3    | Experimental Approach for Density-dependent Flow . . . . .   | 19        |
| 2.3.4    | Non-dimensional Parameters in Coastal Aquifer System . . . . .   | 23        |
| 2.4      | Motivations of the Study . . . . .   | 26        |
| 2.5      | Summary . . . . .  | 27        |
| <b>3</b> | <b>Mathematical Conceptualization</b>  | <b>29</b> |
| 3.1      | Overview . . . . .   | 29        |
| 3.2      | Governing Equations . . . . .  | 29        |
| 3.2.1    | Groundwater Flow Equation for Watertable Waves . . . . .   | 29        |
| 3.2.2    | Derivation of Second-order Boussinesq Equation for Anisotropic Condition . . . . .   | 32        |
| 3.2.3    | Richards' Equation for Variably Saturated-Saturated Flow in Porous Media . . . . .   | 34        |
| 3.2.4    | Transport Equation . . . . .   | 35        |
| 3.3      | Summary . . . . .  | 36        |
| <b>4</b> | <b>Experimental Conceptualization</b>  | <b>37</b> |
| 4.1      | Overview . . . . .   | 37        |

|          |   |            |
|----------|---|------------|
| 4.2      | Experimental Setup . . . . .  | 37         |
| 4.2.1    | Details of Instruments Used . . . . .   | 38         |
| 4.2.2    | Boundary Conditions . . . . .   | 42         |
| 4.3      | Summary . . . . .   | 43         |
| <b>5</b> | <b>Tidal Dynamics without Density Effects</b>   | <b>45</b>  |
| 5.1      | Overview . . . . .  | 45         |
| 5.2      | Analytical Solutions Using the HPM . . . . .  | 45         |
| 5.2.1    | Analytical Solutions for Groundwater Waves Driven by Tidal Oscillations in a Coastal Aquifer with Vertical Beach . . . . .                      | 45         |
| 5.2.2    | Analytical Solution for Groundwater Waves Driven by Tidal Oscillations in a Coastal Aquifer with a Sloping Beach . . . . .                      | 57         |
| 5.2.3    | Analytical Solution of Groundwater Waves in Anisotropic Unconfined Aquifers with Sloping Beach using Second-order Boussinesq Equation . . . . . | 75         |
| 5.3      | Experimental Study on Tidal Dynamics without Density Effects . .  | 82         |
| 5.3.1    | Experimental Procedure . . . . .  | 85         |
| 5.3.2    | CASE-1: Coarse River Sand with Beach Slope $\pi/6$ . . . . .  | 87         |
| 5.3.3    | CASE-2: Grade II IS sand with Beach Slope $\pi/12$ . . . . .  | 109        |
| 5.3.4    | Numerical Modeling to Estimate Hydraulic Conductivity and Porosity . . . . .  | 122        |
| 5.4      | Summary . . . . .   | 126        |
| <b>6</b> | <b>Tidal dynamics with Density Effects</b>  | <b>129</b> |
| 6.1      | Overview . . . . .  | 129        |
| 6.2      | Experiments on Saltwater Intrusion . . . . .  | 129        |
| 6.2.1    | Experimental Procedure . . . . .  | 129        |

|          |  |            |
|----------|--|------------|
| 6.2.2    | Saltwater Intrusion Experiment Details . . . . .     | 131        |
| 6.2.3    | Results and Discussion . . . . .                     | 140        |
| 6.2.4    | Tracer Tests . . . . .                               | 163        |
| 6.3      | Summary . . . . .                                    | 168        |
| <b>7</b> | <b>Conclusions and Future Scope</b>                  | <b>175</b> |
| 7.1      | Overview . . . . .                                   | 175        |
| 7.2      | Conclusions . . . . .                                | 177        |
| 7.3      | Recommendations for Future Works . . . . .           | 178        |
| <b>A</b> | <b>Tidal dynamics WO density effects:Exp Results</b> | <b>181</b> |
| A.1      | CASE-2B to CASE-2E . . . . .                         | 181        |

# List of Tables

|     |  |     |
|-----|--|-----|
| 2.1 | List of analytical solutions based on traditional perturbation approaches for the water table fluctuations in response to tidal oscillations . . . . .     | 11  |
| 2.2 | Comparison of standard codes for simulating saltwater intrusion phenomenon (Dhar, 2007) . . . . .  | 18  |
| 4.1 | Peristaltic pumps calibration data . . . . .   | 41  |
| 5.1 | Parameters used for solution comparisons . . . . .   | 53  |
| 5.2 | Error statistics for the comparison of HPM, Kong et al. (2011), and Teo et al. (2003) solutions with 2D-FEFLOW numerical solutions .                       | 72  |
| 5.3 | Error statistics for the comparison of HPM, Kong et al. (2011), Teo et al. (2003), Yeh et al. (2010) solutions with 2D-FEFLOW numerical solution . . . . . | 73  |
| 5.4 | Mean absolute percentage error (MAPE) between numerical solution and Kong et al. (2011), Roberts et al. (2011), and present solution                       | 80  |
| 5.5 | Parameter details of CASE-1 experiments . . . . .  | 96  |
| 5.6 | CASE-1A: Amplitude of waves corresponding to different frequencies.  | 96  |
| 5.7 | Parameter details of CASE-2 experiments . . . . .  | 109 |
| 5.8 | Error statistics of numerical simulations with details of amplitude errors and cumulative error of mean WL and amplitude . . . . .                         | 124 |
| 5.9 | Error statistics of numerical simulations of amplitude errors . . . . .  | 125 |

|     |   |     |
|-----|---|-----|
| 6.1 | CASE-3: Parameters used for FEFLOW saltwater intrusion modeling . . . . .                       | 147 |
| 6.2 | CASE-4: Parameters used for FEFLOW saltwater intrusion modeling . . . . .                       | 150 |
| 6.3 | CASE-5: Parameters used for FEFLOW saltwater intrusion modeling . . . . .                       | 155 |
| 6.4 | CASE-6: Parameters used for FEFLOW saltwater intrusion modeling . . . . .                       | 159 |
| 7.1 | Summary of analytical solutions of groundwater fluctuations due to tidal oscillations . . . . . | 176 |
| 7.2 | Summary of experimental cases . . . . .   | 177 |

# List of Figures

|     |  |    |
|-----|--|----|
| 1.1 | Simplified representation of coastal unconfined aquifer under for the tidal influence. Saltwater intrusion into aquifer manifests due to density variation between the freshwater in the aquifer and saltwater in the sea. Figure scale is magnified to several orders in the vertical direction. . . . .  | 3  |
| 3.1 | Definition sketch for unconfined coastal aquifer with tidal boundary condition. . . . .  | 31 |
| 4.1 | Schematic diagram of sandbox experimental setup. . . . .   | 39 |
| 4.2 | Peristaltic pumps calibration plots. Two peristaltic pumps named PP A and PP B respectively. . . . .   | 41 |
| 5.1 | Definition sketch for the tidal influence on groundwater table in a coastal unconfined aquifer with vertical beach face. . . . .   | 46 |
| 5.2 | CASE-L: Comparison of Homotopy perturbation solution with Song et al. (2007) second-order solution, Kong et al. (2011) third-order solution, and Roberts et al. (2011) sixth-order solution for an coastal unconfined aquifer with laboratory scale parameters: tidal wave timeperiod=62 s; D=0.0725 m; A=0.0725 m; $\eta_e = 0.3$ ; $\eta_e/K = 44 s/m$ . . . . . | 54 |
| 5.3 | CASE-F: Comparison of Homotopy perturbation solution with Song et al. (2007) second-order solution, Kong et al. (2011) third-order solution, and Roberts et al. (2011) sixth-order solution for an coastal unconfined aquifer with field scale parameters: tidal wave timeperiod=12 hr; D=5 m; A=2 m; $\eta_e = 0.3$ ; $K = 0.0005 m/s$ . . . . .                  | 55 |

|      |  |    |
|------|--|----|
| 5.4  | Convergence of homotopy perturbation solution up to third-order for an coastal unconfined aquifer with laboratory scale parameters: tidal wave timeperiod=62 s; D=0.0725 m; A=0.0725 m; $\eta_e = 0.3$ ; $\eta_e/K = 44 s/m$ . . . . .   | 55 |
| 5.5  | Convergence of homotopy perturbation solution up to third-order by using absolute percentage change for an coastal unconfined aquifer with laboratory scale parameters: tidal wave timeperiod=62 s; D=0.0725 m; A=0.0725 m; $\eta_e = 0.3$ ; $\eta_e/K = 44 s/m$ . . . . .   | 56 |
| 5.6  | Definition sketch for tidal influence on groundwater table in a coastal unconfined aquifer with a sloped beach . . . . .   | 57 |
| 5.7  | Cross-section of 2D FEFLOW simulation and solution comparison to show grid convergence for Scenario-A . . . . .  | 69 |
| 5.8  | Scenario-A: $\beta = \pi/12$ ; Comparison of Homotopy perturbation solution with Teo et al. (2003), Kong et al. (2011), and 2D FEFLOW solution for groundwater table fluctuation with a tidal wave with timeperiod= 12 hrs; D=5 m; A=2 m; $K = 0.0005 m/s$ ; $\eta_e = 0.3$ . . .  | 70 |
| 5.9  | Scenario-B: $\beta = \pi/6$ ; Comparison of Homotopy perturbation solution with Teo et al. (2003), Kong et al. (2011), and 2D FEFLOW solution for groundwater table fluctuation with a tidal wave with timeperiod= 12 hrs; D=5 m; A=2 m; $K = 0.0005 m/s$ ; $\eta_e = 0.3$ . . .   | 71 |
| 5.10 | Scenario-C (vertical beach): $\beta = \pi/2$ ; Comparison of Homotopy perturbation solution with Teo et al. (2003), Yeh et al. (2010) and Kong et al. (2011) for groundwater table fluctuation with a tidal wave with timeperiod= 12 hrs; D=10 m; A=0.5 m; $K = 0.0017 m/s$ ; $\eta_e = 0.2063$ . . . . .                              | 73 |
| 5.11 | Comparison between the numerical solution at the end of two year simulation and three year simulation of 2D FEFLOW numerical solution. Simulation parameters are corresponding to Scenario-C (vertical beach): $\beta = \pi/2$ ; a tidal wave with timeperiod= 12 hrs; D=10 m; A=0.5 m; $K = 0.0017 m/s$ ; $\eta_e = 0.2063$ . . . . . | 74 |
| 5.12 | Comparison of the homotopy perturbation solution for the higher-order Boussinesq equation with Kong et al. (2011), Roberts et al. (2011), and 2D FEFLOW solutions at different time instances for a tidal wave with timeperiod=12 hr; D=5 m; A=2 m; $\eta_e = 0.3$ ; $K = 0.0005 m/s$ ; and $\beta = 30^\circ$ . . . . .               | 80 |

|  |    |
|--|----|
| 5.13 Comparison of the homotopy perturbation solution for the anisotropic higher-order Boussinesq equation with different $K$ values for laboratory scale. . . . .   | 81 |
| 5.14 Comparison of the homotopy perturbation solution for the anisotropic higher-order Boussinesq equation with different $K$ values for laboratory scale. . . . .   | 82 |
| 5.15 Comparison of the homotopy perturbation solution for the anisotropic higher-order Boussinesq equation with different $r$ values for field scale. Parameters: $A = 2.0\text{ m}$ ; $D = 5.0\text{ m}$ ; $\eta_e = 0.3$ ; Time period= 12 hr. . . . . | 83 |
| 5.16 Comparison of the homotopy perturbation solution for the anisotropic higher-order Boussinesq equation with different $K$ values for laboratory scale. . . . .   | 84 |
| 5.17 Schematic of the coastal aquifer modeled in the experimental setup. . . . .   | 88 |
| 5.18 Pressure transducers calibration . . . . .  | 88 |
| 5.19 Raw pressure transducer data in volts and water height after calibration . . . . .  | 89 |
| 5.20 CASE-1A: Waves recorded by the pressure transducers for the clockwise and anticlockwise times of 180 s, resting period of 30 sand DC motor RPM 203. . . . .   | 90 |
| 5.21 CASE-1A: Waves recorded by the pressure transducers for the clockwise and anticlockwise times of 180 s, resting period of 30 sand DC motor RPM 203: magnified . . . . .   | 91 |
| 5.22 Sample waves in the left hand sides and FFT of the sample wave in the right hand side . . . . .   | 93 |
| 5.23 CASE-1A: Time-averages water table, amplitude and phase difference details of waves recorded by the pressure transducers for the clockwise and anticlockwise times of 180 s, resting period of 30 sand DC motor RPM 203. . . . .                    | 94 |
| 5.24 CASE-1A: FFT of waves recorded using pressure transducers pressure transducers for the clockwise and anticlockwise times of 180 s, resting period of 30 sand DC motor RPM 203. . . . .  | 95 |

|   |     |
|---|-----|
| 5.25 CASE-1B: Waves recorded by the pressure transducers for the clockwise and anticlockwise times of 180 s, resting period of 10 s, and DC motor RPM 203: magnified . . . . .  | 97  |
| 5.26 CASE-1B: Time-averages water table, amplitude and phase difference details of waves recorded by the pressure transducers for the clockwise and anticlockwise times of 180 s, resting period of 10 s, and DC motor RPM 203. . . . . | 98  |
| 5.27 CASE-1C: Waves recorded by the pressure transducers for the clockwise and anticlockwise times of 120 s, resting period of 3 s, and DC motor RPM 203: magnified . . . . .   | 98  |
| 5.28 CASE-1C: Time-averages water table, amplitude and phase difference details of waves recorded by the pressure transducers for the clockwise and anticlockwise times of 120 s, resting period of 3 s, and DC motor RPM 203. . . . .  | 99  |
| 5.29 CASE-1D: Waves recorded by the pressure transducers for the clockwise and anticlockwise times of 90 s, resting period of 5 s, and DC motor RPM 203: magnified . . . . .  | 99  |
| 5.30 CASE-1D: Time-averages water table, amplitude and phase difference details of waves recorded by the pressure transducers for the clockwise and anticlockwise times of 90 s, resting period of 5 s, and DC motor RPM 203. . . . .   | 100 |
| 5.31 CASE-1E: Waves recorded by the pressure transducers for the clockwise and anticlockwise times of 60 s, resting period of 5 s, and DC motor RPM 203: magnified . . . . .  | 100 |
| 5.32 CASE-1E: Time-averages water table, amplitude and phase difference details of waves recorded by the pressure transducers for the clockwise and anticlockwise times of 60 s, resting period of 5 s, and DC motor RPM 203. . . . .   | 101 |
| 5.33 Summary of time-averaged water table, and amplitude of waves recorded for CASE-1A to CASE-1E . . . . .   | 101 |
| 5.34 Summary of phases difference from tidal wave and frequencies of tidal waves for CASE-1A to CASE-1E . . . . .   | 102 |

|  |     |
|--|-----|
| 5.35 CASE-1A to CASE-1E: FFT of waves recorded using pressure transducers at Tide point, $PS_1^1, PS_2^1, PS_3^1, PS_4^1, PS_5^1$ . . . . .                                  | 103 |
| 5.36 Summary of phases difference from tidal wave and frequencies of tidal waves for CASE-1A to CASE-1E . . . . .  | 104 |
| 5.37 CASE-1A: Amplitudes of waves for different frequencies at pressure transducer locations . . . . .   | 104 |
| 5.38 CASE-1B: Amplitudes of waves for different frequencies at pressure transducer locations . . . . .   | 105 |
| 5.39 CASE-1C: Amplitudes of waves for different frequencies at pressure transducer locations . . . . .   | 105 |
| 5.40 CASE-1D: Amplitudes of waves for different frequencies at pressure transducer locations . . . . .   | 106 |
| 5.41 CASE-1E: Amplitudes of waves for different frequencies at pressure transducer locations . . . . .   | 106 |
| 5.42 Semi-logarithmic plot of amplitude calculated in time-domain in relation to distance for CASE-1 . . . . .   | 107 |
| 5.43 Semi-logarithmic plot of fundamental frequency amplitude calculated in frequency domain in relation to distance for CASE-1 . . . . .                                    | 107 |
| 5.44 Semi-logarithmic plot of $3\omega$ harmonic amplitude calculated in frequency domain in relation to distance for CASE-1 . . . . .                                       | 108 |
| 5.45 Semi-logarithmic plot of $5\omega$ harmonic amplitude calculated in frequency domain in relation to distance for CASE-1 . . . . .                                       | 108 |
| 5.46 Schematic of the coastal aquifer modeled in the experimental setup for CASE-2 . . . . .   | 109 |
| 5.47 CASE-2A: Waves recorded by the pressure transducers for the clockwise and anticlockwise times of 300 s, resting period of 50 sand DC motor RPM 161: magnified . . . . . | 110 |

|   |     |
|---|-----|
| 5.48 CASE-2A: Time-averaged water table, amplitude and phase difference details of waves recorded by the pressure transducers for the clockwise and anticlockwise times of 300 s, resting period of 50 sand DC motor RPM 161. . . . . | 111 |
| 5.49 CASE-2A: FFT of waves recorded using pressure transducers pressure transducers for the clockwise and anticlockwise times of 300 s, resting period of 50 sand DC motor RPM 161. . . . .   | 112 |
| 5.50 Summary of time-averaged water table, and amplitude of waves recorded for CASE-2A to CASE-2E . . . . .   | 113 |
| 5.51 Summary of phases difference from tidal wave and frequencies of tidal waves for CASE-2A to CASE-2E . . . . .   | 114 |
| 5.52 CASE-2: FFT of waves recorded using pressure transducers at Tide point, $PS_1^2$ , $PS_2^2$ , $PS_3^2$ , $PS_4^1$ , $PS_5^1$ . . . . .   | 115 |
| 5.53 CASE-2A: Amplitudes of waves for different frequencies at pressure transducer locations . . . . .  | 116 |
| 5.54 CASE-2B: Amplitudes of waves for different frequencies at pressure transducer locations . . . . .  | 116 |
| 5.55 CASE-2C: Amplitudes of waves for different frequencies at pressure transducer locations . . . . .  | 117 |
| 5.56 CASE-2D: Amplitudes of waves for different frequencies at pressure transducer locations . . . . .  | 117 |
| 5.57 CASE-2E: Amplitudes of waves for different frequencies at pressure transducer locations . . . . .  | 118 |
| 5.58 Semi-logarithmic plot of amplitudes calculated in time domain in relation to distance for CASE-2 . . . . .   | 118 |
| 5.59 Semi-logarithmic plot of $\omega$ harmonic amplitude calculated in frequency domain in relation to distance for CASE-2 . . . . .   | 119 |
| 5.60 Semi-logarithmic plot of $2\omega$ harmonic amplitude calculated in frequency domain in relation to distance for CASE-2 . . . . .  | 119 |

|      |   |     |
|------|---|-----|
| 5.61 | Semi-logarithmic plot of $3\omega$ harmonic amplitude calculated in frequency domain in relation to distance for CASE-2 . . . . .   | 120 |
| 5.62 | Semi-logarithmic plot of $4\omega$ harmonic amplitude calculated in frequency domain in relation to distance for CASE-2 . . . . .   | 120 |
| 5.63 | Semi-logarithmic plot of $5\omega$ harmonic amplitude calculated in frequency domain in relation to distance for CASE-2 . . . . .   | 121 |
| 5.64 | CASE-1 numerical modeling 2D-FEFLOW mesh . . . . .  | 122 |
| 5.65 | CASE-1B: Comparison of groundwater waves of experimental observation and 2D-FEFLOW model results of hydraulic conductivity $0.0069\text{ m/s}$ ( $600\text{ m/day}$ ) . . . . . | 127 |
| 6.1  | Red food dye from Neoteric DCBA Ideas . . . . .   | 130 |
| 6.2  | Red food dye from Colourmist Aroma, Bakersville India Pltd . . . . .  | 130 |
| 6.3  | Rhodamine B type from Lobachemie . . . . .  | 130 |
| 6.4  | CTD Divers calibration . . . . .  | 131 |
| 6.5  | Aquifer configuration details of saltwater intrusion experiments . . . . .  | 133 |
| 6.6  | CASE-3: Digital photograph detailing the test section of the sand-box model . . . . .   | 134 |
| 6.7  | Stepwise changes of image analysis of digital photograph. Figures are illustrative without proper scales. . . . .   | 139 |
| 6.8  | CASE-3: Concentration of saltwater recorded in CTD-Diver placed inside the saltwater reservoir. . . . .   | 141 |
| 6.9  | CASE-3: Pressure waves of pressure data recorded from time zero s to 8400 s. Timeperiod of the waves is 600 s . . . . .   | 142 |
| 6.10 | CASE-3: Pressure waves of pressure data recorded from time zero s to 8400 s (magnified). Timeperiod of the waves is 600 s . . . . .   | 143 |
| 6.11 | CASE-3: Pressure waves of pressure data recorded from time 8400 s to 24000 s (magnified) . . . . .  | 144 |

|      |   |     |
|------|---|-----|
| 6.12 | Summary of time-averaged water table, and amplitude of waves recorded for CASE-3 . . . . .  | 144 |
| 6.13 | CASE-3: Digital image after 2 hours 10 minutes (7800) from experiment start [freshwater flux reduced to $6.00 \text{ m/d}$ ( $6.944 \times 10^{-5} \text{ m/s}$ )] . . . . .  | 145 |
| 6.14 | CASE-3: Boundary conditions used for FEFLOW simulation . . . . .  | 145 |
| 6.15 | CASE-3: FEFLOW model elements with the salt concentration contours at the end of the experiment. . . . .  | 146 |
| 6.16 | CASE-3: Digital image after 6 hours (21600 s) from experiment start [4 hours and 40 minutes or 280 minutes after freshwater flux reduced to $3.00 \text{ m/d}$ ( $3.472 \times 10^{-5} \text{ m/s}$ )] . . . . .  | 148 |
| 6.19 | CASE-4: Digital image after 1 hours 30 minutes (5400 s) from experiment start [freshwater flux is $3.00 \text{ m/d}$ ( $3.472 \times 10^{-5} \text{ m/s}$ )] . . . . .  | 151 |
| 6.20 | CASE-4: Digital image after 12 hours (43200 s) from experiment start [freshwater flux reduced to $3.00 \text{ m/d}$ ( $3.472 \times 10^{-5} \text{ m/s}$ )] . . . . .   | 152 |
| 6.23 | CASE-4: Comparison digital image when freshwater flux was $6.00 \text{ m/d}$ ( $6.944 \times 10^{-5} \text{ m/s}$ ) at 36000 s and freshwater flux was $3.00 \text{ m/d}$ ( $3.472 \times 10^{-5} \text{ m/s}$ ) at 43200 s . . . . .   | 154 |
| 6.24 | CASE-5: Digital image after 8 hours 30 minutes (30600 s) from experiment start [freshwater flux reduced to $3.00 \text{ m/d}$ ( $3.472 \times 10^{-5} \text{ m/s}$ )] . . . . .   | 154 |
| 6.25 | CASE-5: Concentration of saltwater recorded in CTD-Diver placed inside the saltwater reservoir. The points near zero concentration are the point when CTD-Diver was removed from the experimental setup to verify the concentration data. . . . .   | 156 |
| 6.28 | CASE-6: Concentration of saltwater recorded in CTD-Diver placed inside the saltwater reservoir. . . . .   | 158 |
| 6.29 | CASE-6: Experimental results of freshwater flux $2.50 \text{ m/d}$ ( $2.894 \times 10^{-5} \text{ m/s}$ ). Images are at 6 hours and 8 hours 45 minutes . . . . .   | 160 |
| 6.32 | CASE-6: CASE-6: Velocity vector plots with in a tidal wave period . . . . .<br>Experimental results of freshwater flux $2.50 \text{ m/d}$ ( $2.894 \times 10^{-5} \text{ m/s}$ ).<br>Images are at 6 hours and 8 hours 45 minutes. Scale of vectors is given at bottom right of Figure 6.32j. . . . . | 162 |

|   |     |
|---|-----|
| 6.33 CASE-3: Images for tracer injections from time 12600 s. The tracer plume oscillates along with the tidal water level. . . . .  | 164 |
| 6.34 CASE-3: Images for tracer injections from time 15800 s till the experiment end. Tracer plume shape changes over time with the spread direction changes . . . . .   | 166 |
| 6.35 CASE-3: Tracer plume movement in 2D FEFLOW modelling of tracer injected in freshwater zone. Trace plume The concentration of the tracer was same as tap water used for the freshwater. The tracer plume oscillations along with the tidal water level within a tidal cycle is shown. . . . . | 167 |
| 6.36 CASE-3: Tracer plume movement in 2D FEFLOW modelling of tracer injected in freshwater zone. Trace plume The concentration of the tracer was same as tap water used for the freshwater. Trace plume movement from injection time to end of experiment is shown. 168                           |     |
| 6.37 CASE-3: Images of tracer plumes recorded from time 13800 s to 14880 s. . . . .   | 169 |
| 6.38 CASE-3: Tracer plume movement in 2D FEFLOW modelling of tracer injected inside the saltwater wedge. The concentration of the tracer was 35000 mg/l . . . . .   | 170 |
| 6.39 CASE-3: Tracer plume movement in 2D FEFLOW modelling of tracer injected in freshwater zone. Trace plume The concentration of the tracer was same as tap water used for the freshwater. The tracer plume oscillations along with the tidal water level within a tidal cycle is shown. . . . . | 170 |
| 6.40 CASE-4: Tracer plumes recorded from at different times. Images of the plume injected in the freshwater zone(TP4). . . . .  | 172 |
| 6.41 CASE-4: Tracer plumes recorded from at different times. Images of the plume injected inside saltwater wedge(TP5). . . . .  | 173 |
| 6.42 CASE-4: Tracer plumes recorded from at different times. Images of the plume injected inside saltwater wedge(TP5). . . . .  | 174 |

|   |     |
|---|-----|
| A.1 CASE-2B: Waves recorded by the pressure transducers for the clockwise and anticlockwise times of 181 s, resting period of 30 s and DC motor RPM 161: magnified . . . . .  | 181 |
| A.2 CASE-2B: Time-averages water table, amplitude and phase difference details of waves recorded by the pressure transducers for the clockwise and anticlockwise times of 180 s, resting period of 30 s and DC motor RPM 161. . . . . | 182 |
| A.3 CASE-2C: Waves recorded by the pressure transducers for the clockwise and anticlockwise times of 180 s, resting period of 20 s and DC motor RPM 161: magnified . . . . .  | 182 |
| A.4 CASE-2C: Time-averages water table, amplitude and phase difference details of waves recorded by the pressure transducers for the clockwise and anticlockwise times of 180 s, resting period of 20 s and DC motor RPM 161. . . . . | 183 |
| A.5 CASE-2D: Waves recorded by the pressure transducers for the clockwise and anticlockwise times of 120 s, resting period of 20 s and DC motor RPM 161: magnified . . . . .  | 183 |
| A.6 CASE-2D: Time-averages water table, amplitude and phase difference details of waves recorded by the pressure transducers for the clockwise and anticlockwise times of 120 s, resting period of 20 s and DC motor RPM 161. . . . . | 184 |
| A.7 CASE-2E: Waves recorded by the pressure transducers for the clockwise and anticlockwise times of 90 s, resting period of 20 s and DC motor RPM 161: magnified . . . . .   | 184 |
| A.8 CASE-2E: Time-averages water table, amplitude and phase difference details of waves recorded by the pressure transducers for the clockwise and anticlockwise times of 90 s, resting period of 20 s and DC motor RPM 161. . . . .  | 185 |

# Chapter 1

## Introduction

### 1.1 Overview

Coastal aquifers play an important role in supporting the freshwater needs of the highly populated coastal areas. More than half of the world's population lives within 60 km of the shoreline (UNCED, 1992), and more than 17 million people live in coastal districts of India (MOEFCC, 2017). Groundwater abstraction will increase 39% by 2050 compared to 2010 (Burek et al., 2016). Groundwater dynamics in coastal areas and related saltwater intrusion are important for aquifer management. Apart from providing for the freshwater needs, groundwater fluxes to the sea play an important role in carrying the nutrient, metal, and organic compounds to the oceans (Moore, 2003). Burnett et al. (2003) defined submarine groundwater discharge (SGD) as "all flow of water on continental margins from the seabed to the coastal ocean, regardless of fluid composition or driving force." SGD plays an important role in the discharge of important constituents for the coastal environment. In the near coastal areas, higher density seawater enters coastal aquifers and overlain by freshwater due to the density difference between freshwater and seawater (Figure 1.1). In the mixing zone, the saltwater mixes with the freshwater flux, and it moves along the interface to discharge in the seaward boundary. This process causes seawater circulation in the saltwater region. Tidal fluctuations change the salinity pattern in the intertidal zone and influences the rate and zone of freshwater discharge towards the sea. Tidal effects create separate saltwater circulation zone (Figure 1.1) in the intertidal zone with inverse saline concentration with depth from beach face (Boufadel, 2000; Robinson et al., 2007a, b; Kuan et al., 2012). Freshwater from the inland pinches in between the saltwater region in the bottom and the inverse saline distribution region. Overall, flux from saltwater circulation in the saltwater wedge, freshwater discharging from inland, and saline water discharging from the circulation in the

inverse salt distribution region all are called as submarine groundwater discharge (SGD). There is a dynamic equilibrium between intruding seawater and regional freshwater flux. The equilibrium is negatively influenced by excessive pumping of coastal aquifers, land-use change, the influence of tidal fluctuations on the water table, and rise in seawater level due to climate change impact (in longer timescale) (Werner et al., 2013). The understanding of the processes in coastal aquifers are important for optimal planning of pumping rates, selection of pumping well locations without contaminating the production wells with saltwater, to identify the nutrient or contaminant pathways, and to decide the infrastructures in the coastal zones.

Quantification of tidal influence on the groundwater table is important. Groundwater table waves in a coastal aquifer can be modeled by Boussinesq equation derived based on Dupuit's approximation (Parlange et al., 1984; Nielsen, 1990; Song et al., 2007; Kong et al., 2011). The Boussinesq equation is nonlinear in nature, and the beach slope introduces further complexity in the interaction between groundwater and tidal water. Analytical solution for the Boussinesq equation with a tidal boundary condition is difficult to solve since the boundary (the intersection of seawater and the aquifer) is moving along the beach slope in the intertidal zone. Existing perturbation solutions consider either fixed boundary for sloping beaches (Nielsen, 1990) or uses coordinate transformation to fix the moving boundary (Li et al., 2000; Teo et al., 2003; Jeng et al., 2005a, b; Roberts et al., 2011).

Saltwater intrusion in coastal aquifers can be modeled with two different approaches: a) sharp interface approach in which the freshwater and seawater separated by sharp interface assuming there is no mixing between freshwater and seawater, and b) dispersed interface approach. Dispersed interface approach is based on the hydrodynamic mixing between seawater and fresh water due to forced advection, hydrodynamic dispersion, and free convection. Dispersed interface forms a transition zone of freshwater salt concentration to seawater salt concentration. In reality, it is not possible for a sharp interface since mixing between freshwater and seawater exists. However, if the aquifer has narrow mixing zone, sharp interface approach can be used since it is computationally less expensive when compared to dispersed interface modeling, and also, dispersed interface approach develops numerical dispersion when it is used to model narrow mixing zone. If there is a wide mixing zone, the dispersed interface approach is better suited since the spatial and temporal distributions of salt concentrations become essential. Dispersed interface approach can be modeled by solving coupled groundwater flow and salt transport equations simultaneously. Many works have been done to solve seawater intrusion with numerical modeling and experiments based on density-dependent flow; but,

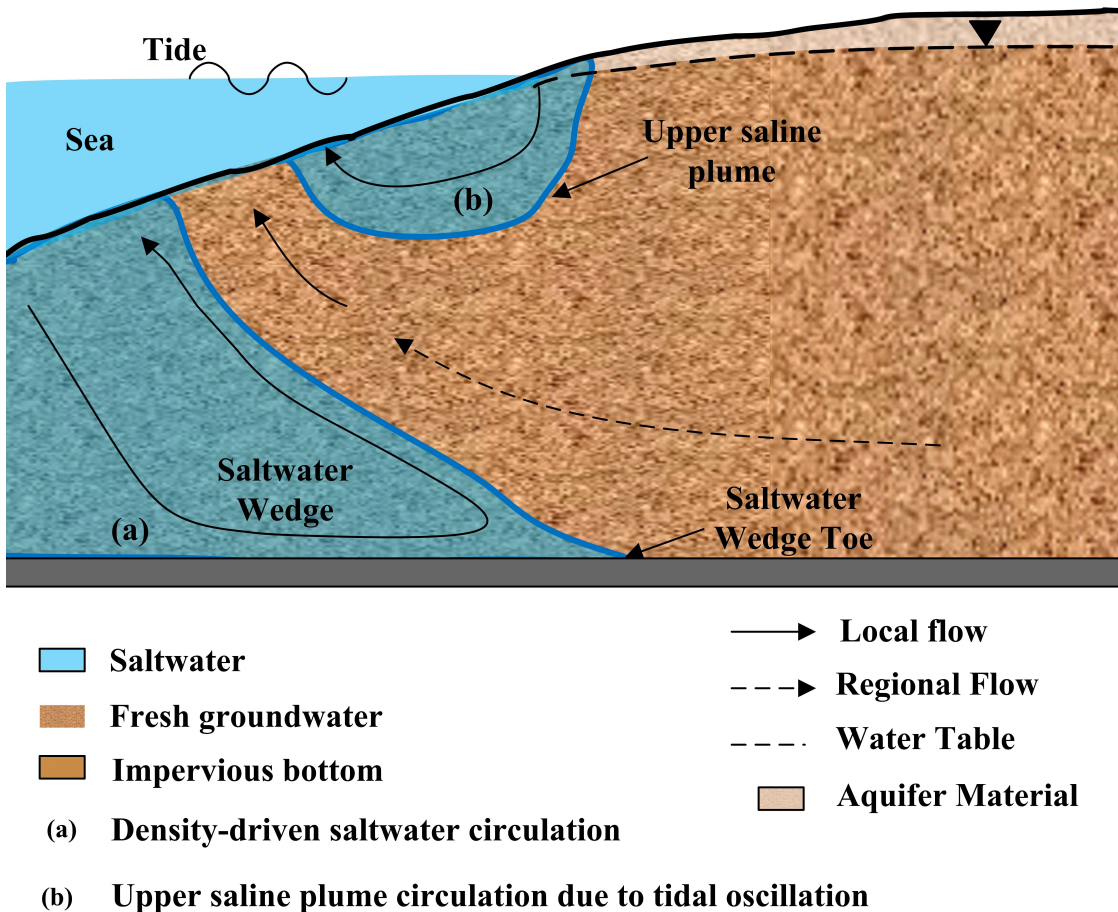


Figure 1.1: Simplified representation of coastal unconfined aquifer under for the tidal influence. Saltwater intrusion into aquifer manifests due to density variation between the freshwater in the aquifer and saltwater in the sea. Figure scale is magnified to several orders in the vertical direction.

very few experimental works completed to understand the influence of tidal fluctuations on coastal aquifers. Similarly, there is a scope to improve the understanding of contaminant transport pathways in the coastal aquifer environment (Chang and Clement, 2013; Oz et al., 2015).

## 1.2 Objectives of the Thesis

The main objective of this study is to understand the influence of tidal fluctuations in coastal aquifers. Additionally, this study also has the following objectives:

1. To develop analytical solutions for groundwater fluctuations due to tidal influence in coastal aquifers.
2. To experimentally investigate the tidal influence in coastal aquifers by using direct pressure measurement method with pressure sensors.
3. To experimentally investigate the saltwater intrusion problem in the coastal aquifer under tidal conditions.

4. To study the tracer movement pathway of the neutral density tracers injected in freshwater and saltwater wedge regions.

### 1.3 Organization of the Thesis

The thesis consists of seven chapters, including this introductory chapter. This chapter discussed the fundamentals of groundwater fluctuations due to tidal oscillations, saltwater intrusion due to density variation between freshwater and saltwater, and the influence of tidal oscillations on the saline distribution in the aquifer.

Chapter 2 deals with the related literature review.

Chapter 3 devoted to the mathematical conceptualization of the problem and related governing equations. Governing equations are given for deriving analytical solutions for groundwater fluctuations due to tidal fluctuations, numerical modeling to validate the analytical solutions, and density-dependent flow governing equations to validate the laboratory experimental results.

Chapter 4 revolves around the experimental conceptualization for laboratory scale experiments, and related instruments used to perform the experiment and record experimental data.

Chapter 5 deals with the tidal dynamics in coastal aquifers without considering the density-dependent flow. This chapter is divided into two major parts: i) Analytical solutions for the groundwater waves by using the Homotopy Perturbation Method (HPM) and ii) Sandbox experiments of groundwater waves in response to tidal oscillations without considering density-dependent flow.

Chapter 6 discusses the experiments on density-dependent flow laboratory experiments under tidal boundary conditions. It also covers the tracers tests done in the experiments to observe the contaminant plume movements. In Chapter 7, an overview of the present study, conclusions, and the recommendations for the future works are presented.

### 1.4 Summary

This chapter provided the introductions of the present study, objectives of this thesis, and the organization of the thesis. Next chapter discusses the relevant literature for the thesis.

# Chapter 2

## Literature Review

### 2.1 Overview

Tidal oscillations affect the dynamics of groundwater in coastal aquifers. The groundwater table in the coastal aquifers oscillates due to its interaction with the tidal oscillations. Freshwater in the coastal aquifers is contaminated by saltwater intrusion process. This chapter discusses the analytical solutions and experimental studies for the groundwater oscillations in response to tidal oscillations without considering density effects. In the later part, studies related to tidal influence on groundwater waves and salinity intrusion due to density effects are discussed. In general, groundwater oscillations and saltwater intrusion studies can be classified as follows: i) Analytical and semi-analytical approach, ii) Experimental approach and iii) Mathematical or numerical modeling approach.

### 2.2 Tidal Influence on Coastal Aquifers without Considering Density Effects

Impact of climate change and associated sea level changes have increased the vulnerability of the coastal aquifers (Feseker, 2007; Oude Essink et al., 2010; Chang et al., 2011). Tidal forcing, often with amplitude between 1 m and 2 m (Kong et al., 2011; Fakir and Razack, 2003), influences the groundwater table variations in coastal aquifers (Parlange et al., 1984; Nielsen, 1990; Fakir and Razack, 2003). The influence of tide-induced water table fluctuations can propagate up to few hundred meters inland from the seaside boundary (Li et al., 2000). The analytical solutions can be used to fit the wave number and amplitude of the free wave models for the propagation of fluctuations in field aquifers by using the observed piezometric head data (Raubenheimer et al., 1999; Fakir and Razack, 2003; Chen et al., 2011).

### 2.2.1 Analytical Solutions for Groundwater Waves in Response to Tidal Oscillations without Considering Density Effects

Philip (1973) provided an exact asymptotic analytical solution for time-averaged effects of nonlinearity on water table introduced by tidal influence in a coastal aquifer with vertical beach face by solving one-dimensional Boussinesq's equation. Philip (1973) considered a homogeneous aquifer with horizontal flow field below the water table (Dupuit-Forchheimer assumption) and provided an asymptotic solution for the time-averaged water table at far away from the beach. Knight (1981) proved that Philip's solution is valid for two-dimensional flow.

Traditionally, the interaction between tide and groundwater can be reasonably modeled by nonlinear Boussinesq's equation or linearized form of Boussinesq's equation (Dagan, 1967; Nielsen, 1990; Li et al., 2000; Song et al., 2007; Kong et al., 2011). Dagan (1967) and Parlange et al. (1984) derived Boussinesq's equation using a small perturbation parameter. Parlange et al. (1984) provided first-order (starting from zeroth-order) solution for water table fluctuations in a coastal aquifer with vertical beach face under tidal boundary condition using amplitude parameter for perturbation expansion. Nielsen (1990) provided a perturbation solution for vertical beach face and sloped beach (without seepage face) using linearized Boussinesq's equation. The perturbation solution was developed using an amplitude parameter ( $A/D$ ) and slope parameter ( $A \cot(\beta) \sqrt{\eta_e \omega / 2KD}$ , where  $\beta$ ,  $\eta_e$ ,  $\omega$  and  $K$  are beach slope angle with the horizontal, effective porosity of the aquifer, frequency of the tidal wave and hydraulic conductivity of the aquifer respectively). However, Nielsen (1990) study has not considered the moving boundary effects in sloped beaches. The asymptotic time-averaged solution matches with the overheight solution provided by Philip (1973) ( $A^2/4D$ ,  $A$  — tidal amplitude,  $D$  — depth of mean sea level above the impervious bed). Nielsen (1990) findings based on field data as well as the analytical solution can be given as, i) the minimum water level in the aquifer is always higher than the low tide level (seepage face develops), ii) due to nonlinear filtering effects of the beach sand there is a temporal asymmetry between the rise of the water table during rising tide and fall of the water table during ebbing tide, iii) water level fluctuation damps with the distance from the beach, and iv) there is a phase lag exist in the water table fluctuation. The difference between the mean sea level and time-averaged watertable for far inland points without any regional groundwater flow is called as overheight. The overheight in the water table is important to quantify the submarine groundwater discharge (SGD) (Burnett et al., 2003; Song et al., 2006).

Teo et al. (2003), Jeng et al. (2005a), Song et al. (2006), and Roberts et al. (2011) introduced moving boundary effects due to beach slope by using coordinate transformation. Liu and Wen (1997) derived a nonlinear, diffusive equation equivalent to Boussinesq's equation for groundwater flow in the shallow porous medium using non-dimensional parameters representing free-surface fluctuations and shallowness of the aquifer using length scale, and provided a solution for periodic tidal forcing. Traditional perturbation solutions for water table fluctuations in vertical beach as well as sloped beaches use either dimensional or non-dimensional physical parameters (Li et al., 2000; Teo et al., 2003; Jeng et al., 2005a; Song et al., 2006, 2007; Roberts et al., 2011; Stojasavljevic et al., 2012). The generation of secular terms (secular terms make the solution unbounded) hinder obtaining higher-order solutions in perturbation methods. Secular terms can be eliminated by using extra perturbation expansion for the boundary conditions (Song et al., 2007; Kong et al., 2011). The solution for the vertical beach was derived using the amplitude parameter and solution for sloping beach derived using  $\epsilon$  for perturbation expansion. The amplitude parameter, wave number and  $\epsilon$  are given as,

$$\alpha_N = \frac{A}{D}, \quad (2.1)$$

$$k_N = \sqrt{\frac{\eta_e \omega}{2KD}}, \quad (2.2)$$

$$\epsilon = k_N A \cot(\beta), \quad (2.3)$$

where  $A$  is the amplitude of the tidal wave,  $D$  is mean sea level above the impervious bottom,  $\eta_e$  is the effective porosity of the aquifer,  $K$  is the hydraulic conductivity of the aquifer,  $\omega$  is the tidal wave angular frequency, and  $\beta$  is the angle of beach slope. Li et al. (2000) considered time-dependent moving boundary effects along the slope of beach in deriving an analytical solution for linearized Boussinesq's equation by using the same perturbation parameters as in Nielsen (1990) solution. Both Nielsen (1990) and Li et al. (2000) solutions are valid for steep slopes. Teo et al. (2003) used the shallow water parameter (without including beach slope) along with amplitude parameter to get a higher-order perturbation solution for the sloped aquifer. The solution shows that the water table fluctuations increase with flatter slope. Jeng et al. (2005a) derived a perturbation solution for two-dimensional, tide-induced water table fluctuation for sinusoidal coastal line by incorporating amplitude parameter, shallow-water parameter (ratio of mean tidal height to the linear decay length) and a separate parameter for shoreline oscillation (coastline parameter). Jeng et al. (2005b) derived a new equation for groundwater flow using steepness parameter ( $\xi$ ) and provided a solution using

non-dimensionalization similar to Teo et al. (2003).

$$\xi = \frac{A}{L_J}, \quad (2.4)$$

$$L_J = \frac{1}{k_N} = \sqrt{\frac{2KD}{\eta_e \omega}}. \quad (2.5)$$

Song et al. (2007) provided a higher-order perturbation solution for a vertical beach face by using one-dimensional Boussinesq's approximation considering a new perturbation parameter, which has a maximum value less than one (0.82). Maximum time-averaged water table height in the unconfined aquifer  $D_{\infty, Song}$  is used to get the perturbation parameter  $\beta_{Song}$ . The secular terms (secular terms are unbounded) generated in the solution process are removed by using a series expansion for the boundary conditions. The parameters used by Song et al. (2007) are given below,

$$\beta_{Song} = A/D_{\infty, Song}, \quad (2.6)$$

$$D_{\infty, Song} = D \sqrt{1 + \alpha_N^2/2}. \quad (2.7)$$

Kong et al. (2011) used two perturbation parameters, including amplitude parameter and a new perturbation parameter ( $r_{Kong}$ ) based on the slope to provide a higher-order solution for one-dimensional Boussinesq's equation considering a sloping beach. Kong et al. (2011) used the unconfined aquifer thickness, including tide-induced overheight  $D_{\infty, Kong}$  for wave number expression to get amplitude parameter  $\alpha_{Kong}$  and  $r_{Kong}$  for a perturbation solution. Kong et al. (2011) eliminated the secular terms from the tidal boundary conditions by using perturbation expansion. In this process, the parameter  $D_{\infty, Kong}$  is obtained by solving an implicit equation. The parameters used by Kong et al. (2011) are defined as,

$$\alpha_{Kong} = A/D_{\infty, Kong}, \quad (2.8)$$

$$r_{Kong} = \epsilon_{Kong}/(1 + \epsilon_{Kong}), \quad (2.9)$$

$$\epsilon_{Kong} = A \cot(\beta) \sqrt{\eta_e \omega / (2KD_{\infty, Kong})}. \quad (2.10)$$

In traditional perturbation methods, nonlinear partial differential equation(s) is/are decomposed into a series of linear partial differential equations using pre-defined perturbation parameter(s). Moreover, the solutions are applicable only for small values of perturbation parameters (Nielsen, 1990; Teo et al., 2003). Homotopy perturbation method eliminates the limitations of traditional perturbation method by introducing virtual parameter(s) for the perturbation approach. By

applying the parameter-expansion approach, the secular terms can be removed. In this removal process, the unknown parameter values are obtained (Xu, 2007). The solutions obtained are valid not only for small parameters, but also for very large parameters. In the present study, a higher-order analytical solution is derived for the Boussinesq's equation with periodic boundary condition in a coastal unconfined aquifer with a vertical beach face by using the homotopy perturbation method with parameter expansion (He, 2014).

Analytical solution for the Boussinesq equation with a tidal boundary condition is difficult to solve since the boundary (the intersection of seawater and the aquifer) is moving along the beach slope in the intertidal zone. Table 2.1 shows the list of analytical solutions for tide-induced groundwater wave oscillations by using traditional perturbation methods for the different governing equations and perturbation parameters. The analytical solutions are provided for the coastal aquifer with vertical beach face or sloping beach face. These analytical solutions can be used for calibration to determine the parameter values for field aquifers (Jha and Singh, 2014). Existing perturbation solutions consider either fixed boundary for sloping beaches (Nielsen, 1990) or uses coordinate transformation to fix the moving boundary (Li et al., 2000; Teo et al., 2003; Jeng et al., 2005a, b; Roberts et al., 2011). Song et al. (2006) derived a solution from linearized Boussinesq equation to obtain expressions for water table overheight by using Fourier-series, and proved that asymptotic water table overheight equals tidal amplitude. Chang et al. (2010) derived groundwater fluctuations under tidal oscillation for oceanic islands of finite lengths with two different sloping beaches on both sides by using traditional perturbation technique. Yeh et al. (2010) provided a closed form analytical solution for anisotropic aquifer with vertical beach based on Fourier sine transformation and Laplace transformation. The solution for two-dimensional groundwater table fluctuation derived by non-dimensionalizing the governing equations and boundary conditions. Second-order slope terms in the free surface boundary condition are neglected. Asadi-Aghbolaghi et al. (2012) derived analytical solutions for coastal aquifer system consisting of a lower confined aquifer overlain by aquitard above it and an unconfined aquifer above it by using Fourier series and studied the effect of the bottom slope. Recently, Hsieh et al. (2015) derived closed-form analytical solutions for linearized Boussinesq equation for a coastal unconfined aquifer with sloping beach, sloping aquifer bottom and rainfall by dividing the aquifer zone to rainfall zone and non-rainfall zone. Hsieh et al. (2015) proved that tidal fluctuation enhanced due to large rainfall intensity. However, steeper aquifer bottom slope decreases the effect of rainfall intensity on fluctuations. Horn (2006) discussed the studies on beach groundwater flow fluctuations till 2006. Hsieh et al. (2015) and

Asadi-Aghbolaghi et al. (2012) discussed the developments on the analytical solutions for groundwater fluctuations due to tidal effects.

Traditional perturbation approaches require pre-defined, non-dimensional perturbation parameters to get an analytical solution of higher-order accuracy. Liao (Liao, 1992, 2004) introduced the Homotopy analysis method (HAM) to derive analytic solutions for nonlinear problems based on the homotopy of topology. The Homotopy analysis method is valid irrespective of the perturbation parameter is small or not (Liao, 1997). However, traditional perturbation techniques need a perturbation parameter(s) to be small. Homotopy analysis method is used by several studies to find solutions for nonlinear problems (Zhu et al., 2009; Nadeem and Hussain, 2009; Si et al., 2011). The homotopy perturbation method (HPM) was introduced by He (He, 1999, 2000, 2003, 2012) to solve nonlinear problems. In the HPM, a homotopy equation is constructed by using virtual parameter(s), and the solution is expanded using virtual perturbation parameter(s) similar to the traditional perturbation approaches. The homotopy equation should deform from the approximate problem to the original one when the virtual parameter(s) deform from zero to one. The homotopy equation can also be constructed using parameter expansions (Munusamy and Dhar, 2016, 2017) and/or auxiliary terms to eliminate secular terms from the solution. The secular terms make the solution unbounded. Hence, secular terms need to be removed to derive higher-order solutions. The auxiliary term is constructed in a way that it does not affect the initial or the final solution. The auxiliary terms (He, 2012) become zero when the perturbation parameter is equal to zero or one.

Fenton (1990) derived a new second-order governing equation for groundwater table dynamics by using the shallow water theories from coastal hydrodynamics and hydraulic engineering. This equation was a simplified form of Dagan's second-order equation (Dagan, 1967). The head at any point was considered to be varying quadratically between the surface and the bottom. Nielsen et al. (1997) obtained the same equation by assuming the vertical velocity was linearly varying between the surface and the bottom. The correction for the deviation from the hydrostatic pressure due to vertical velocity in the pressure distribution was used to derive the second-order Boussinesq's equation for intermediate aquifer depths. The Boussinesq's equation for Dupuit-Forchheimer assumption was used as an initial approximation. Nielsen et al. (1997) provided solutions for the linearized form of the Boussinesq's equation for intermediate depth by assuming small amplitude oscillations. Liu and Wen (1997) derived the second-order equation for Boussinesq's assumption by using two parameters: i) shallowness parameter and ii) nonlinearity parameter (representing the surface displacement) and provided an analytical so-

Table 2.1: List of analytical solutions based on traditional perturbation approaches for the water table fluctuations in response to tidal oscillations

| Reference                  | BE <sup>a</sup>     | NDE <sup>b</sup> | BS <sup>c</sup> | TBC <sup>d</sup> | SO <sup>e</sup>  | STT <sup>f</sup> |
|----------------------------|---------------------|------------------|-----------------|------------------|------------------|------------------|
| Parlange et al. (1984)     | BQE <sup>g</sup>    | Y                | N               | Y                | FO <sup>h</sup>  | N                |
| Nielsen (1990)             | LBQE <sup>i</sup>   | N                | Y               | Y                | FO               | N                |
| Liu and Wen (1997)         | Equivalent to BQE   | Y                | N               | Y                | FO               | N                |
| Li et al. (2000)           | LBQE                | N                | N               | Y                | FO               | N                |
| Teo et al. (2003)          | LE+KBC <sup>j</sup> | Y                | Y               | Y                | SEO <sup>k</sup> | N                |
| Jeng et al. (2005b)        | LE+KBC              | Y                | Y               | Y                | SEO              | N                |
| Song et al. (2007)         | LE+KBC              | Y                | N               | N                | SEO              | STT with BC      |
| Kong et al. (2011)         | BQE                 | Y                | Y               | Y                | SEO              | STT with BC      |
| Stojavljevic et al. (2012) | LE+KBC              | Y                | Y               | N                | NA               | NA               |

Y-Yes;

N-NO;

NA- Not Applicable;

<sup>a</sup> BE-Basic Equation;<sup>b</sup> NDE- Non-dimensional Equation used;<sup>c</sup> BS-Beach Slope;<sup>d</sup> TBCS- Tidal BC Exactly satisfied;<sup>e</sup> SO- Solution Order;<sup>f</sup> STT-Secular Term Treatment;<sup>g</sup> BQE- Boussinesq Equation;<sup>h</sup> FO- First Order;<sup>i</sup> LBQE- Linearized Boussinesq Equation;<sup>j</sup> LE+KBC- Laplace Equation with Kinematic BC;<sup>k</sup> SEO- Second Order.

lution by using a perturbation method. The parameters were assumed to be small ( $\ll 1$ ). Li et al. (2000) introduced additional terms for capillary effects in Nielsen

et al. (1997) equation and provided analytical solutions for the linearized equation for small amplitude oscillations. Castro-Orgaz and Dey (2014) showed that the generalized unsteady flow groundwater flow equation derived by using the Picard's iteration without accretion simplifies to the Dagan's perturbation equation of the shallow aquifer theory.

### 2.2.2 Experimental Studies for Groundwater Waves in Response to Tidal Oscillations without Considering Density Effects

The solutions of groundwater waves by using simple theories assuming Dupuit-Forchheimer assumption, not considering variable saturation due to capillary effects, and small-amplitude fluctuations exhibited that amplitude decay rate and rate of increase in phase lag from the tide as equal (Parlange et al., 1984). However, field data of groundwater oscillations showed that the amplitude decay rate is faster than the phase lag increase rate Nielsen (1990). A few laboratory scale experiments were done to study the water table fluctuations including one-dimensional sand column experiments (Nielsen and Perrochet, 2000) and two-dimensional sandbox experiments Ataie-Ashtiani et al. (1999); Cartwright et al. (2003, 2004). Cartwright et al. (2003) performed laboratory scale experiment of groundwater waves in an unconfined aquifer with a vertical beach face. The ratio of the real part (representing amplitude attenuation rate) to the imaginary part (phase lag increase rate) is more than one (2.7). Since natural geometry is complex, laboratory experimental data are required to understand the physical processes in controlled experimental situations, and the laboratory data can be used to validate the analytical solutions and numerical models (Hsieh et al., 2015). There are few experimental studies available for groundwater waves(Ataie-Ashtiani et al., 1999; Cartwright et al., 2003, 2004). However, still more data needed to cover a wide range of tidal conditions.

## 2.3 Tidal Influence with Density Effects

The density difference between the dense seawater and freshwater in the aquifer causes dense seawater to enter the coastal aquifers. Density gradients due to the density difference cause gravitational instabilities, and it causes free convective transport towards inland in porous medium (Oostrom and Dane, 1992). The hydraulic head difference between seawater and freshwater causes forced convection. Hence, the saltwater intrusion is caused by mixed convection, i.e., combination of free convection and forced convection (Smith, 2004). Saltwater intrusion in the coastal aquifer can be modeled in two different approaches: a) sharp inter-

face approach in which the freshwater and seawater separated by a sharp interface assuming there is no mixing between freshwater and seawater, and b) dispersed interface approach.

Sharp interface models can be approached in two ways generally (Essaid, 1990), i) two fluid approach in which freshwater and saltwater flow equations solved simultaneously and, ii) single fluid approach only considering flow in the freshwater region by assuming saltwater as static (Ghyben-Herzberg assumption). Dispersed interface approach can be modeled by solving groundwater flow equation and salt transport equation simultaneously by coupling the salt concentration and fluid density. The nonlinearity introduced due to the coupling of groundwater flow and salt transport makes the seawater intrusion problem difficult to model. The review of seawater intrusion process and the historical perspective, recent advances and future challenges can be found in Reilly and Goodman (1985), Bear et al. (1999), Simmons et al. (2001), Diersch and Kolditz (2002), Post (2005), and Werner et al. (2013). Tidal effects create separate saltwater circulation zone in the intertidal zone with inverse saline concentration with depth from beach face (Boufadel, 2000; Robinson et al., 2007a, b; Kuan et al., 2012). This zone is called the upper saline plume (USP). Fresh ground discharge pinches in between the saltwater wedge and the upper saline plume, and it is called a freshwater discharge zone (FDZ). Seawater intrusion problem can be solved by following solution methods: i) Analytical and semi-analytical approach, ii) Experimental approach and iii) Mathematical or numerical modeling approach.

### 2.3.1 Analytical and Semi-analytical Approach

Quantitative analysis of freshwater-saltwater relationship shows a highly complex, nonlinear physical system. The seawater intrusion problem rarely treated in terms of fully three-dimensional, density-dependent miscible fluid flow in porous medium (Reilly and Goodman, 1985). Badon Ghyben and Herzberg derived an expression for the depth of interface below mean sea level by assuming using Dupuit's assumption and static interface using relationship between freshwater head and saltwater head at the water table.

$$\xi = \frac{h_f}{\epsilon}, \quad (2.11)$$

where,  $\xi$  — the distance between mean sea level and interface,  $h_f$  — freshwater head and,  $\epsilon = \frac{\rho_s - \rho_f}{\rho_f}$  is density difference factor or buoyancy factor. The interface is located at a depth 40 times the distance between mean sea level and water table from the mean sea level (for  $\rho_s = 1025 \text{ kg/m}^3$ ). Hubbert (1940) related

the pressure at the interface by using separate freshwater head and saltwater head. Glover (1959) provided an analytical solution for the sharp interface using complex potential for flow nets, with freshwater discharge.

Henry (1959) found a solution by assuming a sharp interface with complex potential in a hodograph plane using conformal mapping. Cooper (1959) developed a hypothesis to explain the mixing of seawater and freshwater and the associated seawater circulation near the zone of dispersion and proved it using field data of Biscany aquifer, Florida (Cooper, 1964). Henry (1964) developed a semi-analytical solution by assuming dispersed interface for a two-dimensional vertical slice of a confined aquifer. Aquifer assumed to be homogeneous, isotropic with constant freshwater flux from the landward boundary and hydrostatic saltwater boundary in the seaward side. Flow and salt transport equations developed using stream function and semi-analytical solution for steady state developed using double Fourier series for stream function and salt concentration assuming constant dispersion coefficient. Double Fourier series expanded for 78 terms and the streamlines, and isochlors (line joining same concentration points) found. Henry problem with an aspect ratio of two is considered as a benchmark to validate the numerical codes. Henry problem was improved by modifications on freshwater flux, boundary conditions, anisotropy, and other parameters (Pinder and Cooper, 1970; Segol et al., 1975; Frind, 1982b; Croucher and O'sullivan, 1995; Simpson and Clement, 2004; Dentz et al., 2006; Abarca et al., 2007; Younes and Fahs, 2013). Bear and Dagan (1964), De Jong (1965), and Strack (1972) used hodograph method to find exact analytical solutions for coastal aquifer with a horizontal drain. They considered vertical plane two-dimensional cross section considering Dupuit's assumptions are valid.

Sikkema and Dam (1982), Dam and Sikkema (1982), Bakker (2006) provided analytical solutions for the sharp interface by solving the nonlinear ordinary differential equation for the confined aquifer, semi-confined aquifer and combined confined semi-confined aquifer. Governing equations become one-dimensional ordinary differential equations by assuming Dupuit's assumption valid. Strack (1976) introduced single, continuous potential throughout multi-zone aquifers to overcome the lack of information on the boundary condition. Strack provided a methodology to solve steady-state sharp freshwater-saltwater interface problem with single well for semi-infinite aquifers by assuming Dupuit's assumptions as valid, and vertical flow is negligible compared to horizontal freshwater flux. The analytical solution based on superimposed Thiem's solution is applicable for both confined and unconfined aquifers. Several studies developed techniques to find solution for saltwater intrusion problems using Strack's potential.

Hunt (1985) expanded Strack's (Strack, 1976) solution for the steady-state saltwater interface in the presence of single and multiple recharge wells to get a closed-form analytical solution. Mantoglou (2003) developed an analytical solution for finite rectangle coastal unconfined aquifer using Strack's potential and utilized it to develop pumping optimization model using the method of images. The analytical method is used to optimize the pumping rate using toe constraint and potential constraint separately. Potential constraint problem is a linear one and provides a safer solution compared to a nonlinear, computationally expensive toe constraint problem. Koussis et al. (2012) expanded Strack's analytical solution for sloped aquifer bottom with the flow parallel to the bottom and a well gallery idealised as a sink. In their study, the gravity part of the hydraulic potential linearized to find the analytical solution. The pumping volumes and rates are converted to equivalent two-dimensional well gallery discharge while applying the solution for the Akrotiri coastal aquifer, Cyprus. There are several other analytical solutions for saltwater intrusion developed recently (Strack and Ausk, 2015; Lu et al., 2016; Strack, 2017).

### 2.3.2 Numerical Modeling Approach

Pinder and Cooper (1970) developed a numerical technique for determining transient saltwater front under the effect of dispersion based on the method of characteristics (MOC) for a two-dimensional problem. Flow equation in terms of pressure (Boussinesq's approximation valid and no storage effects) and transport equation in terms of dissolved salt concentration used as governing equations. Method of characteristics equations developed for solute transport equation and solved using an explicit finite difference scheme. Flow equation solved for pressure using alternating direction implicit procedure. Dispersion coefficient assumed as a scalar and constant in space as well as time.

The efficiency of the numerical scheme validated by comparing the transient solution with Henry's steady state sharp interface solution and the 0.5 isochlors of the diffused interface steady state solution. Two initial conditions considered: i) Aquifer is filled with freshwater initially, and the movement of transient interface with time was analysed. ii) Henry's sharp interface steady state solution as an initial condition, and the 0.5 isochlor movements with time were analysed. Transient position of the saltwater front at 100 minutes was simulated. There was no clarification given in the paper whether the solution attains steady state. Flow paths confirmed the existence of saltwater recirculation.

Lee and Cheng (1974) developed a finite element model (FEM) with triangular

elements to study the effect of dispersion on steady state two dimensional saltwater intrusion problem with constant dispersion coefficient for Peclet number higher than Pinder and Cooper (1970) (Pe: 100 — 1000). The numerical method applied to Biscayne aquifer field values. Distance between the toe location and inland boundary as well as dividing nose of seawater recirculation are in a semilogarithmic relationship with Peclet number.

Segol et al. (1975) used Galerkin-finite element method to solve two-dimensional transient, nonlinear flow and transport equations of dispersive saltwater intrusion problems for layered, nonhomogeneous aquifer with two-dimensional tensor representing dispersion coefficient. Nearby seaside vertical boundary, vertical component of velocity is not zero due to the averaging process in the finite element method. The results with linear isoparametric elements and quadratic isoparametric elements compared with 0.5 isochlors of Cooper (1964) and Pinder and Cooper(1970). Simulations were done for 100 mins transient equations. Frind (1982a) developed a Galerkin finite element model using linear elements to reduce the computational effort while simulating long-term transient density-dependent transport in groundwater. Previous transient saltwater intrusion studies neither reached dynamic equilibrium due to computational costs nor used velocity-dependent dispersion coefficients.

Robinson and Gallagher (1999) used two-dimensional, field scale, FEM model for groundwater discharge process in tidal conditions using density-dependent fluid flow approach for unconfined aquifer using equivalent freshwater head and concentration. While comparing the result without tidal fluctuation, the toe of the saltwater wedge moved seaward, and there is a surficial mixing zone with inverse concentration distribution with depth. Robinson and Gallagher (1999) code cannot simulate surficial mixing zone concentration distribution.

Bouzouf et al. (2001) simulated seawater intrusion by solving coupled partial differential equations based on the sharp interface approach using a finite volume. Liu et al. (2002) developed an unstructured mesh, vertex-centered, two-dimensional finite volume model, using triangular elements to solve density-dependent coupled flow and transport equation for a confined aquifer. The numerical scheme accuracy was validated by simulating modified Henry's problem for a transient solution, and they were in good agreement with Huyakorn and Andersen (1987) and Cheng et al. (1998).

Liu et al. (2006) developed two-dimensional control volume finite element model with quadrilateral, nonuniform element mesh developed to simulate saltwater in-

trusion of heterogeneous, anisotropic aquifer system at Gooburrum, Bundaberg, Queensland, Australia. The governing equations are in pressure form for flow equation, and solute transport is in concentration form. The scheme is validated for Henry problem with transient simulation time 100 minutes (Pinder and Cooper, 1970; Frind, 1982a; Voss and Souza, 1987). Steady state solution with uniform areal recharge and transient solutions with pumping wells simulated with time adaptive schemes for the aquifer simulated and they were in good agreement with simulation by SUTRA code.

Hamidi et al. (2006) developed an unstructured mesh, vertex-centered, two dimensional finite volume model using triangular elements to solve density-dependent coupled flow and transport equation for a confined and unconfined aquifer. The numerical scheme accuracy was validated by simulating modified Henry's problem for the transient solution and they were in good agreement with (Huyakorn and Andersen, 1987; Frind, 1982a; Cheng et al., 1998; Liu and Bhatia, 2001). Inouchi et al. (1990) simulated tidal influence on the freshwater-saltwater interface using a hybrid scheme finite element for spatial domain and finite difference discretization for time domain and found that seawater intrudes the furthest inland during ebb tide.

Bouzouf and Chen (2014) sharp interface simulation of unstructured mesh finite volume model for the Llobregat delta aquifer compared quasi three-dimensional sharp interface solutions for the structured finite difference model by Essaid (1990). Finite volume model gives better results compared to the sharp model by Essaid (1990).

Li and Jiao (2013) reviewed the numerical modeling on submarine groundwater discharge under the influence of tidal fluctuation with different beach slope conditions. The review included several numerical modeling codes, e.g., SUTRA, MARUN, SEAWAT2000, COMSOL, and PHWAT.

Table 2.2: Comparison of standard codes for simulating saltwater intrusion phenomenon (Dhar, 2007)

| Code        | Physical Concepts |                 |                 |                 |                 |                 |                 |                 |                 |                 | Spatial dist    |                  |                 | Numerical method |                 |                 |
|-------------|-------------------|-----------------|-----------------|-----------------|-----------------|-----------------|-----------------|-----------------|-----------------|-----------------|-----------------|------------------|-----------------|------------------|-----------------|-----------------|
|             | AD <sup>a</sup>   | SI <sup>b</sup> | SU <sup>c</sup> | St <sup>d</sup> | Ad <sup>e</sup> | CR <sup>f</sup> | SF <sup>g</sup> | TF <sup>h</sup> | ST <sup>i</sup> | TT <sup>j</sup> | Is <sup>k</sup> | NIs <sup>l</sup> | Q3 <sup>m</sup> | 3D <sup>n</sup>  | FD <sup>o</sup> | FE <sup>p</sup> |
| FEFLOW      | ✓                 |                 | ✓               | ✓               | ✓               |                 | ✓               | ✓               | ✓               | ✓               | ✓               | ✓                | ✓               |                  | ✓               |                 |
| FEMWATER    | ✓                 |                 | ✓               |                 |                 | ✓               | ✓               | ✓               | ✓               | ✓               | ✓               | ✓                | ✓               |                  | ✓               |                 |
| HST3D       | ✓                 |                 |                 | ✓               | ✓               | ✓               | ✓               | ✓               | ✓               | ✓               | ✓               | ✓                | ✓               | ✓                | ✓               | ✓               |
| MOCDENSE3D  | ✓                 |                 |                 | ✓               | ✓               |                 |                 | ✓               | ✓               | ✓               | ✓               | ✓                | ✓               | ✓                | ✓               |                 |
| MODHMS      | ✓                 |                 | ✓               |                 |                 |                 |                 |                 |                 |                 |                 |                  |                 |                  | ✓               | ✓               |
| SEAWAT      | ✓                 |                 |                 | ✓               | ✓               |                 | ✓               | ✓               | ✓               | ✓               | ✓               | ✓                | ✓               | ✓                | ✓               |                 |
| SHARP       |                   | ✓               |                 |                 | ✓               |                 |                 | ✓               | ✓               | ✓               | ✓               | ✓                | ✓               | ✓                | ✓               |                 |
| SUTRA       | ✓                 |                 |                 | ✓               |                 | ✓               | ✓               | ✓               | ✓               | ✓               | ✓               | ✓                | ✓               | ✓                | ✓               |                 |
| SWIFT       | ✓                 |                 |                 | ✓               | ✓               | ✓               | ✓               | ✓               | ✓               | ✓               | ✓               | ✓                | ✓               | ✓                | ✓               |                 |
| SWI-Package |                   | ✓               |                 | ✓               |                 |                 |                 | ✓               | ✓               | ✓               |                 |                  | ✓               | ✓                | ✓               |                 |

<sup>a</sup>Advection-Dispersive model (ADM)<sup>b</sup>Sharp interface model (SI)<sup>c</sup>Saturated-unsaturated (SU)<sup>d</sup>Saturated (St)<sup>e</sup>Adsorption (Ad)<sup>f</sup>Chemical Reactions (CR)<sup>g</sup>Steady Flow (SF)<sup>h</sup>Transient Flow (TF)<sup>i</sup>Steady Transport (ST)<sup>j</sup>Transient Transport (TT)<sup>k</sup>Isothermal (Is)<sup>l</sup>Non Isothermal (NIs)<sup>m</sup>Quasi Three Dimension (Q3)<sup>n</sup>Three Dimension (3D)<sup>o</sup>Finite Difference (FD)<sup>p</sup>Finite Elements (FE)<sup>q</sup>Volume Elements (VE)

### 2.3.3 Experimental Approach for Density-dependent Flow

Boufadel (2000) experimentally studied the effects of buoyancy with tidal boundary conditions. Boufadel (2000) performed two experiments: i) with density difference between seawater and freshwater is negligible and ii) significant density difference similar to seawater and freshwater in field aquifers. In the second case, the inverted salinity distribution in the intertidal zone was observed. It was proven that viscosity effects are negligible in the later case.

Zhang et al. (2002) experimentally investigated the different density contaminant plume movements in the freshwater region in an unconfined coastal aquifer under the presence of saltwater diffusion and tidal condition. Image processing technique (Schincariol et al., 1993) used to find the spatial concentration distribution. Optical density was related to solute concentration, and the relationship was found by a calibration experiment in flow tank using different concentration solution. Lesser density plume had a relatively sharp interface and traveled with freshwater flux and exits as a concentrated plume in the upper portion of the aquifer. The denser plume had more diffusive front and became more diffusive when it nears the saltwater interface due to upward flow velocity nearby it. Results show that the saltwater interface influences the contaminant movement.

Volker et al. (2002) investigated the influence of the saltwater wedge on the transport of a dense contaminant plume by experiment and numerical model using finite element code – 2DFEMFAT. Experiments were done using similar set up used by Zhang et al. (2002) without tidal simulation in seawater boundary. The contaminant plume movement in the experiment and numerical simulation compared until the plume reaches the saltwater-freshwater diffusion interface. After the plume reaches the saltwater wedge, only numerical model results were used for analysis. If the numerical simulation neglected the higher dense saltwater boundary the plume traveled further horizontal and exit under the sea. If higher density due to saltwater wedge considered, the contaminant traveled upwards along with the saltwater-freshwater interface and exited nearby shoreline which increases the pollution of the coastline.

Fiber-optic fluorometry was used to detect point related concentration of fluorescein for measuring mixed scale reactive transport by Jose and Cirpka (2004). Same technique applied in large scale sandbox experiment on longitudinal effective dispersion by Jose et al. (2004). At the concentration range of  $100 \mu\text{g/l}$ , the fluorescence intensity of the tracer is proportional to its concentration. Fiber optic measurement probe of diameter 2.5 mm was used to detect the point concentration

of the tracer.

Nakagawa et al. (2005) had done sandbox experiment to find steady state saltwater interface using a red dye solution to compare the performance between constrained interpolation profile (CIP) and method of characteristics (MOC) for solving density-dependent flow and transport equation for saltwater intrusion process. The study established that the CIP method gives acceptable if not accurate results like MOC method, and the CIP method can be an alternative since the MOC method is complex and time-consuming.

Goswami and Clement (2007) had done laboratory scale experiment to get benchmark data for density-dependent seawater intrusion problem. Goswami and Clement (2007) study involved data collection for saltwater interface and freshwater flux for i) steady-state saltwater interface ii) transient, advancing saltwater interface under reduced freshwater and saltwater boundary head difference iii) transient, retreating saltwater interface under increased head difference between freshwater and saltwater. Benchmark datasets checked for numerical simulation with SEAWAT. The evaluation of worthiness of the benchmark data sets had been done by comparing numerical simulation data generated with a density-coupled solution with uncoupled solution method given by Simpson and Clement (2003). From the worthiness analysis, it was found steady state data of low freshwater data, and transient data sets are sensitive to the density-coupling effects; they can be used as benchmark datasets.

Luyun et al. (2009) investigated the dynamics of residual saltwater trapped in the storage area created by a subsurface dam to minimize saltwater intrusion using flow tank experiment in a two dimensional, homogeneous, isotropic porous medium, and numerical simulations using SEAWAT in a coastal unconfined aquifer. After steady-state saltwater wedge develops, cut off wall of 20 cm and 40 cm installed at the bottom of the aquifer and toe of the saltwater wedge recorded until no observable change witnessed. Saltwater storage created in the landward side due to the installation of cutoff is flushed out by freshwater, and it was depended on the size of the cutoff wall. The cutoff size should be more than the saltwater wedge height at that place for full flush out and lesser the size of it faster the flush out process. SEAWAT model adequately simulates the saltwater interface dynamics created by installation of cutoff wall.

Abarca and Clement (2009) used colorimetric method in a laboratory-scale seawater intrusion experiment to identify the dispersive mixing zone. The width of the mixing zone was used to quantify the dispersion coefficients. The experimental set

up was similar to Goswami and Clement (2007) setup with acidic saltwater of pH 4.7, and alkaline freshwater of pH 10.0 used to observe freshwater-saltwater mixing zone. After steady-state saltwater interface developed the freshwater reservoir was replaced with an alkaline freshwater solution of pH 11.6, which had pH indicator phenolphthalein. In the transition zone, alkaline freshwater reacted with acidic saltwater and formed a bright pink mixing zone. Numerical simulations data using SUTRA code fitted with observed data to determine the mixing zone parameters: longitudinal ( $\alpha_L$ ) dispersivity and transverse ( $\alpha_T$ ) dispersivity. This method is limited to advection-dominated systems in which the effects of differences in molecular diffusion coefficients can be disregarded.

Luyun et al. (2011) experimentally investigated the effect of location and application of recharge well and, location and penetration of subsurface barriers which are installed to reduce the seawater intrusion. Subsurface barriers were partially penetrated impervious layer to change the flow field. The steady-state saltwater interface developed using a similar procedure in Luyun et al. (2009) and then continuous recharge of 20% of freshwater flux and 40% freshwater flux applied. Saltwater was mixed with red color dye, and recharge water was mixed with blue color dye for observation. Toe movement and movement of saltwater wedge recorded and compared with Hunt's (Hunt, 1985) closed-form analytical solution for steady-state saltwater intrusion under single or multiple recharge wells. Seawater wedge retreated more with the increase in recharge rate. Subsurface barrier experiments done by installing barriers of four different depths after establishing steady state saltwater wedge and it was found that, with more depth of barrier, the more repulsion of saltwater wedge achieved. The experimental data used to find parameters for numerical simulation by SEAWAT code, and the effective location of the recharge well and subsurface barriers are found. Recharge well should be located near the toe for more effectiveness, and the barrier should be nearby coastline and more depth for more effectiveness. If the barrier was the landward side of the saltwater wedge, then the saltwater intrusion increases with an increase in subsurface barrier depth.

Chang and Clement (2012) investigated the impacts of climate change in saltwater intrusion process using laboratory experiments and numerical modeling for two flux controlled saltwater intrusion problems: regional flow from the inland boundary, and the other areal recharge flux due to climate impact on rainfall. They concluded saltwater intrusion and receding processes are asymmetric, and the timescales are different — for intruding wedge process takes more time to reach steady state than receding wedge.

Kuan et al. (2012) have done laboratory experiments and numerical simulations to investigate the influence of tidal oscillations on transient development of saltwater wedge. Experiments were performed in the two-dimensional sandbox with arrangements to provide constant rate freshwater flux from the landward reservoir and driving mechanism to provide simple sinusoidal tidal oscillations by a variable head overflow column. The seaward boundary slope was maintained 1:3.8 vertical to horizontal. The saltwater solution prepared by dissolving sodium chloride and red food dye. The spatial concentration distribution was found by image analysis of high-resolution photographs taken every 15 s during the experiment. The numerical simulations were done for both laboratory-scale and field-scale by variable saturated variable-density groundwater code SUTRA without any recharge or evapotranspiration. However, image analysis was not comprehensive enough to give information about the concentration distribution.

Tidal influence experiments develop two saltwater circulation zones separated by freshwater discharge zone (FDZ) — an upper saline plume (USP) in the intertidal zone in addition to lower saltwater wedge. Upper saline plume (USP) has circulation flow system which infiltrates at the high tide level and discharges to sea near low tide level. Development of upper saline plume is more rapid than a saltwater wedge, and tidal influence reduces the extent for seawater intrusion toe landwards. The influence of tidal oscillations is more significant for lower freshwater discharge rate. For reduced tidal amplitude, upper saline plume contracted, and saltwater intrudes further inland.

Chang and Clement (2013) investigated the transport process inside the saltwater wedge and the mixing region using laboratory experiment and numerical model. They used red-dyed water for freshwater, green-dyed slug for contaminant injection, and colorless saltwater for the experiment. After creating steady-state condition greed-dyed slug of  $1\text{ g/cm}^3$  injected in the freshwater region (above saltwater wedge) for the test-1 and the numerical modeling parameters fixed on the experimental data. Test-2 was done by injecting slightly dense contaminant slug of density  $1.0125\text{ g/cm}^3$  injected in the freshwater region to test the model performance using calibrated parameter values from test-1. Test-3 was done by injecting dense green-dyed slug of density  $1.025\text{ g/cm}^3$  inside saltwater wedge to observe the contaminant transport inside the saltwater wedge. The density was carefully maintained to match the saltwater density so that the slug acts as a neutral tracer. The dense tracer ( $1.025\text{ g/cm}^3$ ) injected in freshwater region sinks while traveling towards saltwater wedge and moves above saltwater wedge once it reaches the interface. Saltwater wedge acted as no flow boundary for the tracer injected in the freshwater region. The transport of neutral tracer injected inside the saltwater

wedge travels slower than the contaminant transport in the freshwater region, and it did not follow the classical circulation pattern. The tracer slug elongated due to a higher level of mixing activity when it reaches near freshwater saltwater interface. The plume transported rapidly once it reached interface and discharged as a narrow finger instead of the circular slug. For the small-scale laboratory analysis, the transport rate inside the saltwater region was two orders of magnitude lesser than the transport rate inside the saltwater region in field scale. However, large-scale numerical simulations for field scale transport rates shown the transport rate in the saltwater region is comparable or even higher than the transport rate in the freshwater region.

Laboratory scale two-dimensional experiments to study the saltwater intrusion in layered freshwater lenses have been used widely in recent studies (Stoeckl and Houben, 2012; Dose et al., 2014; Stoeckl et al., 2015). A three-dimensional laboratory scale experimental setup was used to validate the steady-state solutions of sharp interface under pumping well conditions (Shi et al., 2011).

### 2.3.4 Non-dimensional Parameters in Coastal Aquifer System

Shoemaker (2004) has studied sensitivity analysis (Hill, 1998) of parameters for a saltwater intrusion model by numerically simulating seawater intrusion using SEAWAT-2000, and universal inverse modeling routine UCODE for identification of the parameters and calibration of the models. Regional groundwater flow, dispersivity, effective porosity, horizontal conductivity, vertical conductivity, and recharge are the parameters considered for sensitivity analysis. By composite scaled sensitivity analysis, it is found that dispersivity as an important parameter for producing a steady-state distribution of seawater intrusion. Shoemaker provided effective observation locations for the hydraulic head, salinity, and flow observation based on sensitivity analysis.

Held et al. (2005) investigated the effective parameters and upscaling of two dimensional, benchmark Henry problem using homogenization upscaling theory to find out the influence of natural heterogeneity and upscaled parameterizations in density-dependent saltwater intrusion problem. The study investigated homogeneous case and heterogeneous case with permeability fields based on cross-correlated random fields obtained by direct Fourier transform method. Large scale solution obtained by homogenizing pressure equation and salt mass fraction equation in two different length scales: i) small length scale represents correlation lengths of heterogeneous permeability scales and ii) large length scale which related macro-

scopic length scale of field observations. Local dispersion coefficients rather than macro-dispersion coefficients determine the extent of saltwater intrusion and width of mixing zone.

Dentz et al. (2006) discussed the influence of non-dimensional numbers on steady-state variable-density flow and transport in homogeneous porous media. Peclet number (Pe) represents the ratio between advective transport rate to diffusive transport rate and coupling parameter ( $\alpha_c$  — ratio of density-induced characteristic velocity to velocity without density effects) represents the importance of density effects. Abarca et al. (2007) introduced and analyzed anisotropic Henry problem using non-dimensional parameters. Henry (1964) problem solution is based on coupling parameter, Peclet number, and aspect ratio.

Pool and Carrera (2011) introduced a correction factor for the error in the analytical solution based on the sharp interface assumption using Strack's potential (Strack, 1976). They compared the analytical solution based on sharp interface assumption and numerical solution for non-dimensional flow and transport equation based on diffused mixing zone assumption for a single well problem in a coastal confined aquifer. The multiplying correction factor is based on non-dimensional parameter using the ratio of transverse dispersivity to the aquifer thickness.

Kaleris and Ziogas (2013) studied the effects of the cutoff wall in controlling the saltwater intrusion using non-dimensional parameters including flow parameters, transport parameters, aquifer dimensions, dimensions of the cutoff wall, and the location of the cutoff wall. Kaleris and Ziogas (2013) analysed the effects of the cutoff wall without extraction, with horizontal drains, and with single extraction well to find safe extraction rate.

From the literature review following non-dimensional parameters identified for density-dependent saltwater intrusion problem:

1. Coupling parameter ( $\alpha_c$ ) (Dentz et al., 2006): the ratio of velocity due to buoyancy effects ( $K\epsilon$ ) to that of with out buoyancy effect ( $\frac{K\Delta h_0}{L}$ ). This is the ratio of buoyancy force to the viscous force.

$$\alpha_c = \frac{\epsilon L}{\Delta h_0} \quad (2.12)$$

Where,

$K$  — hydraulic conductivity of the aquifer,

$\epsilon$  — buoyancy factor,

$$\epsilon = \frac{\rho_s - \rho_f}{\rho_f},$$

$\Delta h_0 = h_0 - d$ ; head difference between freshwater boundary and saltwater boundary without density effects,

$h_0$  — equivalent freshwater head at inland boundary,

$d$  — thickness of the aquifer. In some studies (Segol et al., 1975) inverse of the coupling parameter is used by considering velocity with out density effect as freshwater flux ( $q_f$ ).

$$a = \frac{q_f}{K\epsilon} \quad (2.13)$$

2. Peclet numer (Pe) (Dentz et al., 2006): the ratio of advective transport ( $K\Delta h_0$ ) to diffusive transport ( $D\eta_e$ ).

$$Pe = \frac{K\Delta h_0}{D_m\eta_e} \quad (2.14)$$

Where,

$\eta_e$  — effective porosity of the aquifer,

$D_m$  — constant diffusion coefficient.

3. Aspect ratio ( $\zeta = d/L$ ) (Dentz et al., 2006) of the aquifer with  $L$  is longitudinal length of the aquifer, and  $d$  is depth of the aquifer.
4. Abarca et al. (2007) considered vertical hydraulic conductivity ( $K_Z$ ) for characteristic buoyancy flux to get coupling parameter and the ratio of vertical hydraulic conductivity to horizontal hydraulic conductivity. Non-dimensional numbers from anisotropic dispersive Henry problem are given as (Abarca et al., 2007),

$$a = \frac{q_f}{K_Z\epsilon} \quad (2.15)$$

$$r_K = \frac{K_Z}{K_X} \quad (2.16)$$

$$r_\alpha = \frac{\alpha_T}{\alpha_L} \quad (2.17)$$

$$b_L = \frac{\alpha_L}{d} \quad (2.18)$$

5. Rayleigh number (Ra) (Ataie-Ashtiani et al., 2014), is the ratio of buoyancy forces (free convection transport) to dispersive/viscous forces which disperses

solute and dissipates free convection.

$$Ra = \frac{\rho g k \epsilon d}{\eta_e \mu D_0} \quad (2.19)$$

$$(2.20)$$

Where,

$k$  — intrinsic permeability of the porous medium,

$\mu$  — dynamic viscosity of the fluid,

$D_0$  — diffusion coefficient.

6. Nusselt number (Nu) (Ataie-Ashtiani et al., 2014) is the ratio of the total mass flux through a layer to the diffusive flux.

$$Nu = \frac{Q_L}{\eta D_0 \left( \frac{\Delta C}{d} \right) LW}, \quad (2.21)$$

where,

$Q_L$  — solute mass rate across the layer,

$\frac{\Delta C}{H}$  — solute concentration gradient across the layer,

$L$  — aquifer length,

$W$  — width of the aquifer,

$d$  — aquifer height.

## 2.4 Motivations of the Study

Currently available analytical solutions for the groundwater waves in response to tide-induced oscillations rely on pre-defined, non-dimensional perturbation parameters to get analytical solutions of higher-order accuracy. There is a need for obtaining solution without predefined parameter(s) for groundwater fluctuations under tidal influence for both vertical and sloping beach. Werner et al. (2013) mentioned that "Laboratory and numerical modeling experimentation are typically the tools of choice in seeking to elucidate the influence of individual processes from multifaceted field measurements". Very few experimental pressure data are available for the tidal influence in coastal aquifers by using direct pressure measurement method with pressure sensors. Moreover, there are limited number of laboratory experimental studies on density-dependent flow under tidal boundary conditions for sloping beach system. Hence, more experiments needed to understand the tidal influence on saltwater intrusion. The literature shows that no labo-

ratory study was completed to understand the mixing process within the saltwater wedge and above the freshwater zone with comprehensive image analysis by using neutral density tracers for saltwater intrusion experiments under tidal boundary effects. Hence, there is a need to study the tracer movement to understand the contaminant transport as well as flow circulation in the coastal aquifers.

## 2.5 Summary

In this chapter literature related to the thesis are explained. In the first section the tidal influence without density effects were discussed for previous analytical solutions and experimental studies. In later part, tidal influence with density effects and associated salt water intrusion were discussed. This section was done for analytical solutions, numerical modeling, and experimental studies. In the end, the motivations of the study was detailed.



# Chapter 3

# Mathematical Conceptualization

## 3.1 Overview

This chapter cover the governing equations used in this thesis for groundwater flow and transport. Governing equations are divided into following sections: i) governing equations used to derive analytical solution for groundwater table oscillations due to interaction between the tidal oscillation and the groundwater ii) Richards' equation used to numerically simulate the groundwater wave oscillations in response to tidal oscillations for the validation of analytical solutions iii) mass transport equation to simulate the saltwater intrusion along with contaminant transport.

## 3.2 Governing Equations

### 3.2.1 Groundwater Flow Equation for Watertable Waves

A two-dimensional vertical cross-sectional geometry is considered for the groundwater waves. The horizontal direction is considered to be  $x$ -axis and vertical direction considered as  $z$ -axis. The aquifer considered to be with a flat impermeable boundary as the bottom. The aquifer is unconfined aquifer with homogeneous and isotropic hydraulic conductivity tensor ( $\mathbf{K}$ ). The piezometric head  $\phi(x, z, t)$  expression to calculated the velocity of the flow is defined as,

$$\phi(x, z, t) = \frac{P}{\gamma} + z \quad (3.1)$$

where  $P$  and  $\gamma$  are pressure and specific head of the fluid respectively. The Darcy law is used to get the specific discharge ( $\mathbf{q}$ ) or average velocity of the flow in porous medium. Darcy law can be derived from Stokes law by volume averaging over a control volume based on macroscopic modelling. Darcy law is applicable based on the assumption that the average velocity is directly proportional to the piezometric

head gradient. Average flux based on Darcy law can be expressed as,

$$\mathbf{q} = -\mathbf{K} \cdot \nabla \phi \quad (3.2)$$

Darcy law holds good for the flows with Reynolds number less than one, when the flow is laminar flow, and it is only applicable for Newtonian fluids. For the incompressible and inviscid fluid the piezometric head potential should satisfy Laplace equation. Laplace equation can be written as,

$$\phi_{,xx} + \phi_{,zz} = 0, \quad 0 \leq z \leq h(x, t). \quad (3.3)$$

Since the aquifer is unconfined one, the saturated zone's upper boundary is a free surface boundary, which can be expressed as a function of  $x$  by the expression  $z = h(x, t)$ . In other words,  $h(x, t)$  is nothing but the height of saturated porous medium. Free surface boundary condition for the above equation is given by (Bear and Cheng, 2011),

$$\phi = h \quad \text{at} \quad z = h(x, t), \quad (3.4)$$

$$\phi_{,t} - \frac{K}{\eta_e} \phi_{,x}^2 - \frac{K}{\eta_e} \phi_{,z}^2 + \frac{K}{\eta_e} \phi_{,z} = 0 \quad \text{at} \quad z = h(x, t), \quad (3.5)$$

where  $\eta_e$  is the effective porosity of the porous medium. The impervious bottom of the aquifer can be represented by no flux boundary condition:

$$\phi_{,z} = 0, \quad \text{at} \quad z = 0. \quad (3.6)$$

Initial conditions for the free surface can be given as a function of  $x$  by the following equation,

$$h(x, 0) = \varphi(x) \quad (3.7)$$

### 3.2.1.1 Groundwater Fluctuations Due to Interaction between Tides and Groundwater

The problem of groundwater fluctuations due to the influence of tides is generally solved by introducing small perturbation parameters (Dagan, 1967; Parlange et al., 1984; Jeng et al., 2005b; Artiles and Kraenkel, 2007). Either amplitude parameter ( $\alpha = A/D$ ) or longness parameter ( $\beta = D/\lambda$ ) are used to expand the Laplace equation to obtain first-order, second-order and higher order equations. The notation  $A$  is the amplitude of the tidal wave or amplitude of the surface displacement,  $D$  is the undisturbed fluid depth (mean sea level) and  $\lambda$  is the wave-

length of the perturbation. First-order Boussinesq equation for the groundwater flow based on perturbation theory is given as,

$$h_{,t} = \frac{K}{\eta_e} (h_{,x} h)_{,x}. \quad (3.8)$$

Second-order equation for groundwater table oscillations can be given as (Fenton, 1990; Nielsen et al., 1997)

$$h_{,t} = K/\eta_e (h h_{,x} + h^2 h_{,x} h_{,xx} + \frac{1}{3} h^3 h_{,xxx}),_x \quad (3.9)$$

$(\cdot)_x$ ,  $(\cdot)_{xx}$ , and  $(\cdot)_{xxx}$  are first-order, second-order, and third-order partial differentials with respect to  $x$  respectively. The second-order equation derived by Fenton (1990) is a simplified form of the equation derived by (Dagan, 1967). Nielsen et al. (1997) derived the same equation by assuming that the vertical component of the velocity vector linearly varying between bottom to the free surface. The correction applied for the deviation from the hydrostatic pressure due to consideration of vertical velocity in the pressure distribution is used in the derivation. Boussinesq's equation for Dupuit-Forchheimer assumption is used as an initial approximation for the derivation. Artiles and Kraenkel (2007) derived the first-order and second-order equation by using shallow flow assumption (wave length  $>>$  depth of the saturated zone).

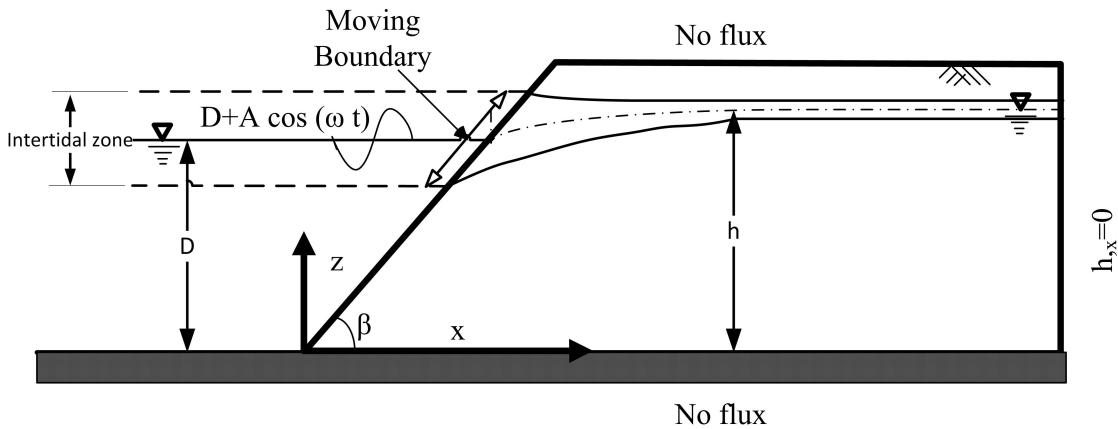


Figure 3.1: Definition sketch for unconfined coastal aquifer with tidal boundary condition.

In coastal aquifers with significant tidal oscillations, the low frequency tidal waves interact with the groundwater in the aquifer. Generally, there are different frequencies of tides due to diurnal, semi-diurnal, spring tide, neap tide influences. We consider only one component of the tide. We consider a coastal aquifer with an impervious horizontal bottom with the beach face is either vertical or sloped

one. The tidal oscillations can be represented as sinusoidal function in the seaside boundary condition as following,

$$h(0, t) = D + A \cos(\omega t), \quad (3.10)$$

where  $A$  and  $\omega$  are amplitude and frequency of the tidal wave respectively.

### 3.2.2 Derivation of Second-order Boussinesq Equation for Anisotropic Condition

Boussinesq equation for transient flow in unconfined aquifers is derived by assuming Dupuit approximation. Dupuit's assumption assumes that vertical flows are negligible. Hence, the the pressure distribution is hydrostatic. Boussinesq equation is widely used to simulate the transient watertable fluctuations in unconfined aquifers. However, when the vertical flows are significant higher order approximations required. Dagan (1967) derived second-order groundwater flow equations for unsteady flow, which requires non-hydrostatic pressure distribution to approximate the vertical flows. Fenton (1990) and Nielsen et al. (1997) derived the same isotropic second-order equation by assuming the pressure distribution varying linearly with depth. This section extends derivation for second-order Boussinesq equation for anisotropic unconfined aquifer (Castro-Orgaz et al., 2013) by using the same approximation used by Fenton (1990) and Nielsen et al. (1997). The first-order approximation corresponding to equation (3.8) are given as,

$$\phi_1(x, t) = h(x, t), \quad (3.11)$$

$$q_{1x} = -K_x \frac{\partial h}{\partial x}, \quad (3.12)$$

where  $K_x$  is the horizontal component of the hydraulic conductivity and equation (3.11) is corresponding to Dupuit's approximation. Continuity equation for the first-order groundwater flow for incompressible flows can be written as,

$$\frac{\partial q_{1x}}{\partial x} + \frac{\partial q_{1z}}{\partial z} = 0. \quad (3.13)$$

The equation (3.12) considered the horizontal velocity is changing with the  $x$ . Hence, vertical velocity should exist to satisfy the continuity equation (3.13). First-order continuity equation can be rearranged to obtain the vertical velocity  $q_{1z}$  as following,

$$q_{1z} = - \int_0^z \frac{\partial q_{1x}}{\partial x} dz. \quad (3.14)$$

Substituting the expression for  $q_{1x}$  in the above equation gives vertical velocity  $q_{1z}$  as following expression,

$$q_{1z} = K_x \frac{\partial^2 h}{\partial x^2} z. \quad (3.15)$$

The first order vertical flow velocity is varying linearly with the depth,  $z$ . The expression for head component  $\phi_2$  can be obtained by rearranging the following Darcy velocity expression and using the equation (3.15),

$$q_{1z} = -K_z \frac{\partial \phi_2}{\partial z} \quad (3.16)$$

$$\phi_2 = -\frac{1}{K_z} \int_z^h q_{1z} dz \quad (3.17)$$

$$= -\frac{1}{K_z} \int_z^h K_z \frac{\partial^2 h}{\partial x^2} z dz$$

$$\phi_2 = \frac{1}{2} \frac{K_x}{K_z} \frac{\partial^2 h}{\partial x^2} (h^2 - z^2). \quad (3.18)$$

Second-order vertical flow velocity can be obtained by using  $\phi_2$  in the Darcy equation as following,

$$q_{2x} = -K_x \frac{\partial \phi_2}{\partial x}$$

$$q_{2x} = -K_x \frac{\partial}{\partial x} \left( \frac{1}{2} \frac{K_x}{K_z} \frac{\partial^2 h}{\partial x^2} (h^2 - z^2) \right). \quad (3.19)$$

First-order Boussinesq equation (3.8) can be rearranged using Darcy equation as following,

$$\eta_e \frac{\partial h}{\partial t} = \frac{\partial}{\partial x} \left( h K_x \frac{\partial h}{\partial x} \right)$$

$$\eta_e \frac{\partial h}{\partial t} = -\frac{\partial (h q_x)}{\partial x}. \quad (3.20)$$

The horizontal velocity component  $q_x$  in the rearranged Boussinesq equation can be expanded as  $q_{x1} + q_{x2}$ . By substituting the expansion for the horizontal flow velocity in the equation (3.20) becomes following form,

$$\eta_e \frac{\partial h}{\partial t} = -\frac{\partial}{\partial x} (h (q_{x1} + q_{x2})). \quad (3.21)$$

The realigned Boussinesq equation(3.21) can be written as a depth integral equation form as following,

$$\eta_e \frac{\partial h}{\partial t} = -\frac{\partial}{\partial x} \int_0^h (q_{x1} + q_{x2}) dz. \quad (3.22)$$

By substituting Darcy equation for  $q_{1x}$  (3.12) and the expression obtained for  $q_{2x}$  (3.19) through the iteration technique in the equation (3.22), the second-order Boussinesq equation for the groundwater flow can be obtained as following,

$$\eta_e \frac{\partial h}{\partial t} = K_x \frac{\partial}{\partial x} \left( h \frac{\partial h}{\partial x} \right) + \frac{K_x^2}{K_z} \frac{\partial}{\partial x} \left( h^2 \frac{\partial h}{\partial x} \frac{\partial^2 h}{\partial x^2} + \frac{1}{3} \frac{\partial^3 h}{\partial x^3} \right). \quad (3.23)$$

By substituting the ratio of horizontal hydraulic conductivity to vertical hydraulic conductivity as  $r$ , the second-order Boussinesq equation can be obtained as following,

$$\eta_e \frac{\partial h}{\partial t} = K_x \frac{\partial}{\partial x} \left[ h \frac{\partial h}{\partial x} + r \left( h^2 \frac{\partial h}{\partial x} \frac{\partial^2 h}{\partial x^2} + \frac{1}{3} \frac{\partial^3 h}{\partial x^3} \right) \right] \quad (3.24)$$

$$r = \frac{K_x}{K_z} \quad (3.25)$$

### 3.2.3 Richards' Equation for Variably Saturated-Saturated Flow in Porous Media

Previous subsection considered the groundwater flow in two-dimensional vertical cross section for saturated flow. The full scale groundwater equation for the variably saturated flow can be written in the form of Richards equation. Richards'equation for variable density flow can be written as (Diersch, 2013),

$$s S_0 \phi_{,t} + \eta_e s_{,t} - \nabla \cdot [k_r \mathbf{K} \cdot (\nabla \phi + \chi \mathbf{e})] = Q_\phi + Q_{\phi w}. \quad (3.26)$$

$s$  is the saturation of fluid in void space  $\eta_e$ ,  $S_0$  is the specific storage coefficient [ $L^{-1}$ ],  $k_r$  is relative permeability [-],  $\mathbf{K}$  hydraulic conductivity tensor [ $LT^{-1}$ ],  $\phi$  is piezometric head [ $L$ ],  $Q_\phi$  is the supply term of flow [ $T^{-1}$ ],  $Q_{\phi w}$  is the specific sink/source function of wells [ $T^{-1}$ ].  $\chi$  is the dimensionless buoyancy coefficient defined as,

$$\chi = \frac{\rho - \rho_0}{\rho_0}, \quad (3.27)$$

where  $\rho$  is density of the fluid [ $ML^{-1}$ ] and  $\rho_0$  is the freshwater density [ $ML^{-1}$ ]. Darcy velocity for the variably saturated porous media can be expressed as,

$$\mathbf{q} = -k_r \mathbf{K} \cdot (\nabla \phi + \chi \mathbf{e}). \quad (3.28)$$

### 3.2.4 Transport Equation

The solute transport equation to model the seawater intrusion can be written as (Diersch, 2013),

$$\eta_e s C_{k,t} + \mathbf{q} \cdot \nabla C_k - \nabla \cdot (\mathbf{D}_k \cdot \nabla C_k) + Q_\phi C_k = Q_k + Q_{kw}, \quad (3.29)$$

where  $C_k$  mass concentration of the species  $k$  [ $ML^{-3}$ ],  $\mathbf{q}$  is the Darcy velocity vector of the fluid [ $LT^{-1}$ ],  $Q_k$  is the source/sink term of species  $k$  [ $ML^{-3}T^{-1}$ ],  $Q_{kw}$  specific  $k$ th-species mass source/sink function of wells [ $ML^{-3}T^{-1}$ ], and  $\mathbf{D}_k$  is hydrodynamic dispersion tensor which can be expressed as,

$$\mathbf{D}_k = D_m \boldsymbol{\delta} + \mathbf{D}_{mech}, \quad (3.30)$$

$$\mathbf{D}_{mech} = \beta_T \parallel \mathbf{q} \parallel \boldsymbol{\delta} + (\beta_L - \beta_T) \frac{\mathbf{q} \otimes \mathbf{q}}{\parallel \mathbf{q} \parallel}, \quad (3.31)$$

where  $\mathbf{q}$  is the Darcy velocity vector,  $\mathbf{q} \otimes \mathbf{q}$  is the tensor product of Darcy velocity vector,  $D_m$  is the molecular diffusion coefficient [ $L^2T^{-1}$ ],  $\mathbf{D}_{mech}$  is the mechanical dispersion coefficient [ $L^2T^{-1}$ ], and  $\boldsymbol{\delta}$  is the Kronecker delta which is defined as,

$$\boldsymbol{\delta} = \delta_{ij} = \begin{cases} 1, & \text{when } i = j \\ 0, & \text{when } i \neq j \end{cases} \quad (3.32)$$

The flow and transport equations defined in Eq. (3.2.3) and (Eq. 3.2.4) respectively are coupled by the variable density. The head acquired from the flow equation is used to solve the transport equation and the concentration  $C_k$  obtained from the transport equation is used to calculate the density using the constitutive relationship between concentration and density. The density calculated by substituting the concentration in the constitutive relationship is used in the governing equation for fluid flow Eq. (3.2.3) to calculate the head for the next iteration. The constitutive relationship between density and concentration is given by the following equation,

$$\rho = \rho_0 [1 + \alpha_k (C_{ks} - C_{k0})], \quad (3.33)$$

where,  $\alpha_k$  is the solutal expansion coefficient of the species  $k[-]$ ,  $\rho_0$  is the freshwater density,  $C_{ks}$  is the maximum mass concentration of the species  $k[ML^{-3}]$ , and  $C_{k0}$  is the mass concentration of the species  $k$  when the density is  $\rho_0 [ML^{-3}]$ . In the present study the effect of viscosity is considered to be negligible and the change in temperature is considered to be small (isothermal condition) have any influence on the density.

### 3.3 Summary

The governing equations used in this thesis for: i) analytical solution for ground-water waves in response to tides, ii) numerical modelling for validating the analytical solutions, and iii) to validate experimental saltwater intrusion under density-dependent flow conditions are explained in the chapter. Second-order Boussinesq equation derivation process has been explained for anisotropic aquifers. The results of the usage of the governing equations and parameters used are explained in consecutive chapters.

# Chapter 4

# Experimental Conceptualization

## 4.1 Overview

The field conditions of the coastal aquifers can be modeled in different ways. A sand box experimental setup is used to create experimental conditions analogous to field conditions. This chapter covers the details of sandbox experimental setup used as a physical model. The experimental setup has features to impose different boundary conditions including tidal boundary condition.

## 4.2 Experimental Setup

The experiment setup was fabricated to perform experiments in a two-dimensional flow system of coastal aquifers. The outer frame in the experimental setup is made of stainless steel and it stands on steel supports wide enough to provide robust support required. The outer frame supports glass walls of the sandbox. The sandbox (Figure 4.1) is with inner dimensions 3300 mm length, 1000 mm height, and 20 mm wide to ensure two dimensional flow and transport. The width of the set up is very small compared to other two dimensions to ensure the two-dimensional flow in the vertical cross section (Cartwright et al., 2004; Goswami and Clement, 2007; Luyun et al., 2011; Kuan et al., 2012; Zhou et al., 2016). The walls are made of glass of thickness of 180 mm in both front and back side of the setup. The sandbox separated into three compartments with middle section of 3150 mm length for filling porous media, 50 mm length freshwater reservoir in the left side of the sand box and 50 mm length saltwater reservoir in the right hand side. Three outlet openings with valves are provided in the saltwater reservoir to provide necessary boundary conditions. The outlets are placed at 110 mm, 310 mm, and 660 mm from the bottom of the setup. The bottom of the setup is made of steel sheet. But, the steel sheet bottom has 18 outlets, including one each at the bottom of the freshwater reservoir and saltwater reservoir. The porous medium

section is separated by thin steel screens to avoid the entry of porous medium material into the reservoirs. Boundary conditions simulated in the experiments are explained in the following sections.

#### 4.2.1 Details of Instruments Used

- **Peristaltic Pumps:** Peristaltic pumps are used to provide freshwater flux at the inland boundary of the aquifer and to maintain the saltwater density at the saltwater boundary condition. Hence, two peristaltic pumps with the flow range  $2.725 \text{ cm}^3/\text{s}$  (250.44 liters per day) is selected for the experimental purpose. Two peristaltic pumps of model variable speed pump PP-50VX from Electrolab are used for the experiments (Electrolab India, 2014). Peristaltic pump motors are connected to silastic tubes of 7-mm internal diameter to supply water to the reservoirs. Silastic tube inlet end is immersed in the water stored in a 20-litre storage unit and the other end (outlet) of the silastic tube is connected to the freshwater reservoir if the pump is used to maintain freshwater flux or saltwater reservoir if the pump is used to maintain the density of the saltwater. The flux is controlled by fixing the RPM (revolutions per minute) of the motor. The range of RPM of the peristaltic pumps is 1 to 200. The pumps are calibrated individually to find the relation between the RPM and flowrate (Table 4.1). Flow rate of pumps can be calculated based on the calibration data (Table 4.2). More details on the Peristaltic pump can be obtained from electrolabindia website (Electrolab India, 2014).
- **CTD-Diver:** CTD-Divers are used to measure the saltwater concentration at the seaside boundary conditions. The model of the Divers used are DI272 manufactured by Schlumberger water services (Schlumberger Water Services (Netherlands) B.V., 2014). CTD-Diver measures absolute pressure, temperature, and conductivity of the water. The diver can measure water depth of 50 m, conductivity range of 0 to 120 mS/cm (equivalent to 0 mg/l to 76800 mg/l) with  $\pm 1\%$  accuracy with a minimum of  $10 \mu\text{S}/\text{cm}$ , and a sampling rate of one second per one reading to 99 hours per one reading. The Diver of 22 mm diameter casing made of ceramic would be suitable to measure brackish or saltwater environment. The Divers are placed inside water column and saltwater reservoir of the setup to measure the saltwater conductivities.

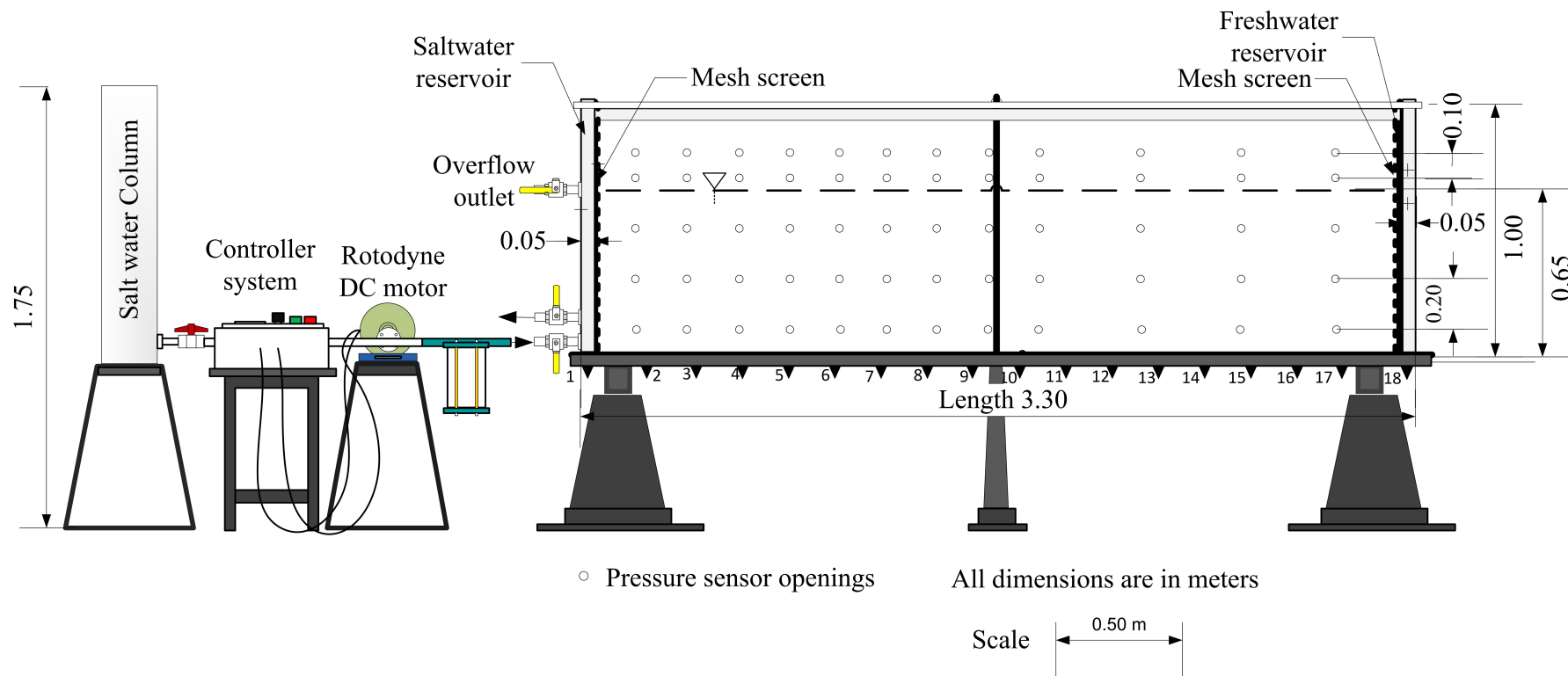


Figure 4.1: Schematic diagram of sandbox experimental setup.

- **Pressure Transducer:** Six Super TJE ultra precision pressure transducers (STJE AP111) from Honeywell are used to measure the water pressure. The pressure transducers are made of 50 mm diameter and 64 mm height cylindrical stainless steel case material. The pressure sensors can measure up to pressure range 10 psig (10 psi gauge pressure) with accuracy of  $\pm 0.05\%$  with infinite resolution. The pressure range and accuracy are 7.0319 m and  $\pm 0.0035$  m or  $\pm 3.52$  mm respectively. Experimental setup is provided with openings in the backside glass wall to connect with the pressure sensors. The openings are connected with flexible tubes for the fluid to transfer pressure on the diaphragm of the pressure transducer by connecting other end with pressure transducers.
- **Data Acquisition System:** The pressure data from the pressure transducers are acquired by using UEILogger 300 from United Electronic Industries, Inc. (2012). The data logger is connected to a PC through ethernet port. The UEILogger is available with the GUI application for the windows operating system and 8 GB SD card is used to store the data. The GUI interface has the options, e.g., start, stop, fix the frequency of the samples collected, realtime diagnostic display.
- **Wave Generation Setup:** A combination DC motor connected with a water column on one side and the saltwater reservoir on another side is used to generate waves by controlling the direction of the DC motor with a control system. The control system has options to fix the time of clockwise and anti-clockwise rotations of the DC motor and a resting period in between the direction change. The RPM of the DC motor can be controlled by a potentiometer available in the control system panel and it is provided with a digital display of approximate RPM of the motor.

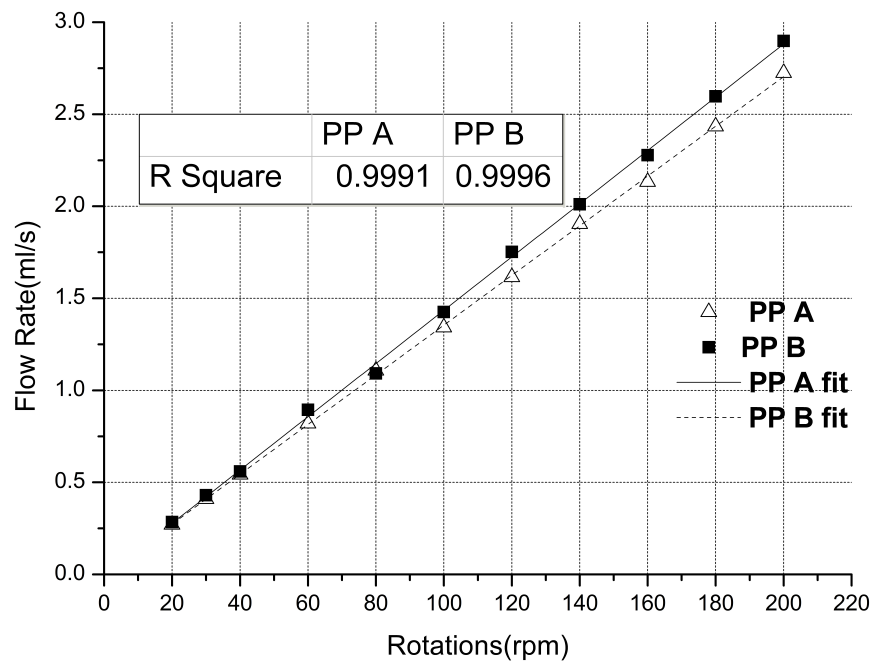


Figure 4.2: Peristaltic pumps calibration plots. Two peristaltic pumps named PP A and PP B respectively.

Table 4.1: Peristaltic pumps calibration data

| Pump A |          |               |                  | Pump B |          |               |                  |
|--------|----------|---------------|------------------|--------|----------|---------------|------------------|
| rpm    | Time (s) | Quantity (ml) | Discharge (ml/s) | rpm    | Time (s) | Quantity (ml) | Discharge (ml/s) |
| 20     | 74       | 20            | 0.270            | 20     | 70.33    | 20            | 0.284            |
| 30     | 48.81    | 20            | 0.410            | 30     | 46.5     | 20            | 0.430            |
| 40     | 36.88    | 20            | 0.542            | 40     | 35.8     | 20            | 0.559            |
| 60     | 36.58    | 30            | 0.820            | 60     | 33.56    | 30            | 0.894            |
| 80     | 27.09    | 30            | 1.107            | 80     | 36.64    | 40            | 1.092            |
| 100    | 44.7     | 60            | 1.342            | 100    | 42.11    | 60            | 1.425            |
| 120    | 30.96    | 50            | 1.615            | 120    | 34.24    | 60            | 1.752            |
| 140    | 52.53    | 100           | 1.904            | 140    | 49.72    | 100           | 2.011            |
| 160    | 46.88    | 100           | 2.133            | 160    | 43.89    | 100           | 2.278            |
| 180    | 41.09    | 100           | 2.434            | 180    | 38.51    | 100           | 2.597            |
| 200    | 36.7     | 100           | 2.725            | 200    | 34.51    | 100           | 2.898            |

### 4.2.2 Boundary Conditions

The concepts of simulating the required boundary conditions are explained in detail in the following text.

#### 4.2.2.1 Freshwater Flux Boundary

The freshwater reservoir is connected with peristaltic pump or any other water supply system. Present study require very small flow rate. The peristaltic pump model PP-50vx from Electrolab is used for creating the freshwater flux towards the seaside boundary from freshwater reservoir side. Hence, two peristaltic pumps with the flow range  $0 - 2.725 \times 10^{-6} \text{ m}^3/\text{s}$  (250.44 liters per day) are selected for the experimental purpose. Peristaltic pump is used to supply freshwater at freshwater reservoir creates freshwater flux boundary condition from inland towards the seaside boundary.

#### 4.2.2.2 No Flow Boundary Condition

- The bottom of the setup is made of flat steel plate which acts as no flow boundary condition for both flow and solute transport. The bottom steel plate has 18 openings — including one each below the freshwater reservoir and saltwater reservoir — connected to valves. The valves are provided to facilitate the removal of aquifer materials and water after experiments. The valves are kept in closed condition while experiment being performed.
- The glass walls on front and back side of the setup( $xz$ -plane) also act as no flow boundary conditions for both flow and solute transport.

#### 4.2.2.3 Seaside Boundary

- **Constant head boundary:** Saltwater reservoir along with the three openings provided can be used to fix the constant head boundary conditions. The saltwater reservoir can be filled with freshwater or saltwater based on the experiment. The reservoir can be filled with saltwater and the outlet valves can always be opened to maintain the constant head.
- **Oscillation wave boundary:** Left hand side reservoir (saltwater reservoir) is connected with a combination of rotodyne and a cylindrical water column for creating waves. The rotodyne is operated by a DC motor connected to a controller system. The other end of DC motor is connected with a cylindrical water column. The controller system provided with the options to

fix time periods for clockwise rotation, anti-clockwise rotation, and a resting time period in between the rotation direction change of the DC motor. The speed of the motor can be controlled by the potentiometer embedded in the control system. The rotodyne revolutions create suction pressure and creates flow towards the saltwater reservoir (forward flow) when the motor is rotating in clockwise direction. Once the time period given for the forward rotation is completed, the rotations will stop for a given time period (resting period). Once the resting period ends, the motor rotates in the anti-clockwise direction to create a reverse flow—flow from sand box to the water column. Apart from the flow due to rotations of the rotodyne, there is a small amount of flow is possible due to the difference between the water levels (head difference) at the sandbox and the water column when the DC motor is in resting time. The saltwater reservoir and water column both can be filled with freshwater and saltwater depends on the experiment being performed. The boundary condition for freshwater experiments would be head calculated based on freshwater density, which is approximately  $1000 \text{ kg/m}^3$ . For saltwater experiments, the density of the salt solution  $\rho_s$  should be used to obtain the head.

- **Concentration boundary:** The concentration boundary for the freshwater tidal wave experiments would be approximately zero up to the water level ( $C \approx 0$ ). The concentration boundary for the saltwater intrusion experiments — the seaside boundary condition — would be the salt concentration of the solution prepared,  $C = C_s$ .

## 4.3 Summary

The details of the experimental setup were explained in this chapter. The details of the sand-box experimental setup to create laboratory scale coastal aquifer setup was explained. Details of the main sandbox and the possible boundary conditions that can be enforced were elaborated. Wave generation system to simulate the tidal boundary effects also explained along with the instruments used to record the pressure and conductivity also explained. More details on the data collection process discussed in next two chapters while discussing experimental methodologies.



# Chapter 5

## Tidal Dynamics without Density Effects

### 5.1 Overview

This chapter presents the tidal dynamics in coastal unconfined aquifers without considering the density effects. The density difference between the tidal water and the freshwater inside the coastal aquifer is neglected. The initial section of this chapter presents analytical solutions for the groundwater waves due to the interaction with the tidal oscillations. Analytical solutions section consists of analytical solution derivations using Homotopy Perturbation Method (HPM) for different governing equations explained in the mathematical conceptualization chapter. Later part of this chapter presents the groundwater waves experiments performed in the laboratory using the sandbox experimental setup and the experimental data analysis.

### 5.2 Analytical Solutions Using the Homotopy Perturbation Method (HPM)

#### 5.2.1 Analytical Solutions for Groundwater Waves Driven by Tidal Oscillations in a Coastal Aquifer with Vertical Beach

This section explains the analytical solution for the groundwater oscillations in an unconfined coastal aquifer with a vertical beach face. A two-dimensional vertical cross-section of the coastal unconfined aquifer is considered. The intersection between the aquifer and the tidal water is vertical (Figure 5.1). The aquifer recharge due to rainfall, the vertical flow velocities, the density difference between saltwater in the sea and the freshwater in the aquifer, and the regional freshwa-

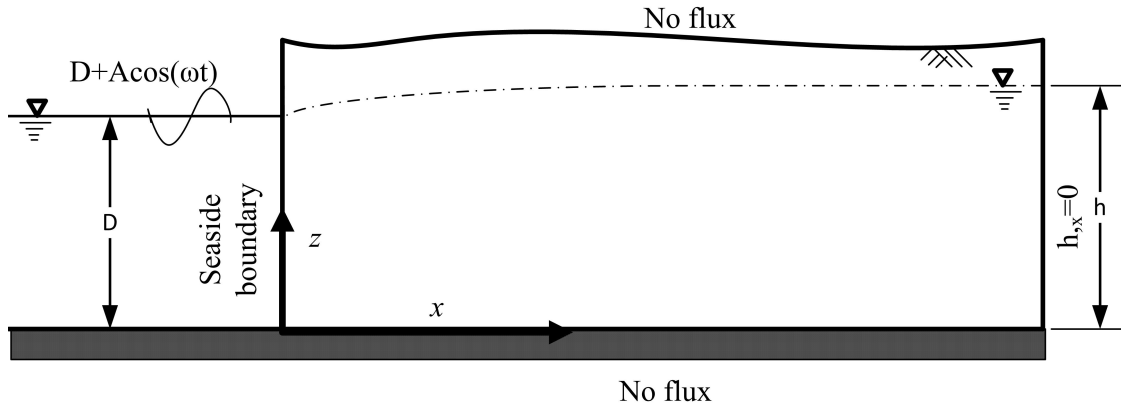


Figure 5.1: Definition sketch for the tidal influence on groundwater table in a coastal unconfined aquifer with vertical beach face.

ter flux from inland to sea are considered to be negligible. Since vertical flows are considered to be negligible (Dupuit's assumption), the Boussinesq equation is considered as the governing equation. There is no decoupling between the water table in the aquifer and the water level in the seaside. In other words, there is no seepage face development in the aquifer-seawater interface. Slooten et al. (2010) work on sensitivity analysis has shown that the variable density does not impact the tidal wave propagation significantly. Hence, density-dependent effects can be neglected. First-order Boussinesq equation (3.8) for the groundwater flow is given as,

$$h_{,t} = \frac{K}{\eta_e} (h_{,x} h)_{,x}. \quad (5.1)$$

The spatial derivative term of the Boussinesq equation is nonlinear. The cosine boundary condition (Equation 3.10) is used for the tidal boundary condition. The aquifer is considered as a semi-infinite one in the  $x$  direction. The oscillations would die down at asymptotic distances from the seaside boundary. Hence, the inland boundary condition of the for the groundwater waves due to tidal influence can be expressed as follows,

$$h_{,x}|_{x \rightarrow \infty} = 0. \quad (5.2)$$

### 5.2.1.1 Homotopy Perturbation Approach

He (1999) proposed the homotopy perturbation method(HPM) by coupling perturbation method with the homotopy technique (Munusamy and Dhar, 2015). Homotopy perturbation method uses virtual perturbation parameter(s) in the place of pre-defined, physical perturbation parameter(s). The first step of HPM is to

construct the homotopy equation using the virtual parameter(s). The homotopy equation should be constructed in a way it ensures that the problem deforms from the approximate equation to the original equation when the perturbation parameter value(s) changes from zero to one. The embedded virtual parameter(s) in the homotopy equation is(are) always small since its range is from zero to one ([0,1]). The homotopy equation for the Boussinesq equation for groundwater flow can be written as,

$$h_{,t} = 0 \cdot h_{,xx} + p [K/\eta_e (h h_{,x})_{,x}] . \quad (5.3)$$

Where the first term on the right-hand side of the equation is second-order spatial derivative with zero coefficient. This term is an additional one added to the existing equation. This particular term approximately represents the physical properties of the nonlinear spatial derivative term in the Boussinesq equation (5.1). The homotopy equation deforms to original Boussinesq equation when the virtual perturbation parameter  $p$  becomes one and the homotopy equation(5.3) deforms to the approximate linear equation when virtual parameter becomes zero. This deformation of one continuous function to another continuous function is called as homotopic in topology. The first step in the homotopy perturbation method is done with the construction of the homotopy equation. Next step is to construct the solution variable as a perturbation function of the virtual parameter,  $p$ . This step is similar to the traditional perturbation techniques. The solution for the Boussinesq equation  $h(x, t)$  can be written as a perturbation expansion of the virtual parameter  $p$  as following,

$$\begin{aligned} h &= \sum_{n=0}^{\infty} p^n h_n \\ &= h_0 + p h_1 + p^2 h_2 + p^3 h_3 + \dots \end{aligned} \quad (5.4)$$

By using a perturbation expansion (Equation 5.30), the standard homotopy perturbation equation(5.3) can be divided into linear parts by comparing the coefficients of  $p^n$  for  $n = 0, 1, 2, \dots$  depending on the solution accuracy needed. The coefficients of the second order spatial derivative can be expanded to eliminate secular terms and to get the higher-order solutions by using embedding parameter  $p$  as follows (He, 2014),

$$0 = w_0 - \sum_{n=1}^{\infty} p^n w_n. \quad (5.5)$$

Substituting equations (5.30) and (5.31) in equations (5.3), (5.2) and (3.10), the equations can be written as,

$$\begin{aligned}
 & (h_0 + p^1 h_1 + p^2 h_2 + p^3 h_3 + \dots)_{,t} \\
 &= (w_0 - p^1 w_1 - p^2 w_2 - p^3 w_3 - \dots) (h_0 + p^1 h_1 + p^2 h_2 + p^3 h_3 + \dots)_{,xx} \\
 &+ p [K/\eta_e ((h_0 + p^1 h_1 + p^2 h_2 + p^3 h_3 + \dots) \\
 &\quad (h_0 + p^1 h_1 + p^2 h_2 + p^3 h_3 + \dots)_{,x})_{,x}].
 \end{aligned} \tag{5.6}$$

By comparing the powers of perturbation parameter  $p$ , perturbation equations along with boundary conditions for the different powers of virtual parameter can be written as,

$$p^0 : \begin{cases} h_{0,t} - w_0 h_{0,xx} = 0, \\ h_0(x, t) = D + A \cos(\omega t), \\ h_{0,t}|_{x \rightarrow \infty} = 0. \end{cases} \tag{5.7}$$

$$p^1 : \begin{cases} h_{1,t} - w_0 h_{1,xx} = \underbrace{K/\eta_e (h_0 h_{0,x})_{,x} - w_1 h_{0,xx}}_{I_1}, \\ h_1(x, t) = 0, \\ h_{1,t}|_{x \rightarrow \infty} = 0. \end{cases} \tag{5.8}$$

$$p^2 : \begin{cases} h_{2,t} - w_0 h_{2,xx} = \underbrace{K/\eta_e (h_1 h_{0,x} + h_0 h_{1,x})_{,x} - w_1 h_{1,xx} - w_2 h_{0,xx}}_{I_2}, \\ h_2(x, t) = 0, \\ h_{2,t}|_{x \rightarrow \infty} = 0. \end{cases} \tag{5.9}$$

$$p^3 : \begin{cases} h_{3,t} - w_0 h_{3,xx} = \underbrace{K/\eta_e (h_2 h_{0,x} + h_1 h_{1,x} + h_0 h_{2,x})_{,x}}_{I_{31}} \\ \quad - \underbrace{(w_3 h_{0,xx} + w_2 h_{1,xx} + w_1 h_{2,xx})}_{I_{32}}, \\ h_3(x, t) = 0, \\ h_{3,t}|_{x \rightarrow \infty} = 0. \end{cases} \tag{5.10}$$

Where  $I_1$ ,  $I_2$  and  $I_3$  ( $= I_{31} + I_{32}$ ) are the inhomogeneous terms for first-order, second-order and third-order equations respectively. By solving the linear differential equations for  $h_0$ ,  $h_1$ ,  $h_2, \dots$  higher-order solution can be obtained by using  $p = 1$  in the equation(5.30) as follows,

$$h = \lim_{p \rightarrow 1} \sum_{n=0}^{\infty} p^n h_n = h_0 + h_1 + h_2 + h_3 + \dots \tag{5.11}$$

Similarly the equation for parameters  $w_0, w_1, w_2, w_3, \dots$  can be obtained by using  $p = 1$  in the equation (5.31),

$$w_0 = w_1 + w_2 + w_3 + \dots \quad (5.12)$$

The parameters  $w_0, w_1, w_2, w_3, \dots$  can be determined from the resulting equations by forcing non-generation of secular terms. Solution for zeroth-order equation(5.7) is given by,

$$h_0(x, t) = D + Ae^{-k_1 x} \cos[\omega t - k_1 x], \quad (5.13)$$

where  $k_1$  defined as,

$$k_1 = \sqrt{\frac{\omega}{2w_0}}. \quad (5.14)$$

### 5.2.1.2 Secular Terms

In the perturbation solution process, secular terms being generated due to non-linearity in the partial differential equations. Secular terms are the terms with unbounded solutions for the particular integral. The inhomogeneous partial differential equation can be written as,

$$f(\Delta, \Delta')h(x, t) = g(x, t), \quad (5.15)$$

where  $f(\Delta, \Delta')$  is the function with partial differentials with respect to independent variables (x and t),  $\Delta$  is the partial differential with respect to  $x$  ( $=\partial/\partial x$ ),  $\Delta'$  is the partial differential with respect to  $t$  ( $=\partial/\partial t$ ),  $h(x, t)$  is the dependent variable and  $g(x, t)$  is inhomogeneous term. For the secular terms, the particular integral  $h_{P.I}(x, t)$  gives numerator/0 as the solution,

$$h_{P.I}(x, t) = \frac{1}{f(\Delta, \Delta')}g(x, t) = \frac{\text{Numerator}}{0} \quad (5.16)$$

### 5.2.1.3 First-order Solution

By substituting (5.13) in the expression (5.8) the inhomogeneous term is given by,

$$\begin{aligned} I_1 &= \frac{A^2 K \omega}{2w_0 \eta_e} \left\{ e^{-2k_1 x} - e^{-2k_1 x} \sin[2\omega t - 2k_1 x] \right\} \\ &\quad - \frac{A \omega}{w_0} \left( \frac{KD}{\eta_e} - w_1 \right) \underbrace{e^{-k_1 x} \sin[\omega t - k_1 x]}_{\text{Secular term}}. \end{aligned} \quad (5.17)$$

Requirement of no secular term in inhomogeneous term  $I_1$  needs the coefficient of the secular terms to be zero. By forcing the coefficient of secular to zero,  $w_1$  can be expressed as,

$$w_1 = \frac{KD}{\eta_e}. \quad (5.18)$$

For solution up to first-order ( $w_0 = w_1$ ), the zeroth-order equation becomes linearized Boussinesq's equation (Nielsen, 1990). Solution of the first order equation (5.8) can be obtained by adding the particular integral with the complementary function,

$$h_1(x, t) = \frac{A^2 K}{4w_0 \eta_e} \left\{ 1 - e^{-2k_1 x} - 2 e^{-2k_1 x} \cos[2\omega t - 2k_1 x] + 2 e^{-\sqrt{2}k_1 x} \cos[2\omega t - \sqrt{2}k_1 x] \right\}. \quad (5.19)$$

#### 5.2.1.4 Second-order Solution

Second order solution ( $h_2$ ) for equation (5.9) can be given as,

$$h_2(x, t) = \frac{A^3 K^2}{w_0^2 \eta_e^2} \left\{ \begin{aligned} & \frac{1}{16} (-2 + 3\sqrt{2}) e^{-\sqrt{3}k_1 x} \cos[3\omega t - \sqrt{3}k_1 x] \\ & + \frac{3}{8} e^{-3k_1 x} \cos[3\omega t - 3k_1 x] + \frac{11}{20} e^{-3k_1 x} \cos[\omega t - k_1 x] \\ & - \frac{3}{10} e^{-k_1 x} \cos[\omega t - k_1 x] \\ & - \frac{1}{4} e^{-(1+\sqrt{2})k_1 x} \cos[\omega t + (1 - \sqrt{2})k_1 x] \\ & - \frac{1}{16} (4 + 3\sqrt{2}) e^{-(1+\sqrt{2})k_1 x} \cos[3\omega t - (1 + \sqrt{2})k_1 x] \\ & - \frac{1}{10} e^{-3k_1 x} \sin[\omega t - k_1 x] \\ & - \frac{1}{80} (-8 + 5\sqrt{2}) e^{-k_1 x} \sin[\omega t - k_1 x] \\ & + \frac{1}{8\sqrt{2}} e^{-(1+\sqrt{2})k_1 x} \sin[\omega t + (1 - \sqrt{2})k_1 x] \end{aligned} \right\} \quad (5.20)$$

Requirement of no secular terms in inhomogeneous terms  $I_2$  and  $I_3$  ( $=I_{31} + I_{32}$ ) needs,

$$w_2 = \frac{A^2 K^2}{4w_0 \eta_e^2} \quad (5.21)$$

$$w_3 = 0 \quad (5.22)$$

### 5.2.1.5 Third-order Solution

Third order solution ( $h_3$ ) for equation (5.10) can be given as,

$$\begin{aligned}
h_3(x, t) = & \frac{A^4 K^3}{w_0^3 \eta_e^3} \left\{ \frac{1}{32} + \frac{1}{160} (-10 e^{-2\sqrt{2}k_1 x} - 59 e^{-4k_1 x} + 24 e^{-2k_1 x}) \right. \\
& - \frac{1}{8} e^{-2\sqrt{2}k_1 x} \cos[4\omega t - 2\sqrt{2}x] - \frac{1}{3} e^{-4k_1 x} \cos[4\omega t - 4k_1 x] \\
& + \frac{(4218 + 2969\sqrt{2})}{7312 + 4992\sqrt{2}} e^{-(2+\sqrt{2})k_1 x} \cos[2\omega t - \sqrt{2}k_1 x] \\
& - \frac{(29453 + 21393\sqrt{2})}{480(457 + 312\sqrt{2})} e^{-\sqrt{2}k_1 x} \cos[2\omega t - \sqrt{2}k_1 x] \\
& - \frac{65}{96} e^{-4k_1 x} \cos[2\omega t - 2k_1 x] + \frac{3}{10} e^{-2k_1 x} \cos[2\omega t - 2k_1 x] \\
& + \frac{(-1061 - 897\sqrt{2} + 958\sqrt{3} + 747\sqrt{6})}{48(457 + 312\sqrt{2})} e^{-2k_1 x} \cos[4\omega t - 2k_1 x] \\
& + \frac{(8368 + 5921\sqrt{2})}{32(457 + 312\sqrt{2})} e^{-(2+\sqrt{2})k_1 x} \cos[4\omega t - (2 + \sqrt{2})k_1 x] \\
& - \frac{(958 + 747\sqrt{2})}{32(457 + 312\sqrt{2})} e^{-(1+\sqrt{3})k_1 x} \cos[2\omega t + (1 - \sqrt{3})k_1 x] \\
& - \frac{(958 + 747\sqrt{2})(3 + 2\sqrt{3})}{96(457 + 312\sqrt{2})} e^{-(1+\sqrt{3})k_1 x} \cos[4\omega t - (1 + \sqrt{3})k_1 x] \\
& + \frac{1}{4} e^{-(2+\sqrt{2})k_1 x} \cos[(2 - \sqrt{2})k_1 x] + \frac{5}{32} e^{-4k_1 x} \sin[2\omega t - 2k_1 x] \\
& + \frac{17(43 + 32\sqrt{2})}{8(457 + 312\sqrt{2})} e^{-(2+\sqrt{2})k_1 x} \sin[2\omega t - \sqrt{2}k_1 x] \\
& - \frac{(-13701 - 9846\sqrt{2} + 4790\sqrt{3} + 3735\sqrt{6})}{480(457 + 312\sqrt{2})} e^{-\sqrt{2}k_1 x} \sin[2\omega t - \sqrt{2}k_1 x] \\
& - \frac{7(211 + 149\sqrt{2})}{8(457 + 312\sqrt{2})} e^{-(2+\sqrt{2})k_1 x} \sin[2\omega t - \sqrt{2}k_1 x] \\
& - \frac{536 + 211\sqrt{2}}{80(457 + 312\sqrt{2})} e^{-2k_1 x} \sin[2\omega t - 2k_1 x] \\
& + \frac{(958 + 747\sqrt{2})}{32\sqrt{3}(457 + 312\sqrt{2})} e^{-(1+\sqrt{3})k_1 x} \sin[2\omega t + (1 - \sqrt{3})k_1 x] \\
& \left. - \frac{624 + 457\sqrt{2}}{32(457 + 312\sqrt{2})} e^{-(2+\sqrt{2})k_1 x} \sin[(2 - \sqrt{2})k_1 x] \right\} \quad (5.23)
\end{aligned}$$

### 5.2.1.6 Discussions

The homotopy perturbation solution procedure leads to the determination of parameters  $w_1$ ,  $w_2$ , and  $w_3$  by the removal of secular terms. The damping rate and

phase of the water table response depends on the parameter  $w_0$ . The parameter  $w_0$  can be obtained by solving the implicit equation (5.31), for  $p \rightarrow 1$ . The damping rate and phase of the groundwater fluctuation, changes according to the order of the solution as additional terms are added in the equation for  $w_0$  with the increasing order of accuracy ( $w_1, w_2, w_3, \dots$ ).

To investigate the accuracy of the present solution, it is compared with the existing second-order solutions obtained by Song et al. (2007), Kong et al. (2011), and Roberts et al. (2011). All three previous solutions mentioned above are obtained by non-dimensionalizing the governing equations and by using pre-defined perturbation parameters. However, the present solution obtained from dimensional Boussinesq's equation uses only a virtual parameter. The solutions are plotted for two different cases: i) CASE-L: to analyze the solution for laboratory scale with parameters values used in Song et al. (2007) [ $\eta_e = 0.3$ ,  $\eta_e/K = 44 \text{ s/m}$ ,  $D = 0.0725 \text{ m}$ ,  $A = 0.0725 \text{ m}$ , and  $\omega = (2\pi/62) / \text{s}$ ; Figure 5.2], and i) CASE-F: to analyze the solution for the field scale with parameters values used in Kong et al. (2011) [ $\eta_e = 0.3$ ,  $K = 0.0005 \text{ m/s}$ ,  $D = 5 \text{ m}$ ,  $A = 2 \text{ m}$ , and  $\omega = (2\pi/12) / \text{hr}$ ; Figure 5.3]. The non-dimensional solution provided by Song et al. (2007) was up to second-order for a costal unconfined aquifer with vertical beach. However, Kong et al. (2011) and Roberts et al. (2011) solutions are third-order and sixth-order non-dimensional solutions for sloped beaches. The corresponding solutions for vertical beach can be obtained by using beach face angle  $90^\circ$ . Song et al. (2007) and Kong et al. (2011) used maximum time-averaged water table height ( $D_{song}$ ) and thickness of the unconfined aquifer including tide-induced over-height ( $D_{kong}$ ) to non-dimensionalize the governing equations. The maximum value of the perturbation parameters based on the amplitude of the tidal oscillations- $\beta_{song}$  and  $\beta_{kong}$  are always less than one. Roberts et al. (2011) solution is derived by using the amplitude parameter ( $\alpha$ ) as a non-dimensional perturbation parameter and the maximum value of  $\alpha$  is one in the CASE-L.

The non-dimensional parameters used to plot the solutions are given in Table 5.4. The CASE-L is considered to analyze the homotopy solution for a very high value of amplitude parameter  $A/D$  (one). Figure 5.2 shows the water table fluctuations at four different times during ebbing tide. The plot included a  $A + D$  line to analyze the conformity of the solution at the boundary. Song et al. (2007) solution deviates at the seaside boundary due to the addition of extra terms in the boundary condition, as shown in the magnified part of Figure 5.2a. However, present solution, Kong et al. (2011), and Roberts et al. (2011) solutions conform with the seaside boundary condition. However, Roberts et al. (2011) solutions deviate from the other solutions and not a smooth curve nearby seaside boundary, as

shown in magnified plots since  $\alpha$  is equal to one for CASE-L. The water table from the present study is always slightly higher than the Kong et al. (2011) solution for the domain. However, the Kong et al. (2011) solution matches well if the present solution is considered only till second-order. The present solution merges with the Song et al. (2007) solution as the distance from the seaside boundary increases. The CASE-F is considered to analyze the homotopy solution for field scale aquifer parameters. The present solution is accurate compared to other analytical solutions, including Roberts et al. (2011) at the exact boundary and the region nearby boundary as shown in Figure 5.3. Roberts et al. (2011) solution underestimates the asymptotic water table height.

Table 5.1: Parameters used for solution comparisons

| CASE                         | Present              | Song et al. (2007)    |                       |                       | Kong et al. (2011)    |                       |                       | Roberts et al. (2011) |                |
|------------------------------|----------------------|-----------------------|-----------------------|-----------------------|-----------------------|-----------------------|-----------------------|-----------------------|----------------|
|                              | $w_0$<br>( $m^2/s$ ) | $D_{song}$<br>( $m$ ) | $\beta_{Song}$<br>(-) | $L_{song}$<br>( $m$ ) | $D_{kong}$<br>( $m$ ) | $\beta_{Kong}$<br>(-) | $L_{Kong}$<br>( $m$ ) | $\epsilon$<br>(-)     | $L$<br>( $m$ ) |
| CASE-L<br>( $\alpha = 0$ )   | 5.047                | 0.089                 | 0.816                 | 0.141                 | 0.087                 | 0.828                 | 0.140                 | 0.4020                | 0.180          |
| CASE-F<br>( $\alpha = 0.4$ ) | 0.092                | 5.196                 | 0.385                 | 7.716                 | 5.193                 | 0.385                 | 7.714                 | 0.4671                | 10.705         |

Note:  $D_{song} = \sqrt{1 + \alpha^2/2}$ ;  $\beta_{song} = A/D_{song}$ ;  $L_{song} = \sqrt{D_{song} K/(\eta_e \omega)}$ ;  $D_{kong}$  is obtained by solving the implicit equation [Eqn (50) from Kong et al. (2011)];  $\beta_{kong} = A/D_{kong}$ ;  $L_{kong} = \sqrt{D_{kong} K/(\eta_e \omega)}$ ;  $\epsilon = \sqrt{\eta_e \omega D/(2K)}$ ; and  $L = \sqrt{2KD/(\eta_e \omega)}$ .

### 5.2.1.7 Convergence

The convergence of the homotopy solution is analyzed by comparing the consecutive order solutions up to zeroth-order, first-order, second-order, and third-order, as shown in Figure 5.4 and the plot of distance vs. absolute maximum percentage error as shown in Figure 5.5. The consecutive order solutions compared for the CASE-L at  $t=8$  s. The zeroth-order solution underestimates the water table height. The difference between the zeroth-order solution and the first-order solution is relatively large compared to consecutive order solutions. The absolute maximum percentage errors for different distances from the seaside boundary are obtained by calculating the maximum percentage change over the full tidal cycle at each point. The absolute percentage error can be calculated by using the following expression,

$$\varepsilon_{i,i-1}(x) = \max_t \left( \frac{\sum_0^i h_i(x, t) - \sum_{i=0}^{i-1} h_{i-1}(x, t)}{\sum_{i=0}^{i-1} h_{i-1}(x, t)} \times 100 \right). \quad (5.24)$$

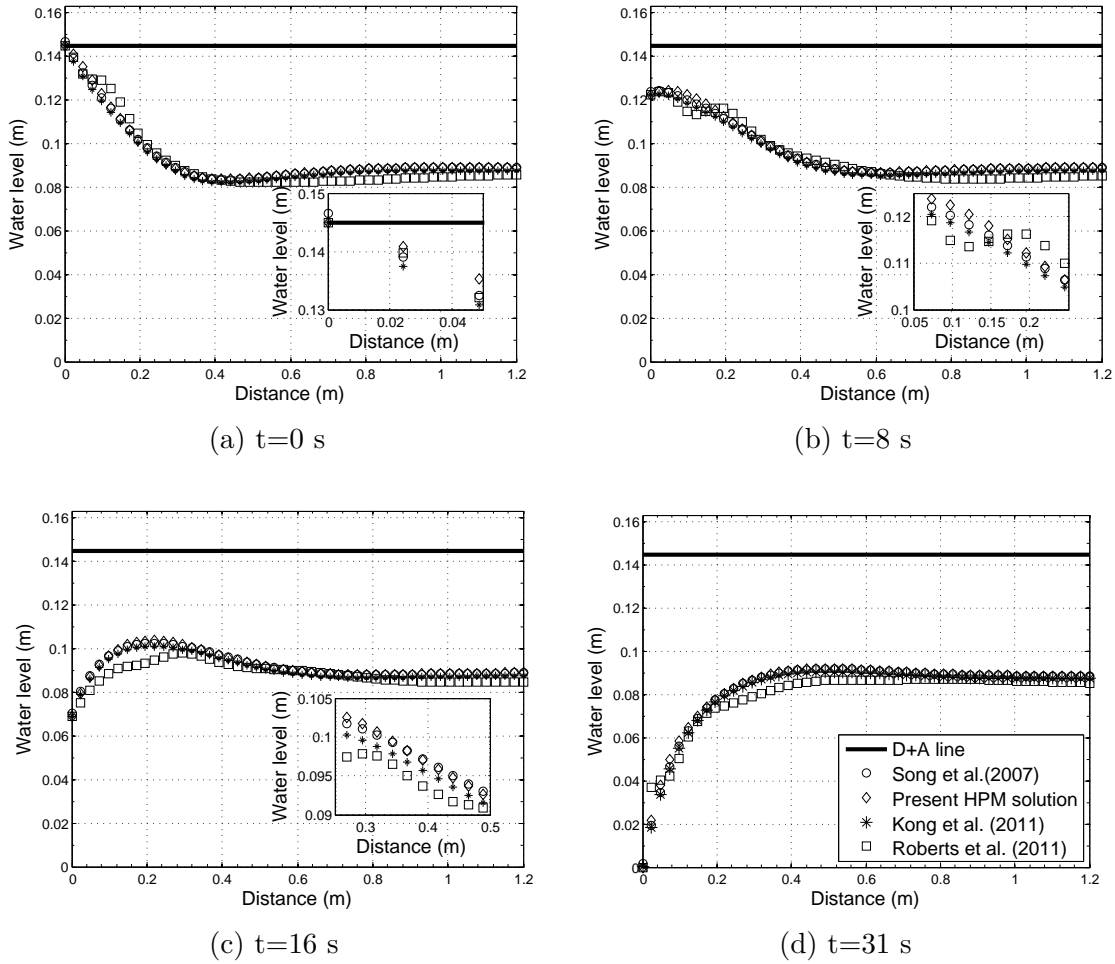


Figure 5.2: CASE-L: Comparison of Homotopy perturbation solution with Song et al. (2007) second-order solution, Kong et al. (2011) third-order solution, and Roberts et al. (2011) sixth-order solution for an coastal unconfined aquifer with laboratory scale parameters: tidal wave timeperiod=62 s;  $D=0.0725$  m;  $A=0.0725$  m;  $\eta_e = 0.3$ ;  $\eta_e/K = 44$  s/m.

Where,  $\varepsilon_{i,i-1}(x)$  is the absolute maximum percentage error between the solution up to  $i^{th}$  order and the solution up to  $(i-1)^{th}$  over full tidal cycle at the distance  $x$  from the seaside boundary,  $\sum_0^i h_i(x, t)$  is the solution up to  $i^{th}$  order, and  $\sum_{i=0}^{i-1} h_i(x, t)$  is the solution up to  $(i-1)^{th}$  order. The maximum absolute percentage error between first-order and zeroth-order is relatively very high while compared to the same of higher-order solutions. The  $\varepsilon_{1,0}(x)$  reached 22% at  $x$  equal to 0.6 m. The error between first-order and second-order solution increases up to the maximum of 5% before decreasing to zero error at 0.32 m. The error again increases up to 1% before decreasing zero error at an asymptotic distance from the sea. The maximum absolute error between second-order and third-order reaches its maximum value of 4% before maximums for zeroth-order and first order as well as first-order and second-order. The convergence for higher-orders can be since the maximum absolute errors decreasing with higher-order solutions.

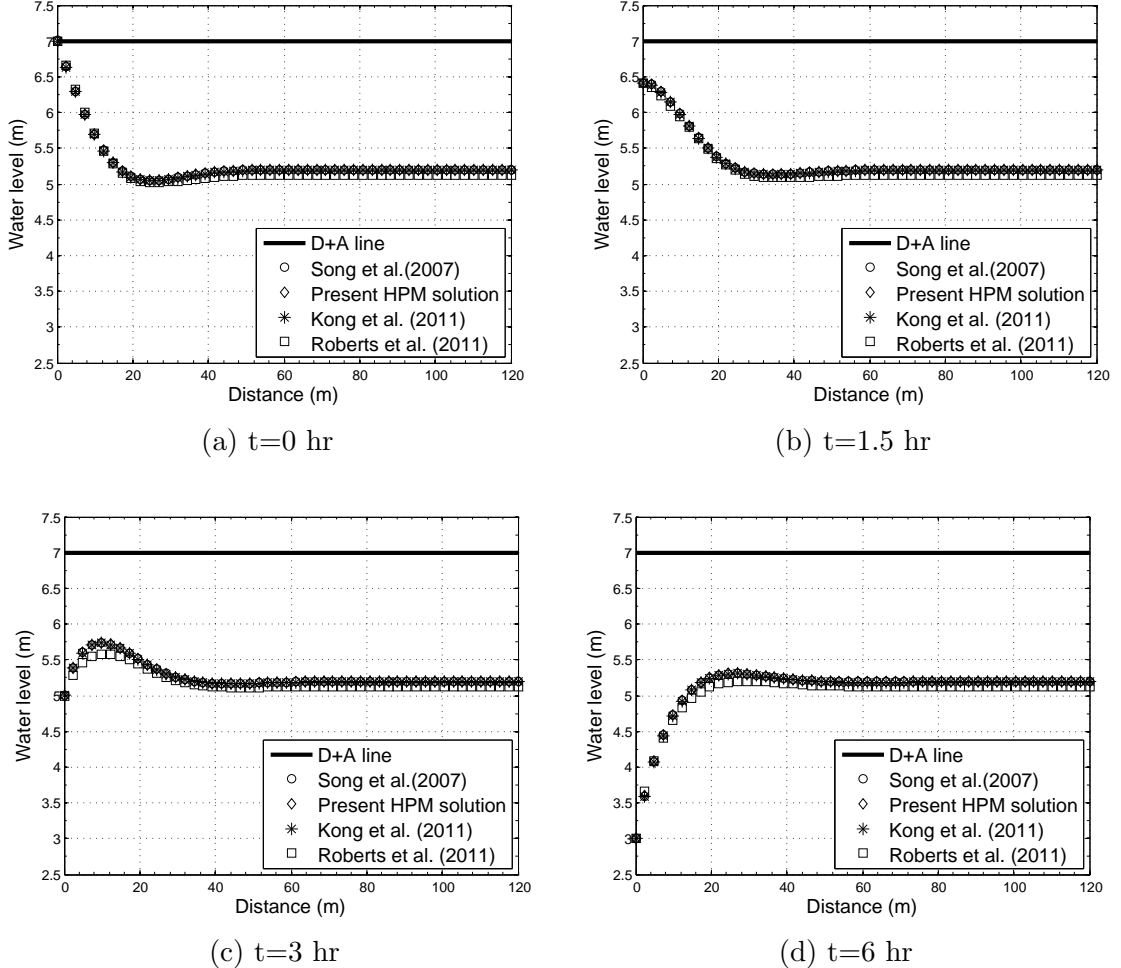


Figure 5.3: CASE-F: Comparison of Homotopy perturbation solution with Song et al. (2007) second-order solution, Kong et al. (2011) third-order solution, and Roberts et al. (2011) sixth-order solution for an coastal unconfined aquifer with field scale parameters: tidal wave timeperiod=12 hr;  $D=5$  m;  $A=2$  m;  $\eta_e = 0.3$ ;  $K = 0.0005$  m/s.

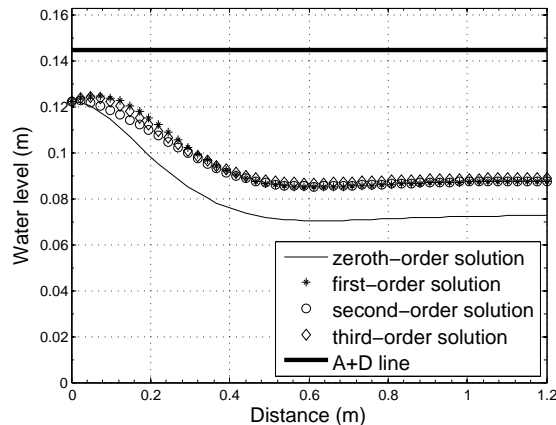


Figure 5.4: Convergence of homotopy perturbation solution up to third-order for an coastal unconfined aquifer with laboratory scale parameters: tidal wave timeperiod=62 s;  $D=0.0725$  m;  $A=0.0725$  m;  $\eta_e = 0.3$ ;  $\eta_e/K = 44$  s/m.

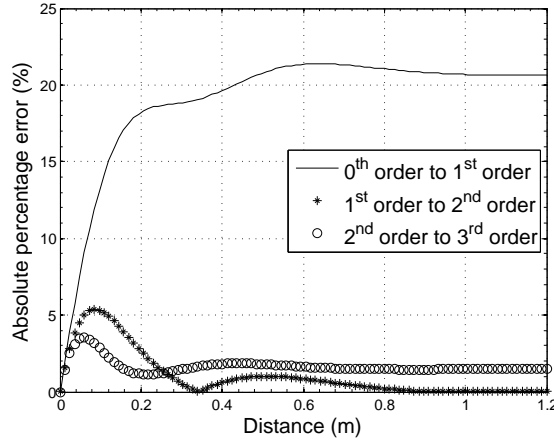


Figure 5.5: Convergence of homotopy perturbation solution up to third-order by using absolute percentage change for an coastal unconfined aquifer with laboratory scale parameters: tidal wave timeperiod=62 s;  $D=0.0725$  m;  $A=0.0725$  m;  $\eta_e = 0.3$ ;  $\eta_e/K = 44$  s/m.

### 5.2.1.8 Conclusions

In the present work, a new higher-order dimensional analytical solution for groundwater fluctuations in a coastal unconfined aquifer under tidal boundary condition is derived. The homotopy perturbation method with parameter expansion is utilized to remove the secular terms. Based on the comparison with analytical solution by Song et al. (2007), Kong et al. (2011), and Roberts et al. (2011) the following conclusions can be drawn.

- The analytical solution does not require non-dimensionalization and pre-defined perturbation parameter.
- Requirement of no secular term in the  $I_1$  generates  $w_1 (KD/\eta_e)$ . Thus, the zeroth-order equation becomes linearized Boussinesq's equation.
- Dimensional solution is valid for all ranges of  $A/D$  values. There is no deviation between the tidal water level and the groundwater table at the boundary.

The homotopy perturbation method can easily be extended to the problems with groundwater table fluctuations under periodic boundary condition with sloping beach and an oceanic island of finite length (Chang et al., 2010).

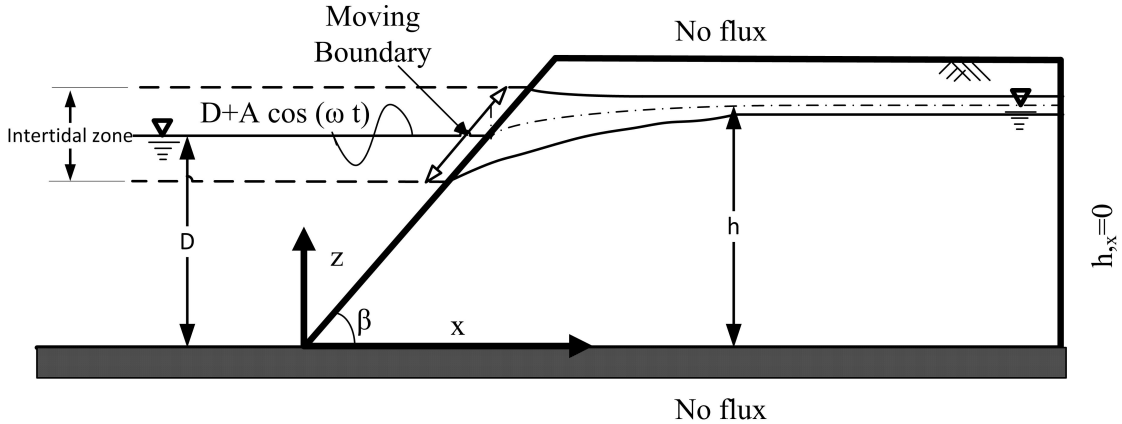


Figure 5.6: Definition sketch for tidal influence on groundwater table in a coastal unconfined aquifer with a sloped beach

### 5.2.2 Analytical Solution for Groundwater Waves Driven by Tidal Oscillations in a Coastal Aquifer with a Sloping Beach

In the previous section, the solution for groundwater waves derived for a beach with a vertical slope. In this section, the solution for groundwater waves under tidal boundary condition is derived for coastal aquifers with a sloping beach (figure 5.6). The governing equation and the boundary conditions used for the solution are same Boussinesq equation (Equation 5.1), cosine wave boundary condition (Equation 3.10) for seaside boundary and asymptotic boundary condition (Equation 5.2) for inland boundary condition. The aquifer bottom is impervious. The aquifer is homogenous and isotropic. Apart from the slope of the beach, all other assumptions are the same as the previous section. The coordinate axis moves on the sloping beach face with the different tide water levels at different times. The moving boundary can be changed to the fixed boundary by using the following coordinate transformation. The coordinate at the moving boundary  $x_0(t)$  can be written using beach slope angle  $\beta$  as given below,

$$x_0(t) = \cot(\beta) A \cos(\omega t), \quad (5.25)$$

$$x^* = x - x_0(t), \quad (5.26)$$

By substituting the coordinate transformation  $x^*$  in the governing equation (5.1), it changes to the following,

$$h_{,t} = K/\eta_e (h h_{,x^*})_{,x^*} - A\omega \cot[\beta] \sin[\omega t] h_{,x^*}. \quad (5.27)$$

The moving boundary problem has one non-linear diffusion term and another non-linear term for slope effects Eq. (5.27). To find the best match with different

terms, we can construct a homotopy equation with two virtual parameters (He, 2014) as given below,

$$h_{,t} = \underbrace{0.h_{,x^*x^*}}_{\text{virtual term}} + p_1(K/\eta_e (h h_{,x^*}),_{x^*} + p_2(-s_p \sin[\omega t] h_{,x^*}) + \underbrace{\alpha p_2 (1 - p_2) f(x, t)}_{\text{auxiliary term}}, \quad p_1 \in [0, 1], p_2 \in [0, 1], \quad (5.28)$$

$$s_p = A\omega \cot(\beta), \quad (5.29)$$

where  $p_1$  and  $p_2$  are virtual perturbation parameters which deform the equation from linear function to original non-linear function when  $p_1$  and  $p_2$  both are changed from 0 to 1; and  $\alpha$  is the auxiliary term coefficient. In the homotopy equation, the virtual term consists of a second-order spatial derivative ( $h_{,x^*x^*}$ ) — which approximates the physical properties of the non-linear term in the Boussinesq equation — is added with a coefficient zero. The term is used to eliminate the secular term generated from the nonlinear diffusion term in Boussinesqs equation. However, it does not contribute to the homotopy equation since it is multiplied by zero coefficient. Hence, it is referred to as a virtual term. Auxiliary term becomes zero when  $p_2$  is either zero or one. Hence, it does not contribute to either approximate equation or the original equation. Auxiliary term is used to remove the secular term generated by slope term. The coefficient zero is expanded using unknown parameters to eliminate the secular terms as given in Eq. (5.31). The solution for the groundwater table is expanded in the perturbation form using virtual parameters ( $p_1, p_2$ ) as follows,

$$h = \sum_{m=0}^{N_p} \sum_{n=0}^{N_p} p_1^m p_2^n h_{m,n} B_{[m+n \leq N_p]}, \quad (5.30)$$

where  $B_{[m+n \leq N_p]}$  is a Boolean function which has value one, when  $[m+n \leq N_p]$ , and zero otherwise; and  $N_p$  is the order of the series expansion. Similarly, the coefficient of second-order spatial derivative (zero) and the coefficient of the auxiliary term ( $\alpha$ ) in the Eq. (5.28) are also expanded in the perturbation form to eliminate secular terms from the solution,

$$0 = \sum_{m=0}^{N_p} \sum_{n=0}^{N_p} p_1^m p_2^n \Gamma_{m,n} B_{[m+n \leq N_p]}. \quad (5.31)$$

The secular term generated from the non-linear term [term with coefficient  $p_1$  of equation (5.28)] can be removed by using parameter expansion for coefficient zero (Munusamy and Dhar, 2016). The coefficient zero of the virtual term in the

homotopy equation (5.28) can be expanded with unknown parameters as defined in the equation (5.31). The unknown parameters are determined during the secular term elimination process by forcing the coefficients of the secular term to be zero. The term containing  $\alpha$  is referred to as an auxiliary term (He, 2012). It becomes zero when the parameter  $p_2$  is zero or one. The auxiliary term in the homotopy equation is constructed using  $p_2$  to remove the secular terms generated due to the presence of slope effects [term with coefficient  $p_2$  of equation (5.28)], where  $f(x, t)$  is the possible secular term. The perturbation expansion for the auxiliary term can be written as follows,

$$\alpha = \sum_{m=0}^{N_p} \sum_{n=0}^{N_p} p_1^m p_2^n \alpha_{m,n} B_{[m+n \leq N_p]}. \quad (5.32)$$

The secular terms and the unknown parameters in the equation (5.32) can be determined during the solution process. By fixing  $N_p = 2$ , and substituting homotopy equation to convert the non-linear partial differential equation into a set of linear partial differential equations. The order of the solutions is reduced to 2 for the brevity of the text. The solution can be extended for higher orders easily, depending on the required accuracy. By solving the linear differential equations for  $h_{0,0}$ ,  $h_{1,0}$ ,  $h_{0,1}$ ,  $h_{2,0}$ ,  $h_{1,2}$  and  $h_{0,2}$ , a higher-order solution can be obtained by using  $p_1 \rightarrow 1$  and  $p_2 \rightarrow 1$  in the equation (5.30).

$$\begin{aligned} h &= \lim_{p_1 \rightarrow 1} \lim_{p_2 \rightarrow 1} \sum_{m=0}^{N_p} \sum_{n=0}^{N_p} p_1^m p_2^n h_{m,n} B_{[m+n \leq N_p]}, \\ &= h_{0,0} + h_{1,0} + h_{0,1} + h_{2,0} + h_{1,1} + h_{0,2}. \end{aligned} \quad (5.33)$$

By defining wave number  $k_1$ , the homotopy equation becomes,

$$\begin{aligned} h_{,t} &= \omega/2k_1^2 h_{,x^*x^*} + p_1(K/\eta_e (h h_{,x^*}),_{x^*} + p_2(-s_p \sin[\omega t] h_{,x^*}) \\ &\quad + \alpha p_2 (1 - p_2) f(x, t), \end{aligned} \quad (5.34)$$

$$k_1 = \sqrt{\frac{\omega}{2\Gamma_{0,0}}}. \quad (5.35)$$

By substituting the equations (5.30) and (5.31) into (5.34), perturbation equations along with boundary conditions for different powers of virtual parameters can be

written as,  $p_1^0 p_2^0$  equation:

$$(h_{0,0})_{,t} - \frac{\omega}{2k_1^2} (h_{0,0})_{,x^*x^*} = 0, \quad (5.36)$$

$$h_{0,0}(0, t) = D + A \cos[\omega t], \quad (5.37)$$

$$(h_{0,0})_{,x^*} \big|_{x^* \rightarrow \infty} = 0. \quad (5.38)$$

$p_1^1 p_2^0$  equation:

$$(h_{1,0})_{,t} - \frac{\omega}{2k_1^2} (h_{1,0})_{,x^*x^*} = \underbrace{-\Gamma_{1,0} (h_{0,0})_{,x^*x^*} + K/\eta_e [h_{0,0} (h_{0,0})_{,x^*}]_{,x^*}}_{I_{1,0}}, \quad (5.39)$$

$$h_{1,0}(0, t) = 0, \quad (5.40)$$

$$(h_{1,0})_{,x^*} \big|_{x^* \rightarrow \infty} = 0. \quad (5.41)$$

$p_1^0 p_2^1$  equation:

$$(h_{0,1})_{,t} - \frac{\omega}{2k_1^2} (h_{0,1})_{,x^*x^*} = \underbrace{-\Gamma_{0,1} (h_{0,0})_{,x^*x^*}}_{I_{0,1}^1} \underbrace{-s_p \sin[\omega t] (h_{0,0})_{,x^*}}_{I_{0,1}^2} \underbrace{+ \alpha_{0,0} f(x, t)}_{I_{0,1}^3}, \quad (5.42)$$

$$h_{0,1}(0, t) = 0, \quad (5.43)$$

$$(h_{0,1})_{,x^*} \big|_{x^* \rightarrow \infty} = 0. \quad (5.44)$$

$p_1^2 p_2^0$  equation:

$$(h_{2,0})_{,t} - \frac{\omega}{2k_1^2} (h_{2,0})_{,x^*x^*} = \underbrace{-\Gamma_{1,0} (h_{1,0})_{,x^*x^*} - \Gamma_{2,0} (h_{0,0})_{,x^*x^*}}_{I_{2,0}^1} \underbrace{+ K/\eta_e [h_{1,0} (h_{0,0})_{,x^*} + h_{0,0} (h_{1,0})_{,x^*}]_{,x^*}}_{I_{2,0}^2}, \quad (5.45)$$

$$h_{2,0}(0, t) = 0, \quad (5.46)$$

$$(h_{2,0})_{,x^*} \big|_{x^* \rightarrow \infty} = 0. \quad (5.47)$$

$p_1^1 p_2^1$  equation:

$$(h_{1,1})_t - \frac{\omega}{2k_1^2} (h_{1,1})_{x^* x^*} = \underbrace{-\Gamma_{0,1} (h_{1,0})_{x^* x^*} - \Gamma_{1,0} (h_{0,1})_{x^* x^*} - \Gamma_{1,1} (h_{0,0})_{x^* x^*}}_{I_{1,1}^1} + \underbrace{K/\eta_e [h_{0,0} (h_{0,1})_{x^*} + h_{0,1} (h_{0,0})_{x^*}]}_{I_{1,1}^2}, \underbrace{-s_p \sin[\omega t] (h_{1,0})_{x^*} + \alpha_{1,0} f(x, t)}_{I_{1,1}^3}, \quad (5.48)$$

$$h_{1,1}(0, t) = 0, \quad (5.49)$$

$$(h_{1,1})_{x^*} \big|_{x^* \rightarrow \infty} = 0. \quad (5.50)$$

$p_1^0 p_2^2$  equation:

$$(h_{0,2})_t - \frac{\omega}{2k_1^2} (h_{0,2})_{x^* x^*} = \underbrace{-\Gamma_{0,1} (h_{0,1})_{x^* x^*} - \Gamma_{0,2} (h_{0,0})_{x^* x^*}}_{I_{0,2}^1} + \underbrace{-s_p \sin[\omega t] (h_{0,1})_{x^*} + (-\alpha_{0,0} + \alpha_{0,1}) f(x, t)}_{I_{0,2}^2}, \underbrace{(-\alpha_{0,0} + \alpha_{0,1}) f(x, t)}_{I_{0,2}^3}, \quad (5.51)$$

$$h_{0,2}(0, t) = 0, \quad (5.52)$$

$$(h_{0,2})_{x^*} \big|_{x^* \rightarrow \infty} = 0. \quad (5.53)$$

Where,  $I_{1,0}$ ,  $I_{0,1}$  ( $= I_{0,1}^1 + I_{0,1}^2 + I_{0,1}^3$ ),  $I_{2,0}$  ( $= I_{2,0}^1 + I_{2,0}^2$ ),  $I_{1,1}$  ( $= I_{1,1}^1 + I_{1,1}^2 + I_{1,1}^3$ ), and  $I_{0,2}$  ( $= I_{0,2}^1 + I_{0,2}^2 + I_{0,2}^3$ ) are inhomogeneous terms for  $p_1^1 p_2^0$ ,  $p_1^0 p_2^1$ ,  $p_1^2 p_2^0$ ,  $p_1^1 p_2^1$ , and  $p_1^0 p_2^2$  equations respectively. Solutions for each  $p_1^m p_2^n$  are obtained for  $N_p < 3$ . Solution for the  $p_1^0 p_2^0$  equation (5.36) is given by,

$$h_{0,0}(x^*, t) = D + A e^{-k_1 x^*} \cos[\omega t - k_1 x^*]. \quad (5.54)$$

By substituting Eq. (5.54) in the expression (5.39) the inhomogeneous term ( $I_{1,0}$ ) can be written as,

$$I_{1,0} = \frac{A^2 k_1^2 K}{\eta_e} \{e^{-2k_1 x^*} - 2 e^{-2k_1 x^*} \sin[2\omega t - 2k_1 x^*]\} + \frac{2A k_1^2}{\eta_e} [KD - \eta_e \Gamma_{1,0}] \underbrace{e^{-k_1 x^*} \sin[\omega t - k_1 x^*]}_{\text{secular term}}. \quad (5.55)$$

Requirement of no secular term in inhomogeneous term  $I_{1,0}$  needs,

$$\Gamma_{1,0} = \frac{KD}{\eta_e}. \quad (5.56)$$

If  $\Gamma_{0,0}$  is replaced with  $\Gamma_{1,0}$  from expression (5.56), the equation (5.36) represents linearized Boussinesq equation. Particular integral for the  $p_1^1 p_2^0$  equation is given as,

$$h_{1,0}^{PI}(x^*, t) = -\frac{A^2 k_1^2 K}{2\eta_e \omega} e^{-2k_1 x^*} \{1 + 2 \cos[2\omega t - 2k_1 x^*]\}. \quad (5.57)$$

Boundary condition can be satisfied by expressing the solution  $h_{1,0}$  as addition of particular integral  $[h_{1,0}^{PI}]$  and complementary function  $(h_{1,0}^{CF})$ ,

$$h_{1,0}(0, t) = h_{1,0}^{PI}(0, t) + h_{1,0}^{CF}(0, t) = 0, \quad (5.58)$$

$$h_{1,0}^{CF}(x^*, t) = \frac{A^2 k_1^2 K}{2\eta_e \omega} \left\{ 1 + 2 e^{-\sqrt{2}k_1 x^*} \cos[2\omega t - \sqrt{2}k_1 x^*] \right\}. \quad (5.59)$$

Solution for the  $p_1^1 p_2^0$  equation ( $h_{1,0}$ ) can be given as,

$$\begin{aligned} h_{1,0}(x^*, t) = & \frac{A^2 k_1^2 K}{2\eta_e \omega} \left\{ 1 - e^{-2k_1 x^*} \right. \\ & - 2e^{-2k_1 x^*} \cos[2\omega t - 2k_1 x^*] \\ & \left. + 2 e^{-\sqrt{2}k_1 x^*} \cos[2\omega t - \sqrt{2}k_1 x^*] \right\}. \end{aligned} \quad (5.60)$$

By substituting Eq. (5.60) in the Eq. (5.42), the inhomogeneous term  $I_{0,1}$  is given by,

$$\begin{aligned} I_{0,1} = & \frac{Ak_1 s_p e^{-k_1 x^*}}{2} \left\{ -\cos[k_1 x^*] + \cos[2\omega t - k_1 x^*] \right. \\ & + \sin[k_1 x^*] + \sin[2\omega t - k_1 x^*] \} \\ & + 2Ak_1^2 \Gamma_{0,1} e^{-k_1 x^*} \sin[\omega t - k_1 x^*] \\ & \left. + \alpha_{0,0} f(x, t) \right. \end{aligned} \quad (5.61)$$

Eliminating the secular term in particular integral by forcing the coefficient of secular term to zero,

$$\Gamma_{0,1} = 0, \quad (5.62)$$

$$\alpha_{0,0} = 0. \quad (5.63)$$

Solution for the  $p_1^0 p_2^1$  equation ( $h_{0,1}$ ) can be obtained as,

$$h_{0,1}(x^*, t) = \frac{Ak_1 s_p}{2\omega} \left\{ 1 - e^{-k_1 x^*} \cos[k_1 x^*] - e^{-k_1 x^*} \cos[2\omega t - k_1 x^*] + e^{-\sqrt{2}k_1 x^*} \cos[2\omega t - \sqrt{2}k_1 x^*] - e^{-k_1 x^*} \sin[k_1 x^*] + e^{-k_1 x^*} \sin[2\omega t - k_1 x^*] - e^{-\sqrt{2}k_1 x^*} \sin[2\omega t - \sqrt{2}k_1 x^*] \right\}. \quad (5.64)$$

By eliminating secular terms from  $I_{2,0}$ , the expressions for  $\Gamma_{2,0}$  and  $\alpha_{0,0}$  can be obtained as,

$$\Gamma_{2,0} = \frac{A^2 k_1^2 K^2}{2\eta_e^2 \omega}, \quad (5.65)$$

$$\alpha_{0,0} = 0, \quad (5.66)$$

Solution for the  $p_1^2 p_2^0$  equation ( $h_{2,0}$ ) can be given as,

$$h_{2,0}(x^*, t) = \frac{A^3 k_1^4 K^2}{\eta_e^2 \omega^2} \left\{ \frac{3}{2} e^{-3k_1 x^*} \cos[3\omega t - 3k_1 x^*] - \frac{1}{4} (4 + 3\sqrt{2}) e^{-(1+\sqrt{2})k_1 x^*} \cos[3\omega t - (1 + \sqrt{2})k_1 x^*] + \frac{1}{4} (-2 + 3\sqrt{2}) e^{-\sqrt{3}k_1 x^*} \cos[3\omega t - \sqrt{3}k_1 x^*] + \frac{11}{5} e^{-3k_1 x^*} \cos[\omega t - k_1 x^*] - \frac{6}{5} e^{-k_1 x^*} \cos[\omega t - k_1 x^*] - e^{-(1+\sqrt{2})k_1 x^*} \cos[\omega t + (1 - \sqrt{2})k_1 x^*] + \frac{2}{5} e^{-3k_1 x^*} \sin[\omega t - k_1 x^*] - \frac{1}{20} (-8 + 5\sqrt{2}) e^{-k_1 x^*} \sin[\omega t - k_1 x^*] + \frac{1}{2\sqrt{2}} e^{-(1+\sqrt{2})k_1 x^*} \sin[\omega t + (1 - \sqrt{2})k_1 x^*] \right\}. \quad (5.67)$$

By substituting equations (5.54), (5.60) and (5.64) in the equation (5.48), and eliminating the secular terms (by forcing the coefficient of secular terms to zero) in  $I_{1,1}$ ,

$$\Gamma_{1,1} = \frac{Ak_1 K s_p}{2\eta_e \omega}, \quad (5.68)$$

$$\alpha_{1,0} = 0. \quad (5.69)$$

Solution for the  $p_1^0 p_2^2$  order can be given as,

$$\begin{aligned} h_{0,2}(x^*, t) = & \frac{Ak_1^2 s_p^2}{\omega^2} \left\{ -\frac{1}{4} e^{-k_1 x^*} \sin[3\omega t - k_1 x^*] \right. \\ & + \frac{1}{\sqrt{2}} e^{-\sqrt{2}k_1 x^*} \sin[3\omega t - \sqrt{2}k_1 x^*] \\ & - \frac{1}{4} (-1 + 2\sqrt{2}) e^{-\sqrt{3}k_1 x^*} \sin[3\omega t - \sqrt{3}k_1 x^*] \\ & - \frac{1}{\sqrt{2}} e^{-k_1 x^*} \sin[\omega t - k_1 x^*] \\ & \left. + \frac{1}{\sqrt{2}} e^{-\sqrt{2}k_1 x^*} \sin[\omega t - \sqrt{2}k_1 x^*] \right\}. \end{aligned} \quad (5.70)$$

Solution for the  $p_1^1 p_2^1$  equation ( $h_{1,1}$ ) can be given as,

$$\begin{aligned}
h_{1,1}(x^*, t) &= \frac{A^2 k_1^3 K s_p}{\eta_e \omega^2} \left\{ e^{-2k_1 x^*} \cos[\omega t] + e^{-2k_1 x^*} \cos[3\omega t - 2k_1 x^*] \right. \\
&\quad - \frac{1}{\sqrt{2}} e^{-\sqrt{2}k_1 x^*} \cos[3\omega t - \sqrt{2}k_1 x^*] \\
&\quad + \frac{1}{8} (-4 + 7\sqrt{2}) e^{-\sqrt{3}k_1 x^*} \cos[3\omega t - \sqrt{3}k_1 x^*] \\
&\quad - \frac{1}{8} (4 + 3\sqrt{2}) e^{-(1+\sqrt{2})k_1 x^*} \cos[3\omega t - (1 + \sqrt{2})k_1 x^*] \\
&\quad + \frac{3}{8} (-4 + \sqrt{2}) e^{-k_1 x^*} \cos[\omega t - k_1 x^*] \\
&\quad + e^{-2k_1 x^*} \cos[\omega t - 2k_1 x^*] \\
&\quad - \frac{1}{\sqrt{2}} e^{-\sqrt{2}k_1 x^*} \cos[\omega t - \sqrt{2}k_1 x^*] \\
&\quad + \frac{1}{8} (-4 + \sqrt{2}) e^{-(1+\sqrt{2})k_1 x^*} \cos[\omega t + (1 - \sqrt{2})k_1 x^*] \\
&\quad - e^{-2k_1 x^*} \sin[3\omega t - 2k_1 x^*] \\
&\quad + \frac{1}{\sqrt{2}} e^{-\sqrt{2}k_1 x^*} \sin[3\omega t - \sqrt{2}k_1 x^*] \\
&\quad - \frac{1}{8} (-4 + 7\sqrt{2}) e^{-\sqrt{3}k_1 x^*} \sin[3\omega t - \sqrt{3}k_1 x^*] \\
&\quad + \frac{1}{8} (4 + 3\sqrt{2}) e^{-(1+\sqrt{2})k_1 x^*} \sin[3\omega t - (1 + \sqrt{2})k_1 x^*] \\
&\quad - \frac{1}{8} (-4 + 5\sqrt{2}) e^{-k_1 x^*} \sin[\omega t - k_1 x^*] \\
&\quad - e^{-2k_1 x^*} \sin[\omega t - 2k_1 x^*] \\
&\quad + \frac{1}{\sqrt{2}} e^{-\sqrt{2}k_1 x^*} \sin[\omega t - \sqrt{2}k_1 x^*] \\
&\quad \left. + \frac{1}{8} (4 + \sqrt{2}) e^{-(1+\sqrt{2})k_1 x^*} \sin[\omega t + (1 - \sqrt{2})k_1 x^*] \right\}. \tag{5.71}
\end{aligned}$$

By substituting equations (5.54) and (5.64) in the equation (5.51), and eliminating the secular term  $e^{-k_1 x^*} \sin[\omega t - k_1 x^*]$  from inhomogeneous term  $I_{0,2}$ ,

$$\Gamma_{0,2} = 0. \tag{5.72}$$

There is a new secular term  $e^{-k_1 x^*} \cos[\omega t + k_1 x^*]$  present in the inhomogeneous term  $I_{0,2}$ . By defining  $f(x, t)$  and eliminating it by forcing its coefficient to zero,

$\alpha_{0,1}$  can be obtained as,

$$f(x, t) = e^{-k_1 x^*} \cos[\omega t + k_1 x^*], \quad (5.73)$$

$$\alpha_{0,1} = -\frac{Ak_1^2 s_p^2}{2\omega}. \quad (5.74)$$

Groundwater fluctuation due to tidal oscillations for a coastal aquifer with vertical beach face is given as,

$$\begin{aligned} h(x^*, t) = & D + A e^{-k_1 x^*} \cos[\omega t - k_1 x^*] \\ & \frac{A^2 k_1^2 K}{2\eta_e \omega} \left\{ 1 - e^{-2k_1 x^*} \right. \\ & - 2e^{-2k_1 x^*} \cos[2\omega t - 2k_1 x^*] \\ & + 2 e^{-\sqrt{2}k_1 x^*} \cos[2\omega t - \sqrt{2}k_1 x^*] \left. \right\} \\ & + \frac{A^3 k_1^4 K^2}{\eta_e^2 \omega^2} \left\{ \frac{3}{2} e^{-3k_1 x^*} \cos[3\omega t - 3k_1 x^*] \right. \\ & - \frac{1}{4} (4 + 3\sqrt{2}) e^{-(1+\sqrt{2})k_1 x^*} \cos[3\omega t - (1 + \sqrt{2})k_1 x^*] \\ & + \frac{1}{4} (-2 + 3\sqrt{2}) e^{-\sqrt{3}k_1 x^*} \cos[3\omega t - \sqrt{3}k_1 x^*] \\ & + \frac{11}{5} e^{-3k_1 x^*} \cos[\omega t - k_1 x^*] \\ & - \frac{6}{5} e^{-k_1 x^*} \cos[\omega t - k_1 x^*] \\ & - e^{-(1+\sqrt{2})k_1 x^*} \cos[\omega t + (1 - \sqrt{2})k_1 x^*] \\ & + \frac{2}{5} e^{-3k_1 x^*} \sin[\omega t - k_1 x^*] \\ & - \frac{1}{20} (-8 + 5\sqrt{2}) e^{-k_1 x^*} \sin[\omega t - k_1 x^*] \\ & \left. + \frac{1}{2\sqrt{2}} e^{-(1+\sqrt{2})k_1 x^*} q \sin[\omega t + (1 - \sqrt{2})k_1 x^*] \right\}. \quad (5.75) \end{aligned}$$

### 5.2.2.1 Discussions and Solution Comparisons

The HPM does not use any pre-defined perturbation parameter. However, some non-dimensional parameters emerge in the solution. For example, the amplitude of  $h_{1,0}$  can be written as the multiplication of  $A$  and  $Ak_1^2 K / (2\eta_e \omega)$ . By substituting the expression for wave number (5.35), the amplitude of  $h_{1,0}$  (Eq. 5.60) is multiplication of  $A$  and  $[AK / (\eta_e \Gamma_{0,0})]^1$ . Similarly, the amplitude of  $h_{2,0}$   $[A^3 k_1^4 K^2 / (\eta_e^2 \omega^2)]$  can be expressed as the multiplication of  $A$  and  $[AK / (\eta_e \Gamma_{0,0})]^2$ . Hence, it can be observed from the solutions of order  $p_1^a p_2^0$  with  $a = 0, 1, 2, \dots$  equations that  $[AK / (\eta_e \Gamma_{0,0})]^a$  is acting as a non-dimensional parameter[By sub-

stituting equation(5.35)into the non-dimensional parameter]. All the solutions of  $p_1^a p_2^0$  with  $a = 0, 1, 2, \dots$  equations, have the above non-dimensional parameter with an multiplier  $A$  as their amplitude. Similarly, for  $p_1^0 p_2^b$  equations, the expression  $[k_1 s_p / \omega]^b$  emerges as a non-dimensional parameter. The amplitudes of the solutions of  $p_1^0 p_2^b$  equations are equal to the multiplication of  $[k_1 s_p / \omega]^b$  and  $A$ . For the cross product terms  $p_1^a p_2^b$ , with  $a > 0$  and  $b > 0$ , that is  $h_{1,1}$ ,  $h_{2,2}$  etc., the product of  $[AK/(\eta_e \Gamma_{0,0})]^a$  and  $[k_1 s_p / \omega]^b$  emerge as a non-dimensional parameter. The amplitudes of the solutions of the equations  $p_1^a p_2^b$ , with  $a > 0$  and  $b > 0$ , are products of the non-dimensional parameters  $[AK/(\eta_e \Gamma_{0,0})]^a$ ,  $[k_1 s_p / \omega]^b$ , and  $A$ . For example the solution for  $p_1^1 p_2^1$  equation, which has  $a = 1 = b$ , is given below,

$$\frac{A^2 k_1^3 K s_p}{\eta_e \omega^2} = \left( \frac{A k_1^2 K}{\omega \eta_e} \right)^1 \times \left( \frac{k_1 s_p}{\omega} \right)^1. \quad (5.76)$$

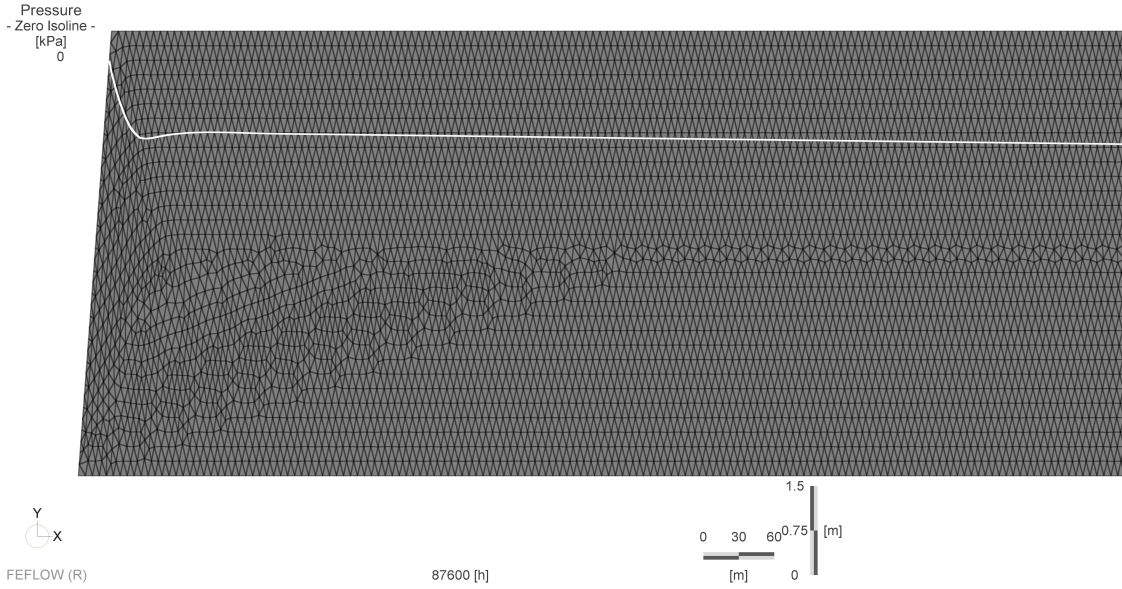
By the elimination of secular terms using parameter expansion in homotopy perturbation method, the parameters  $\Gamma_{1,0}$ ,  $\Gamma_{0,1}$ ,  $\Gamma_{2,0}$ ,  $\Gamma_{1,1}$ ,  $\Gamma_{0,2}$  are determined(The procedure for the same is explained in Appendix). The parameter  $\Gamma_{0,0}$  can be determined by solving the implicit equation (5.31), for  $p_1 \rightarrow 1$  and  $p_2 \rightarrow 1$ . The damping rate and phase of the solution, which depends on  $\Gamma_{0,0}$ , changes with the order of the solution. The implicit equation of  $\Gamma_{0,0}$  contains amplitude of the tidal wave ( $A$ ), frequency of the tidal wave ( $\omega$ ), hydraulic conductivity of the aquifer ( $K$ ), porosity of the aquifer ( $\eta_e$ ), mean sea level ( $D$ ) and slope of the beach ( $\beta$ ).

The solution accuracy is examined by using comparison plots between the present solution obtained by using HPM, Teo et al. (2003), Kong et al. (2011), and two-dimensional numerical solution. A two-dimensional numerical solution for the vertical cross-section is obtained by using finite element based variable saturated flow and transport simulator FEFLOW (Diersch, 2013). The unsaturated flow is modeled with the Richards equation. The soil-water characteristics curve is modeled by using van Genuchten (Van Genuchten, 1980) analytic function. The values  $14.5(1/m)$  and  $2.68$  are used respectively for the scale parameter and slope parameter in the water retention curve Munusamy and Dhar (2017). The above parameters are obtained from Carsel and Parrish (1988) probability-distribution tables for soil water retention characteristics curves. The seaside boundary condition is simulated by using the hydraulic head boundary condition with a time series representing the tidal fluctuations. The mean sea level is used as the initial condition of the domain. The domain size in the x-direction is  $10000\text{ m}$  and in the y-direction is  $7.5\text{ m}$ . The analytical solution uses an asymptotic boundary condition for the inland boundary. But, in numerical modeling, the domain size of infinite distance cannot be defined. Hence, the domain size in the x-direction

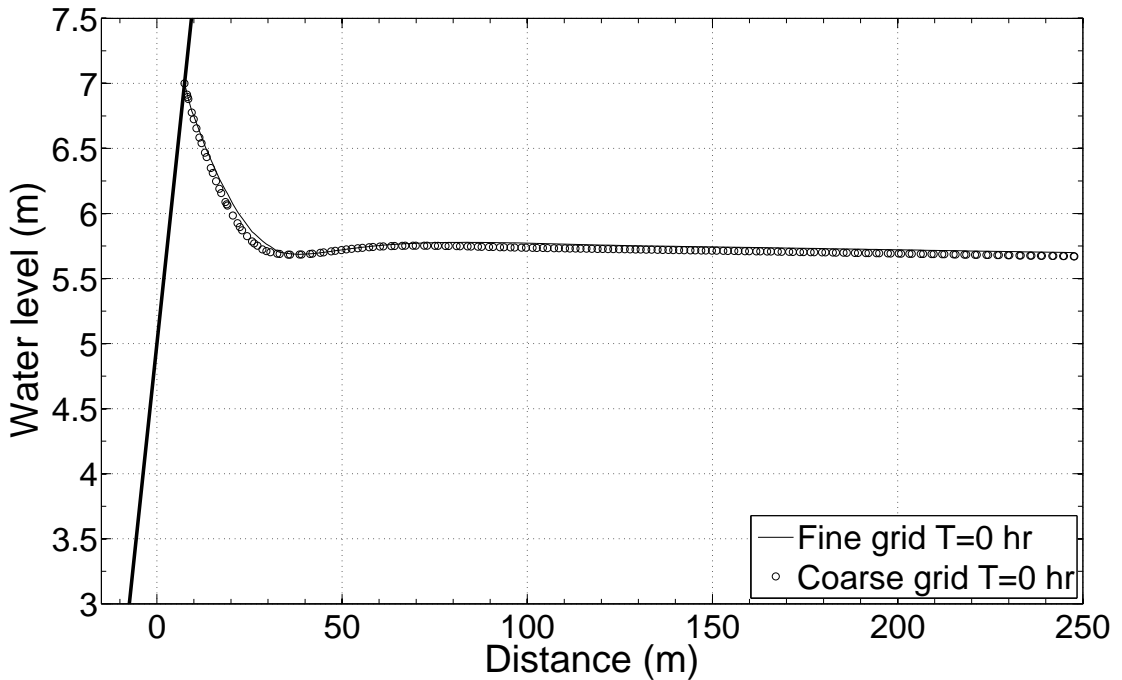
is chosen as a very large one to avoid the inland boundary effects. The inland boundary at  $x = 10000\text{ m}$  [no flow boundary condition]. The numerical solution for the slope  $\pi/12$  is tested for grid convergence by simulating for a coarse grid with 105685 elements (54572 nodes) and a fine grid with 415671 elements (211293 nodes) for three years time-period (2190 tide cycles). It is observed that the results for pressure values converged for coarse grid simulation. The simulation using the coarse grid is done for ten year simulation period (7300 tide cycles) to obtain a quasi-steady state solution. The plot for grid convergence study is given in Fig 5.7.

The parameter values of Kong et al. Kong et al. (2011) are used for plotting (Parameter values:  $\eta_e = 0.3$ ,  $K = 5 \times 10^{-4}\text{ m/s}$ ,  $D = 5\text{ m}$ ,  $A = 2\text{ m}$ , and  $\omega = 4\pi/\text{day}$ ). The water table is obtained by plotting zero isolines (water table) for (pressure Fig. 5.7). The plots at different time instances of the tidal cycle are provided for  $15^\circ$  (Scenario-A, Fig. 5.8) and  $30^\circ$  (Scenario-B, Fig. 5.9) beach face angle ( $\beta$ ). The deviation is prominent for the slope of  $\pi/6$ . Similar trends are observed for Teo et al. (2003) and Kong et al. (2011) solutions. The boundary condition for the inland boundary is different for the analytical solution and numerical 2D solution. Analytical solution reaches a constant water table level around 70 m inland from the seaside boundary. Also, the constant water table level for the analytical solution is raised above 5 m. But, for the numerical solution, the asymptotic water level is 5 m, which is the same as the initial condition for the full domain. Hence, the numerical solution reaches an asymptotic water level of 5 m with a gradual change from the seaside boundary to the inland. So, the comparison is made for the region near to the seaside boundary only. Hence, the plots and error statistics are compared for  $x < 250\text{ m}$ . The error statistics for mean absolute deviation(MAD) and RMSE (Root mean square error) are provided in Table 5.2. The maximum errors for HPM solution based on both MAD and RMSE for slope  $\pi/12$  are 2.9135% and  $0.2152\text{ m}$  respectively. The maximum errors for HPM solution based on both MAD and RMSE for slope  $\pi/6$  are 2.7865% and  $0.1784\text{ m}$  respectively. Both MAD and RMSE maximum error values correspond to the milder slope( $\pi/12$ ). The present solution compares well with the previous analytical solutions for steep slopes. However, when the slope decreases, the deviation from the 2D FEFLOW solution increases. The deviation is prominent for the lower values of  $\beta$  ( $s_p \rightarrow 1$ ). Similar trend is also observed for Teo et al. (2003) and Kong et al. (2011).

The parameters used in Teo et al. (2003) are physical (shallow-water parameter and amplitude parameter) and in Kong et al. (2011) are artificial (based on pre-defined  $D_{\infty, Kong}$ ). Teo et al. (2003) and Kong et al. (2011) used expansion



(a) Vertical 2D FEFLOW model domain. Water table variation in 2D FEFLOW simulation at  $t=0$  hr for Scenario-A. The domain in the x-direction is shown up to 800 m of total 10000 m length



(b) Grid convergence 2D FEFLOW simulation at  $t=0$  hr for Scenario-A after simulation period of 3 years. Coarse grid is with 105685 elements and fine grid is with 415671 elements

Figure 5.7: Cross-section of 2D FEFLOW simulation and solution comparison to show grid convergence for Scenario-A

within expansion to include the effect of two pre-defined parameters. The governing equation is expanded with one perturbation parameter initially to get the deformed equations of different powers. Then the deformed equations are again expanded using another parameter. This dual expansion generates a few extra

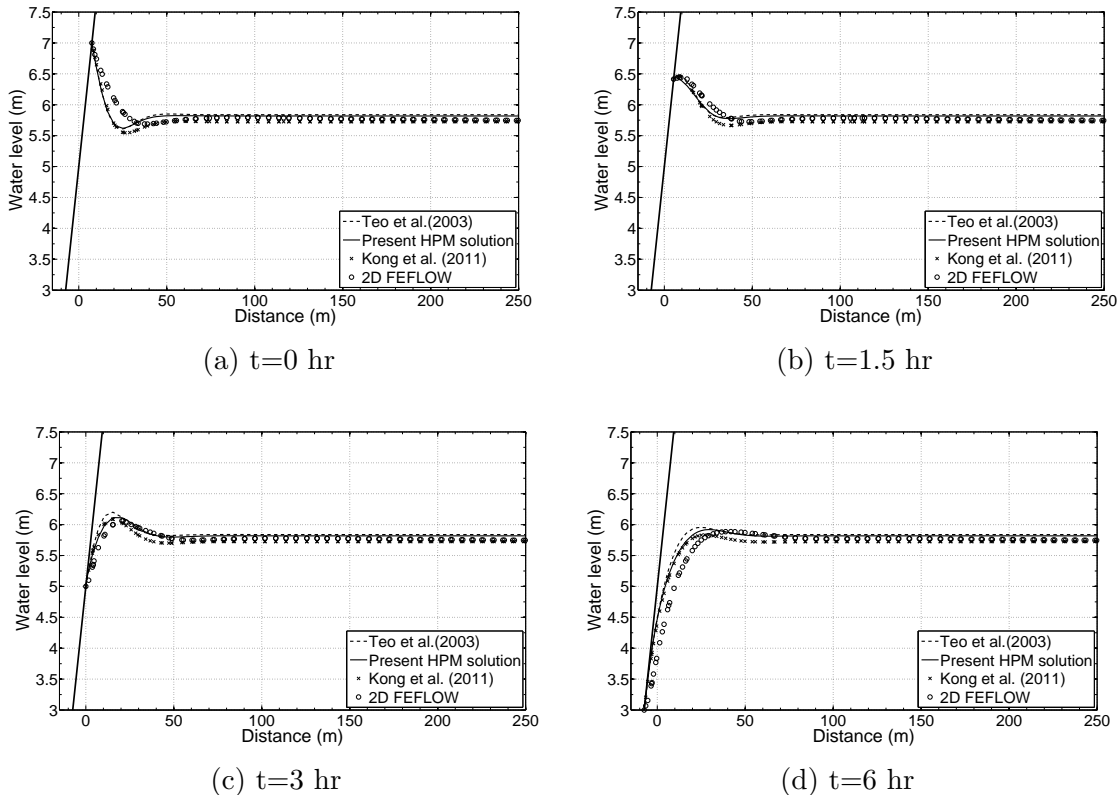


Figure 5.8: Scenario-A:  $\beta = \pi/12$ ; Comparison of Homotopy perturbation solution with Teo et al. (2003), Kong et al. (2011), and 2D FEFLOW solution for ground-water table fluctuation with a tidal wave with timeperiod= 12 hrs;  $D=5$  m;  $A=2$  m;  $K = 0.0005$  m/s;  $\eta_e = 0.3$

terms. In the present study, a single expansion combining two virtual homotopy parameters is used to represent the solution. Moreover, the coefficient expansion and auxiliary term expansion are used to eliminate secular terms. The present dimensional solution does not require any pre-defined non-dimensional parameters. The non-dimensional parameter groups generated during the solution process are based on physical parameters. The maximum difference between the solutions of two years and three-years simulations is in the order of  $10^{-5}$ . Hence the solutions are converged.

### 5.2.2.2 Special Case: Vertical Beach

The present solution is also plotted (Fig. 5.10) for vertical beach with beach angle  $\beta = 90^\circ$  (Scenario-C, Parameter values:  $\eta_e = 0.206$ ,  $K = 0.0017 \text{ m/s}$ ,  $D = 10 \text{ m}$ ,  $A = 0.5 \text{ m}$ , and  $\omega = 4\pi/\text{day}$ ). Apart from Teo et al. (2003) and Kong et al. (2011) solutions, the homotopy perturbation solution is also compared with the closed form solution provided by Yeh et al. (2010). The solutions for Yeh et al. (2010) were extracted digitally. The solution for vertical beach contains only  $p_1^a p_2^0$  terms since  $s_p$  becomes zero for vertical beach ( $x_0(t)$  and  $\Gamma_{1,1}$  also zero). The

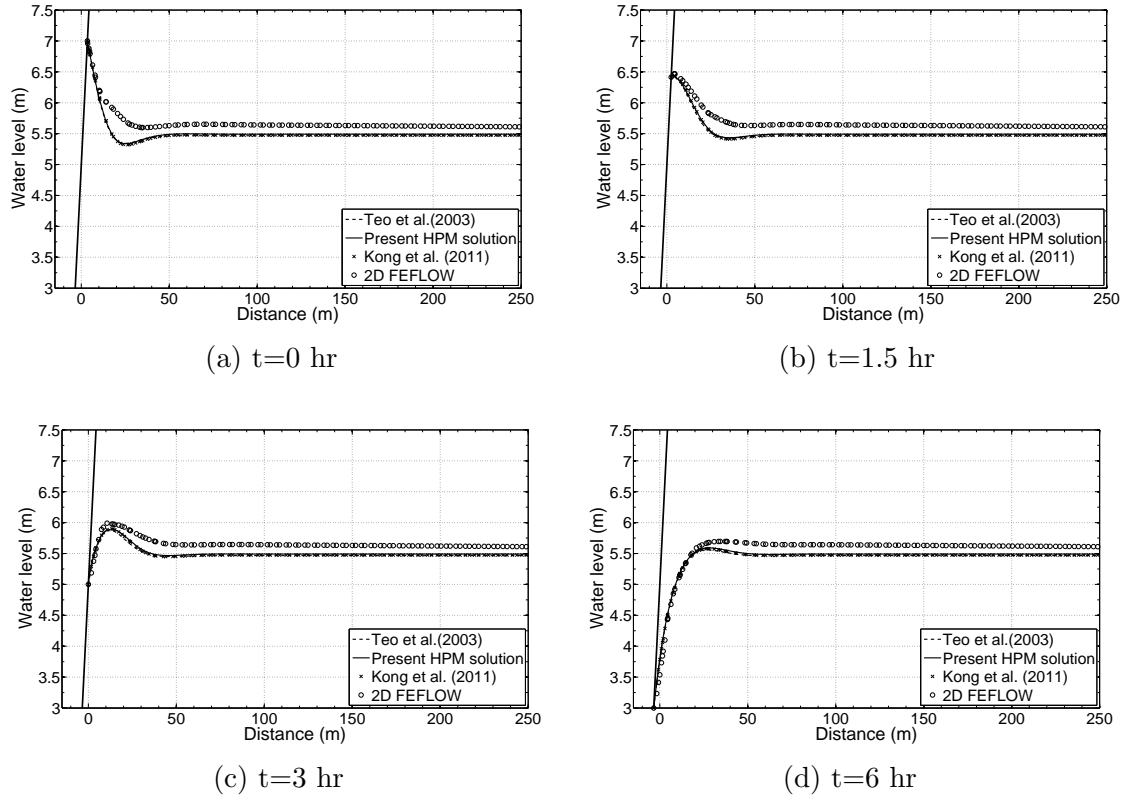


Figure 5.9: Scenario-B:  $\beta = \pi/6$ ; Comparison of Homotopy perturbation solution with Teo et al. (2003), Kong et al. (2011), and 2D FEFLOW solution for groundwater table fluctuation with a tidal wave with timeperiod= 12 hrs;  $D=5$  m;  $A=2$  m;  $K = 0.0005$  m/s;  $\eta_e = 0.3$

implicit equation for vertical beach to determine  $\Gamma_{0,0}$  is given as,

$$\Gamma_{0,0} = \Gamma_{1,0} + \Gamma_{2,0} = \frac{KD}{\eta_e} + \frac{A^2 K^2}{4\Gamma_{0,0}\eta_e^2}. \quad (5.77)$$

The error statistics for vertical beach face solutions are provided in Table 5.3. It can be observed from the tables Table 5.2 and Table 5.3 for error statistics that analytical solutions are more accurate for steeper slopes. The convergence of the simulation is verified by comparing the solution at the end of two year and three year simulation results(Fig. 5.11). The maximum difference between the solutions of two year and three year simulations is in the order of  $10^{-5}$ . Hence the solutions are converged.

### 5.2.2.3 Conclusions for the Analytical Solution for Groundwater Waves in a Sloping Beach

A dimensional analytical solution for groundwater table fluctuations in response to tidal forcing in a coastal aquifer with a sloping beach face is developed by using the homotopy perturbation method with two expansion parameters and one auxiliary term. Apart from the nonlinear term in the Boussinesq equation, the

Table 5.2: Error statistics for the comparison of HPM, Kong et al. (2011), and Teo et al. (2003) solutions with 2D-FEFLOW numerical solutions

| Slope $\pi/12$ |        |        |        |        |
|----------------|--------|--------|--------|--------|
| Solution       | Time   |        |        |        |
|                | 0 hr   | 1.5 hr | 3 hr   | 6 hr   |
| HPM MAD (%)    | 1.3962 | 1.0020 | 1.0634 | 2.9135 |
| HPM RMSE       | 0.1240 | 0.0659 | 0.0730 | 0.2152 |
| Kong MAD (%)   | 1.3022 | 0.9695 | 1.1114 | 2.6806 |
| Kong RMSE      | 0.1230 | 0.0724 | 0.0823 | 0.1946 |
| Teo MAD (%)    | 1.7053 | 1.2858 | 1.5145 | 3.4133 |
| Teo RMSE       | 0.1350 | 0.0794 | 0.1080 | 0.2454 |
| Slope $\pi/6$  |        |        |        |        |
| Solution       | Time   |        |        |        |
|                | 0 hr   | 1.5 hr | 3 hr   | 6 hr   |
| HPM MAD (%)    | 2.7865 | 2.6370 | 2.4684 | 2.4440 |
| HPM RMSE       | 0.1784 | 0.1577 | 0.1439 | 0.1375 |
| Kong MAD (%)   | 3.0023 | 2.8742 | 2.7037 | 2.5998 |
| Kong RMSE      | 0.1894 | 0.1713 | 0.1586 | 0.1480 |
| Teo MAD (%)    | 3.1451 | 3.0532 | 2.8830 | 2.7762 |
| Teo RMSE       | 0.1959 | 0.1809 | 0.1689 | 0.1574 |

time-dependent moving boundary effects due to slope effects introduces additional complexity. The homotopy equation is constructed using two virtual parameters. The secular terms generated in the perturbation method from nonlinear diffusion are eliminated by introducing a virtual linear term, and secular terms generated from slope effects are eliminated by using an auxiliary term. The coefficients of the virtual term and auxiliary terms are expanded using unknown parameters to derive higher order solution. The following conclusions can be drawn from the solution:

- The method does not require non-dimensionalization of the governing equation or pre-defined perturbation parameters.
- Two non-dimensional parameters emerge in the solution though no pre-defined parameter used for perturbation approach. The non-dimensional parameters are  $Ak_1^2 K / (\omega \eta_e)$  and  $k_1 s_p / \omega$  for non-linear diffusive term( $p_1$ ) and

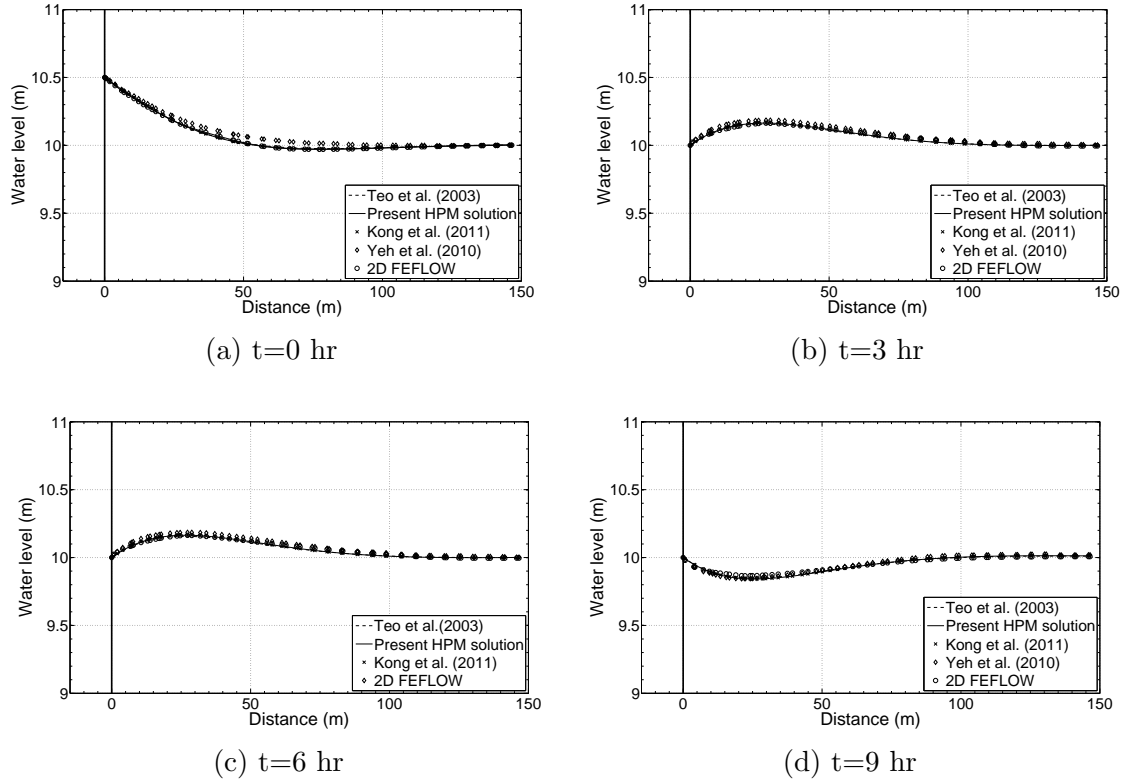


Figure 5.10: Scenario-C (vertical beach):  $\beta = \pi/2$ ; Comparison of Homotopy perturbation solution with Teo et al. (2003), Yeh et al. (2010) and Kong et al. (2011) for groundwater table fluctuation with a tidal wave with timeperiod= 12 hrs;  $D=10$  m;  $A=0.5$  m;  $K = 0.0017$  m/s;  $\eta_e = 0.2063$

Table 5.3: Error statistics for the comparison of HPM, Kong et al. (2011), Teo et al. (2003), Yeh et al. (2010) solutions with 2D-FEFLOW numerical solution

| Slope $\pi/2$ |        |        |        |        |
|---------------|--------|--------|--------|--------|
| Time          |        |        |        |        |
| Solution      | 0 hr   | 3 hr   | 6 hr   | 9 hr   |
| HPM MAD (%)   | 0.0350 | 0.0673 | 0.1168 | 0.1089 |
| HPM RMSE      | 0.0048 | 0.0086 | 0.0155 | 0.0134 |
| Kong MAD (%)  | 0.0350 | 0.0673 | 0.1169 | 0.1089 |
| Kong RMSE     | 0.0048 | 0.0086 | 0.0155 | 0.0135 |
| Teo MAD (%)   | 0.0363 | 0.0745 | 0.0911 | 0.0787 |
| Teo RMSE      | 0.0045 | 0.0093 | 0.0123 | 0.0100 |
| Yeh MAD (%)   | 0.2480 | 0.1579 | 0.2380 | 0.1495 |
| Yeh RMSE      | 0.0305 | 0.0179 | 0.0281 | 0.0164 |

linear slope term ( $p_2$ ) respectively.

- Damping rate and phase of the fluctuations depends on  $\Gamma_{0,0}$ , which is deter-

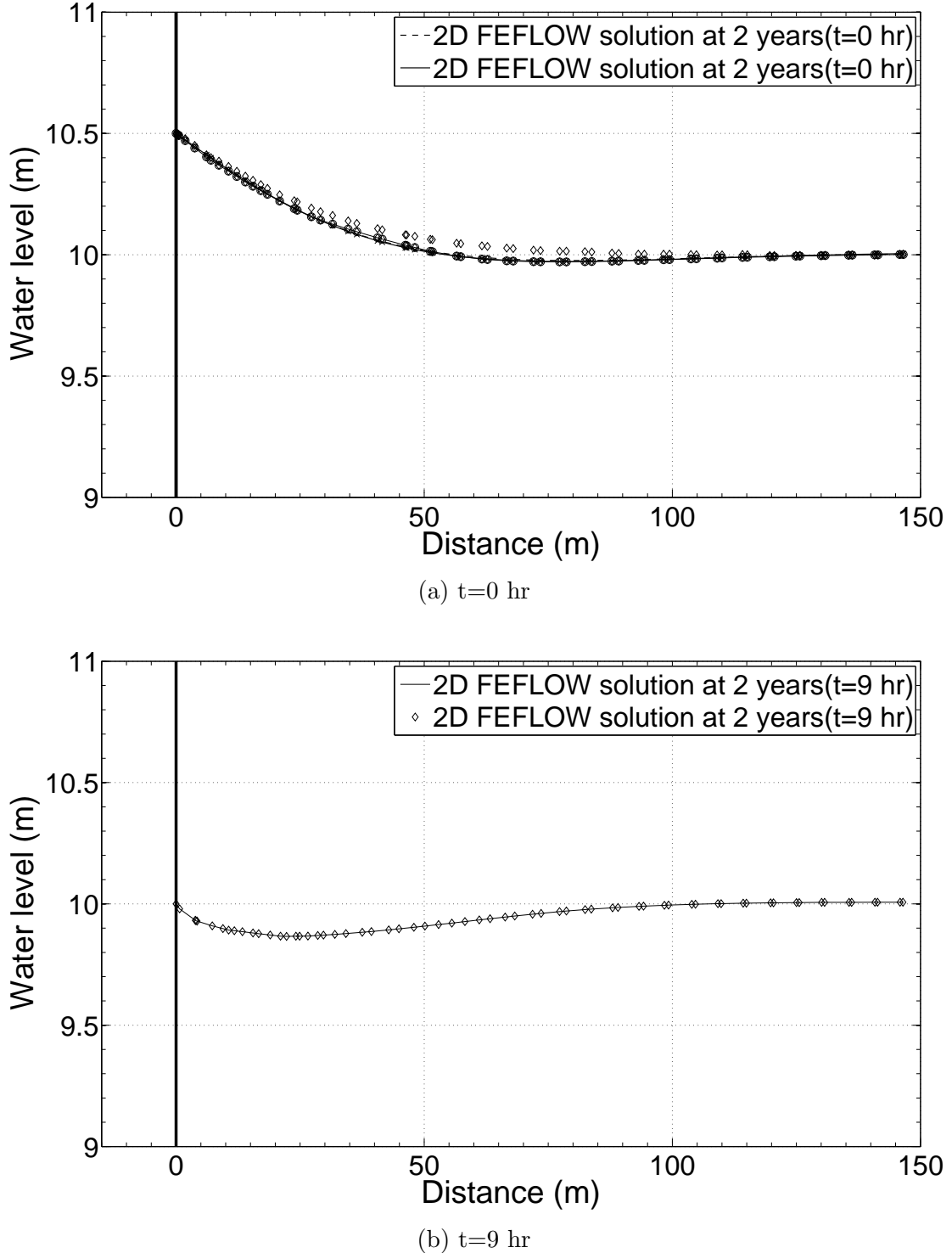


Figure 5.11: Comparison between the numerical solution at the end of two year simulation and three year simulation of 2D FEFLOW numerical solution. Simulation parameters are corresponding to Scenario-C (vertical beach):  $\beta = \pi/2$ ; a tidal wave with timeperiod= 12 hrs;  $D=10$  m;  $A=0.5$  m;  $K = 0.0017$  m/s;  $\eta_e = 0.2063$ .

mined by solving an implicit equation. The non-linear parameter  $Ak_1^2K/(\omega\eta_e)$  is equivalent to amplitude parameter ( $A/D$ ) only if  $p_1^0p_2^0$  and  $p_1^1p_2^0$  [ $\Gamma_{0,0} = KD/\eta_e$ ].

- The comparison of the solution with 2D FEFLOW simulation shows that HPM solution is more accurate for steep beach slopes.

### 5.2.3 Analytical Solution of Groundwater Waves in Anisotropic Unconfined Aquifers with Sloping Beach using Second-order Boussinesq Equation

In this section, the solution for groundwater waves in anisotropic-unconfined aquifers is derived. The second-order Boussinesq equation (3.24) derived in the Mathematical conceptualization chapter is used as the governing equation, and the boundary conditions are the same as previous sections. Homotopy equation for the second-order Boussinesq equation can be written as,

$$h_{,t} = \underbrace{0.h_{,x^*x^*}}_{\text{virtual term}} + p_1 K_x / \eta_e \left[ h h_{,x^*} + r \left( h^2 h_{,x^*} h_{,x^*x^*} + \frac{1}{3} h^3 h_{,x^*x^*x^*} \right) \right]_{,x^*} + p_2 (-s_p \sin[\omega t] h_{,x^*}) + \underbrace{\alpha p_1 (1 - p_1) h_{,x^*}}_{\text{auxiliary term}}, \quad (5.78)$$

$$s_p = A\omega \cot(\beta), \quad (5.79)$$

where,  $p_1$  and  $p_2$  are the virtual perturbation parameters,  $\alpha$  is the coefficient of the auxiliary term. The equation deforms from the original nonlinear equation to approximate linear equation when the embedding parameters change from one to zero ( $p_1 \rightarrow 0, p_2 \rightarrow 0$ ) as per the homotopy definition. The parameter  $p_1$  is used for nonlinear terms from second-order Boussinesq equation and  $p_2$  is used for the term representing slope effects. The virtual term and auxiliary term (He, 2012) are added to eliminate the secular terms. The auxiliary term becomes zero when the virtual parameter  $p_1$  is equal to zero or one. The solution can be expanded in series form by using the two perturbation parameters from the homotopy equation as follows,

$$h = \sum_{m=0}^{N_p} \sum_{n=0}^{N_p} p_1^m p_2^n h_{m,n} B_{[m+n \leq N_p]}, \quad (5.80)$$

where,  $N_p$  is the order of series expansion,  $m$  and  $n$  are incremental index variables, and  $B_{[m+n \leq N_p]}$  is a Boolean function. The Boolean function has value one when  $[m + n \leq N_p]$ , and zero otherwise. The second-order spatial derivative with zero coefficient (virtual term) in the RHS of the equation (5.78) is the physical approximation of the first nonlinear term in the RHS. The coefficient zero can be replaced with parameter expansion to eliminate the secular terms generated from the first

nonlinear term in the RHS of the equation (5.78). The parameter expansion for coefficient zero can be written as,

$$0 = w_{0,0} - \sum_{m=0}^{N_p} \sum_{n=0}^{N_p} p_1^m p_2^n w_{m,n} B_{[m+n \leq N_p]} B_{[m+n > 0]}. \quad (5.81)$$

The secular terms generated by second and third nonlinear terms can be eliminated by using the auxiliary term in the homotopy equation. The coefficient of the auxiliary term  $\alpha$  can also be expanded in the following form,

$$\alpha = \alpha_{0,0} + \sum_{m=0}^{N_p} \sum_{n=0}^{N_p} p_1^m p_2^n \alpha_{m,n} B_{[m+n \leq N_p]} B_{[m+n > 0]}. \quad (5.82)$$

By substituting equations, (5.80), (5.81), and (5.82) in the equation (5.78), the partial differential equations along with the boundary conditions for the different perturbation powers of virtual parameter can be written as,

$$p_1^0 p_2^0 : \begin{cases} (h_{0,0}),_t - \omega/2k_1^2 (h_{0,0}),_{x^*x^*} = 0, \\ h_0(x^*, t) = D + A \cos[\omega t], \\ (h_{0,0}),_{x^*} |_{x^* \rightarrow \infty} = 0. \end{cases} \quad (5.83)$$

$$p_1^1 p_2^0 : \begin{cases} (h_{1,0}),_t - \omega/2k_1^2 (h_{1,0}),_{x^*x^*} = \\ \underbrace{[-w_{1,0}(h_{0,0}),_{x^*x^*}]}_{I_{1,0}^1} \\ + \underbrace{[K_x/\eta_e (h_{0,0} (h_{0,0}),_{x^*} + r h_{0,0}^2 (h_{0,0}),_{x^*} (h_{0,0}),_{x^*x^*} + r 1/3 h_{0,0}^3 (h_{0,0}),_{x^*x^*x^*}),_{x^*}]}_{I_{1,0}^2} \\ + \underbrace{[\alpha_{0,0} (h_{0,0}),_{x^*}]}_{I_{1,0}^3} \\ h_{1,0}(x^*, t) = 0 \\ (h_{1,0}),_{x^*} |_{x^* \rightarrow \infty} = 0. \end{cases} \quad (5.84)$$

$$p_1^0 p_2^1 : \begin{cases} (h_{0,1}),_t - \omega/2k_1^2 (h_{0,1}),_{x^*x^*} = \\ \underbrace{[-w_{0,1}(h_{0,0}),_{x^*x^*}]}_{I_{0,1}^1} + \underbrace{[-s_p \sin[\omega t] (h_{0,0}),_{x^*}]}_{I_{0,1}^2} \\ h_{0,1}(x^*, t) = 0 \\ (h_{0,1}),_{x^*} |_{x^* \rightarrow \infty} = 0. \end{cases} \quad (5.85)$$

Where,  $I_{1,0}$  ( $= I_{1,0}^1 + I_{1,0}^2 + I_{1,0}^3$ ) and  $I_{0,1}$  ( $= I_{0,1}^1 + I_{0,1}^2$ ) are the inhomogeneous terms of  $p_1^1 p_2^0$  and  $p_1^0 p_2^1$  respectively.  $k_1$  is the wave number defined as,

$$k_1 = \sqrt{\frac{\omega}{2w_{0,0}}} \quad (5.86)$$

The procedure of the removal of secular terms is the same as previous derivations. The inhomogeneous terms are written in the appendix. By forcing secular terms to zero,  $\alpha_{0,0}$  and  $w_{1,0}$  can be obtained as,

$$\alpha_{0,0} = -\frac{4D^3 k_1^3 K_x r}{3\eta_e} \quad (5.87)$$

$$w_{1,0} = \frac{KD}{\eta_e} + \frac{2}{3} \frac{D^3 k_1^2 K_x r}{\eta_e} \quad (5.88)$$

The solution  $h_{1,0}(x^*, t)$ , for the  $p_1^0 p_2^1$  equation Eq. (5.84) can be given as,

$$\begin{aligned} h_{1,0}(x^*, t) &= \frac{A^2 k_1^2 K_x}{2\eta_e \omega} - \frac{A^2 k_1^2 K_x}{2\eta_e \omega} e^{-2k_1 x^*} - \frac{A^2 k_1^2 K_x}{\eta_e \omega} e^{-2k_1 x^*} \cos[2\omega t - 2k_1 x^*] \\ &+ \frac{A^4 k_1^4 K_x}{18\eta_e \omega} e^{-4k_1 x^*} \cos[2\omega t - 2k_1 x^*] + r \left( \frac{A^2 k_1^2 K_x}{\eta_e \omega} e^{-\sqrt{2}k_1 x^*} \cos[2\omega t - \sqrt{2}k_1 x^*] \right. \\ &- \frac{A^4 k_1^4 K_x}{18\eta_e \omega} e^{-\sqrt{2}k_1 x^*} \cos[2\omega t - \sqrt{2}k_1 x^*] + \frac{A^3 k_1^4 K_x D}{5\eta_e \omega} e^{-3k_1 x^*} \cos[\omega t - k_1 x^*] \\ &- \frac{A^3 k_1^4 K_x D}{5\eta_e \omega} e^{-k_1 x^*} \cos[\omega t - k_1 x^*] - \frac{2A^4 k_1^4 K_x}{9\eta_e \omega} e^{-2k_1 x^*} \sin[4\omega t - 2k_1 x^*] \\ &+ \frac{2A^4 k_1^4 K_x}{9\eta_e \omega} e^{-4k_1 x^*} \sin[4\omega t - 4k_1 x^*] + \frac{3A^3 k_1^4 K_x D}{2\eta_e \omega} e^{-3k_1 x^*} \sin[3\omega t - 3k_1 x^*] \\ &- \frac{3A^3 D k_1^4 K_x}{2\eta_e \omega} e^{-\sqrt{3}k_1 x^*} \sin[3\omega t - \sqrt{3}k_1 x^*] + \frac{7A^4 k_1^4 K_x}{18\eta_e \omega} e^{-4k_1 x^*} \sin[2\omega t - 2k_1 x^*] \\ &+ \frac{4A^2 k_1^4 K_x D^2}{\eta_e \omega} e^{-2k_1 x^*} \sin[2\omega t - 2k_1 x^*] - \frac{7A^4 k_1^4 K_x}{18\eta_e \omega} e^{-\sqrt{2}k_1 x^*} \sin[2\omega t - \sqrt{2}k_1 x^*] \\ &- \frac{4A^2 k_1^4 K_x D^2}{\eta_e \omega} e^{-\sqrt{2}k_1 x^*} \sin[2\omega t - \sqrt{2}k_1 x^*] + \frac{11A^3 k_1^4 K_x D}{10\eta_e \omega} e^{-3k_1 x^*} \sin[\omega t - k_1 x^*] \\ &\left. - \frac{11A^3 k_1^4 K_x D}{10\eta_e \omega} e^{-k_1 x^*} \sin[\omega t - k_1 x^*] \right) \end{aligned} \quad (5.89)$$

By forcing the coefficients of the secular terms [ $e^{-k_1 x^*} \sin(\omega t - k_1 x^*)$ ] to zero,  $w_{0,1}$  can be given as,

$$w_{0,1} = 0. \quad (5.90)$$

The solution  $h_{0,1}(x^*, t)$ , for the  $p_1^0 p_2^1$  equation (5.84) can be given as,

$$\begin{aligned} h_{0,1}(x^*, t) &= \frac{Ak_1 s_p}{2\omega} - \frac{Ak_1 s_p}{2\omega} e^{-k_1 x^*} \cos[k_1 x^*] - \frac{Ak_1 s_p}{2\omega} e^{-k_1 x^*} \cos[2\omega t - k_1 x^*] \\ &+ \frac{Ak_1 s_p}{2\omega} e^{-\sqrt{2}k_1 x^*} \cos[2\omega t - \sqrt{2}k_1 x^*] - \frac{Ak_1 s_p}{2\omega} e^{-k_1 x^*} \sin[k_1 x^*] \\ &+ \frac{Ak_1 s_p}{2\omega} e^{-k_1 x^*} \sin[2\omega t - k_1 x^*] - \frac{Ak_1 s_p}{2\omega} e^{-\sqrt{2}k_1 x^*} \sin[2\omega t - \sqrt{2}k_1 x^*]. \end{aligned} \quad (5.91)$$

By solving the linear differential equations for  $h_{0,0}$ ,  $h_{1,0}$ ,  $h_{0,1}$ , ... the higher-order solution can be obtained by using  $p_1 \rightarrow 1$  and  $p_2 \rightarrow 1$  in the equation (5.80). The solution can be written as,

$$h = \lim_{p_1 \rightarrow 1} \sum_{m=0}^{N_p} \sum_{n=0}^{N_p} p_1^m p_2^n h_{m,n} B_{[m+n \leq N_p]} = h_{0,0} + h_{1,0} + h_{0,1} \quad (5.92)$$

Similarly, the implicit equation for  $w_{0,0}$  can be obtained by using  $p_1 \rightarrow 1$  and  $p_2 \rightarrow 1$  in the equation (5.31). Since the solution is up to only first-order ( $m + n \leq 1$ ), the implicit equation for  $w_{0,0}$  becomes,

$$w_{0,0} = w_{1,0} + w_{0,1} = \frac{K_x D}{\eta_e} + \frac{2}{3} \frac{r D^3 k_1^2 K_x}{\eta_e} \quad (5.93)$$

The parameter  $w_{0,0}$  becomes influential one since the wave number  $k_1$  is dependent on  $w_{0,0}$ . The parameter  $w_{0,0}$  is dependent on the solution order since more terms added to the equation (5.93) with the increasing order of the solution. The amplitude and phase of water table wave are dependent on the hydraulic conductivity of the aquifer ( $K$ ), anisotropic factor ( $r$ ), mean sea level above aquifer bottom ( $D$ ), effective porosity of the aquifer ( $\eta_e$ ), amplitude (A), angular frequency of the tidal wave ( $\omega$ ), and slope of the beach face ( $\beta$ ). The magnitude of  $h_{1,0}$  term is dependent on slope of the beach face since all terms are multiplied by  $Ak_1 s_p / \omega$ . Similarly from the parameters  $w_{0,0}$  and solution  $h_{0,1}$ , it is evident that  $KD/\eta_e$ ,  $D^3 k_1^2 K_x r / \eta_e$ ,  $A^2 k_1^2 K / (\eta_e \omega)$ ,  $A^4 k_1^4 K / (\eta_e \omega)$  and  $A^3 k_1^4 K D / (\eta_e \omega)$  are the controlling parameter groups of the groundwater waves.

### 5.2.3.1 Solution Comparisons and Convergence Analysis under Isotropic Conditions ( $r=1$ )

The HPM solution for second-order Boussinesq equation is compared with Kong et al. (2011), Roberts et al. (2011) and 2D FEFLOW numerical solution under isotropic conditions. The aquifer is isotropic when  $r = 1$ . The parameters provided in Kong et al. (2011) are used for solution comparison:  $\eta_e = 0.3$ ,  $K = 5 \times 10^{-4} m/s$ ,

$D = 5\text{ m}$ ,  $A = 2\text{ m}$ , and  $\omega = 2\pi/(12 * 60 * 60)$  radians/s (Figure 5.12). The initial head inside the aquifer has taken as mean sea level (5 m) for the numerical simulation. The implicit parameter  $w_{0,0}$  is  $0.0094\text{ m}^2/\text{s}$  (obtained by solving 5.93) for the above parameter values. The solution plots are provided for times at 0 hr, 1.5 hr, 3 hr, and 6 hr. The present solution compares well with the Kong et al. (2011) third-order solution. Roberts et al. (2011) solution compares reasonably with the present solution. However, Roberts et al. (2011) solution deviates from present solution and Kong et al. (2011) solution nearby seaside boundary region. All three analytical solutions overestimate the asymptotic water table level compared to the 2D FEFLOW numerical solution. Roberts et al. (2011) solution methodology is based on inclusion and exclusion of terms based on relative sizes of the magnitudes. Roberts et al. (2011) solution is semi-analytical one based on mathematica automation. Kong et al. (2011) solution is based on non-dimensional perturbation parameters with secular term removal is done using perturbation expansion for boundary condition, which introduces a small correction to the boundary. The handling of secular terms in the present solution is unique and does not introduce any correction at the boundary. Moreover, the homotopy based first order solution of second-order Boussinesq equation is well in agreement with sixth-order and third-order solutions by Roberts et al. (2011) and Kong et al. (2011), respectively. From the present solution, it can be observed that with a minimum order of the solution, an accurate solution can be derived compared to previous analytical solutions (Table 5.4). The second-order Boussinesq equation captures the streamline curvatures Castro-Orgaz and Dey (2014). The higher-order solutions can be derived by extending the homotopy method with an additional auxiliary term for handling the secular term  $[e^{-k_1 x^*} \cos(\omega t + k_1 x^*)]$  generated from the nonlinear slope term. The homotopy solution is derived without any pre-defined physical parameters. However, the beach slope emerged as an implicit parameter from the solution process (Eq. 5.91). The parameter  $s_p$  ( $= A\omega \cot(\beta)$ ) is inversely proportional to beach slope angle becomes large. The solution accuracy is affected for mild beach slopes Cartwright et al. (2004). Hence, the present solution is valid for beaches with slopes more than  $20^\circ$ .

### 5.2.3.2 Solution Comparisons and Convergence Analysis under Anisotropic Conditions ( $r > 1$ )

The solutions for different anisotropy  $r$  values are compared for laboratory scale. The parameter values of the laboratory scale used are: Parameters:  $A = 0.2\text{ m}$ ;  $D = 0.6\text{ m}$ ;  $\eta_e = 0.3$ ;  $\beta = 30^\circ$ ; Time period= 300 s. The figure 5.13 is given for the different  $K$  values for a set of  $r$  values. The asymptotic water level (the locations inland from where the water table level is horizontal) is highest for the least  $r$

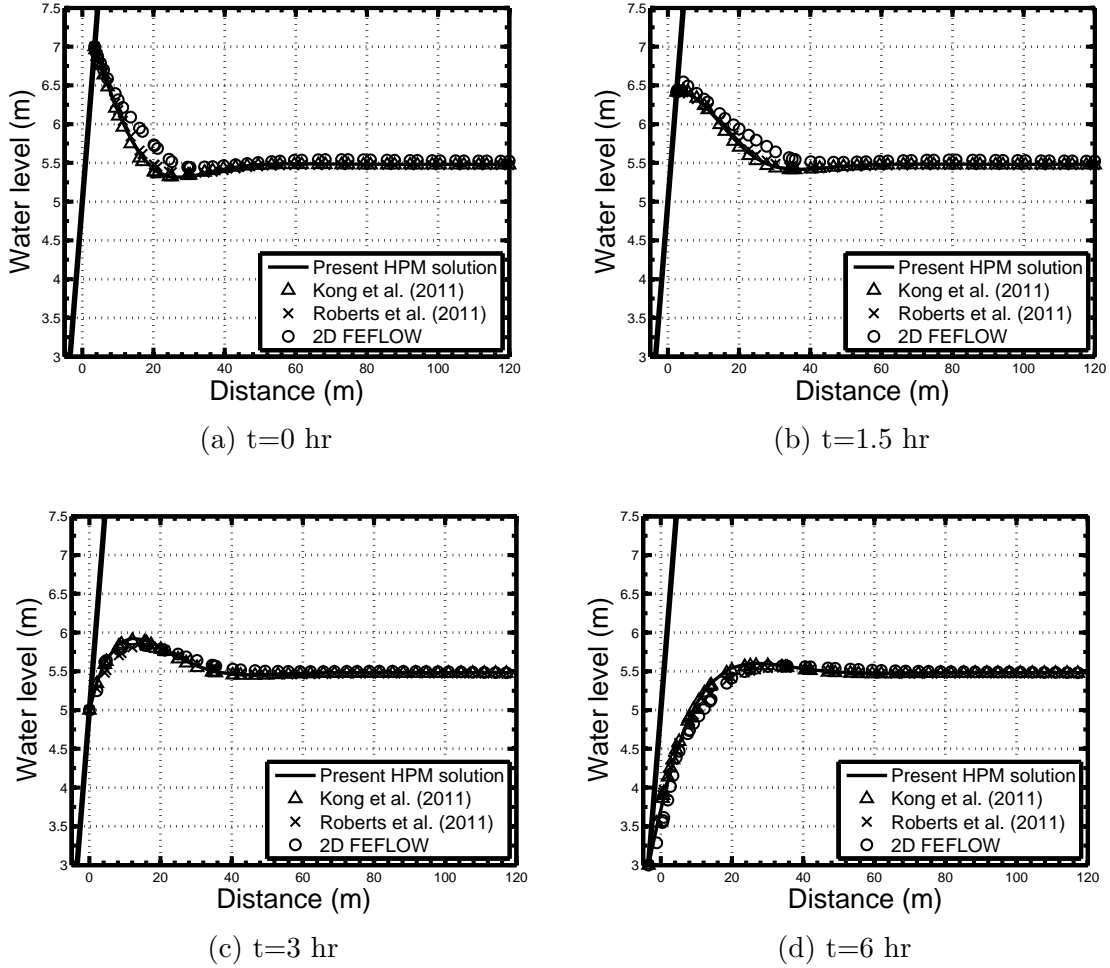


Figure 5.12: Comparison of the homotopy perturbation solution for the higher-order Boussinesq equation with Kong et al. (2011), Roberts et al. (2011), and 2D FEFLOW solutions at different time instances for a tidal wave with timeperiod=12 hr;  $D=5$  m;  $A=2$  m;  $\eta_e = 0.3$ ;  $K = 0.0005$  m/s; and  $\beta = 30^\circ$ .

Table 5.4: Mean absolute percentage error (MAPE) between numerical solution and Kong et al. (2011), Roberts et al. (2011), and present solution

| Solution                         | $t = 0$ hr | $t = 1.5$ hr | $t = 3.0$ hr | $t = 6.0$ hr |
|----------------------------------|------------|--------------|--------------|--------------|
|                                  | (%)        | (%)          | (%)          | (%)          |
| Kong et al. (2011)               | 0.8778     | 0.8091       | 2.8033       | 2.2650       |
| Roberts et al. (2011)            | 0.8006     | 0.9726       | 2.9411       | 6.0992       |
| Second-order Boussinesq equation | 0.8582     | 0.8053       | 2.1766       | 2.3062       |
| HPM solution                     |            |              |              |              |

Parameters: timeperiod=12 hr,  $D = 5$  m,  $A = 2$  m,  $\eta_e = 0.3$ ,  $K = 0.0005$  m/s, and  $\beta = 30^\circ$ .

values, and the water level reduces gradually with the increase in the  $r$  value. This is true for both orders of hydraulic conductivity  $K$  values. By comparing the figure 5.13b and figure 5.13b, it is clear that the fluctuation reaches the asymptotic zone for smaller hydraulic conductivity first when moving from seaside boundary to

inland. In other words, larger the hydraulic conductivity, the zone of fluctuation is larger (the fluctuation takes large distance to dissipate).

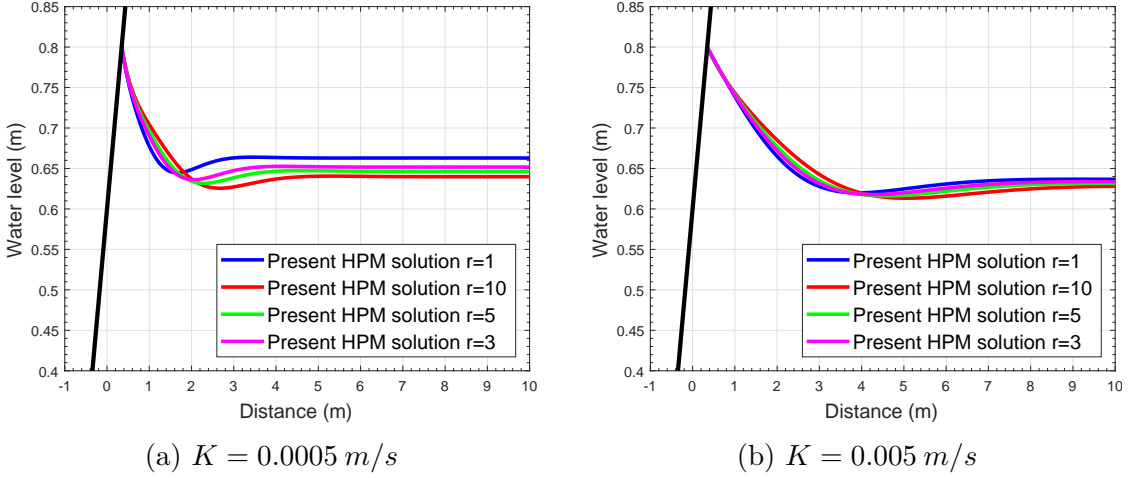


Figure 5.13: Comparison of the homotopy perturbation solution for the anisotropic higher-order Boussinesq equation with different  $r$  values for laboratory scale a)  $K = 0.0005 \text{ m/s}$  b)  $K = 0.005 \text{ m/s}$ . Parameters:  $A = 0.2 \text{ m}$ ;  $D = 0.6 \text{ m}$ ;  $\eta_e = 0.3$ ;  $\beta = 30^\circ$ ; Time period= 300 s.

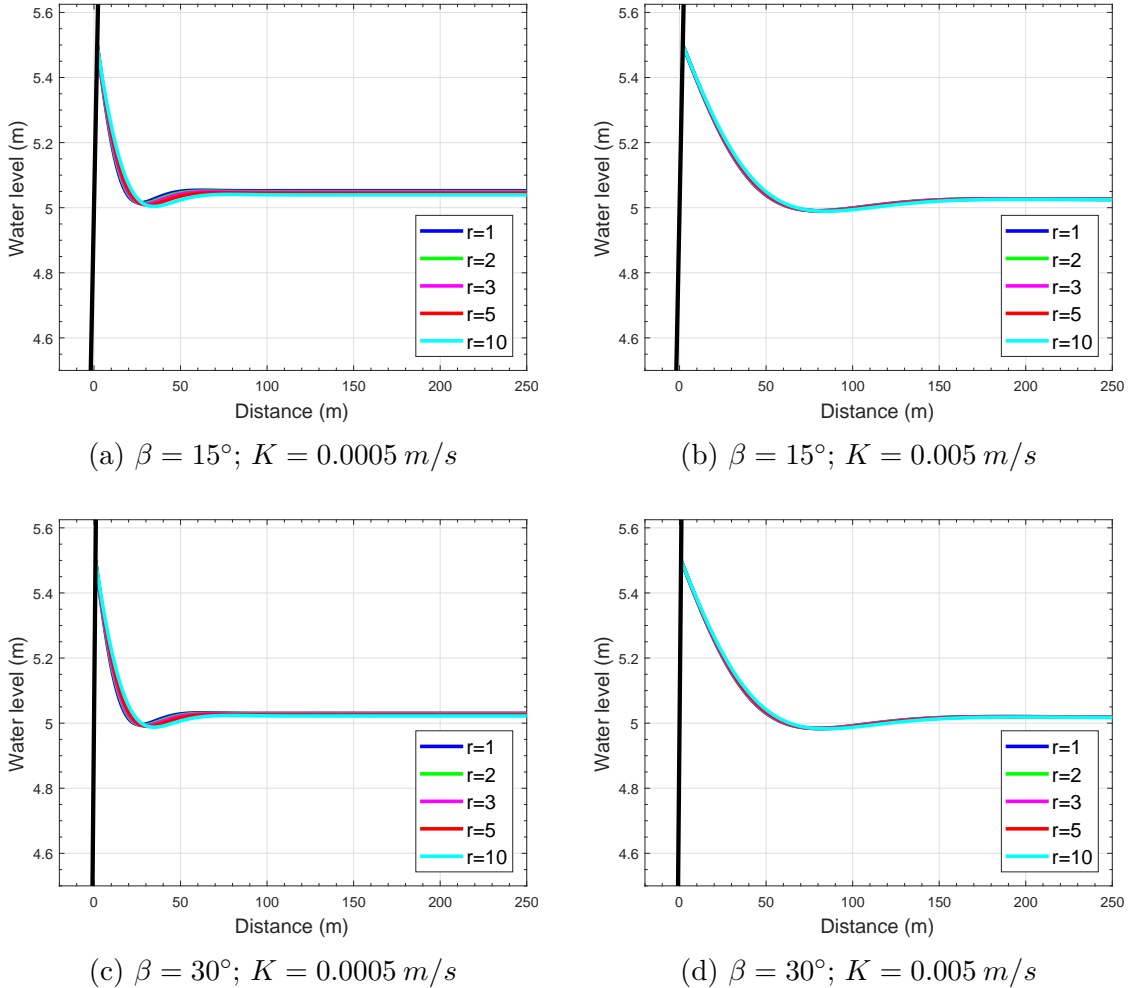


Figure 5.14: Comparison of the homotopy perturbation solution for the anisotropic higher-order Boussinesq equation with different  $r$  values for field scale a)  $K = 0.0005 \text{ m/s}$  b)  $K = 0.005 \text{ m/s}$ . Parameters:  $A = 0.5 \text{ m}$ ;  $D = 5.0 \text{ m}$ ;  $\eta_e = 0.3$ ; Time period= 12 hr.

### 5.3 Experimental Study on Tidal Dynamics without Density Effects

Experiments were performed in the sand-box experimental setup detailed in chapter to obtain a clear interpretation of the tidal dynamics. Two major different aquifer setups were used to perform experiments to analyse the tidal interaction in the laboratory coastal aquifers. This section experiments were done without considering the density-dependent effects. Hence, the experiments are performed with clear water. The experiments were performed in two major configurations of the aquifer setup, and they are mentioned as CASE-1 and CASE-2 in the text hereafter. These cases consist of following combinations: two beach slopes, which are approximately  $\pi/6$  and  $\pi/12$ , two different kinds of sands—namely, normal river coarse sand and Grade II IS-650 sand Bureau of Indian Standards (2007). The two major categories of experiments are performed for different tidal wave frequencies, different amplitudes, and different locations of pressure sensors. The experiments

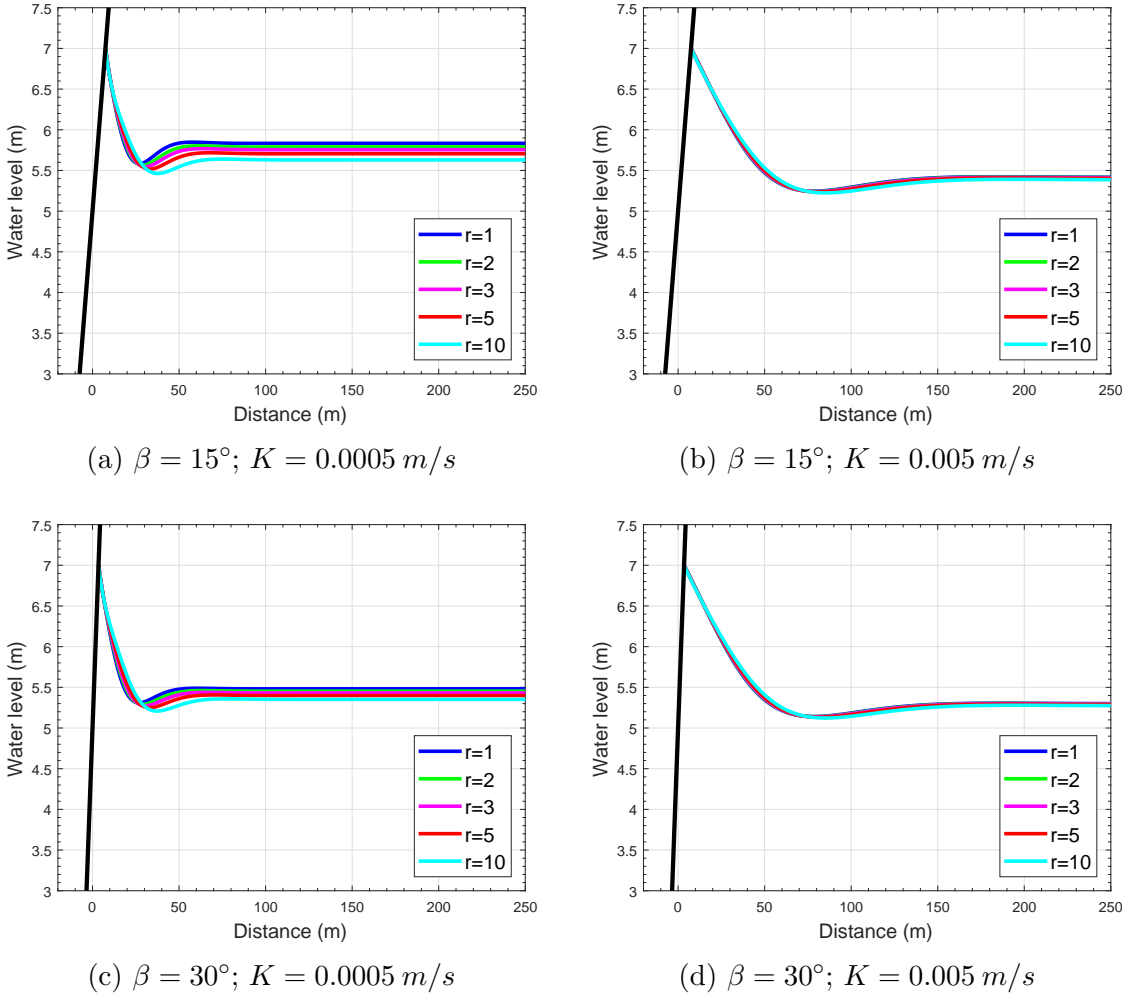


Figure 5.15: Comparison of the homotopy perturbation solution for the anisotropic higher-order Boussinesq equation with different  $r$  values for field scale. Parameters:  $A = 2.0 \text{ m}$ ;  $D = 5.0 \text{ m}$ ;  $\eta_e = 0.3$ ; Time period = 12 hr.

under each case are explained in the following subsections.

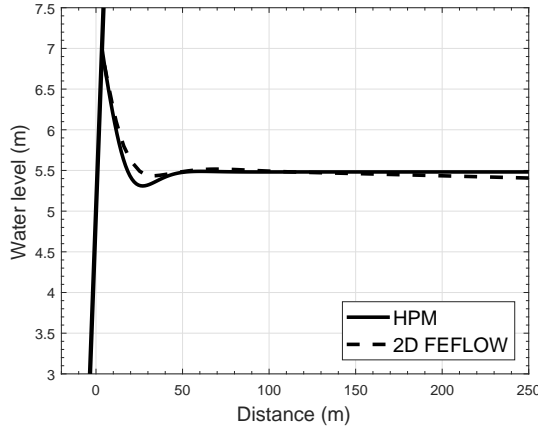
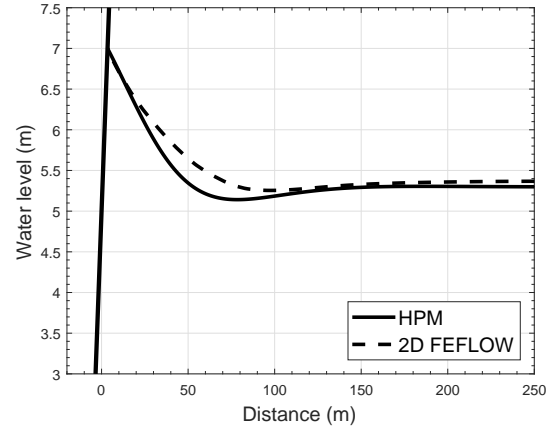
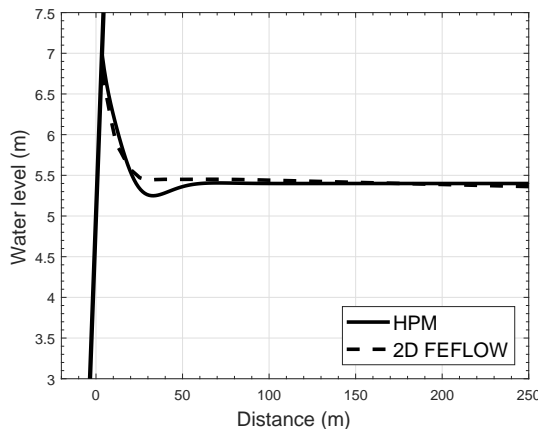
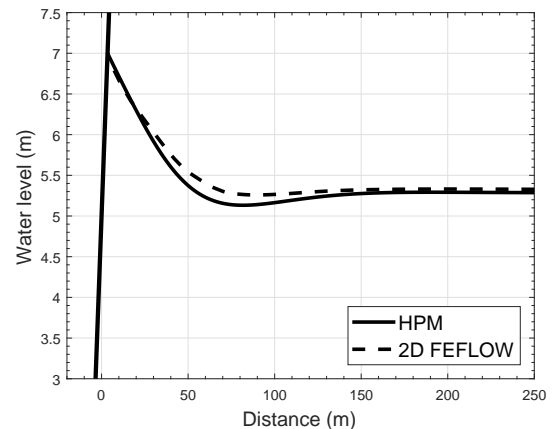
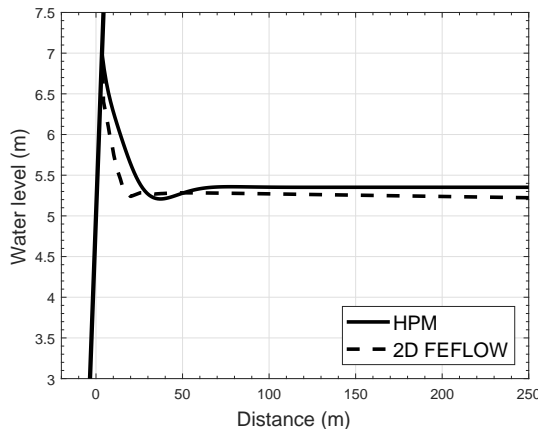
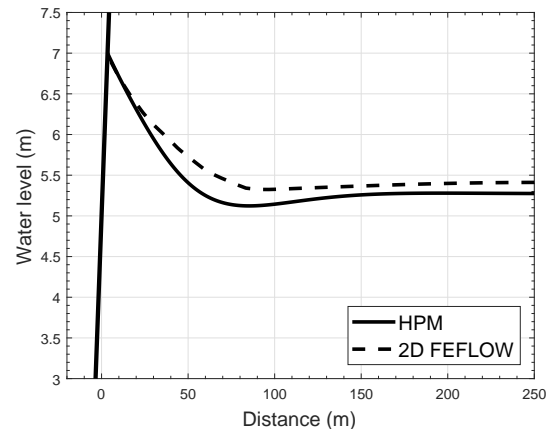
(a)  $\beta = 30^\circ$ ;  $K = 0.0005 \text{ m/s}$ ;  $r=1$ (b)  $\beta = 30^\circ$ ;  $K = 0.005 \text{ m/s}$ ;  $r=1$ (c)  $\beta = 30^\circ$ ;  $K = 0.0005 \text{ m/s}$ ;  $r=5$ (d)  $\beta = 30^\circ$ ;  $K = 0.005 \text{ m/s}$ ;  $r=5$ (e)  $\beta = 30^\circ$ ;  $K = 0.0005 \text{ m/s}$ ;  $r=10$ (f)  $\beta = 30^\circ$ ;  $K = 0.005 \text{ m/s}$ ;  $r=10$ 

Figure 5.16: Comparison of the homotopy perturbation solution for the anisotropic higher-order Boussinesq equation with 2D FEFLOW solutions. Parameters:  $A = 2.0 \text{ m}$ ;  $D = 5.0 \text{ m}$ ;  $\eta_e = 0.3$ ; Time period= 12 hr.

### 5.3.1 Experimental Procedure

#### 5.3.1.1 Aquifer Material and Packing

The aquifer material (sand) was packed using the wet packing method, as mentioned in Cartwright et al. (2004), Goswami and Clement (2007), and Luyun et al. (2011). The openings connecting wave generation setup and the sandbox, including water column cylinder are at the bottom of the seaside reservoir. The rising and ebbing waves and the associated horizontal forcing, including suction, might cause erosion at the bottom left-hand side of the aquifer. A stick made of the acrylic sheet was placed as an obstruction to avoid the erosion. The acrylic stick was of dimensions 0.02 m length, 0.02 m wide, and 0.20 m height. This stick provided stability for the slope of the aquifer as well. The aquifer slope starts from 0.20 m above the bottom plate to avoid the erosion due to wave, which is most probable if the slope starts from the bottom. A grid of 0.10 m horizontal by 0.05 m vertical was drawn on the front side glass wall of the sandbox setup using a permanent marker pen. Moreover, different slopes also have drawn on the glass wall. The grids along with the slope lines are employed to give guidance for packing.

In wet packing method, the sand packing was done in layers of 0.05 m inside water, and after each layer filled it was tamped down using a tamping rod to achieve homogenous packing without any layers or air bubbles. Initially, the water was filled in the empty sandbox to approximately 0.20 m height. After that sand was dropped from the top of the sandbox up to 0.05 m level. Then gentle tamping is done with the tamping rod. This cycle was continued until the sand was filled to the desired height. The sand height cannot be controlled when the water level is too high due to higher buoyancy makes the sand float, and it becomes chaotic settling. Hence, the water height was always maintained slightly above the sand layer height. The water height increased gradually depends on the sand height to get better control in packing. The inland portion of the aquifer was filled first, and then the slope of the aquifer was adjusted gradually with a flat plate which is connected to the tamping rod at a sloped angle. Tamping made the adjustment of the slope of the aquifer easier. After the packing of the aquifer and fixing the required slope, the aquifer was allowed to settle for 24 hours or more.

#### 5.3.1.2 Pressure Transducers Calibration

Pressure sensors were connected to the port openings available in the backside glass wall of sandbox setup by using flexible pipes as connectors. Flexible pipes

were connected to the port openings with a nylon cloth lining as a filter between the sandbox and the pipe opening. This was done to prevent the sand from entering the flexible pipes. Other ends of the flexible pipes were connected to pressure transducers. All six pressure transducers were placed on a bench like a platform to keep them at the same elevation and horizontal position. All six pressure transducers were of the same model. However, all pressure sensors needed to be calibrated individually due to the following reasons: i) Each pressure transducer reads different values of voltage for the same pressure ii) the pressure range needed to be measured is very small compared to the pressure transducer measuring range iii) The nature of the medium in contact with the pressure transducers are not always the same iv) Most pressure sensors are connected to the aquifer region (sand portion). But, one or more pressure transducers were directly in contact in with the free water region in the seaside zone. The pressure exerted by a head change may induce different pressure level changes in the pressure transducers depends on the pore structure in the aquifers where the pressure transducer is connected. The pressure transducer reading induced by the same head change can be different for free water region and aquifer region where porosity is different.

Pressure transducers were connected to the openings before the packing of the aquifer medium. Before connecting the transducers, the water level of the sandbox setup was maintained above the ports, where the pressure transducers are connected, to avoid air bubbles entering the flexible pipes. Next, the aquifer packing was done, as explained in the previous section and allowed to settle for 24 hours. After 24 hours, the calibration procedure started. The pressure readings for different known water levels were recorded to determine the calibration equation. The water levels inside the aquifer are not visible to eyes. The water levels were left undisturbed for 45 minutes to 1 hour after changing to result in hydrostatic pressure condition. In hydrostatic pressure condition, the water level inside the aquifer is the same as seawater side free surface, which is in the visible portion. The calibration was done in both raising and falling directions to get the calibration equation. This calibration equation was used to get the pressure values during the experimental process.

### 5.3.1.3 Wave Generation and Recording of Pressure Data

The volume of water needed to fill the experimental setup for the required wave amplitudes was calculated approximately, and accordingly, the cylindrical water column is filled with tap water. The concentration and density of the tap water are approximately  $0 \text{ mg/l}$  and  $1000 \text{ kg/m}^3$ . The valves which control the flow from the water column to the rotor and the sandbox setup to rotor were kept

in a fully open condition. The rotor is connected to the DC motor. The control system timers for clockwise rotation and anti-clockwise rotation of DC motor were fixed approximately half of the required time period of the wave. The RPM of the motor was also fixed using the potentiometer attached to the control system. The resting time between the direction changes was also fixed. The wave frequency, time-averaged water level or mean sea level, amplitude, and wave shapes (raising and falling limbs) were influenced by the rotation times, resting time, and the RPM of the motor. The water in sandbox and the water column were in the same water level under the hydrostatic condition before the motor is started. As soon as the motor was started, the rotor rotates in clockwise direction and water gets transferred from the water column to sandbox. As a result, the water level in the sandbox started increasing gradually to create rising tide until the clockwise rotation stopped. In the resting time, flow direction changes and flow from sandbox to the water column occurs due to the head difference between sandbox and the water column. Once the resting time period was completed rotor rotates in the anti-clockwise direction to maintain the flow towards the water column, which created an ebbing tide situation. The cycle continued till the motor is switched off.

The pressure transducers were started using the UEI data logger software to record the data. The sampling frequency should be more than the Nyquist criteria (Smith et al., 1997) to eliminate any aliasing effects. The time period of the tidal waves generated in the sandbox experimental setup was always more than 100 s for all experiments (frequencies lesser than 0.01 Hertz). As per the Nyquist criterion, the sampling frequency should be more than 0.026 Hertz. Hence, the sampling frequency of 20 Hz was chosen. The data collection was done for approximately for 20 tidal cycles for all experiments, and then the pressure transducer recording and wave generation process was stopped. The Data analysis part is explained in the text explaining the different cases later.

### 5.3.2 CASE-1: Coarse River Sand with Beach Slope $\pi/6$

A commercially available coarse sand was chosen for the physical model representing unconfined coastal aquifer. The coarse sand was relatively uniform with a median diameter  $d_{50} = 1.02 \text{ mm}$  and the uniformity coefficient is 1.4 (based on the sieve analysis). A total of six experiments were performed to observe the groundwater dynamics for different amplitude and frequency values (CASE-1A to CASE-1F). One pressure transducer was fixed at the seaside part to record the tidal wave condition created in the seaside boundary. Other pressure transducers fixed inside the aquifer as given in the Figure 5.17. All pressure transducers were

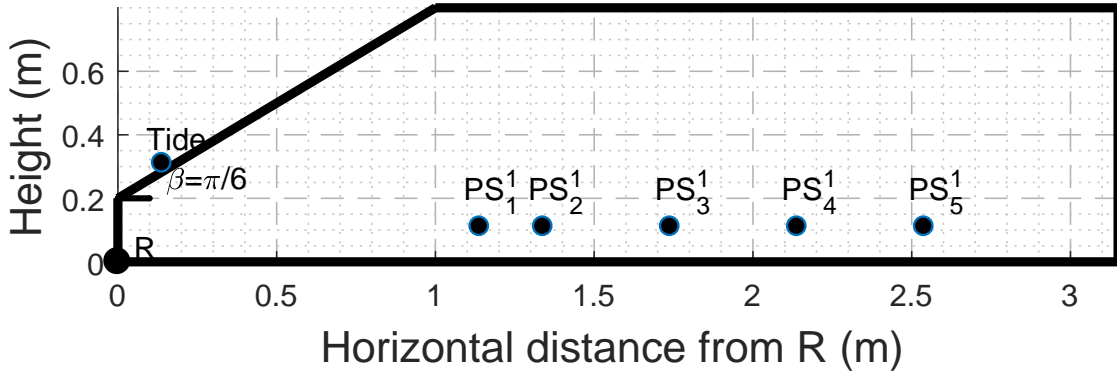


Figure 5.17: Schematic of the coastal aquifer modeled in the experimental setup.

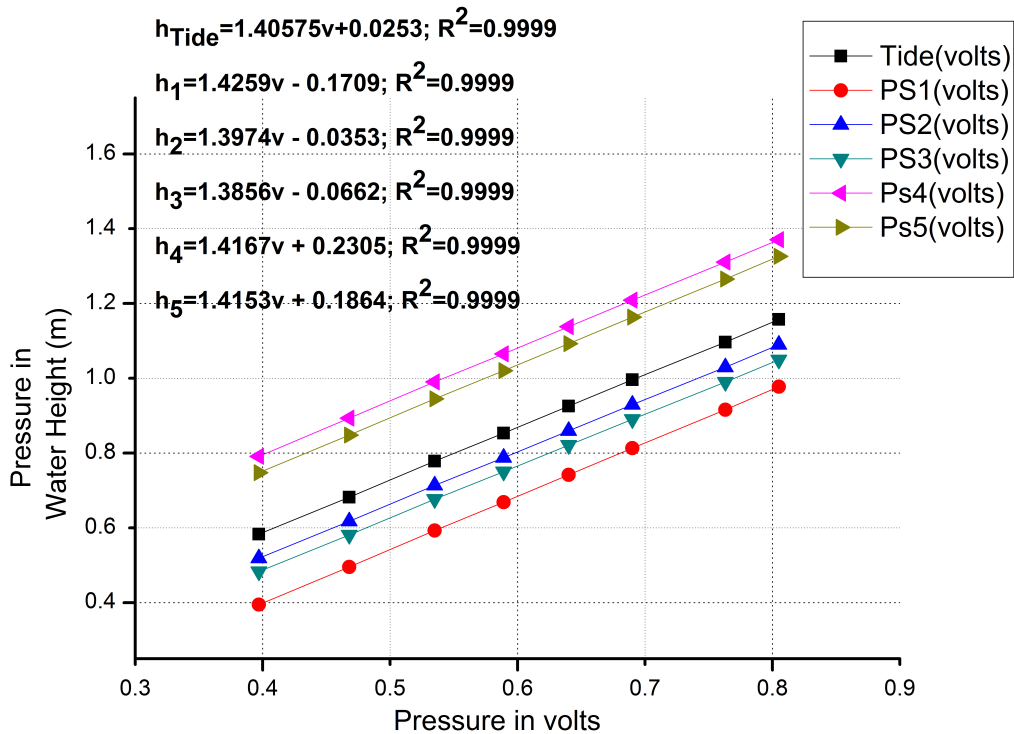


Figure 5.18: Pressure transducers calibration

connected at the same horizontal line. Pressure transducers calibration was done, as explained in the previous section (Figure 5.18).

The pressure transducers provide the data in the range of 0-10 volts DC. The volts to water level calibration equation is used to convert the voltage to water height. Next, the data were smoothed by moving average filter to remove the abrupt changes. As the moving average window size increases, the data becomes smoother. In this analysis, moving average window of eight was used (160 data samples for 20 Hz sampling rate). The plots of pressure transducer readings in volts and converted to water height were given in Figure 5.19. Six experiments performed in the CASE-1 and data of few of the experiments are presented here as CASE-1A, CASE-1B, CASE-1C, CASE-1D, CASE-1E, and CASE-1F. CASE-1A is for

the waves recorded by the pressure transducers for the clockwise and anticlockwise times of 180 s, resting period of 30 s and DC motor RPM 203. Figure 5.20 and Figure 5.21 show the waves recorded by the pressure transducers in larger time axis and a magnified time axis respectively. In CASE-1, the pressure transducer to record the tidal wave was placed at 0.34 m above the bottom of the aquifer to record the data directly in contact with the water. Other pressure transducers were located inside the aquifer portion at the bottom-most pressure sensor port available at 0.14 m above the aquifer bottom. The pressure transducers 1 to 5 are placed well away from the sloped portion of the aquifer slope. Hence, the pressure data at the seepage face region is not recorded.

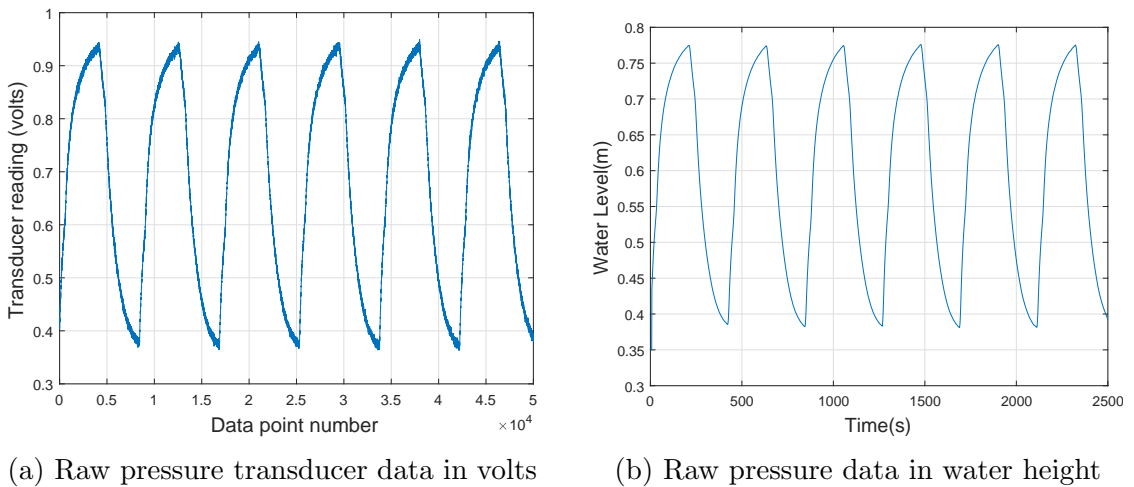


Figure 5.19: Raw pressure transducer data in volts and water height after calibration

The time-averaged water table, amplitudes of the waves, and phase differences between the tidal wave and waves at different transducer points of CASE-1A are shown in Figure 5.23. Time-averaged water table heights were calculated by averaging the wave data after calibrating the pressure data to water height. The amplitudes of waves were calculated by calculating half of the difference between the maximum of the wave and minimum of the wave. The plots clearly show that the amplitudes of the groundwater wave get attenuated while moving inland and the time-averaged water table height shows the existence of overheight (Nielsen, 1990).

### 5.3.2.1 Discrete Fourier Transform (DFT)

The signals are analysed in the frequency domain by converting the time domain data to the frequency domain by applying the Discrete Fourier Transform (DFT). Discrete Fourier Transform (DFT) is used to convert the time domain discrete and periodic signals to frequency domain discrete spectrum. The Fast Fourier Transform (FFT) algorithm function available in MATLAB<sup>TM</sup> was used for DFT.

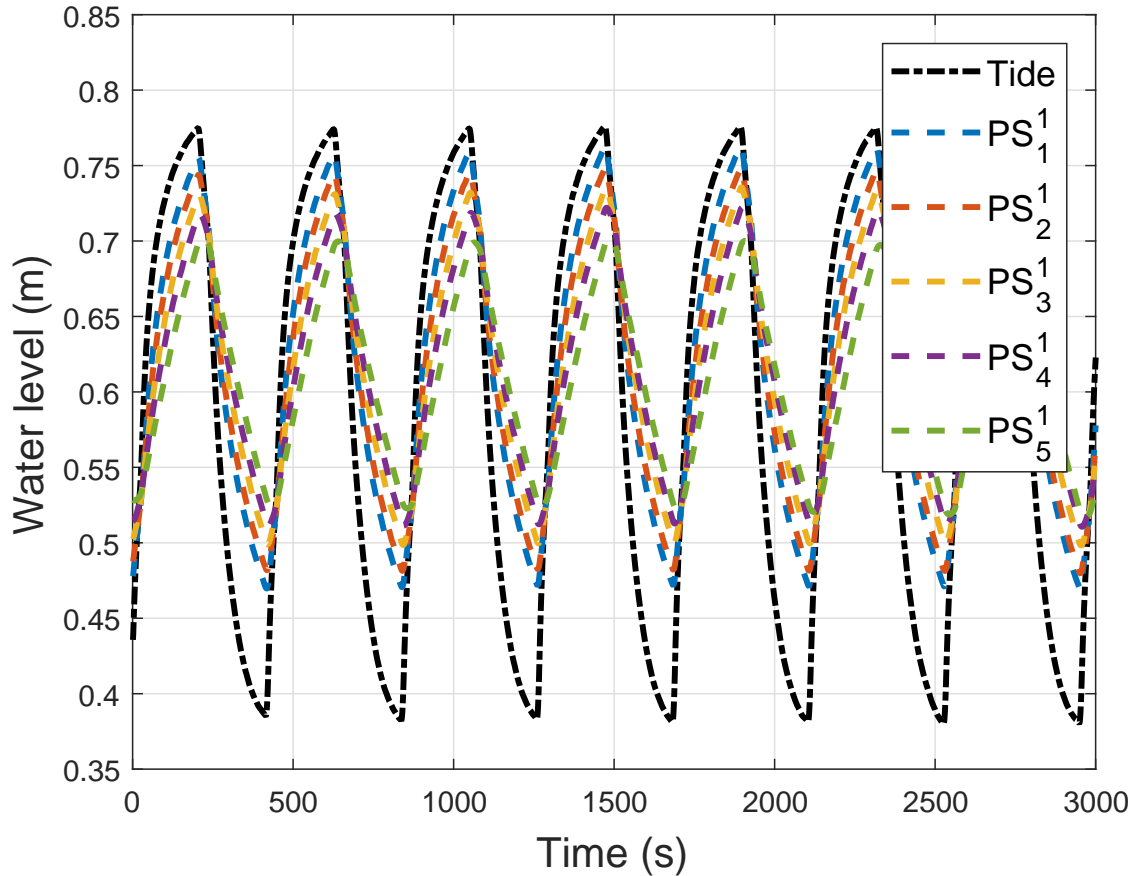


Figure 5.20: CASE-1A: Waves recorded by the pressure transducers for the clockwise and anticlockwise times of 180 s, resting period of 30 sand DC motor RPM 203.

The FFT algorithm provides the amplitudes and phase shift of the oscillation frequencies via Fourier coefficients (Zhou et al., 2016). Before applying DFT, the signal was demeaned to remove the DC bias and detrended to remove any linear trend in the signal. MATLAB<sup>TM</sup> uses complex Fourier transform which uses complex time domain data. However, the pressure waves recorded by the pressure transducers are real numbers (Smith et al., 1997). Hence, the imaginary part is zero. The forward complex DFT equation written in polar form is given by,

$$\begin{aligned}
 H[k_n] &= \frac{1}{N} \sum_{n=0}^{N-1} h[n] e^{-J2\pi k_n n/N} \\
 H[k_n] &= \frac{1}{N} \sum_{n=0}^{N-1} h[n] (\cos[2\pi k_n n/N] - J \sin[2\pi k_n n/N]), \quad (5.94)
 \end{aligned}$$

where,  $h[n]$  is a periodic signal in time domain with  $N$  data points,  $N$  is number of data points recorded,  $J$  is complex symbol with value  $\sqrt{-1}$ ,  $n$  is time domain data index with values  $0, 1, \dots, N-1$ ,  $k_n$  is frequency domain index with values  $0, 1, \dots, N-1$ . The forward complex DFT process to transform the time-domain signal to the frequency domain is called analysis. Euler relation for the polar form to

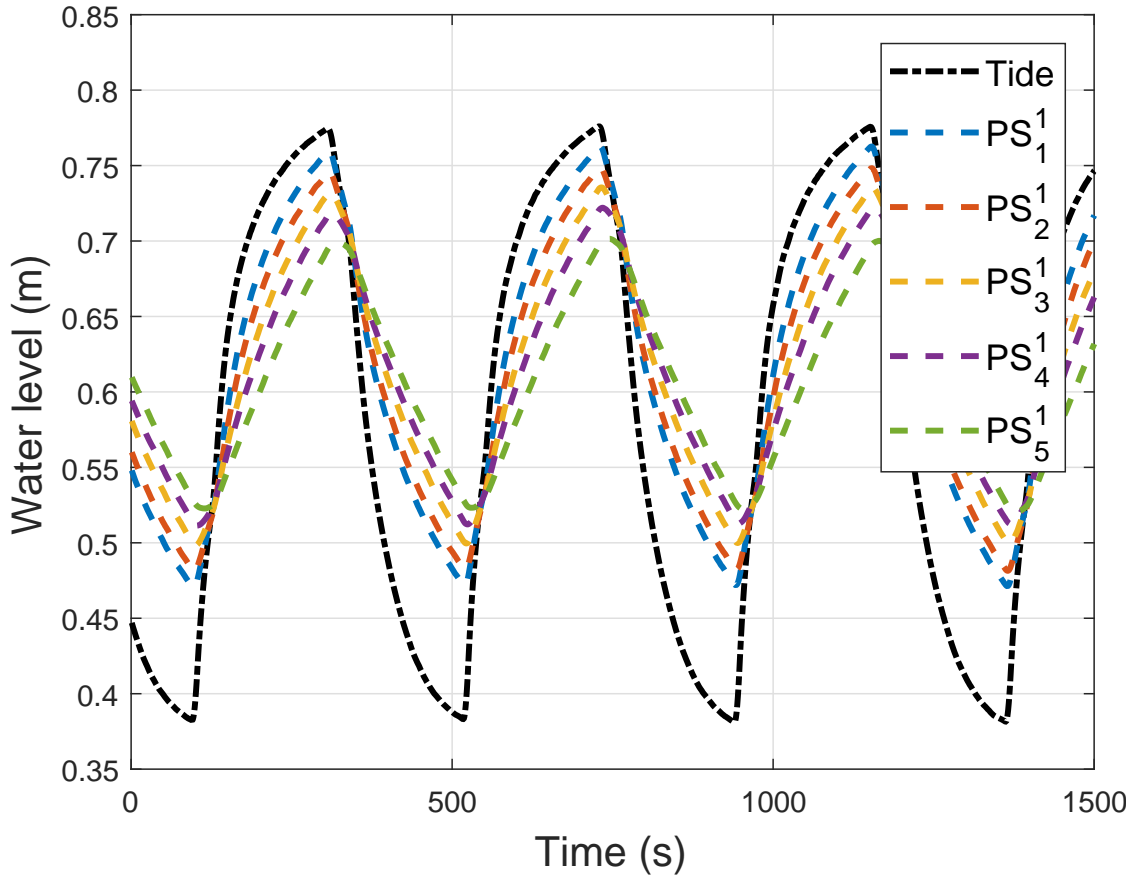


Figure 5.21: CASE-1A: Waves recorded by the pressure transducers for the clockwise and anticlockwise times of 180 s, resting period of 30 sand DC motor RPM 203: magnified

rectangular form is important to understand the complex numbers. Euler relation can be given as,

$$e^{Jx} = \cos(x) + J \sin(x) \quad (5.95)$$

If a complex number is represented as  $x + Jy$ , the magnitude and phase of the complex number is given as,

$$\begin{aligned} |x + Jy| &= \sqrt{x^2 + y^2} \\ \text{phase}(x + Jy) &= \tan^{-1} y/x \end{aligned} \quad (5.96)$$

Sinusoids can be written in exponential form using Euler relations as following,

$$\begin{aligned} \cos(\omega t) &= \frac{e^{-Jt} + e^{Jt}}{2} \\ \sin(\omega t) &= \frac{e^{-Jt} - e^{Jt}}{2} \end{aligned} \quad (5.97)$$

From the above equations, it can be observed that both sine and cosine waves have both positive ( $\omega$ ) and negative ( $-\omega$ ) frequencies. By using Euler's relation the

analysis equation or forward DFT equation can be written as,

$$H[k_n] = \frac{1}{N} \sum_{n=0}^{N-1} h[n] (\cos(2\pi k_n n/N) - J \sin(2\pi k_n n/N)) \quad (5.98)$$

Each value of time domain data has real and imaginary parts in the frequency domain. The magnitude of the complex number  $H[k_n]$  is the amplitude of the harmonic with a frequency corresponding to  $k_n$ . Inverse DFT equation or synthesis equation can be given as,

$$h[n] = \sum_{k=0}^{N-1} H[k_n] e^{J2\pi k_n n/N} \quad (5.99)$$

The inverse DFT process to convert the frequency domain data to time domain signal is called synthesis. More details on the DFT can be found in (Smith et al., 1997). In Matlab<sup>TM</sup>, the function FFT is used to obtain the frequency domain data. For N number of data points in time domain,  $k_n = 0, 1, \dots, N/2$  data index points are corresponding to positive frequencies and  $k_n = N/2, N/2+1, \dots, N-1$  are negative frequencies. After applying FFT, the array is scaled by dividing the resultant array by  $N$  for normalization. The positive and negative frequencies in the frequency domain is periodic. The negative frequencies corresponding to  $N/2$  to  $N-1$  is same as positive frequencies. Hence, the frequency spectrum from 0 to  $N/2$  is sufficient for analysis. Hence, the positive frequency amplitude is added with negative frequency amplitude is equal to twice the amplitude of positive frequency amplitude. Hence, the FFT array after the normalization is multiplied by 2 to get the amplitude value of each frequency and plotted (Figure 5.35). The FFT gives the frequency domain data up to half of the sampling frequency from zero frequency. Figure 5.22 show some sample sinusoidal waves and respective FFT plots. The FFT plot (Figure 5.22) clearly shows the amplitudes at the frequencies of the sinusoidal waves.

The phase difference between the tides and the pressure transducer data at different points are calculated using the MATLAB (Smith et al., 1997) function phdiffmeasure developed by Hristo Zhivomirov (2016). The code was developed based on the theory described in Sedláček (2003). The theory says, "phase difference between two fundamental harmonic components of the two measured signals is found as phase difference of the fundamental harmonics DFT phase spectrum values (method DFT) of the two measured signals." In other words, maximum amplitudes of the signals are found based on the complex magnitude of their FFT, and their phases also found. The difference between the phases gives the phase

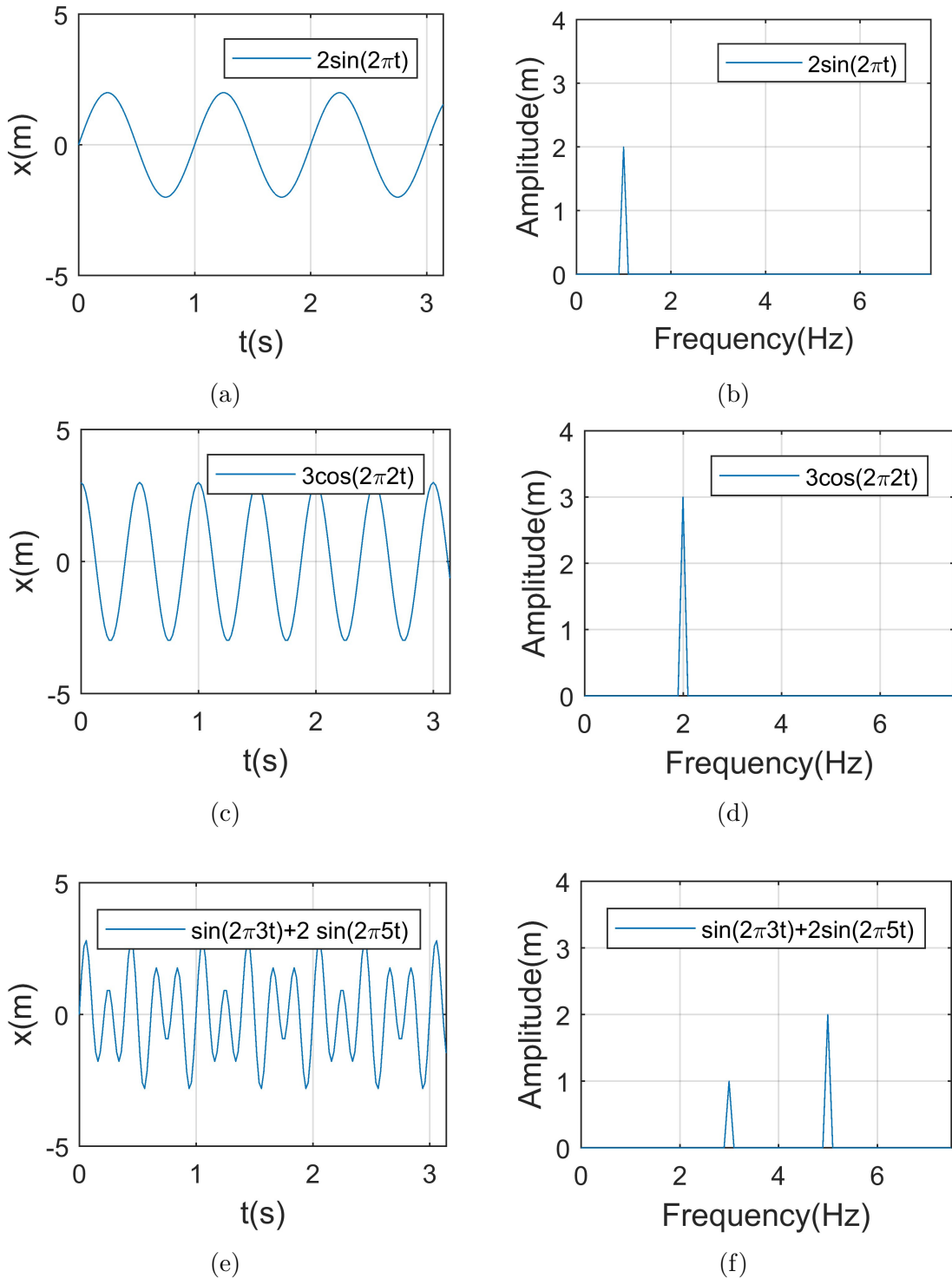


Figure 5.22: Sample waves in the left hand sides and FFT of the sample wave in the right hand side

difference between the two signals (corresponding to fundamental harmonics).

The phase differences are calculated by finding the difference in locations of the maximum of FFT of the respective signals. The calculated phase differences then converted to degrees from radians. The phase differences for CASE-1A are shown in Figure 5.23b. The phase difference increases in the clockwise direction with

increasing distance from the seaside boundary. The FFT of the CASE-1A tidal wave data shows amplitudes of five frequencies (Figure 5.35). The first frequency  $\omega$  is called fundamental frequency. The second dominant frequency and other dominant frequencies are multiples of fundamental frequency. They are called as harmonics. The frequencies and corresponding amplitudes up to  $5\omega$  are tabulated in Table 5.6. The main frequency  $\omega$  is  $0.0151 \text{ rad/s}$  (Wave timeperiod=416.66 s). The amplitudes of odd number frequencies (or odd harmonics), that is  $n\omega$ , when  $n = 1, 3, 5, \dots$  have higher amplitudes than the next even number frequency amplitudes,  $n\omega$  when  $n = 2, 4, 6, \dots$  at all pressure transducers. The amplitudes of all frequencies are attenuated with the distance from the seaside boundary.

Amplitudes calculated in time domain shows that the amplitude of the waves gets attenuated with distance from the seaside boundary (Figure 5.23). But, time-averaged water table height is not following monotonic relation with the distance from the seaside boundary at all points. However, all points show that there is an overheight as observed by many studies earlier (Knight, 1981; Nielsen, 1990; Ataie-Ashtiani et al., 2001). The phase difference of waves with respect to tidal wave at each pressure transducer point is linearly increasing with distance for all cases (CASE-1A to CASE-1E). The parameter details of all experiments in CASE-1 is provided in Table 5.5. However, the pressure sensor  $PS_1^5$  deviates from other phase differences. The proximity of the freshwater boundary may cause the wave to reflect, which affects the phase of the wave and possibly amplitude and mean water level as well.

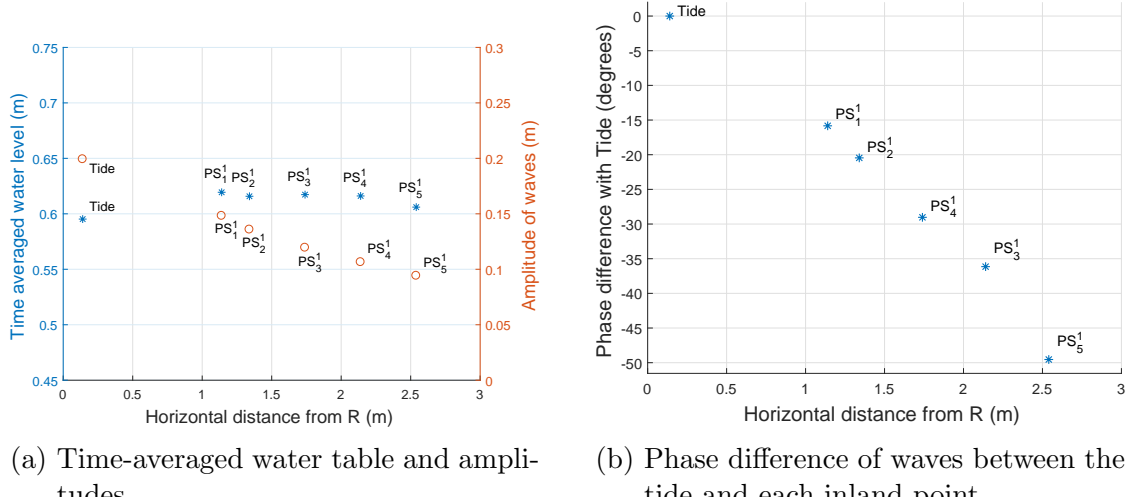


Figure 5.23: CASE-1A: Time-averages water table, amplitude and phase difference details of waves recorded by the pressure transducers for the clockwise and anticlockwise times of 180 s, resting period of 30 sand DC motor RPM 203.

The amplitudes of waves for harmonics are analysed by plotting distance vs. logarithmic of amplitude for each frequency. The FFT of the tidal wave data is

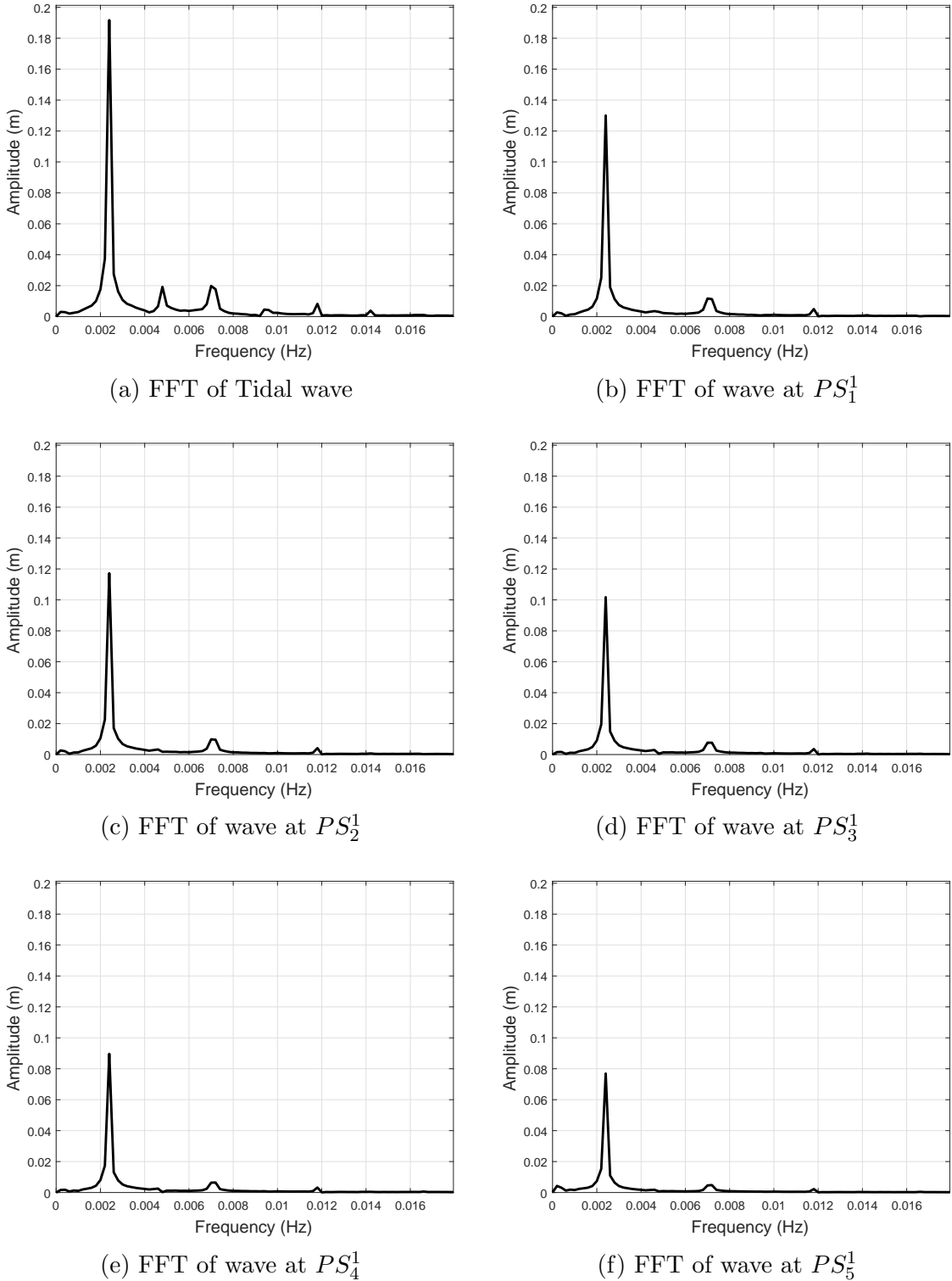


Figure 5.24: CASE-1A: FFT of waves recorded using pressure transducers pressure transducers for the clockwise and anticlockwise times of 180 s, resting period of 30 sand DC motor RPM 203.

taken after subtracting the mean of the wave. The FFT of tidal wave of CASE-1A (Figure 5.35) shows that there are five different frequencies with its amplitudes. These frequencies are multiples of  $\omega$  starting from  $\omega$  to  $5\omega$ . Other cases analysed for up to these 5 frequencies. The frequency  $\omega$  is corresponding to the time period of

Table 5.5: Parameter details of CASE-1 experiments

| CASE    | Mean WL | Amplitude | f,     | A/D    | Wave number | $A \cot(\beta)*$ |
|---------|---------|-----------|--------|--------|-------------|------------------|
|         | D, (m)  | A, (m)    | (Hz)   | (-)    | WN(1/m)     | WN(-)            |
| CASE-1A | 0.5952  | 0.1992    | 0.0024 | 0.3347 | 0.8326      | 0.2873           |
| CASE-1B | 0.6009  | 0.1945    | 0.0026 | 0.3236 | 0.8624      | 0.2905           |
| CASE-1C | 0.6096  | 0.1714    | 0.0041 | 0.2811 | 1.0753      | 0.3192           |
| CASE-1D | 0.6059  | 0.1454    | 0.0052 | 0.2400 | 1.2146      | 0.3059           |
| CASE-1E | 0.6113  | 0.1055    | 0.0077 | 0.1726 | 1.4715      | 0.2689           |

f is the fundamental frequency and  $\omega = 2\pi f$

Mean WL is the time-averaged mean water level

$WN = \sqrt{\eta_e \omega / (2KD)}$  (Nielsen, 1990)

the tidal wave. The amplitude corresponding to  $2\omega$  is smaller than the amplitude of  $3\omega$  and amplitude corresponding to  $4\omega$  is smaller than the amplitude of  $5\omega$ . In other words, the amplitudes corresponding to even multiple frequencies are lower than the same of next odd multiple frequencies. The amplitudes of each frequency are attenuating with distance ( $PS_1^1$  to  $PS_5^1$ ) similar to overall amplitude in time domain analysis. The FFT analysis of other frequencies is not provided individually for the brevity. The amplitudes corresponding to even harmonics( $2\omega$  and  $4\omega$ ) dissipated rapidly to become insignificant at points inside the aquifer. Hence, only odd harmonics( $3\omega$  and  $5\omega$ ) are significant to analyse.

Table 5.6: CASE-1A: Amplitude of waves corresponding to different frequencies.

| Amplitudes for different frequencies(m) |        |        |        |        |        |
|---|--------|--------|--------|--------|--------|
| Frequencies (Hz)                        | f      | 2f     | 3f     | 4f     | 5f     |
|   | 0.0024 | 0.0048 | 0.0070 | 0.0094 | 0.0118 |
| Tide                                    | 0.1917 | 0.0192 | 0.0198 | 0.0046 | 0.0082 |
| $PS_1^1$                                | 0.1301 | 0.0035 | 0.0117 | 0.0012 | 0.0005 |
| $PS_2^1$                                | 0.1172 | 0.0033 | 0.0098 | 0.0010 | 0.0005 |
| $PS_3^1$                                | 0.1017 | 0.0030 | 0.0077 | 0.0008 | 0.0004 |
| $PS_4^1$                                | 0.0897 | 0.0025 | 0.0064 | 0.0007 | 0.0004 |
| $PS_5^1$                                | 0.0766 | 0.0018 | 0.0048 | 0.0005 | 0.0003 |

The waves recorded, the amplitude of waves, the time-averaged water level of waves to analyse overheight, and phase difference of waves from tides of cases CASE-1B to CASE-1E are given in figures from Figure 5.26 to Figure 5.30. The summary of time-averaged water level and amplitudes of waves are provided in Figure 5.33. As explained in the previous paragraphs, the time-averaged water table shows overheight in all inland points except  $PS_5^1$  of CASE-1E. This may

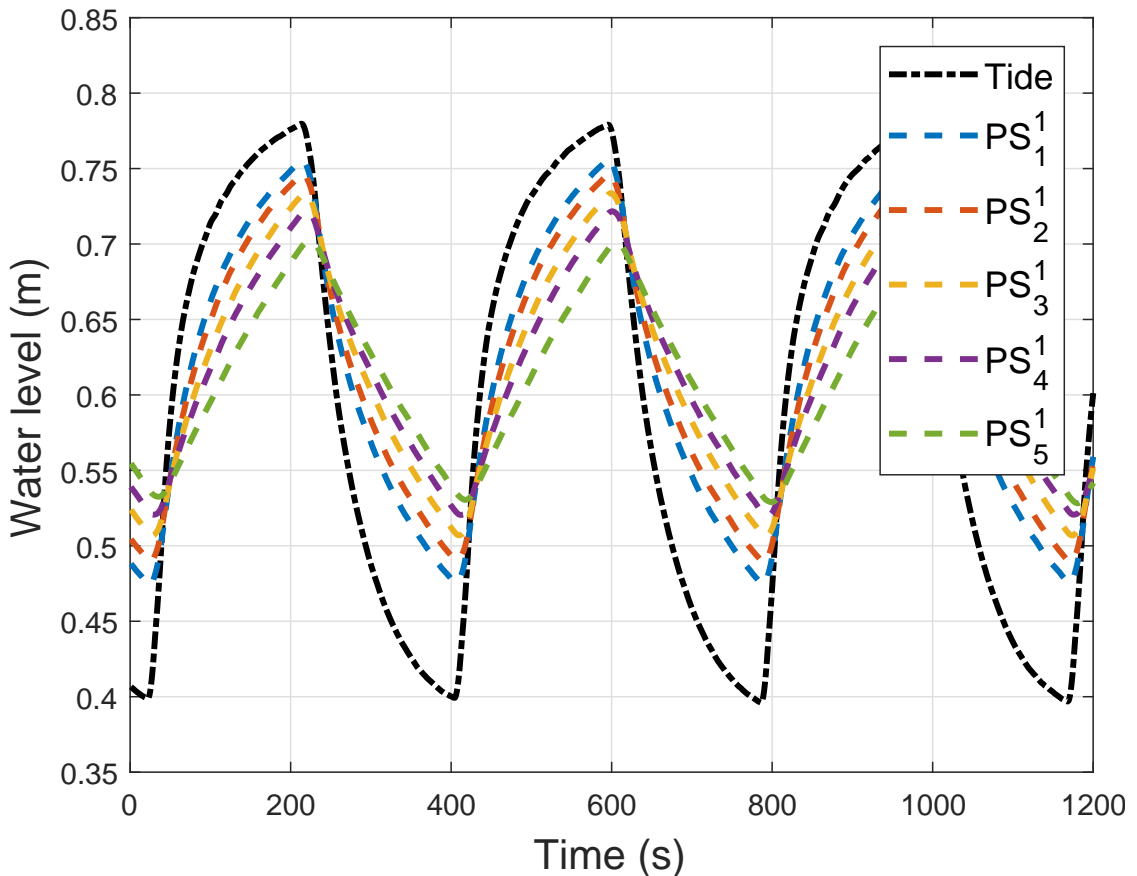
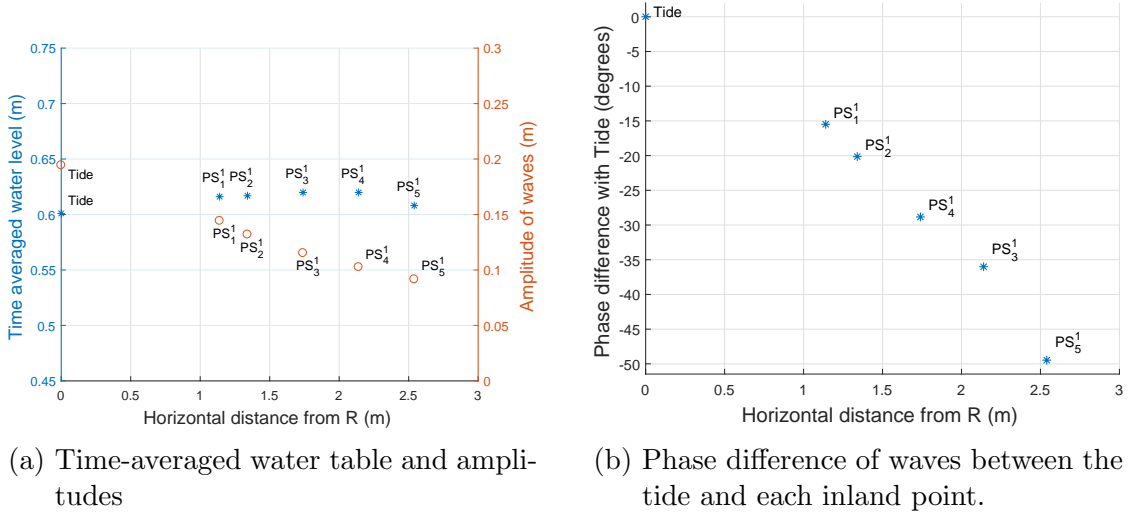


Figure 5.25: CASE-1B: Waves recorded by the pressure transducers for the clockwise and anticlockwise times of 180 s, resting period of 10 s, and DC motor RPM 203: magnified

be due to the boundary effect due to the proximity of the point at the inland boundary. The waves may get reflected by the impervious inland boundary, and CASE-1E waves are of highest frequency compared to other experiments. Hence, the water level changes are fastest among all, which makes it more vulnerable to the reflection. CASE-1A to CASE-1D also shown the time-averaged water level lower than the other points of the aquifer though they show small overheight compared to the mean water level of the tide.

The summary of the time-averaged water height, the amplitude of waves recorded at different pressure transducer locations, and the phase difference of waves with the tidal wave are given in Figure 5.33 and Figure 5.36. The fundamental frequency and harmonics of all cases are provided in Figure 5.36. The amplitudes of each harmonic for CASE-1A to CASE-1E are plotted in Figure 5.35. The higher frequency harmonics of CASE-1E dissipates rapidly compared to other cases. The waves of CASE-1E is rapid with a higher frequency compared to other cases, and the wave number (WN) (Nielsen, 1990) calculated based on fundamental frequency is highest of all experiments of CASE-1.



(a) Time-averaged water table and amplitudes  
 (b) Phase difference of waves between the tide and each inland point.

Figure 5.26: CASE-1B: Time-averages water table, amplitude and phase difference details of waves recorded by the pressure transducers for the clockwise and anticlockwise times of 180 s, resting period of 10 s, and DC motor RPM 203.

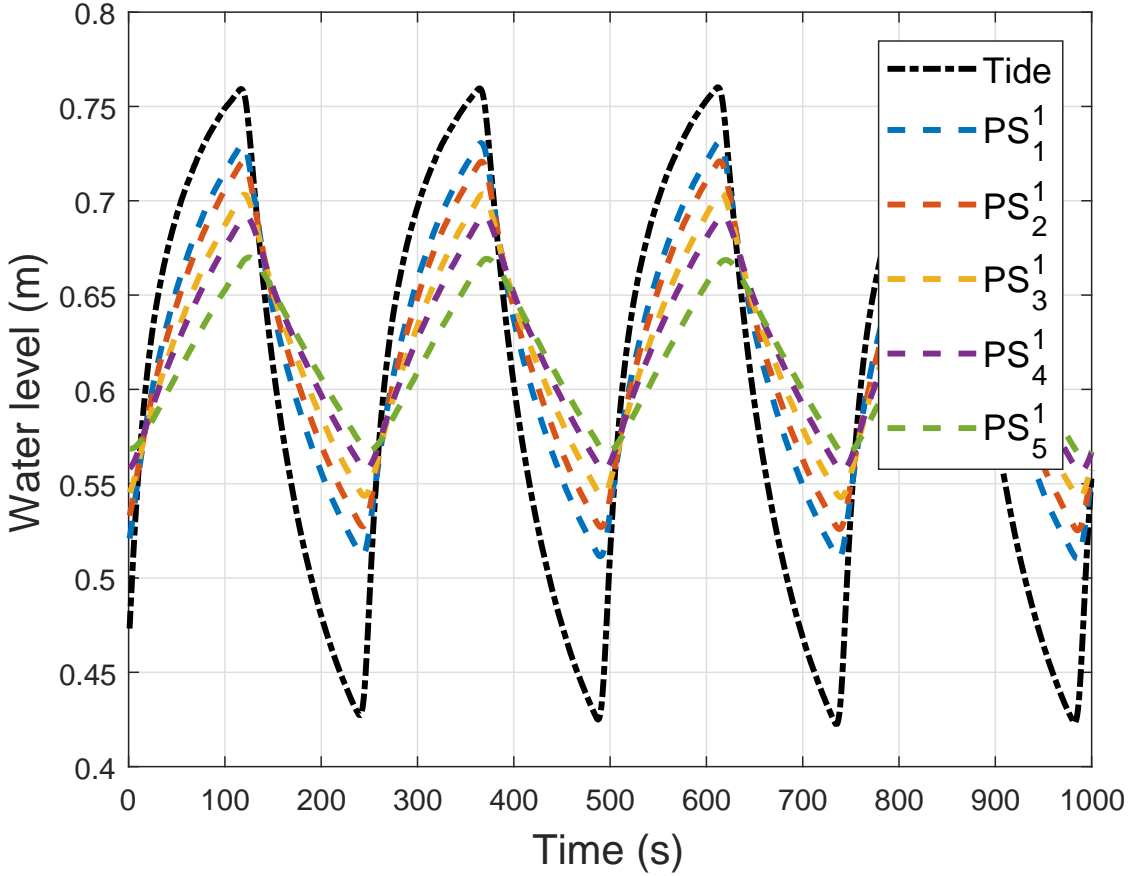


Figure 5.27: CASE-1C: Waves recorded by the pressure transducers for the clockwise and anticlockwise times of 120 s, resting period of 3 s, and DC motor RPM 203: magnified

The data is analysed for individual harmonics behaviour with distance from seaside boundary (Figure 5.37, Figure 5.38, Figure 5.39, Figure 5.40, and Figure 5.41). The plot of distance vs. fundamental frequency amplitudes is plotted

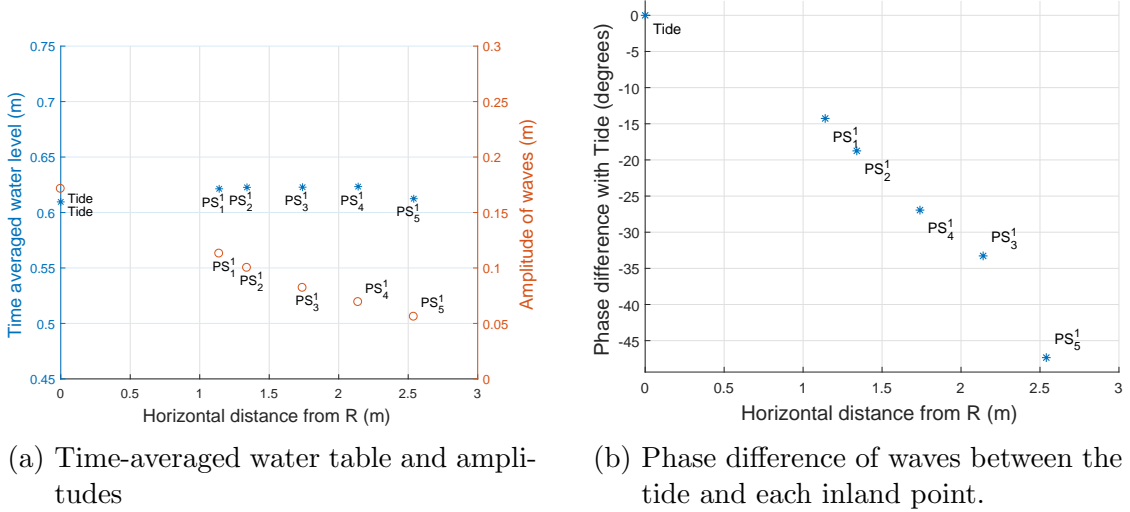


Figure 5.28: CASE-1C: Time-averages water table, amplitude and phase difference details of waves recorded by the pressure transducers for the clockwise and anticlockwise times of 120 s, resting period of 3 s, and DC motor RPM 203.

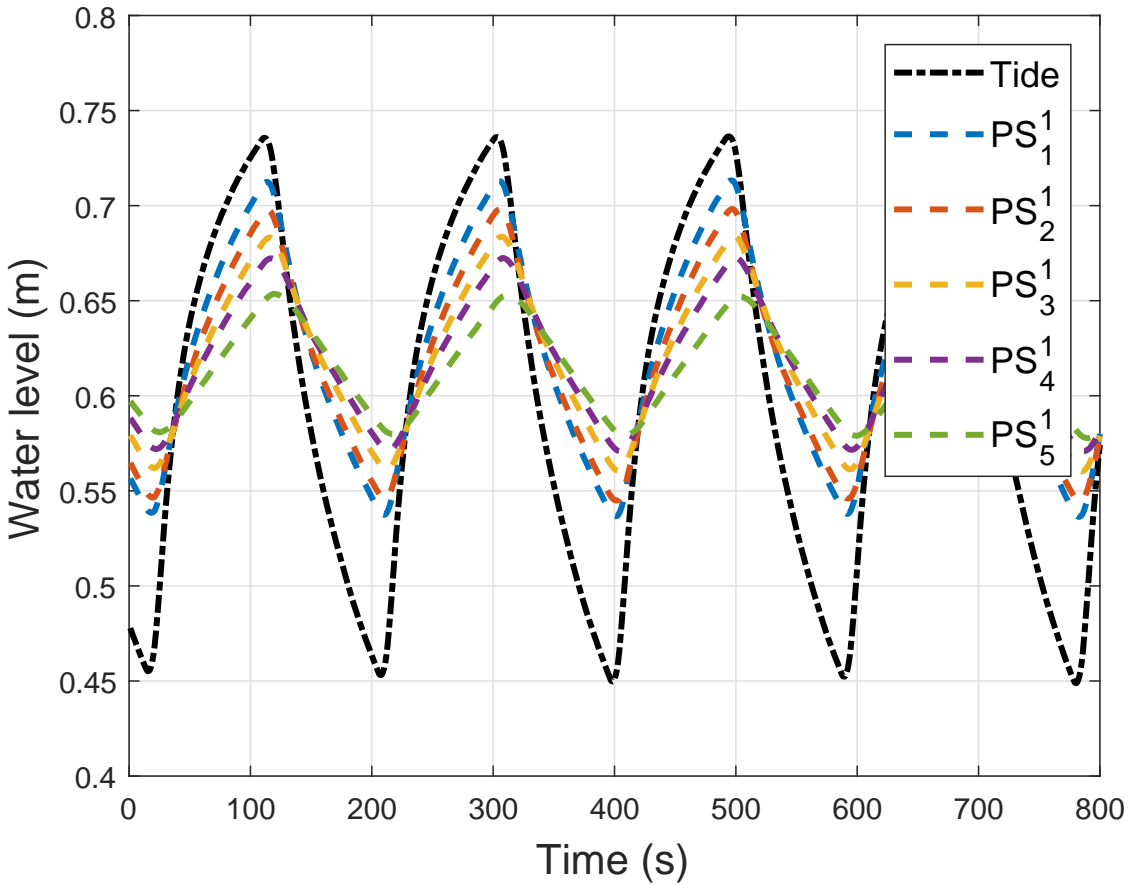


Figure 5.29: CASE-1D: Waves recorded by the pressure transducers for the clockwise and anticlockwise times of 90 s, resting period of 5 s, and DC motor RPM 203: magnified

individually since its amplitude range is much higher than the higher harmonics. Higher harmonic amplitudes are plots with respect to distance are plotted together. All harmonics amplitudes get attenuated with distance from the seaside

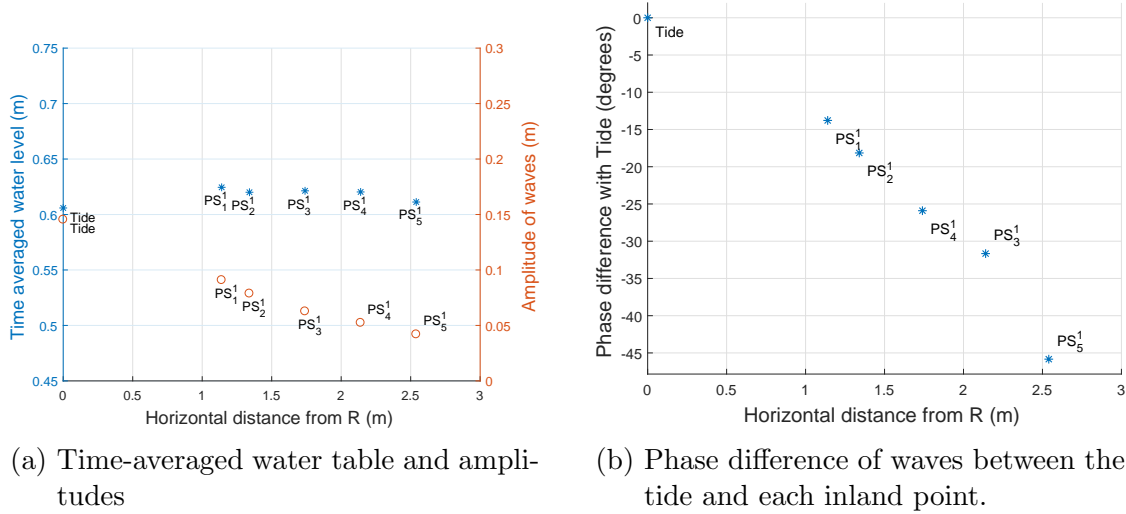


Figure 5.30: CASE-1D: Time-averages water table, amplitude and phase difference details of waves recorded by the pressure transducers for the clockwise and anticlockwise times of 90 s, resting period of 5 s, and DC motor RPM 203.

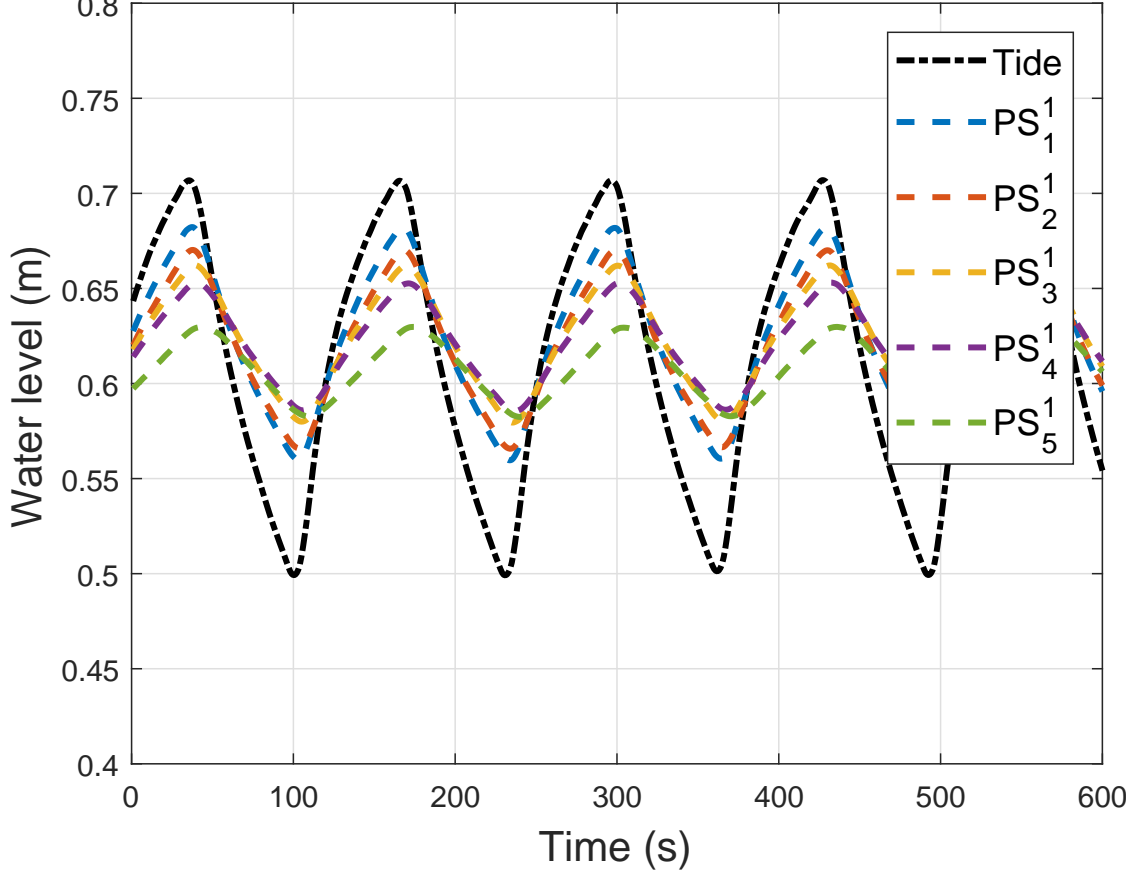


Figure 5.31: CASE-1E: Waves recorded by the pressure transducers for the clockwise and anticlockwise times of 60 s, resting period of 5 s, and DC motor RPM 203: magnified

boundary. But, they do not follow a linear relationship. Hence, they are plotted in semi-logarithmic plots with amplitudes converted to logarithmic values.

The semi-logarithmic plots of amplitudes calculated based on the time-domain

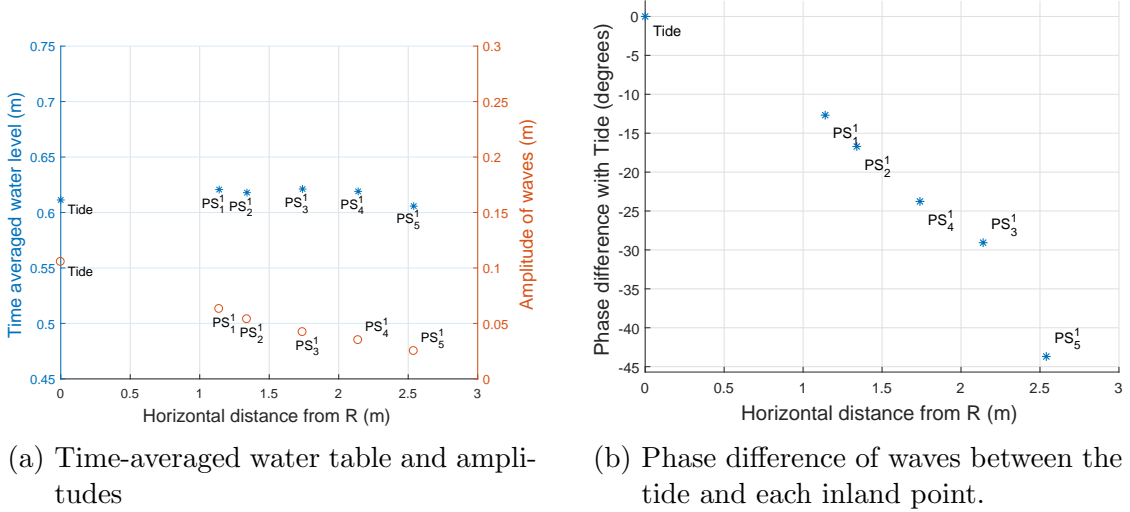


Figure 5.32: CASE-1E: Time-averages water table, amplitude and phase difference details of waves recorded by the pressure transducers for the clockwise and anticlockwise times of 60 s, resting period of 5 s, and DC motor RPM 203.

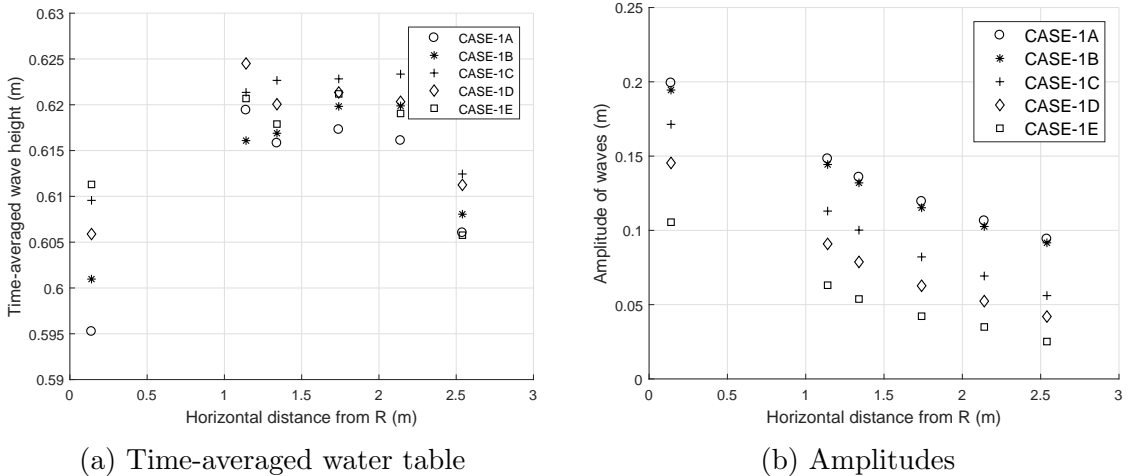
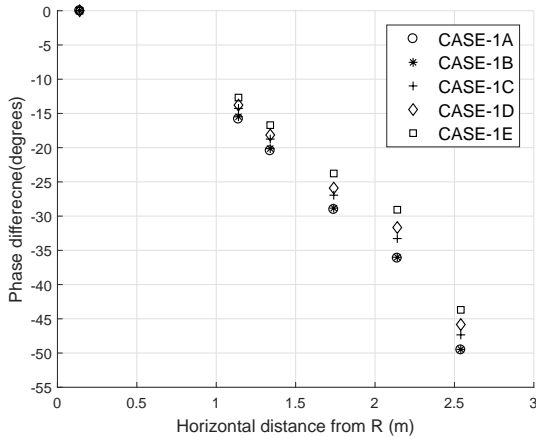
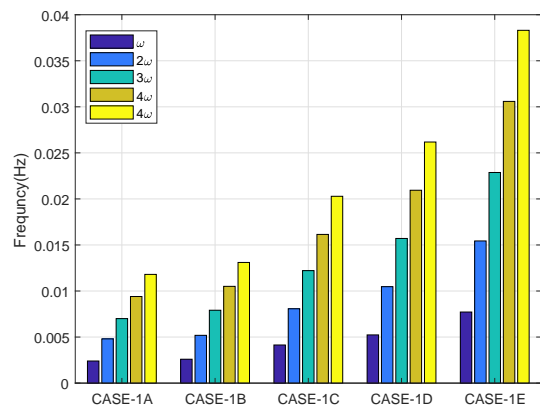


Figure 5.33: Summary of time-averaged water table, and amplitude of waves recorded for CASE-1A to CASE-1E

analysis in relation to horizontal distance are given in Figure 5.42. The portion circled in red is the location of the pressure sensor in tidal water level. This is located at the seaward side of the intertidal zone. Apart from this point, all other amplitudes are linear in the logarithmic scale. Hence, the amplitudes are attenuating in exponential relation with distance from the seaside boundary. The amplitude of  $PS_5^1$  of CASE-1E is not exactly lying on the linear line of  $PS_2^1$  to  $PS_4^1$ . The higher fundamental frequency of this case might have led to the reflection of the wave as explained earlier. The semi-logarithmic plot of fundamental frequency amplitude calculated in the frequency domain in relation to distance for CASE-1 also behaves in a similar way (Figure 5.43). The semi-logarithmic plots of  $3\omega$  (Figure 5.44) and  $3\omega$  (Figure 5.45) also show exponential decay of amplitude except CASE-1E. The  $3\omega$  harmonic amplitudes of CASE-1E are very small (due to rapid



(a) Summary of phase difference of waves with tides for CASE-A to CASE-E



(b) Summary of frequencies of tidal waves for CASE-A to CASE-E

Figure 5.34: Summary of phases difference from tidal wave and frequencies of tidal waves for CASE-1A to CASE-1E

dissipation) compared to other cases.

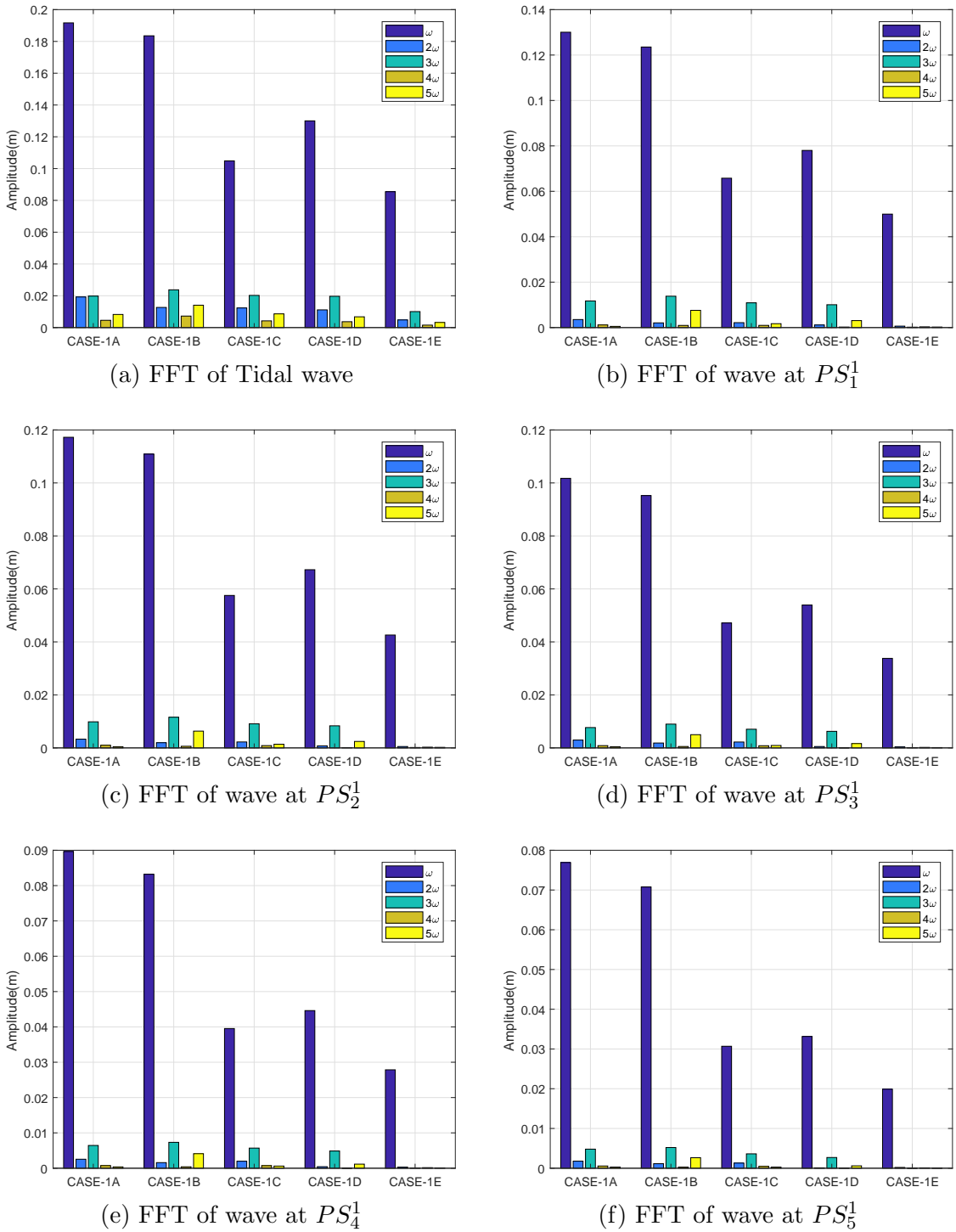
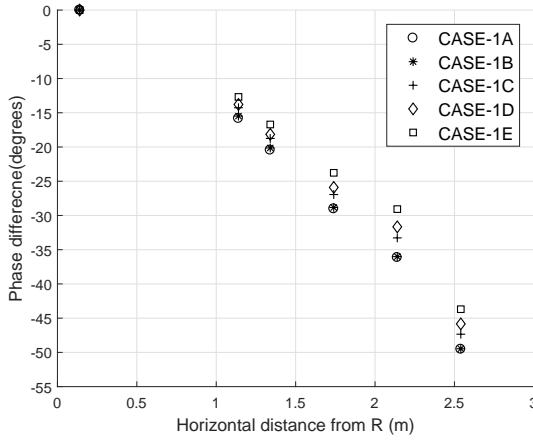
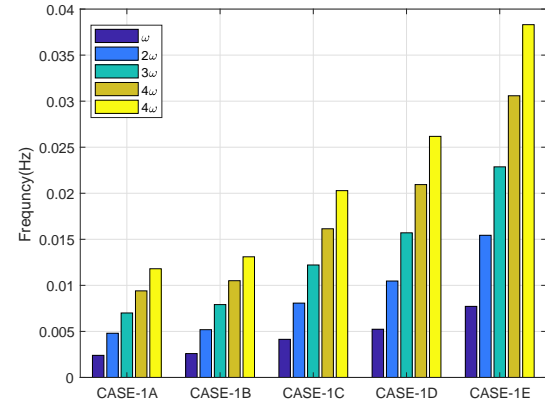


Figure 5.35: CASE-1A to CASE-1E: FFT of waves recorded using pressure transducers at Tide point,  $PS_1^1$ ,  $PS_2^1$ ,  $PS_3^1$ ,  $PS_4^1$ , and  $PS_5^1$

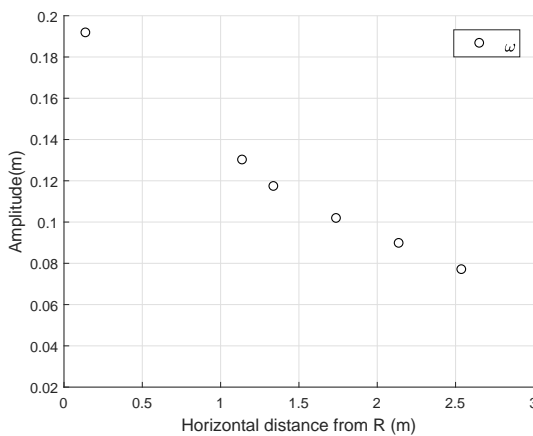


(a) Summary of phase difference of waves with tides for CASE-1A to CASE-1E

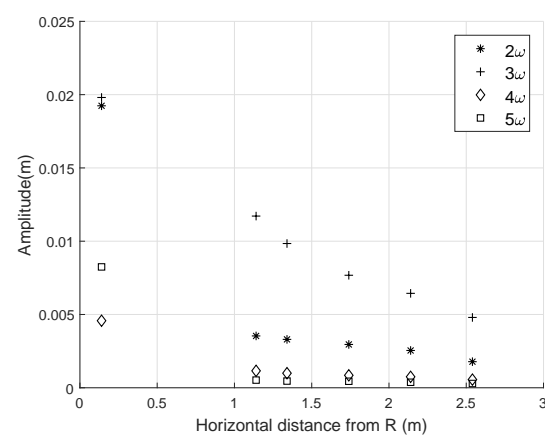


(b) Summary of frequencies of tidal waves for CASE-1A to CASE-1E

Figure 5.36: Summary of phases difference from tidal wave and frequencies of tidal waves for CASE-1A to CASE-1E



(a) Amplitudes of waves for frequency  $\omega$  at pressure transducer locations



(b) Amplitudes of waves for frequency  $2\omega$ ,  $3\omega$ ,  $4\omega$ , and  $5\omega$

Figure 5.37: CASE-1A: Amplitudes of waves for different frequencies at pressure transducer locations

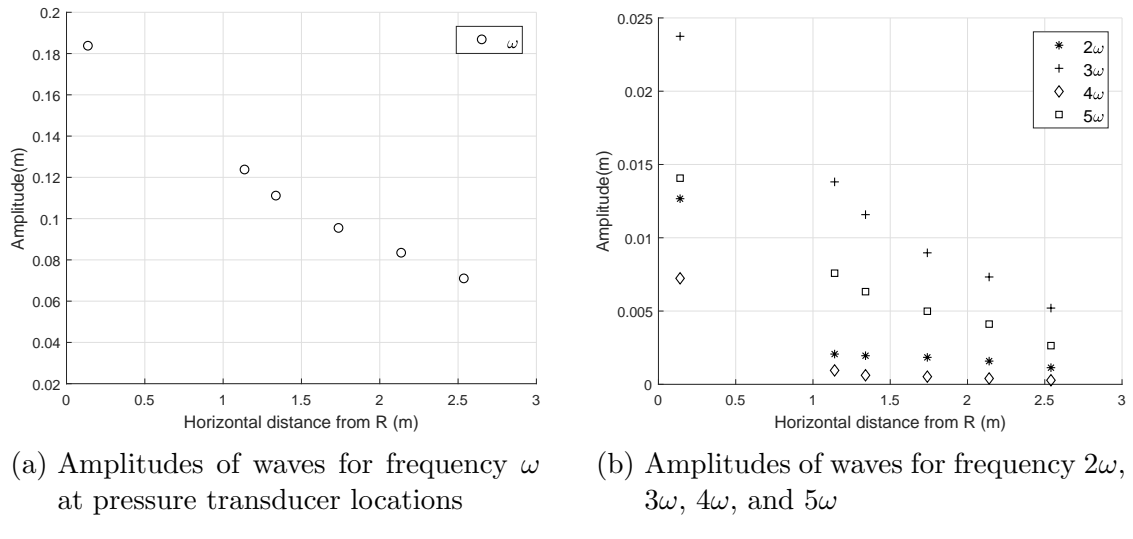


Figure 5.38: CASE-1B: Amplitudes of waves for different frequencies at pressure transducer locations

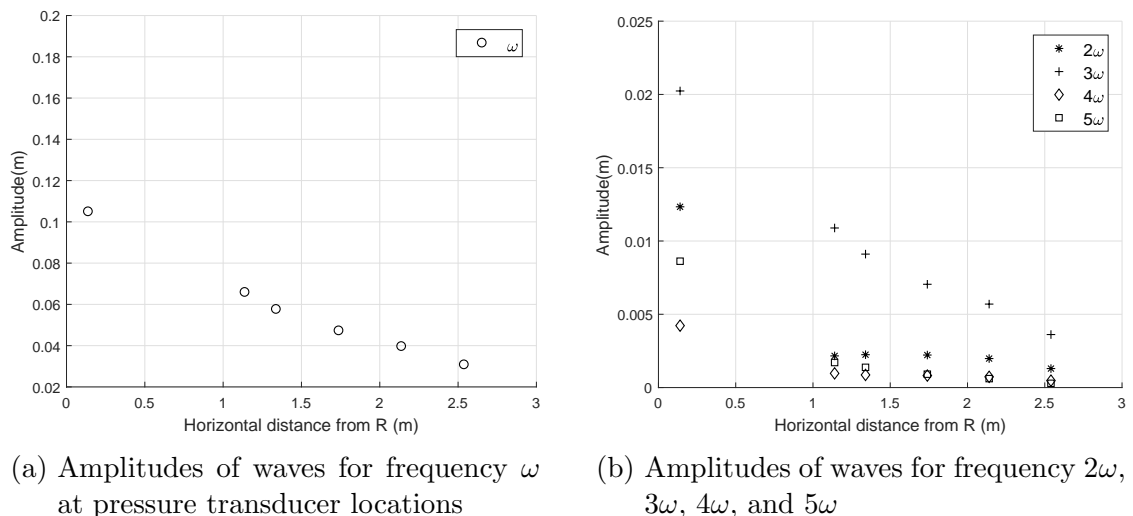


Figure 5.39: CASE-1C: Amplitudes of waves for different frequencies at pressure transducer locations

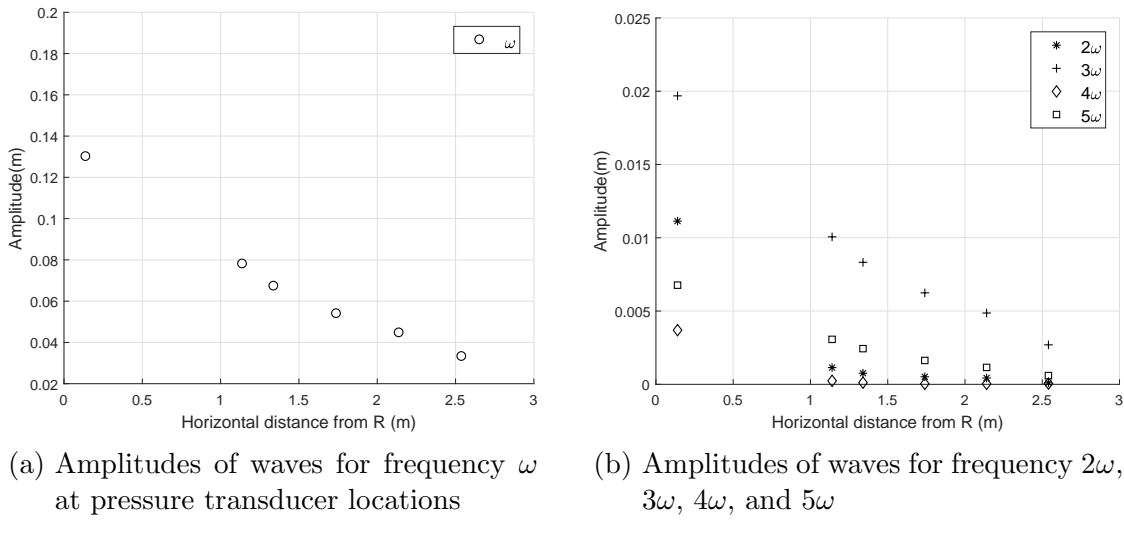


Figure 5.40: CASE-1D: Amplitudes of waves for different frequencies at pressure transducer locations

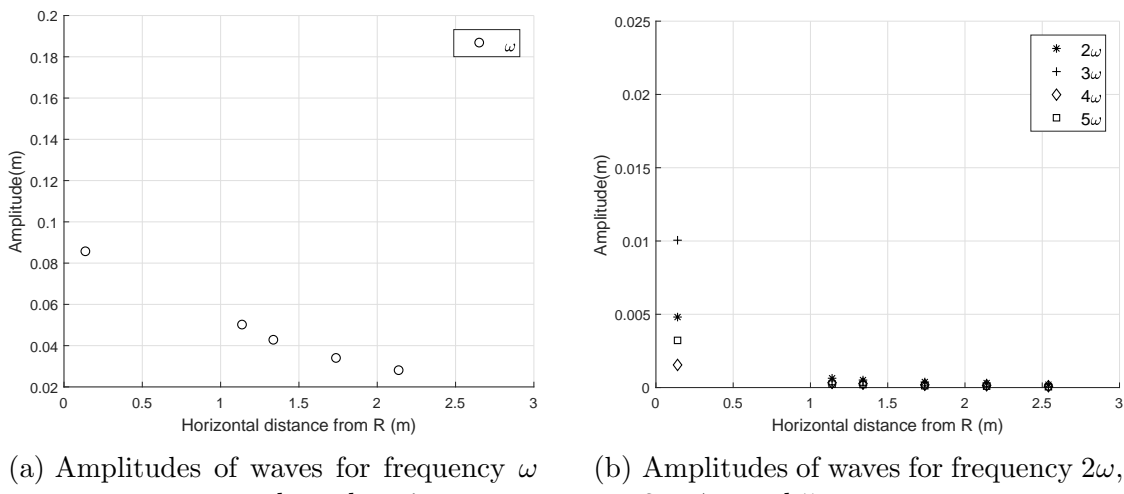


Figure 5.41: CASE-1E: Amplitudes of waves for different frequencies at pressure transducer locations

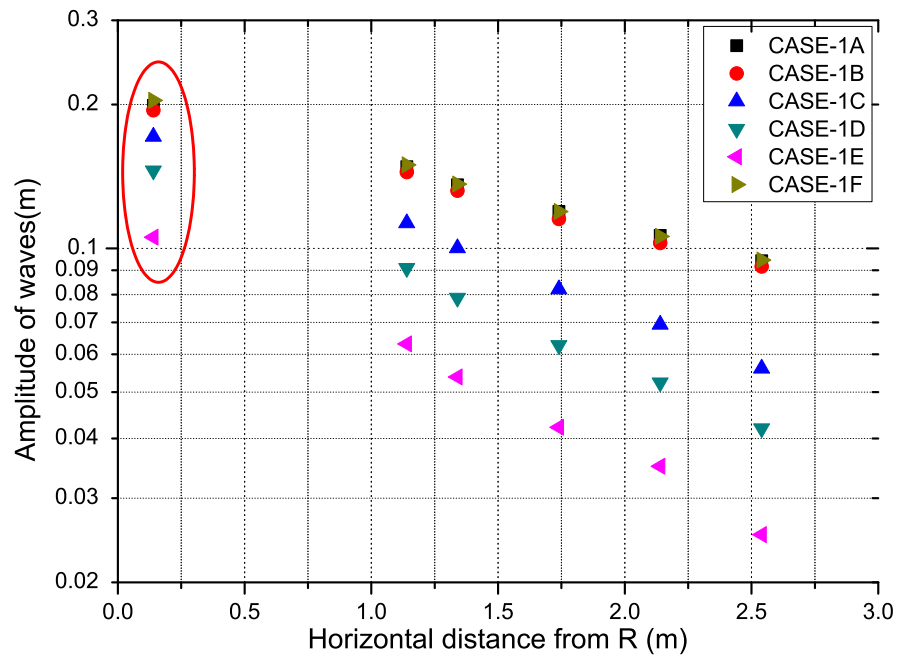


Figure 5.42: Semi-logarithmic plot of amplitude calculated in time-domain in relation to distance for CASE-1

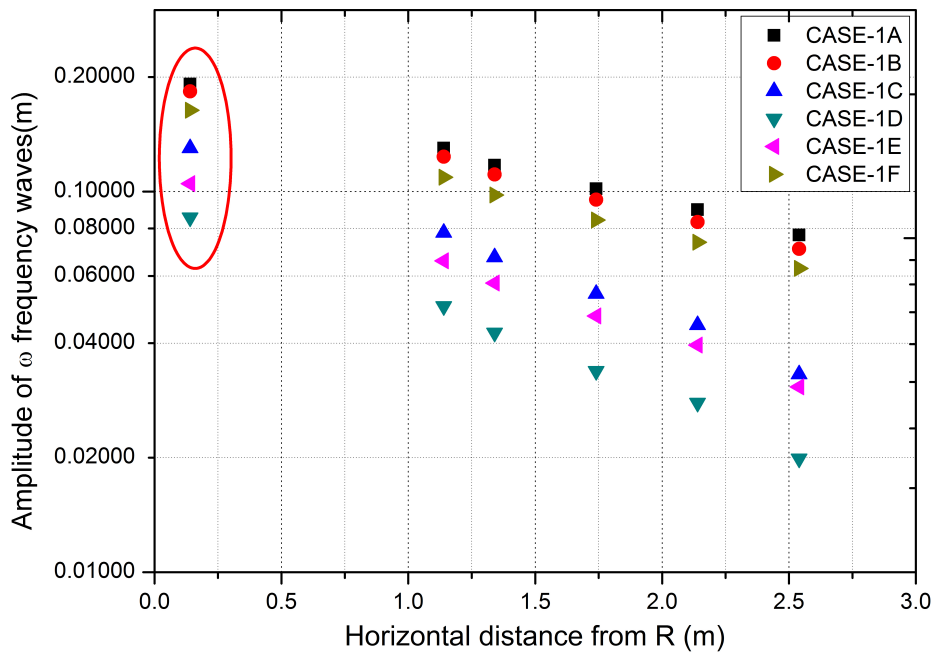


Figure 5.43: Semi-logarithmic plot of fundamental frequency amplitude calculated in frequency domain in relation to distance for CASE-1

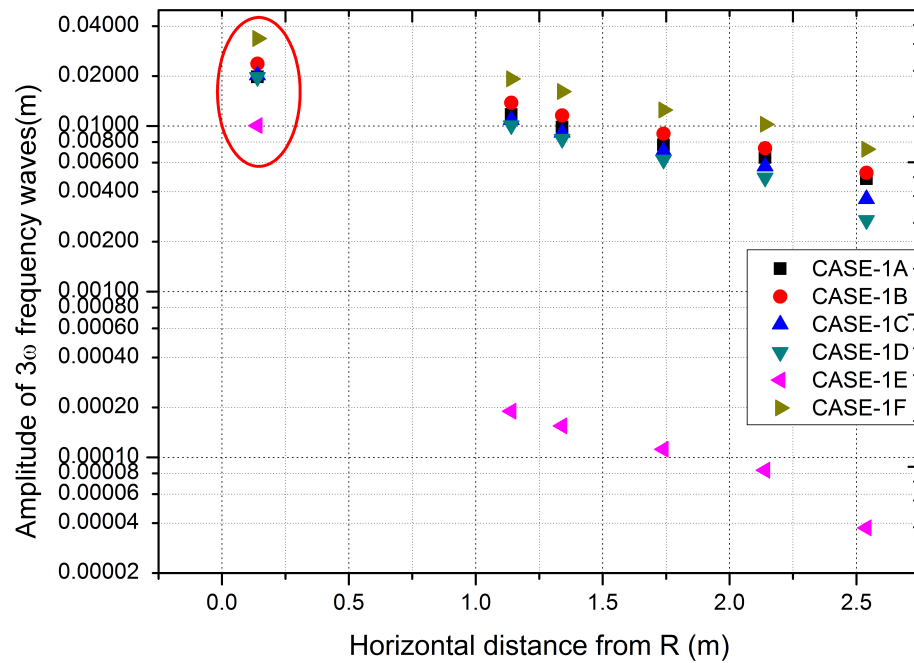


Figure 5.44: Semi-logarithmic plot of  $3\omega$  harmonic amplitude calculated in frequency domain in relation to distance for CASE-1

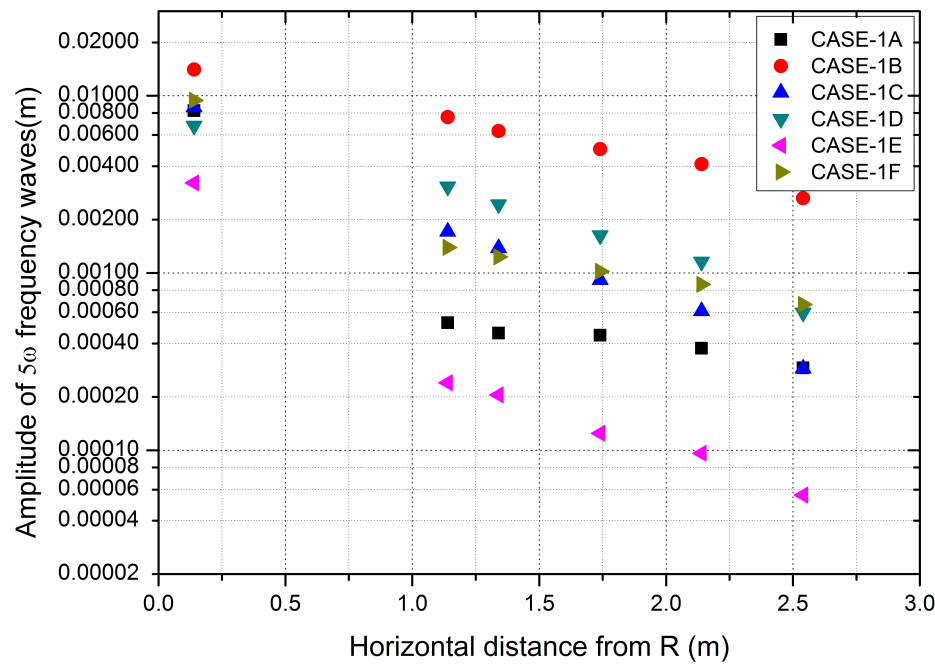


Figure 5.45: Semi-logarithmic plot of  $5\omega$  harmonic amplitude calculated in frequency domain in relation to distance for CASE-1

### 5.3.3 CASE-2: Grade II IS sand with Beach Slope $\pi/12$

The CASE-2 experiments were done for milder slope, lesser hydraulic conductivity sand. The Grade II Indian Standard (IS) sand (Bureau of Indian Standards, 2007) with beach slope of  $\pi/12$  was used for this set of experiments. The IS sand (IS 650: 1991) is manufactured exclusively by Tamilnadu Minerals Limited at Ennore factory. The IS sand is used for testing of cement and concrete and to study many other building material properties. The IS sand is being used as a replacement for Leighton-Buzzard sand used for cement testing in the UK. The grade II of IS sand particles size is 0.5 mm to 1.0 mm. The IS sand is gone through the purification process to make it free from impurities. The sand packing method is same as CASE-1 experiments. The dimensions of the aquifer model and the pressure transducer locations are shown in Figure 5.46. The amplitudes of CASE-2 experiments are relatively maintained smaller than CASE-1 since the horizontal extent of the intertidal zone is larger in milder slopes. Another significant difference is most of the pressure transducers are located within the intertidal zone.

Table 5.7: Parameter details of CASE-2 experiments

| CASE    | Mean WL<br>D, (m) | Amplitude<br>A, (m) | f,<br>(Hz) | A/D<br>(-) | Wave number<br>WN(1/m) | $A \cot(\beta)*$<br>WN(-) |
|---------|-------------------|---------------------|------------|------------|------------------------|---------------------------|
| CASE-2A | 0.6419            | 0.0846              | 0.0014     | 0.1318     | 0.8017                 | 0.2531                    |
| CASE-2B | 0.6291            | 0.0931              | 0.0023     | 0.1481     | 1.0380                 | 0.3607                    |
| CASE-2C | 0.6462            | 0.0675              | 0.0025     | 0.1045     | 1.0678                 | 0.2690                    |
| CASE-2D | 0.6248            | 0.1265              | 0.0035     | 0.2025     | 1.2849                 | 0.6066                    |
| CASE-2E | 0.6452            | 0.0964              | 0.0046     | 0.1494     | 1.4495                 | 0.0521                    |

$f$  is the fundamental frequency and  $\omega = 2\pi f$

Mean WL is the time-averaged mean water level

$WN = \sqrt{\eta_e \omega / (2KD)}$  (Nielsen, 1990),  $K = 0.0020$  m/s assumed for calculation

The parameter details of corresponding to CASE-2 given in Table 5.7. The ex-

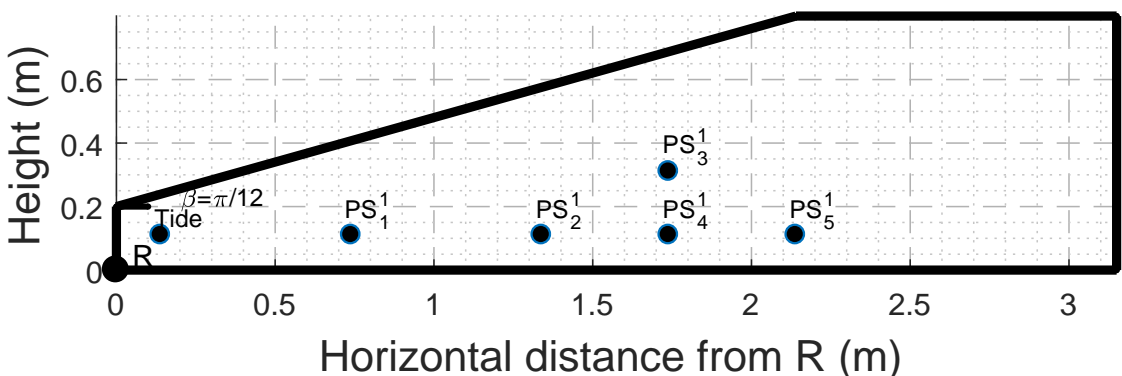


Figure 5.46: Schematic of the coastal aquifer modeled in the experimental setup for CASE-2

periments were done for time-averaged mean water level for the range of 0.6248  $m$  to 0.6462  $m$ . The amplitudes range of experiments were 0.0675  $m$  to 0.1265  $m$ . The frequency of tidal waves generated were from varied from 0.0014  $m$  (time period 695.41  $s$ ) to 0.0046  $m$  (time period 218.29  $s$ ). The pressure sensor recording the tidal wave was placed inside the sand portion of the aquifer (at 0.14  $m$  from the bottom). Figure 5.47 shows the waves generated in CASE-2A, which corre-

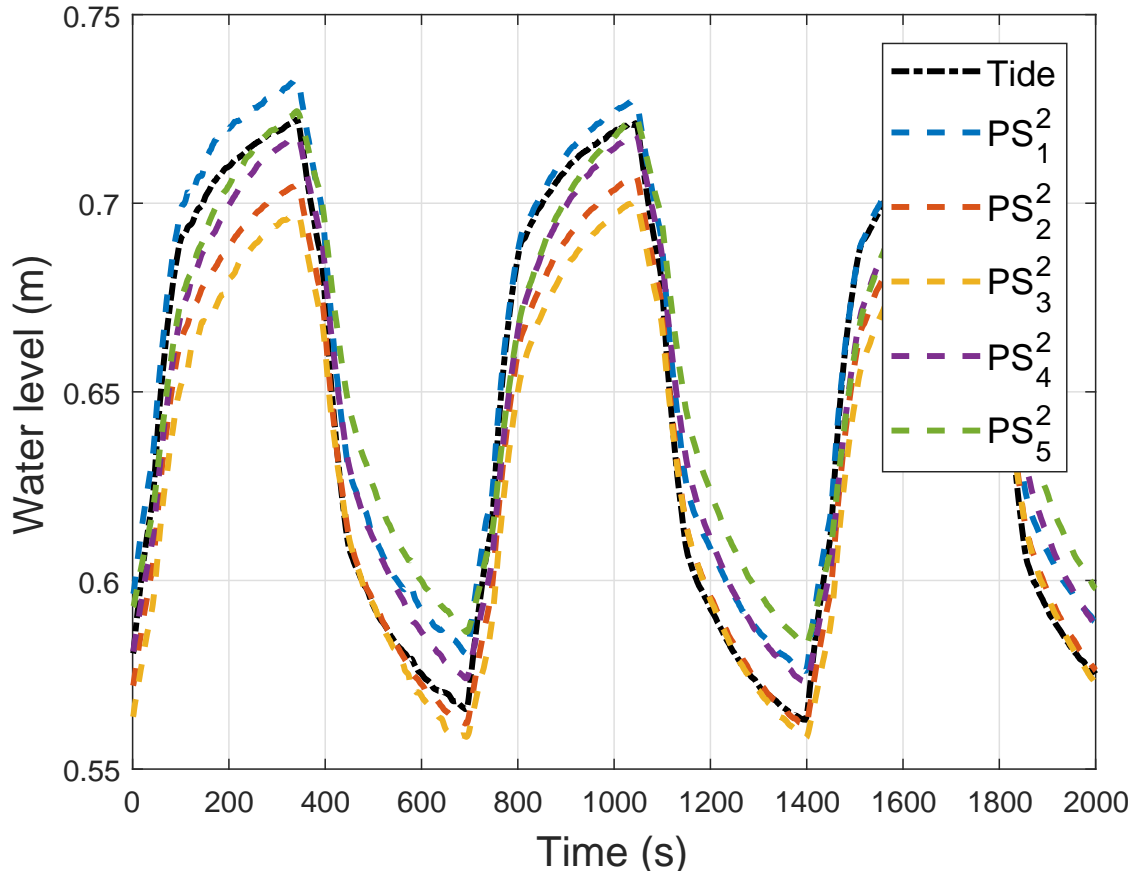


Figure 5.47: CASE-2A: Waves recorded by the pressure transducers for the clockwise and anticlockwise times of 300  $s$ , resting period of 50 sand DC motor RPM 161: magnified

sponds to maximum frequency and minimum wave number of the experiments done. Time-averaged water table of CASE-2A (Figure 5.48) has not shown significant overheight. The pressure transducers are mostly placed in the intertidal region of the aquifer and the pressure transducer  $PS_5^2$  is very close to the seaside boundary to show significant overheight. Frequency of the tidal wave is too small (larger time period) which results in larger decay length (inverse of wave number, WN) to dissipate within the zone of pressure transducer locations. It can be confirmed by the amplitude of the waves at all points are the same as the tidal wave. The maximum phase difference of the groundwater waves with respect to tidal wave is small compared to CASE-1. The maximum phase difference of CASE-2A was 14 degrees while the same for CASE-1 experiments were in the range of 40 to

50 degrees. Smaller hydraulic conductivity of CASE-2A, pressure sensors located very close to the seaside boundary, and larger decay length are the reasons for the smaller phase differences. Two pressure sensors are placed in the same vertical line with  $PS_3^2$  located at 0.34 m above the bottom and  $PS_4^2$  located at 0.14 m above the bottom. Time-averaged water level at  $PS_4^2$  is more than  $PS_3^2$ . Hence, there is a vertical upward flow in that region. Similarly, amplitudes recorded also higher at  $PS_4^2$  compared to  $PS_3^2$ . The analysis of pressure data in frequency domain (Figure 5.49) shown that the amplitudes of odd harmonics are higher than the even harmonics ( $2\omega$ ,  $4\omega$ , ...). This is in agreement the frequency domain results of CASE-1. The wave details of CASE-2B, CASE-2C, CASE-2D, and CASE-2E are given in Appendix A.

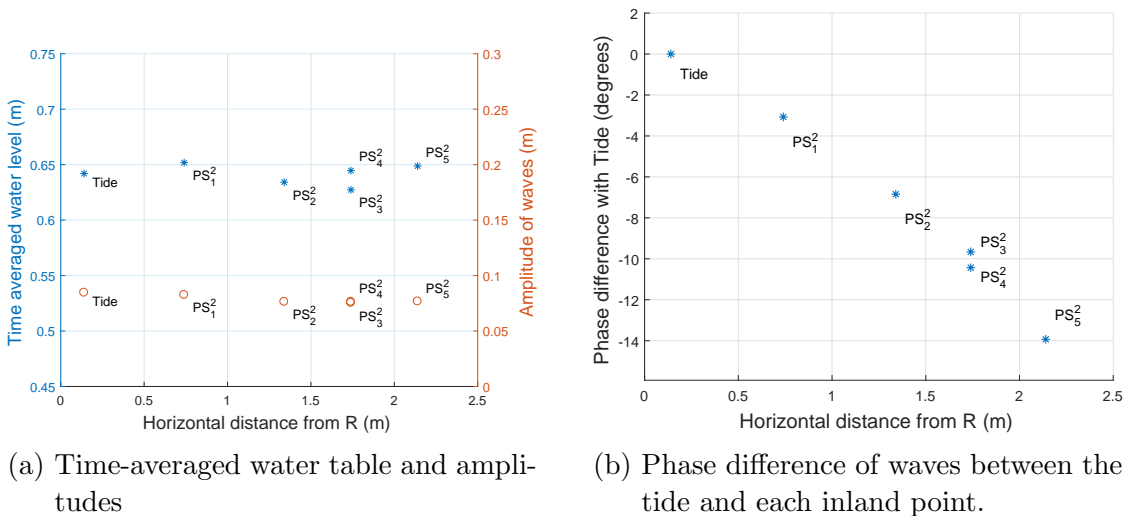


Figure 5.48: CASE-2A: Time-averaged water table, amplitude and phase difference details of waves recorded by the pressure transducers for the clockwise and anticlockwise times of 300 s, resting period of 50 sand DC motor RPM 161.

Summary of the time-averaged water table and amplitude of waves recorded for CASE-2A to CASE-2E (Figure 5.50) have shown similar trends as CASE-2A. The values of the time-averaged water table at points located within the intertidal zone does not show significant overheight and some points ( $PS_2^2$ ) even shows lesser average water level than the tidal mean water level. The point  $PS_5^2$  which is most inland shows overheight for all cases. CASE-2B and CASE-2C are of approximately similar frequencies. However, the tidal amplitude of CASE-2B (0.0931 m) is higher than the same as of CASE-2C (0.06752 m). CASE-2B and CASE-2D are of approximately same mean tidal level. However, CASE-2D amplitude (0.1265 m) was significantly higher than CASE-2B amplitude (0.0931 m). The overheight at  $PS_5^2$  is higher for the higher amplitude case (CASE-2D), which is in agreement with the analytical solutions. Analytical solutions mean water level in the groundwater is directly proportional to the  $A/D$  ratio. Summary of the phase difference

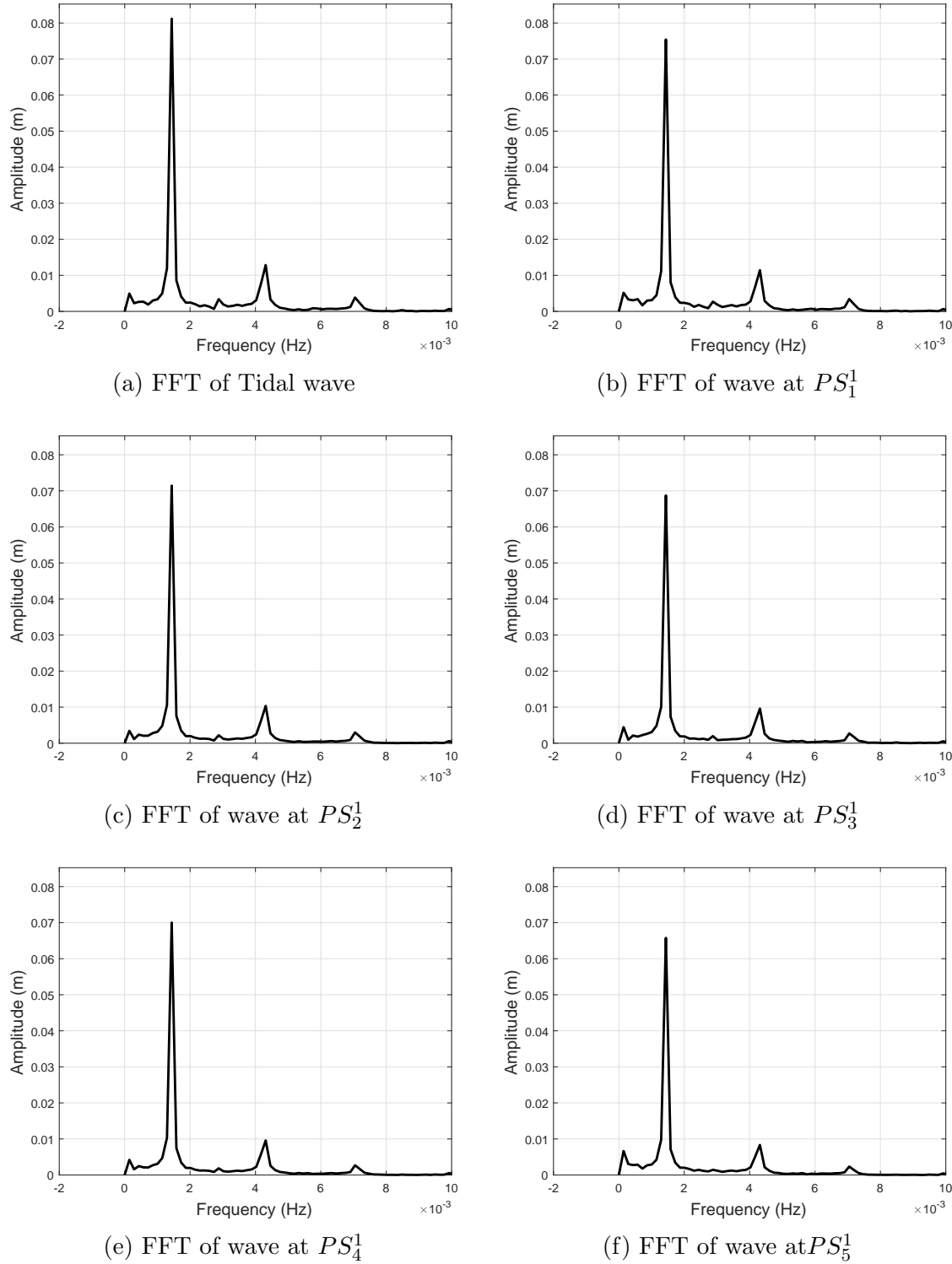


Figure 5.49: CASE-2A: FFT of waves recorded using pressure transducers pressure transducers for the clockwise and anticlockwise times of 300 s, resting period of 50 sand DC motor RPM 161.

of waves (Figure 5.51) follows the linearly increasing relation when moving inland as in CASE-1. The phase difference of the point at the bottom of the same vertical line is more than the point at the top ( $PS_4^2$  is more than that of  $PS_3^2$ ). The dominant frequencies and corresponding amplitudes for CASE-2A are given in Figure 5.52. Summary of dominant frequencies and corresponding amplitudes for

all CASE-2 experiments are given in Figure 5.52. Odd frequencies have significant amplitudes compared to even frequencies. The frequencies apart from fundamental frequency dissipated for cases with highest values of  $WNA \cot(\beta)$  (least wave time periods: CASE-2D and CASE-2E) dissipated for all points except the tidal wave recording point (Figure 5.56 and Figure 5.57). The amplitudes calculated in time-domain (Figure 5.58) and the amplitudes corresponding to fundamental frequency ( $\omega$ ) obtained in frequency domain by using FFT (Figure 5.59) show attenuation of amplitude in exponential relation with distance for all CASE-2 experiments, except CASE-2C in time domain plot. CASE-2C is the case with least amplitude among the experiments, and  $PS_2^2$  point is an anomaly in the semi-logarithmic plot of time-domain. However, the frequency domain plot of  $\omega$  follows exponential relationship. The amplitude of tidal wave point is an exception as in CASE-1. Amplitudes of  $2\omega$  (Figure 5.60) are also following exponential attenuation except the cases CASE-2D and CASE-2E which are corresponding to highest time period waves with highest  $WNA \cot(\beta)$  values. These two cases have rapid dissipation in their amplitudes of higher harmonics. Amplitudes of the same are almost negligible compared to the order of amplitudes of fundamental frequencies. Amplitudes of harmonics of frequency more than  $3\omega$  also have negligible amplitudes and do not follow exponential attenuation.

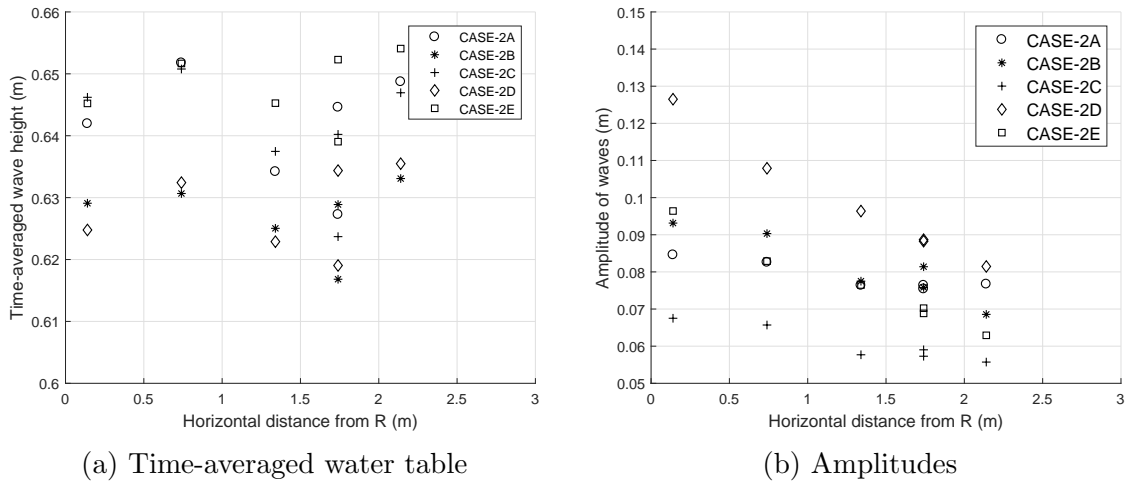


Figure 5.50: Summary of time-averaged water table, and amplitude of waves recorded for CASE-2A to CASE-2E

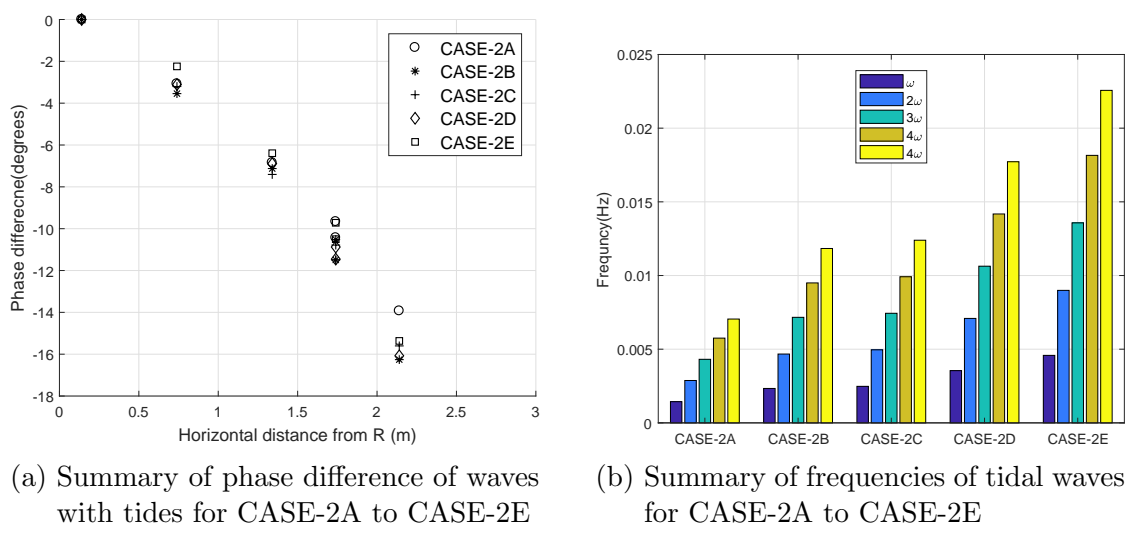


Figure 5.51: Summary of phases difference from tidal wave and frequencies of tidal waves for CASE-2A to CASE-2E

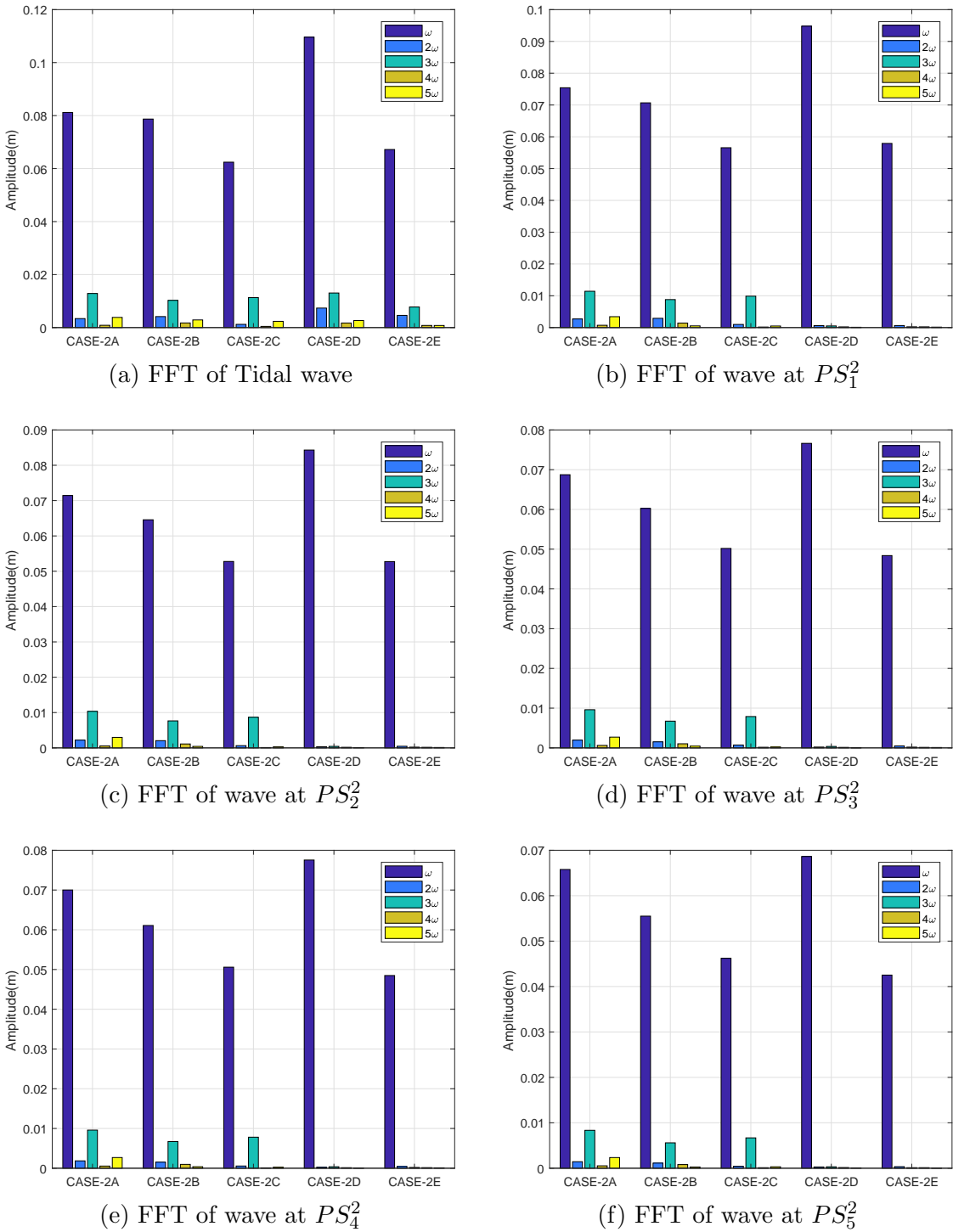


Figure 5.52: CASE-2: FFT of waves recorded using pressure transducers at Tide point,  $PS_1^2$ ,  $PS_2^2$ ,  $PS_3^2$ ,  $PS_4^2$ , and  $PS_5^2$

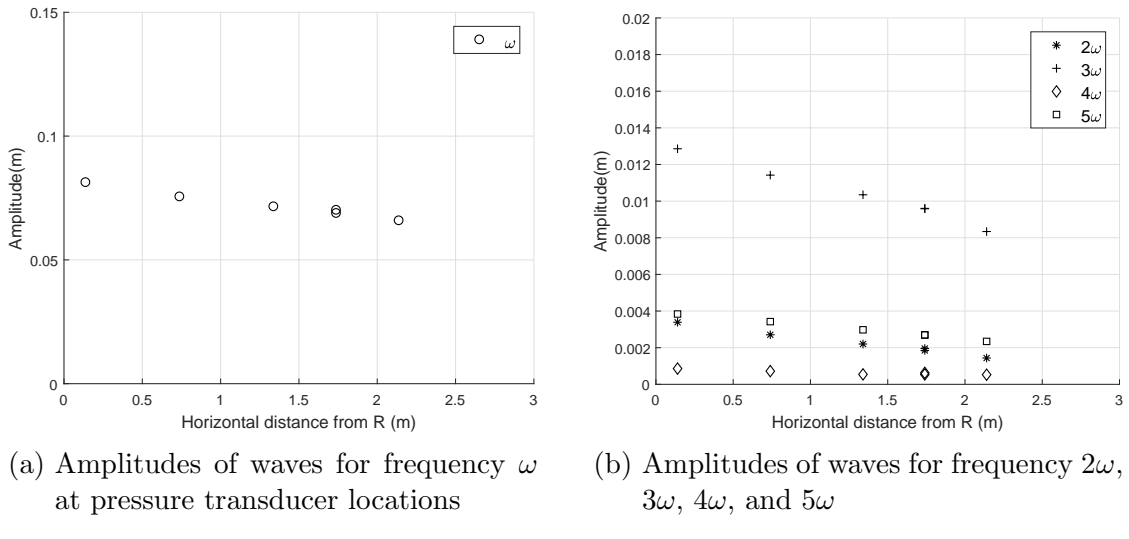


Figure 5.53: CASE-2A: Amplitudes of waves for different frequencies at pressure transducer locations

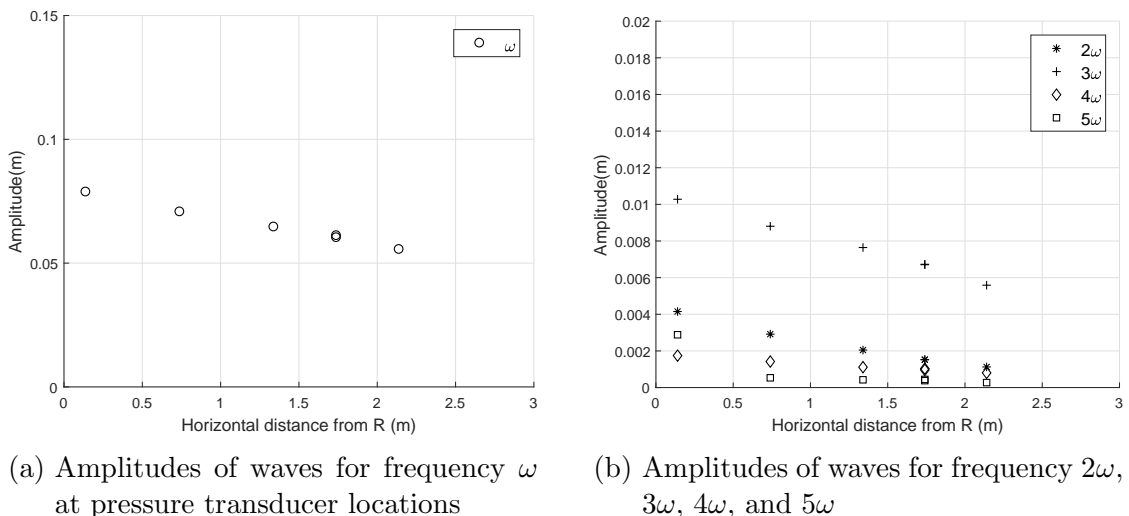


Figure 5.54: CASE-2B: Amplitudes of waves for different frequencies at pressure transducer locations

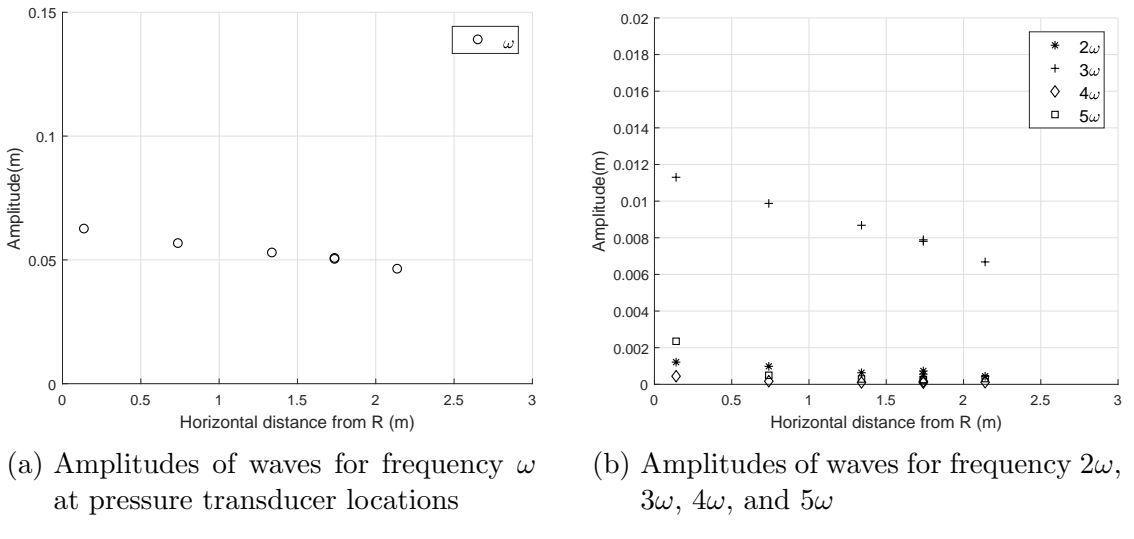


Figure 5.55: CASE-2C: Amplitudes of waves for different frequencies at pressure transducer locations

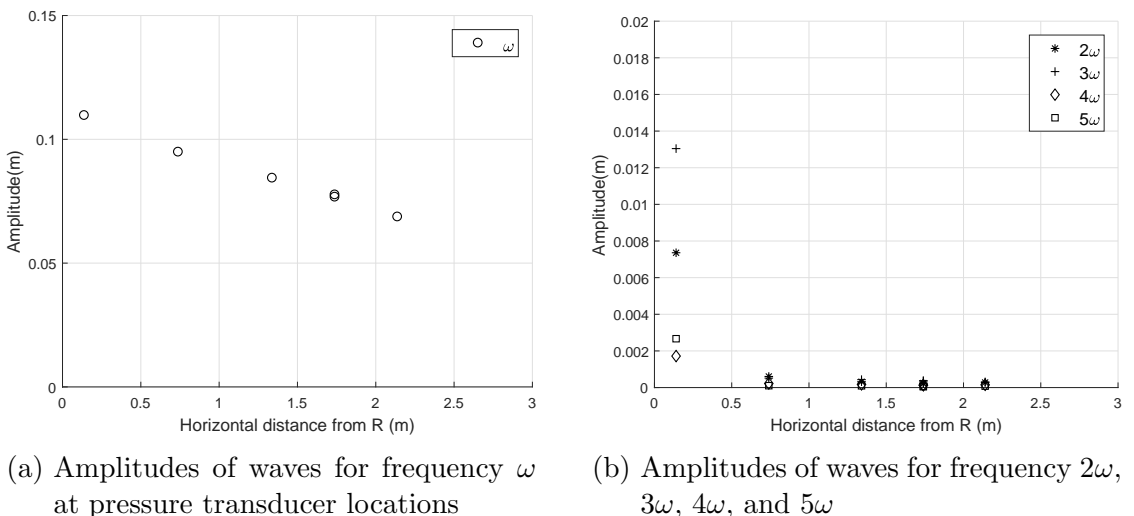


Figure 5.56: CASE-2D: Amplitudes of waves for different frequencies at pressure transducer locations

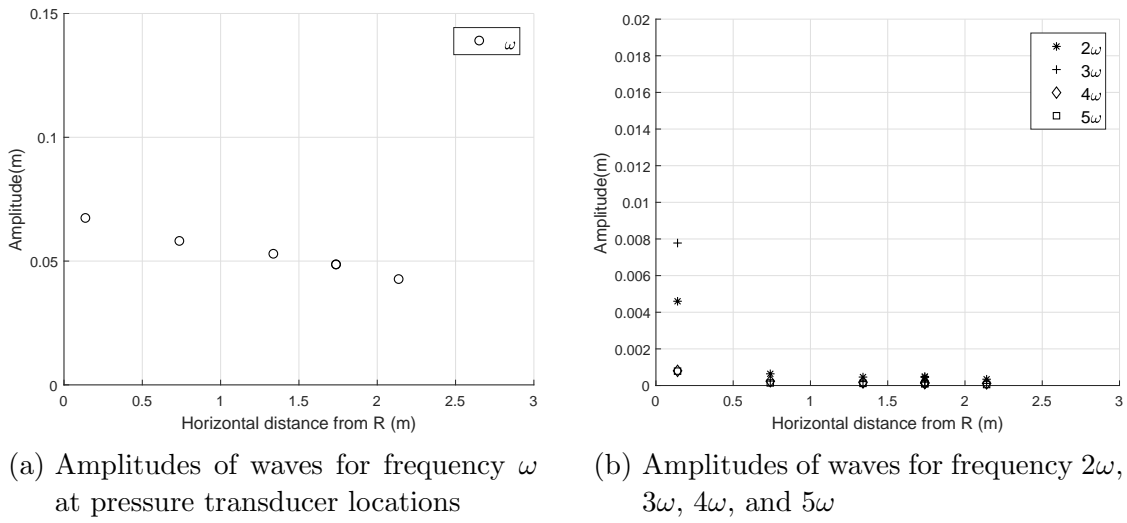


Figure 5.57: CASE-2E: Amplitudes of waves for different frequencies at pressure transducer locations

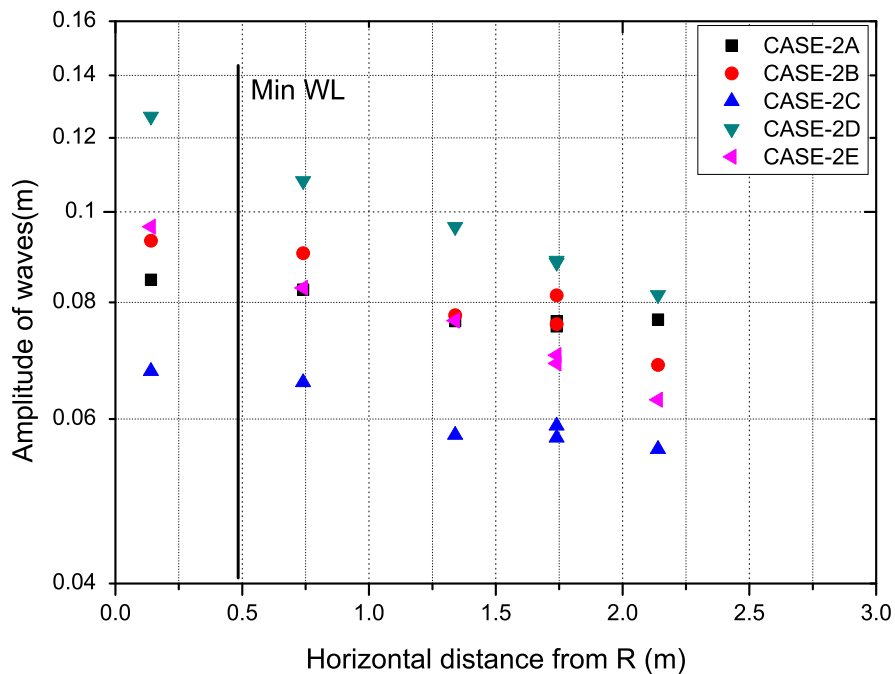


Figure 5.58: Semi-logarithmic plot of amplitudes calculated in time domain in relation to distance for CASE-2

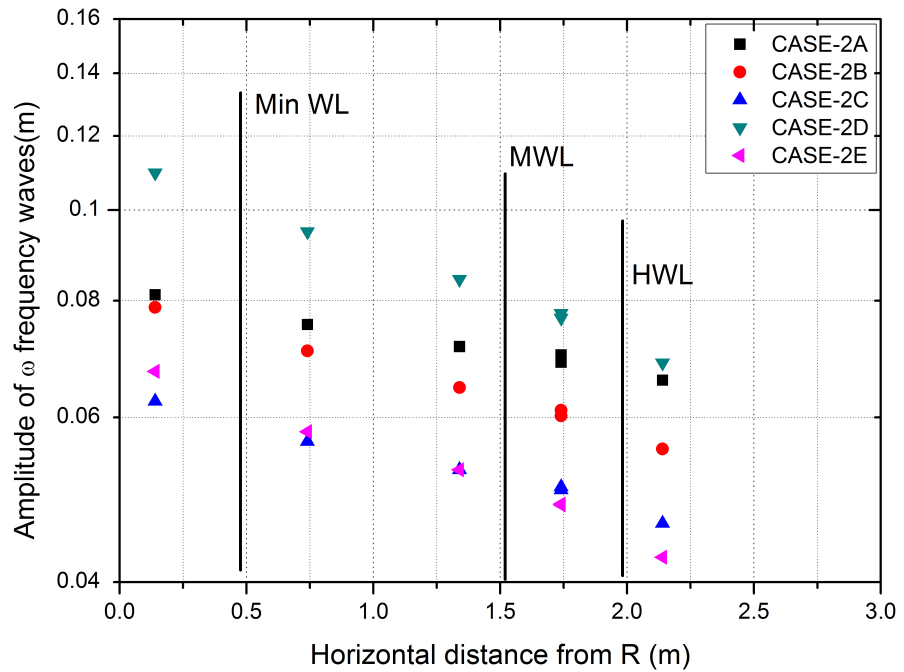


Figure 5.59: Semi-logarithmic plot of  $\omega$  harmonic amplitude calculated in frequency domain in relation to distance for CASE-2

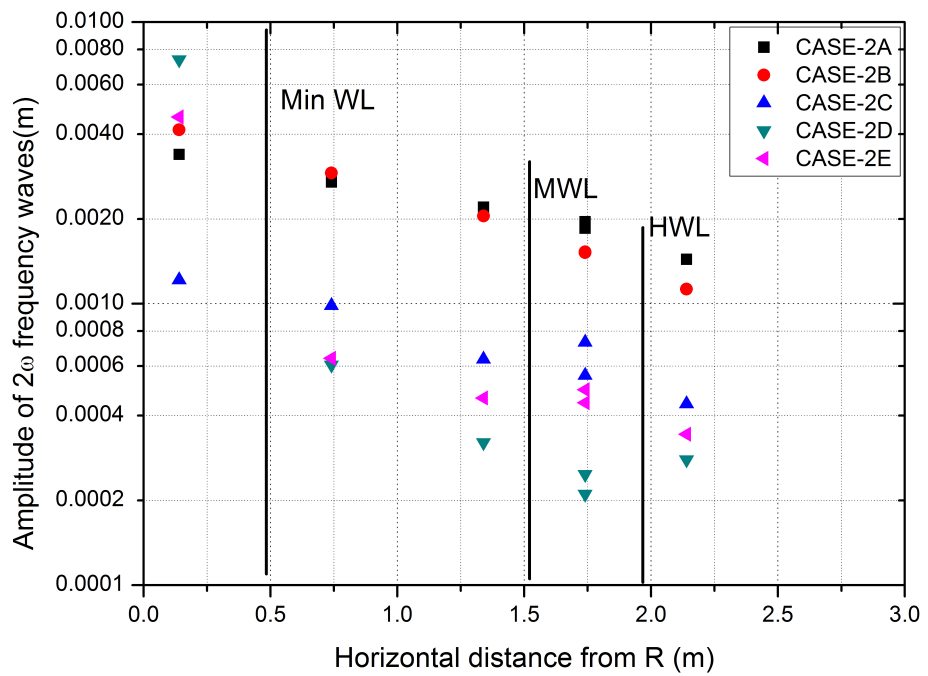


Figure 5.60: Semi-logarithmic plot of  $2\omega$  harmonic amplitude calculated in frequency domain in relation to distance for CASE-2

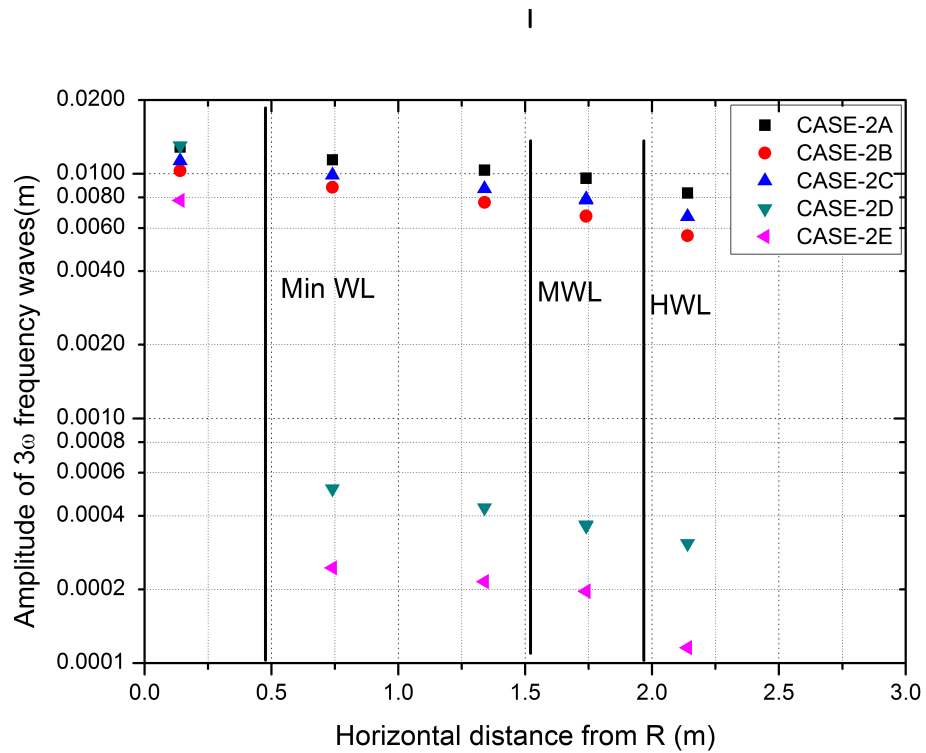


Figure 5.61: Semi-logarithmic plot of  $3\omega$  harmonic amplitude calculated in frequency domain in relation to distance for CASE-2

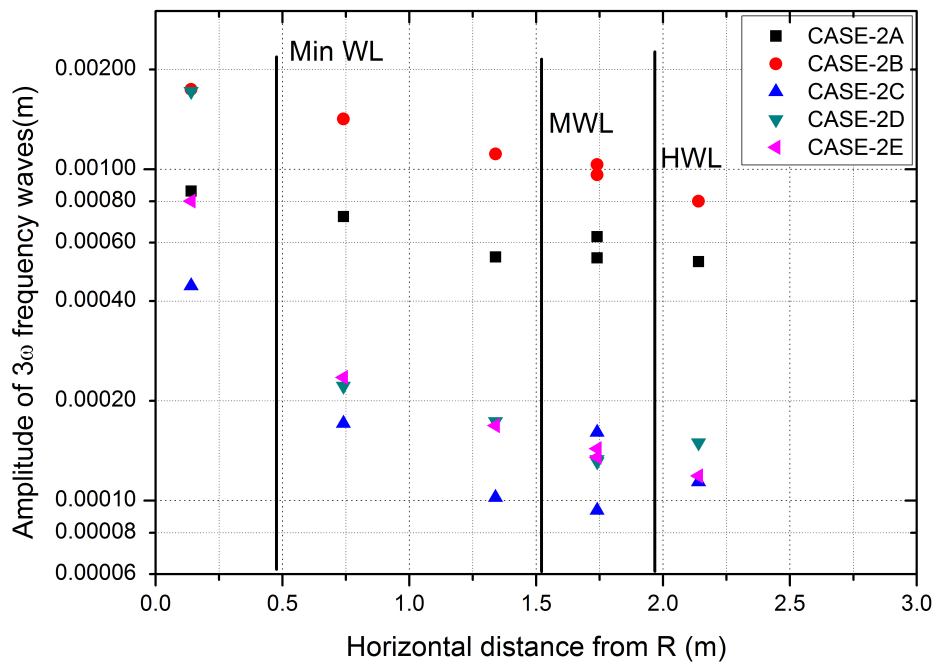


Figure 5.62: Semi-logarithmic plot of  $4\omega$  harmonic amplitude calculated in frequency domain in relation to distance for CASE-2

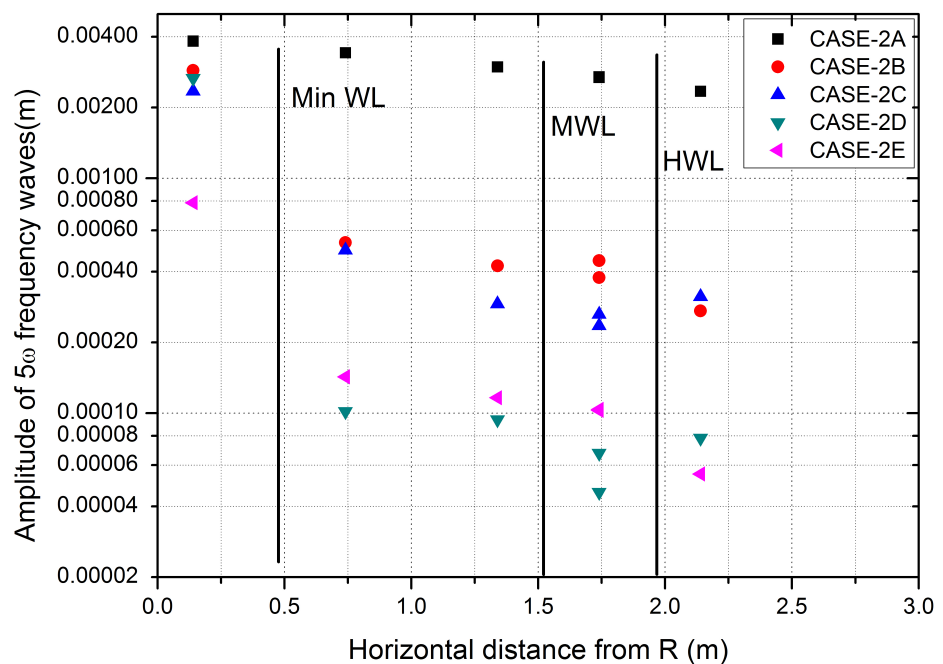


Figure 5.63: Semi-logarithmic plot of  $5\omega$  harmonic amplitude calculated in frequency domain in relation to distance for CASE-2

### 5.3.4 Numerical Modeling to Estimate Hydraulic Conductivity and Porosity

Hydraulic conductivity and porosity of aquifer are important parameters. They are measured in in-situ or laboratory experiments. In this study, the groundwater waves data are used to determine the hydraulic conductivity and porosity by using numerical modeling for calibration of the parameters. Numerical models are run for different values of the parameters needed to minimize the error from experimental observations. The combination of parameter value corresponding to minimum error is the parameter value of the experimental setup. For CASE-1 experiments CASE-1A to CASE-1E are used for calibration. Two-dimensional vertical cross-section is used to model the experimental domain (Figure 5.64). Mesh convergence study was performed before fixing the optimum number of triangular elements. The mesh consists of 70756 triangular elements. The simulation is run by using Richards equations with van Genuchten parameters 10.0 ( $1/m$ ) and 2.68 are used respectively for the scale parameter and slope parameter in the water retention curve (Carsel and Parrish, 1988). Residaul saturation value was taken as 0.1. Simulations are run for 66320 s ( $\approx 18hr$ ) to create quasi-steady state condition. The pressure data at the pressure transducer observation points are analysed in time-domain for amplitude and time-averaged mean water level to compare with the experimental data. Porosity of value of 0.38 is taken for the simulations. Initially the hydraulic conductivities of  $0.0001\ m/s$  ( $10/\ : m/day$ ) were simulated. However, the amplitudes of the waves in the aquifer were very small. Thus the hydraulic conductivity value was increased gradually for one case and finally hydraulic conductivity values of  $0.0041\ m/s$  ( $350\ m/day$ ) to  $0.0075\ m/s$  ( $650\ m/day$ ) were fixed for calibration. Mean water level and amplitude of waves at the boundary (tide) and other five pressure sensor locations of numerical simulations are compared with experimental data. Mean error of mean water level of

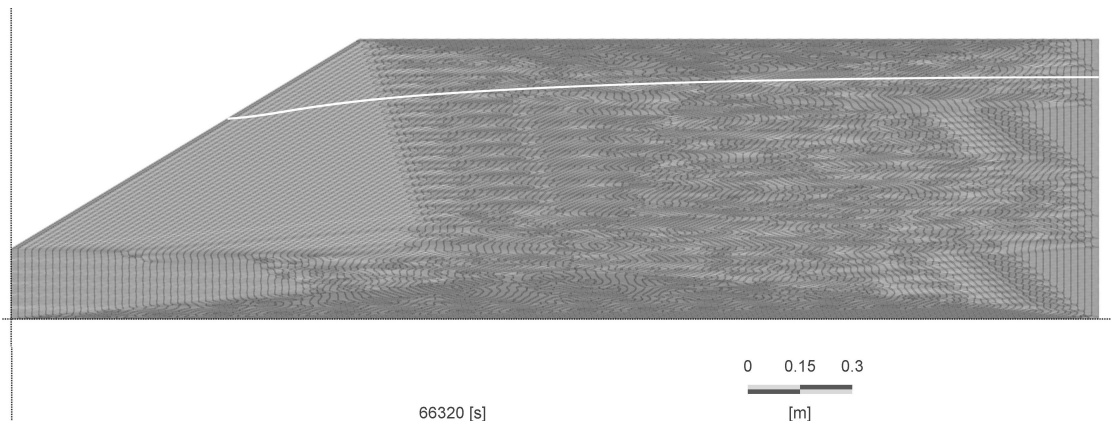


Figure 5.64: CASE-1 numerical modeling 2D-FEFLOW mesh

waves [*Mean Error* ( $h_{MeanWL}$ )] calculated as following,

$$Mean\ Error\ (h_{MeanWL}) = \frac{1}{6} \sum_{n=0}^{n=5} \left( \frac{MeanWL_{exp_n} - MeanWL_{num_n}}{MeanWL_{exp_n}} \right) 100\ \% \quad (5.100)$$

where,  $MeanWL_{exp_n}$  is time-averaged mean water level of  $PS_n$  from experiments,  $MeanWL_{num_n}$  is time-averaged mean water level of  $PS_n$  from numerical simulation and  $n$  is the incremental index with  $n = 0$  corresponds to tidal data recording point. Similarly the Mean error of amplitude ( $Mean\ Error(h_{amp})$ ) calculated as following,

$$Mean\ Error\ (h_{amp}) = \frac{1}{6} \sum_{n=0}^{n=5} \left( \frac{A_{exp_n} - amp_n}{A_{num_n}} \right) 100\ \% \quad (5.101)$$

where,  $A_{exp_n}$  and  $A_{num_n}$  are experimental amplitude and numerical amplitude at point  $PS_n$  respectively, and  $n$  is the incremental index with  $n = 0$  corresponds to tidal data recording point.

Table 5.8: Error statistics of numerical simulations with details of amplitude errors and cumulative error of mean WL and amplitude

| Hydraulic conductivity | Mean Percentage error in amplitude %    | Mean error of             |                         | Mean of error in |
|------------------------|---|---------------------------|-------------------------|------------------|
|                        |   | Amplitude for all cases % | Mean WL for all cases % |                  |
| K(m/s)                 | CASE-1B CASE-1C CASE-1D CASE-1E CASE-1F |                           |                         |                  |
| 0.0041                 | 35.02 33.27 24.99 11.29 30.68           | 27.05                     | 1.31                    | 14.18            |
| 0.0046                 | 27.62 19.72 12.56 5.51 20.21            | 17.12                     | 1.13                    | 9.12             |
| 0.0052                 | 20.18 12.31 6.27 6.40 13.60             | 11.75                     | 1.05                    | 6.40             |
| 0.0058                 | 15.90 8.43 5.07 8.06 9.96               | 9.48                      | 1.02                    | 5.25             |
| 0.0064                 | 2.20 3.89 5.17 16.69 3.30               | 6.25                      | 1.02                    | 3.63             |
| 0.0069                 | 6.75 3.02 5.56 13.52 2.36               | 6.23                      | 0.98                    | 3.61             |
| 0.0075                 | 11.41 4.66 4.59 10.48 5.65              | 7.36                      | 1.01                    | 4.18             |

Table 5.9: Error statistics of numerical simulations of amplitude errors

| Hydraulic conductivity | Mean Percentage error in amplitude for case % |         |         |         |         | Mean error of Mean WL for all cases % |
|------------------------|---|---------|---------|---------|---------|---------------------------------------|
|                        | CASE-1B                                       | CASE-1C | CASE-1D | CASE-1E | CASE-1F |                                       |
| K(m/s)                 |   |         |         |         |         |                                       |
| 0.0041                 | 1.39  | 0.76    | 0.72    | 0.61    | 3.09    | 1.31                                  |
| 0.0046                 | 1.16  | 0.57    | 0.66    | 0.59    | 2.69    | 1.13                                  |
| 0.0052                 | 1.01  | 0.55    | 0.62    | 0.59    | 2.46    | 1.05                                  |
| 0.0058                 | 0.94  | 0.61    | 0.61    | 0.58    | 2.34    | 1.02                                  |
| 0.0064                 | 0.97  | 0.84    | 0.75    | 0.57    | 1.97    | 1.02                                  |
| 0.0069                 | 0.92  | 0.76    | 0.57    | 0.58    | 2.10    | 0.98                                  |
| 0.0075                 | 0.92  | 0.69    | 0.59    | 0.58    | 2.27    | 1.01                                  |

Table 5.8 and Table 5.9 shows the error statistics of amplitude and mean water level of numerical simulation of different hydraulic conductivity values with respect to experimental data. The error percentages of amplitudes are very sensitive to the hydraulic conductivities compared to the mean water level. The larger base of mean water level compared to the amplitude is the reason. Hydraulic conductivity value of  $0.0069\text{ m/s}$  ( $600\text{ m/day}$ ) has minimum error for mean water level and amplitude when all cases as considered. Similar analysis is done for CASE-2 IS sand as well and hydraulic conductivity of  $0.0052\text{ m/s}$  ( $450\text{ m/day}$ ) was found to be the suitable hydraulic conductivity. The vaules of calibrated hydraulic conductivities are within the range of past literature available (Schincariol and Schwartz, 1990; Goswami and Clement, 2007; Abarca and Clement, 2009; Röper et al., 2015). The comparison of numerical simulation waves and experimental waves are shown in Figure 5.65.

## 5.4 Summary

This chapter presented the following: analytical solutions for groundwater waves in response to tidal forcing, experimental study of tidal influence in a laboratory setup and data analysis. Analytical solutions were derived for vertical beach face and sloping beach face by using Boussinesq equation as the governing equation. Homotopy perturbation method (HPM) which uses virtual perturbation parameter was used to derive the solutions. Homotopy solutions are more accurate for steeper slopes. Later, analytical solutions were derived using higher-order Boussinesq equation. Higher-order Boussinesq equation captures vertical flows better than Boussinesq equation. Groundwater waves in response to tidal waves were studied by recording groundwater waves in a sand box experimental setup. The experiments were performed for slopes  $\pi/6$ (CASE-1) and  $\pi/12$ (CASE-2) by using coarse sand available commercially and IS sand of grade II (IS 650 : 1991) respectively. The amplitudes were attenuating exponentially with distance from the seaside boundary as in Cartwright et al. (2004). Odd harmonics were more significant than even harmonics in the frequency domain analysis. Finally, experimental data were used to estimate hydraulic conductivity of the aquifer by numerical calibration.

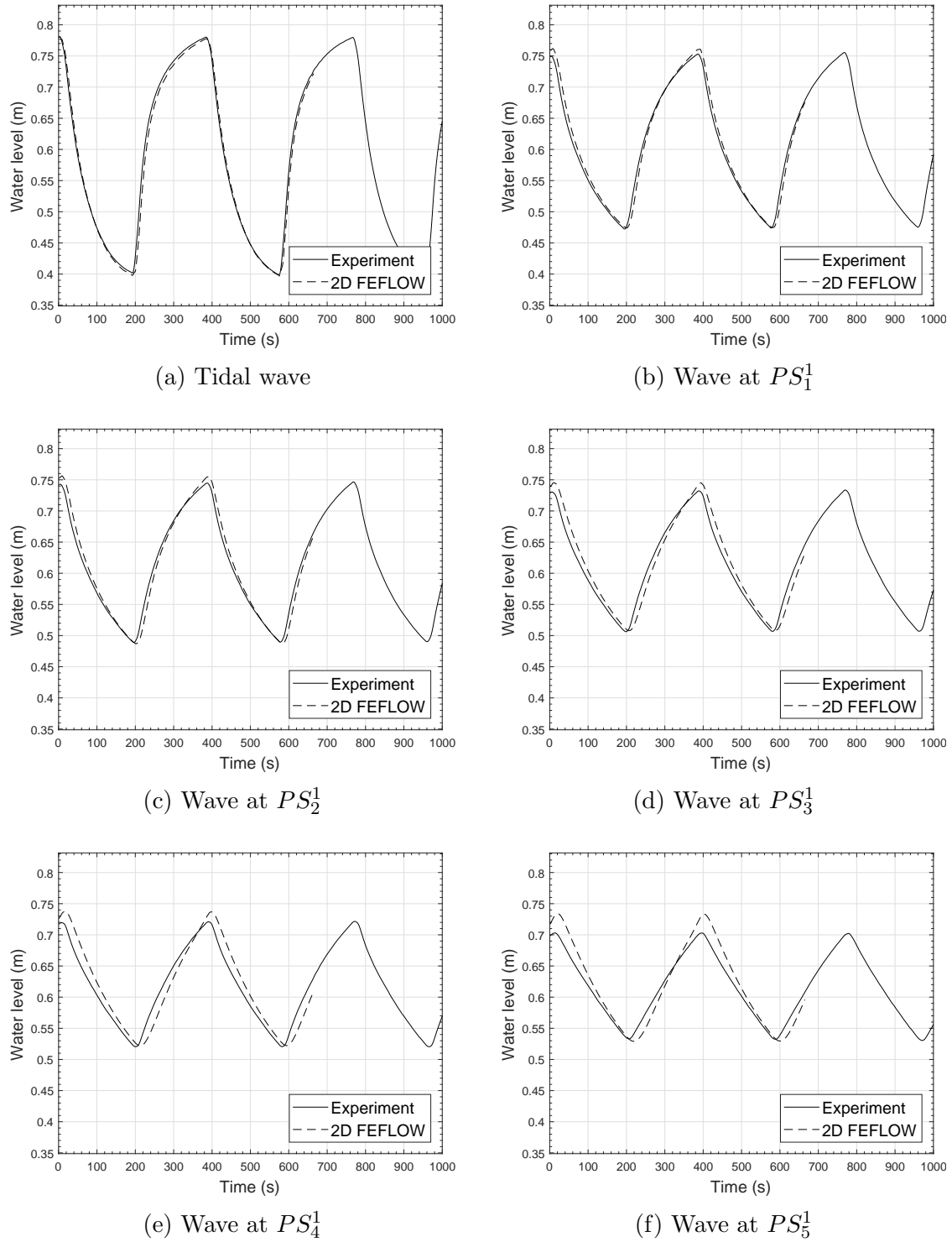


Figure 5.65: CASE-1B: Comparison of groundwater waves of experimental observation and 2D-FEFLOW model results of hydraulic conductivity  $0.0069 \text{ m/s}$  ( $600 \text{ m/day}$ )



# Chapter 6

## Tidal Dynamics with Density Effects

### 6.1 Overview

This chapter presents the laboratory scale experiments on saltwater intrusion under tidal boundary conditions. The experiments were performed for two kinds of sands mentioned in the Chapter 5 [coarse sand and IS sand-Grade II (Bureau of Indian Standards, 2007)] and two different slopes ( $\pi/6$  and  $\pi/12$ ). Colour dyes were used to delineate the saltwater zone and the freshwater zone. The experiments were recorded with sequential photographs for the analysis. Image analysis of sequential photographs was used to study the movement of the saltwater front and plumes. Pressure transducer reading recorded at multiple locations are used to calibrate the parameters and validate the model. Numerical simulations are done to study the saltwater intrusion for the boundary condition used for the laboratory experiments. Apart from saltwater intrusion, contaminant transport pathway was also studied by injecting different color contaminant with neutral density.

### 6.2 Experiments on Saltwater Intrusion

#### 6.2.1 Experimental Procedure

The experiments were performed in the sandbox experimental setup described in the previous chapter. The procedure of sand packing and pressure sensor calibration procedures were the same. However, boundary conditions enforced for this saltwater experiments were different. The freshwater reservoir in the right-hand side (Figure 4.1) was supplied with a constant flux of freshwater through peristaltic pumps to create freshwater flux from inland boundary to seaside boundary. On the seaside boundary condition, a saltwater solution prepared by mixing commercial salt (food grade), with the tap water and dye was filled in the saltwater reservoir

and water column connected to it to generate tidal waves. There were several dyes used in trial experiments on a small sandbox experimental setup to select the suitable dye. Few photographs of the dye testing for Red food dye from Neoteric DCBA Ideas (Figure 6.1), Red food dye from Colourmist Aroma, Bakersville India Pltd (Figure 6.2), and Rhodamine B type from Lobachemie (Figure 6.4) are shown in figures. Apart from the above dyes, potassium permanganate ( $KMnO_4$ ), Malachite Green from Loba chemicals, and Fluorescein Sodium from Loba Chemicals were also tested. Finally, Rhodamine was selected for the brightness that provided. The Rhodamine B type dye was added at the ratio of 2500 mg for 20 liters of water (125 mg/l). The ratio of dye was decided after several trials. The saltwater solution was prepared by mixing required commercial salt (NaCl) and then the dye was mixed with the resulting solution. CTD Divers used to monitor the saltwater concentration were calibrated (Figure 6.4) for different concentrations of salt solution. More details on the experiments explained in the following sections.



Figure 6.1: Red food dye from Neoteric DCBA Ideas

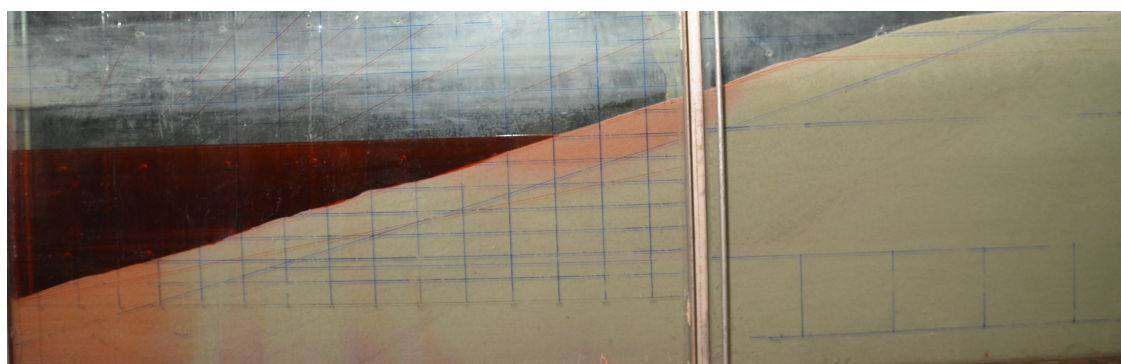


Figure 6.2: Red food dye from Colourmist Aroma, Bakersville India Pltd



Figure 6.3: Rhodamine B type from Lobachemie

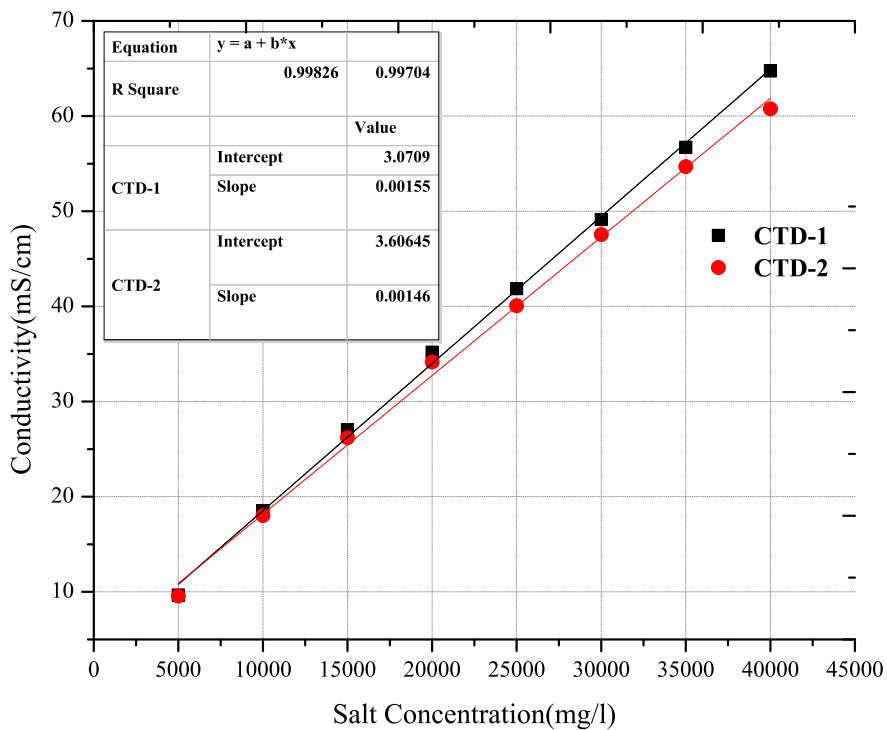
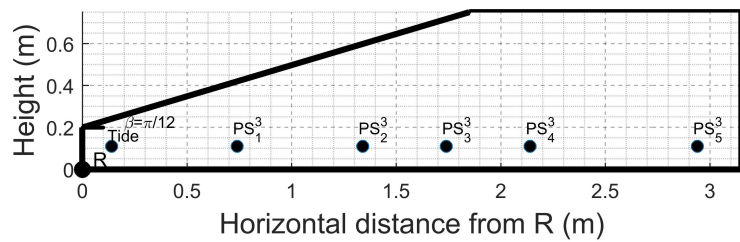


Figure 6.4: CTD Divers calibration

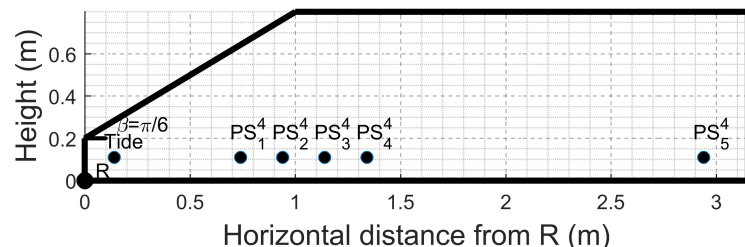
### 6.2.2 Saltwater Intrusion Experiment Details

The wet packing mentioned in the CASE-1 and CASE-2 experiments was used to configure the aquifer in the sandbox experimental setup. The coarse sand was relatively uniform with a median diameter of  $d_{50} = 1.02\text{mm}$ , and the uniformity coefficient is 1.4 (based on the sieve analysis). The dimensions of the physical models and the locations of the pressure transducers are shown in Figure 6.5. All pressure transducers were placed inside the aquifer portion, and last pressure transducer  $PS_5^3$  (Pressure sensor 5 for CASE-3) was located at the most inland point of the aquifer to record the head created by the freshwater flux. Discharge from the peristaltic pump creates the freshwater flux in the right-hand side boundary (inland boundary). Aquifer depth was reduced to 0.75 m for this experiment to reduce the sloping portion of the aquifer occupying the larger part of the experimental setup. This was done to avoid the higher tidal level point is being very close to the inland boundary. Pressure transducer calibrations were done following the same procedure as in previous cases (CASE-1 and CASE-2). Potable tap water was used as the freshwater. Initially, the aquifer was saturated with the potable tap water up to the height of 0.64 m from aquifer bottom. The outflow valve at the height of 0.64 m from the bottom of the aquifer was used to maintain the higher tidal

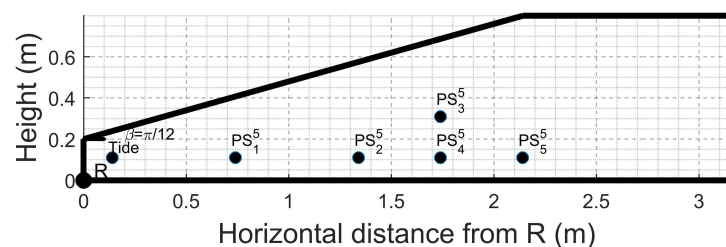
level by keeping it in a fully open condition. The saltwater solution was prepared in 20 liters batches by mixing 40000  $mg/l$  with the tap water and 0.125  $mg/l$  of Rhodamine B type dye (Loba Chemie Private Ltd). Generally, the salt concentration in the seawater is 35000  $mg/l$ . However, due to the freshwater component of submarine groundwater discharge (SGD) in laboratory experiment, some dilution happens at the seaside boundary. Hence, 5000  $mg/l$  of salt added additionally. The density of the saltwater was measured using mass to volume ratio, and also CTD divers were used to monitor the saltwater concentration during the experiments. Two CTD divers were used for this purpose. One CTD Diver was placed inside the water column used to generate waves, and another was placed inside the saltwater reservoir of the sandbox setup. The conductivity values were recorded for every 15 s. The fresh water was supplied to the freshwater reservoir (20 liters bucket) by a peristaltic pump via a silastic tube of 7 mm internal diameter. Similarly saltwater also supplied to the water column from a saltwater reservoir (20 liters bucket). Some trial experiments were done earlier, and it was observed that the concentration of the saltwater side was gradually reducing. Saltwater is supplied continuously to the water column to prevent the decrease in saltwater conductivity. The saltwater is supplied to the water column so that the process of wave generation would allow the homogenous mixing of the solution.



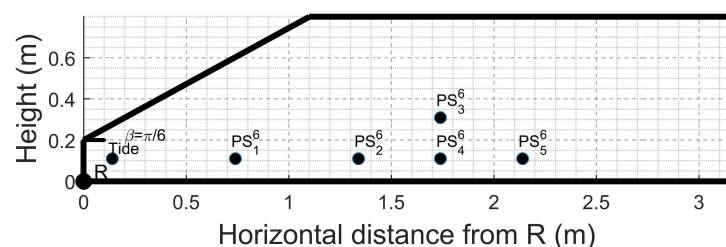
(a) CASE-3: Schematic of the coastal aquifer modeled in the experimental setup. Aquifer model of beach slope  $\pi/12$  made using coarse sand



(b) CASE-4: Schematic of the coastal aquifer modeled in the experimental setup. Aquifer model of beach slope  $\pi/6$  made using coarse sand



(c) CASE-5: Schematic of the coastal aquifer modeled in the experimental setup. Aquifer model of beach slope  $\pi/12$  made using Grade II IS sand



(d) CASE-6: Schematic of the coastal aquifer modeled in the experimental setup. Aquifer model of beach slope  $\pi/6$  made using Grade II IS sand

Figure 6.5: Aquifer configuration details of saltwater intrusion experiments

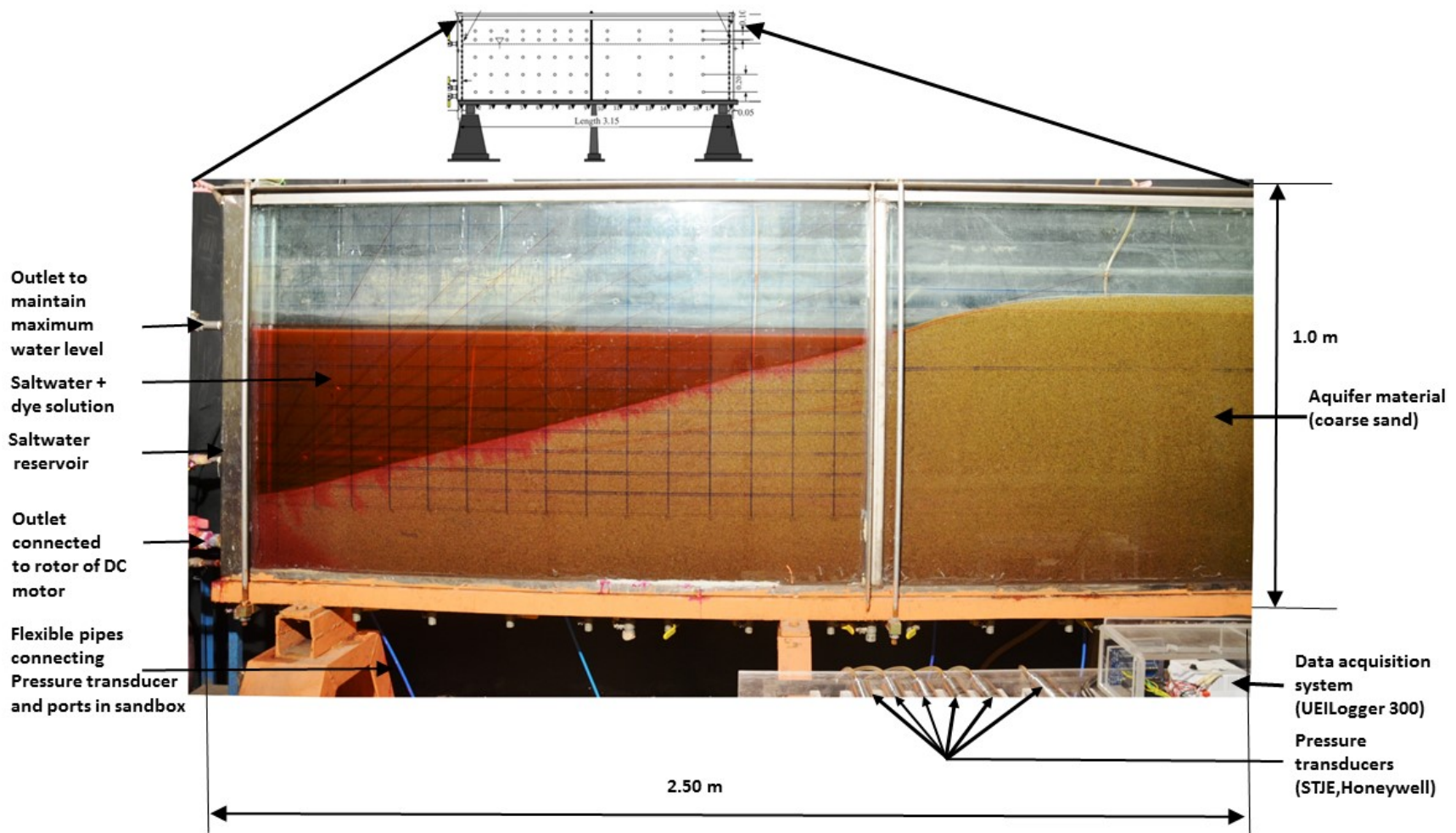


Figure 6.6: CASE-3: Digital photograph detailing the test section of the sandbox model

The saltwater intrusion process in the aquifer was photographed to record the saltwater front from the freshwater region based on the dye tracers (Figure 6.6). The rectangular grid (0.1 m horizontal to 0.05 m vertical rectangles) imprinted on the front side surface was used to get reference frame for fixing the camera covering the frame. Four points on the grid were used as the static reference points to fix the camera. Grids are important to maintain the scale and orientation of the images in a unique reference frame. Two Halogen Lights of 1000 Watt power from SUNGUN photographic products were placed in the front side of the experimental setup to ensure the homogeneity of the light during the experiment. A Digital single-lens reflex (DSLR) camera from Nikon (Nikon D5100) was installed on the fixed tripod carefully to maintain the frame. The feature available to trigger the camera to record images on a fixed time intervals was used to record automatic images for fixed intervals.

All of the following processes were done before starting the wave generation process: i) Preparation of the saltwater solution, and filling the water column. Water column valves were kept in closed condition. ii) The aquifer was saturated up to the height of 0.64 *m* with freshwater. The peristaltic pump in the inland boundary was started to supply required freshwater flux. The outlet valve at 0.64 *m* height was kept open to maintain the water level. iii) Pressure transducers were connected and calibrated. The procedure explained below is corresponding to CASE-3. The pressure data recording was started just before the wave generation started. iv) The camera was fixed along with the lighting arrangements. After all of these were done, the wave generation process was started, and the camera image recording process also started at the same moment. The peristaltic pump at the inland flux boundary was fixed as 100 RPM initially, and the peristaltic pump connected to the saltwater column was fixed at 120 RPM (6.00 *m/d*). The wave generation set up was fixed with clockwise and anti-clockwise rotation times fixed at 240 s each, and the resting period was fixed as 60 s (The wave time period would be approximately 600 s). The DC motor rotation was set at 150 RPM. The experiment was run for 8400 s (2 hours and 20 minutes) with the above boundary condition, and the photographs were recorded. However, the upper saline plume (Kuan et al., 2012) was very thin with these boundary conditions. The upper saline plume areal extent was small due to very high freshwater flux. Hence, the freshwater flux was reduced to 50 RPM (3.00 *m/d*) at 8400 s, and correspondingly saltwater supplying peristaltic pump speed also reduced to 70 RPM. The experiment was continued for a total 24000 s (6 hours). The concentration of saltwater recorded at the seaside boundary was maintained around 35000 *mg/l* after initial time fluctuation to due to mixing of freshwater in the sandbox (Figure 6.8). The pressure data were recorded

and analysed in the later parts.

The analysis of the experiment is done in two parts. First part is the time from zero s to 8400 s when the freshwater flux was  $6.00\text{ m/d}$ . Next part was from 8400 s to 24000 s when the freshwater flux was  $3.00\text{ m/d}$ . The analyses consist of numerical simulation using the finite element method subsurface model FEFLOW (Diersch, 2013), image analyses using the photographs taken during the experiments, and the pressure data recorded in the experiments.

### 6.2.2.1 Image Analyses

The image analysis techniques emerged as a measurement technique for tracer and contaminant transport experiments. The analysis of images for solute or contaminant transport was studied extensively by many researchers in the past (Catania et al., 2008; Jaeger et al., 2009; Oates and Harvey, 2006; sa Olsson and Grathwohl, 2007; Werth et al., 2010; Zinn et al., 2004). However, all of them followed very complex methodologies. Present work tried a simplified methodology to identify the saltwater-freshwater interface. The movement of the saltwater front was analysed by image analysis of the digital photographs taken. The photographs cover a certain area of the sandbox model. This area was managed to be the same for all photographs by fixing the same reference frame. In RGB mode photographs, the colours are mixtures of following three channels: red(R), green(G), and blue(B) (Aeby et al., 1997). The colour humans realise in the vision is a mixture of energies in the wavelengths of the visible spectrum. Hence, the colour is considered as a vector of three columns with columns representing red, green, and blue. The digital photographs taken in the experiments are a collection of pixels, and each pixel has own values of the red channel, the green channel, and the blue channel. Hence, each pixel has three colour coordinates. MATLAB<sup>TM</sup> was used to analyse the image data. The values of RGB channels are in the range of 0-255 (total 256 values). The third dimension always is the size of 3 with each one corresponding to red(R), green(G), and blue(B). However, each pixel has one salt concentration value. This causes multiplicity since for a pixel containing a single concentration value has three values in RGB.

To reduce this multiplicity, the photographs were studied in imtool mode in MATLAB<sup>TM</sup>, and it was observed that the area of photographs with dye parts have very low values in blue channels. However, the blue channel values of the sand portion where the dye intrusion was not visible also have low values. Hence, the blue channel can be neglected from the analysis since it did not show any significant distinction between dye intruded portion and unintruded portion. The

channels of red and green alone considered for the analyses. The dye zone (Figure 6.7b) inside the aquifer differs from non-dyed zones vary in red and green channels. The Rhodamine dye is significantly of the red color channel. Thus, by maximizing the red color channel identification of the dye zone can be performed. Hence, pixel value modification can be done to maximize the red color value while reducing the green color value. The following simplified expression can be used,

$$\overline{C_{i,j}} = D_{i,j}^R + (255 - D_{i,j}^G) \quad (6.1)$$

The steps of image analyses are illustrated in Figure 6.13. Initially, the image was cropped to the areal extent of analyses needed (Figure 6.7a). The brightness of the cropped image was adjusted in the next step (Figure 6.7b). The image was imported in MATLAB<sup>TM</sup> and the Equation 6.1 applied to get the modified pixel values. Then averaging filter was used to remove the stray pixels with noises. The resultant modified pixel values are shown in Figure 6.7c as a contour plot. The contour plot has a wide range. By trial and error, it was found that the modified values beyond a range can be fixed to zero for better delineation. This particular experiment (CASE-3) provided better result by modifying  $\overline{C_{i,j}}$  to zero. The resultant contour plot is shown in Figure 6.7d. There were two colours on the contour map. The yellow region dye region of saltwater both inside aquifer and outside aquifer portion. These zones can be delineated using the known slope line coordinates. CASE-3 experiment used brown coloured coarse river sand. Hence, the delineation was more difficult since the dye color was much closer to the brown coloured sand background. In later experiments using IS Sand (Bureau of Indian Standards, 2007), it is shown that the proposed image analyses are more effective. The coordinates of the border of yellow color region of the final contour provides the saltwater front. This contour can be obtained by MATLAB code available to find the boundary of objects in images.

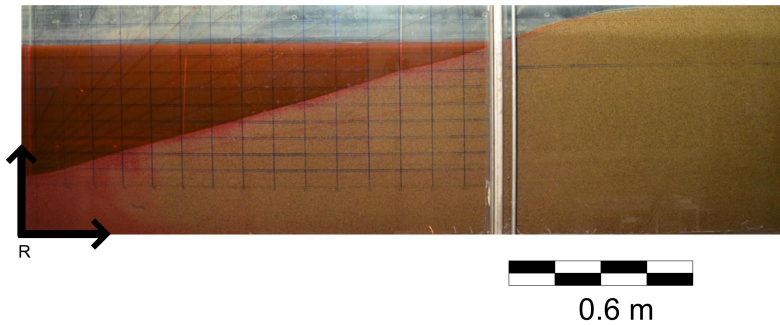
### 6.2.2.2 Numerical Modeling

Two dimensional (longitudinal–vertical) unsaturated flow model of FEFLOW was used to simulate the experiments. Richards equation (3.2.3) was used to model the variably saturated-saturated flow. FEFLOW model runs the coupled flow and transport model. The flow equation is coupled with the transport equation by the relationship between density and concentration. The numerical models were run for transient problems with full upwinding to handle the numerical dispersion due to high complexity in the coupled model. The model domain used to FEFLOW

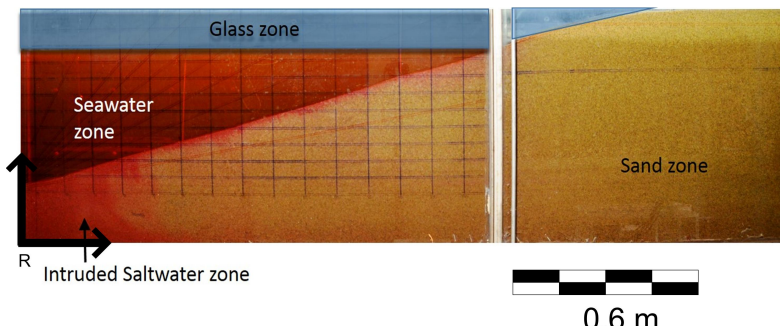
model for CASE-3 is shown in Figure 6.15 with saltwater contours corresponding to 25%, 50%, and 75% contour values. The white line in the figure indicates the zero pressure isoline corresponding to the water table.

The 50% salt concentration contour (Figure 6.13e and Figure 6.13f) shown in solid black line is matched to the toe location, the point in which the saltwater intrusion is maximum distance from the seaside boundary, of the image analysis saltwater wedge. The hydraulic conductivity was calibrated by comparing the pressure transducer data with the numerical simulation results, and the hydraulic conductivity corresponding to minimum error is chosen. The boundary conditions used for the FEFLOW model are shown in Figure 6.14. Unsaturated hydraulic conductivity was modeled by using van Genuchten model where  $10.00(1/m)$  and 2.68 were used respectively for the scale parameter and slope parameter in the water retention curve. A fine mesh up to 256013 elements was used for grid convergence study. The maximum element face size in both horizontal and vertical directions was less than 0.3 cm in the fine mesh made nearby seaside boundary. The saltwater boundary was given as time series of the equivalent freshwater head as a Dirichlet boundary condition at each saltwater boundary node (Diersch, 2009).

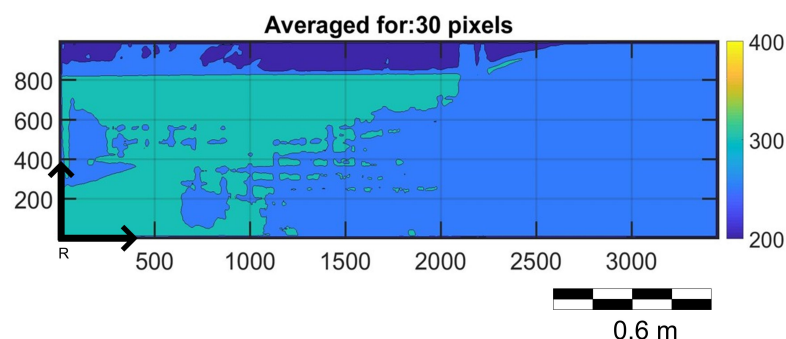
Similarly, for mass transport Dirichlet type mass concentration boundary was enforced. The transient concentration data from the CTD Diver was applied as a time series at the seaside boundary. Aquifer bottom boundary was an impervious boundary for both flow and mass transport equation. The inland boundary was a Neumann boundary condition for the flow equation with mass concentration zero for mass transport. The freshwater flux injected by the peristaltic pump was divided by the cross-sectional area to get the freshwater flux in  $LT^{-1}$  dimension.



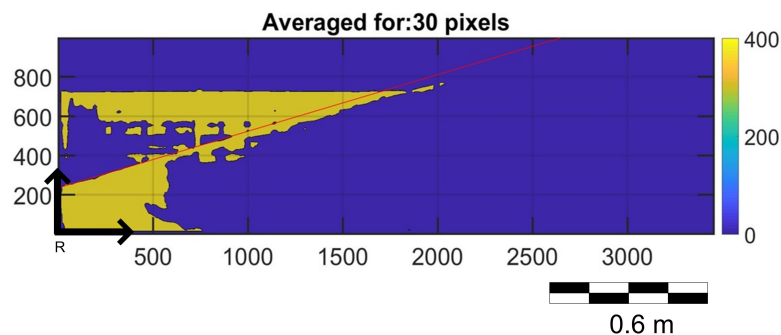
(a) Image after cropping



(b) Image after brightness adjusted and zones mentioned



(c) Plot of resultant pixel values after applying image analysis formula (Equation 6.1) and averaging filter using contour function



(d) Plot of resultant pixel values after applying image analysis formula after averaging to smoothen the image and replacing all values less than 305 to zero using contour function. This image shows the saltwater interface clearly.

Figure 6.7: Stepwise changes of image analysis of digital photograph. Figures are illustrative, not exact scales.

### 6.2.3 Results and Discussion

This section discusses the experimental results of all four cases (CASE-3, CASE-4, CASE-5, and CASE-6) of saltwater intrusion (with density effect) in different subsections.

#### 6.2.3.1 CASE-3: Coarse Sand with Beach Slope $\pi/12$

CASE-3 experiment was performed with coarse sand mentioned in the previous chapter with beach slope  $\pi/12$  (Figure 6.5a). The concentration values recorded at the saltwater reservoir are given in Figure 6.8. Initially, the saltwater entering the sandbox from the saltwater column took some time to mix with the freshwater inside the sandbox. Hence, there are oscillations in the concentration until the system stabilizes. However, the oscillation range is small values of  $5000 \text{ mg/l}$ - $1/7$ th of the maximum concentration of the saltwater in the experiment-and the mean value during the concentration oscillation happened is approximately  $32500 \text{ mg/l}$ , which was close to the maximum concentration of the experiment. Hence, this oscillation can be neglected. The tidal waves were approximately of time period 600 s. The freshwater flux from the peristaltic pump is at the rate of  $6 \text{ m/d}$  ( $6.944 \times 10^{-5} \text{ m/s}$ ) from the initial stage. This boundary condition was maintained till time 8400 s, and the saltwater front moved slowly. However, the upper saline plume was very thin (Figure 6.13a). Upper saline plume is a portion of the salt intruded portion. Upper saline plume is separated from the saltwater wedge. Freshwater discharge zone separates saltwater wedge and upper saline plume (Kuan et al., 2012). Upper saline plume has inverted saltwater concentration-the salt concentrations at the interface of aquifer and waves are higher, and the concentration gradually reduces when moving down and landwards from the beach face. Freshwater flux discharges to the seaside boundary below upper saline plume. Higher freshwater flux from the freshwater boundary must be resisting the saltwater from entering in the intertidal zone. Hence the freshwater flux was halved at time 8400 s to increase the upper saline plume extent for the experimental observation. Pressure waves of pressure data recorded from time zero s to 8400 s are shown in Figure 6.9 and Figure 6.11. The summary of time-averaged mean water level and amplitudes are shown in Figure 6.12. The experiment continued for 24000 s (six hours and 40 minutes).

The image analyses steps are detailed in Figure 6.13. Initially, the digital images captured are cropped to a fixed reference frame. Next, the image analyses based on pixel values explained in the previous section (Section 6.2.2.1) is done. Next, the resultant image is compared with numerical results. Figure 6.13 shows the image analyses result at time 7800 s for saltwater intrusion at higher water level

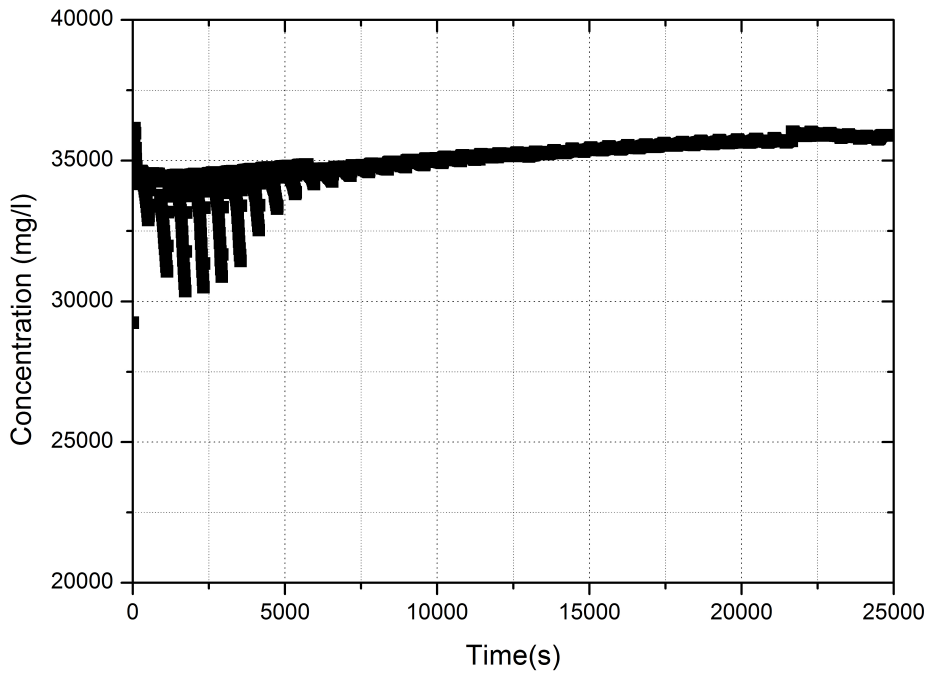


Figure 6.8: CASE-3: Concentration of saltwater recorded in CTD-Diver placed inside the saltwater reservoir.

and lower water level with a comparison of 50% saltwater contour from numerical modelling. It can be observed that the upper saline plume extent is very small. In the second portion of the experiment — after the freshwater flux reduced to  $3 \text{ m/d}$  ( $3.472 \times 10^{-5} \text{ m/s}$ ) — the saltwater wedge moves inland since the reduced freshwater flux at the inland boundary reduces the hydraulic gradient towards the seaside boundary. The upper saline plume extent also increases in landward and downward direction gradually. The freshwater is discharging from aquifer to seawater side in the zone separating upper saline plume and saltwater wedge. The image analysis resultant image at the end of the experiment shows the upper saline plume, saltwater wedge, and freshwater discharge zone (Figure 6.13f). The saltwater wedge starts below the minimum tidal level (Figure 6.13e) and extends towards the aquifer bottom. The toe location for the freshwater flux  $6 \text{ m/d}$  at 7800 s is 160 cm. However, numerical result is not showing any upper saline plume while the digital photograph shows a small zone of intrusion in the intertidal zone, when the tidal wave is at the highest water level. This cannot be considered as an upper saline plume since it vanishes in the ebbing tide.

The images of saltwater intrusion at the end of the experiment are shown in Figure 6.16. Freshwater flux boundary for these conditions was  $3 \text{ m/d}$ . Digital images at the higher tide level (Figure 6.16a and Figure 6.16b) show that the saltwater wedge gets extended more landwards and clear upper saline plume were

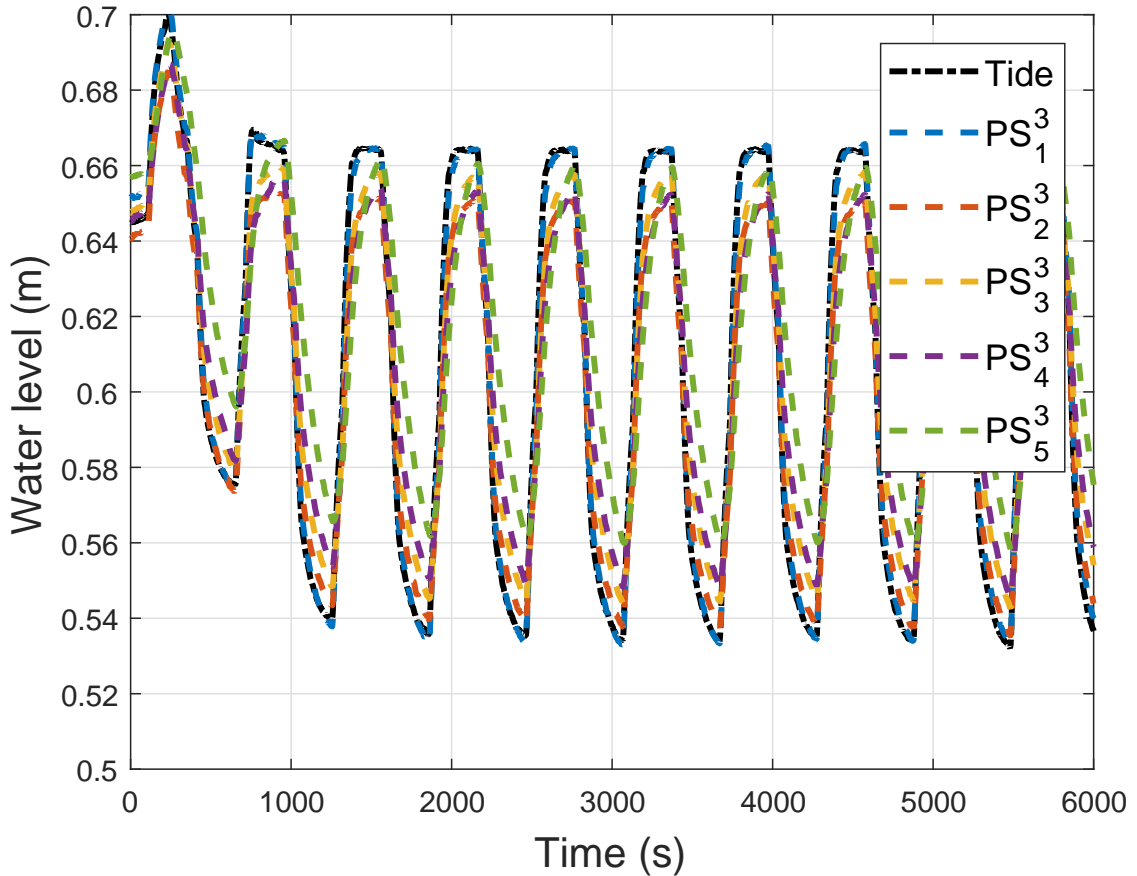


Figure 6.9: CASE-3: Pressure waves of pressure data recorded from time zero s to 8400 s. Timeperiod of the waves is 600 s

visible. The fluorescein yellow color between the upper saline plume and the saltwater wedge was a tracer injected at coordinates 2.20 m and 0.45 meter from the origin R. The tracer was injected to check the flow path of the freshwater. Analysis of the tracer movement will be discussed in later sections (Section 6.2.4). It is evident from the images that the freshwater was discharging between upper saline plume and saltwater wedge. The freshwater discharge zone was just below the intersection of lower tide level and aquifer beach face. In the rising tide, the upper saline plume extent increased and the freshwater discharge zone also intruded by saltwater. Due to wave direction change, the hydraulic gradient also rapidly changes.

The comparison of salt extent in image analysis and the 50% salt contour (0.5 isochlor) at 7800 s (Figure 6.13e and Figure 6.13f) show good match for the saltwater wedge. However, upper saline plume is nonexistent in the numerical results. Similarly, the results at the end of the experiments also in a good match (Figure 6.13e and Figure 6.13f). Upper saline plume extent of the experiment was larger since the diffusion of the dye is large. The pressure data of the experiment and the numerical modeling was compared for the time-averaged water levels and amplitudes of the waves (Figure 6.17 and Figure 6.18). Time-averaged mean water

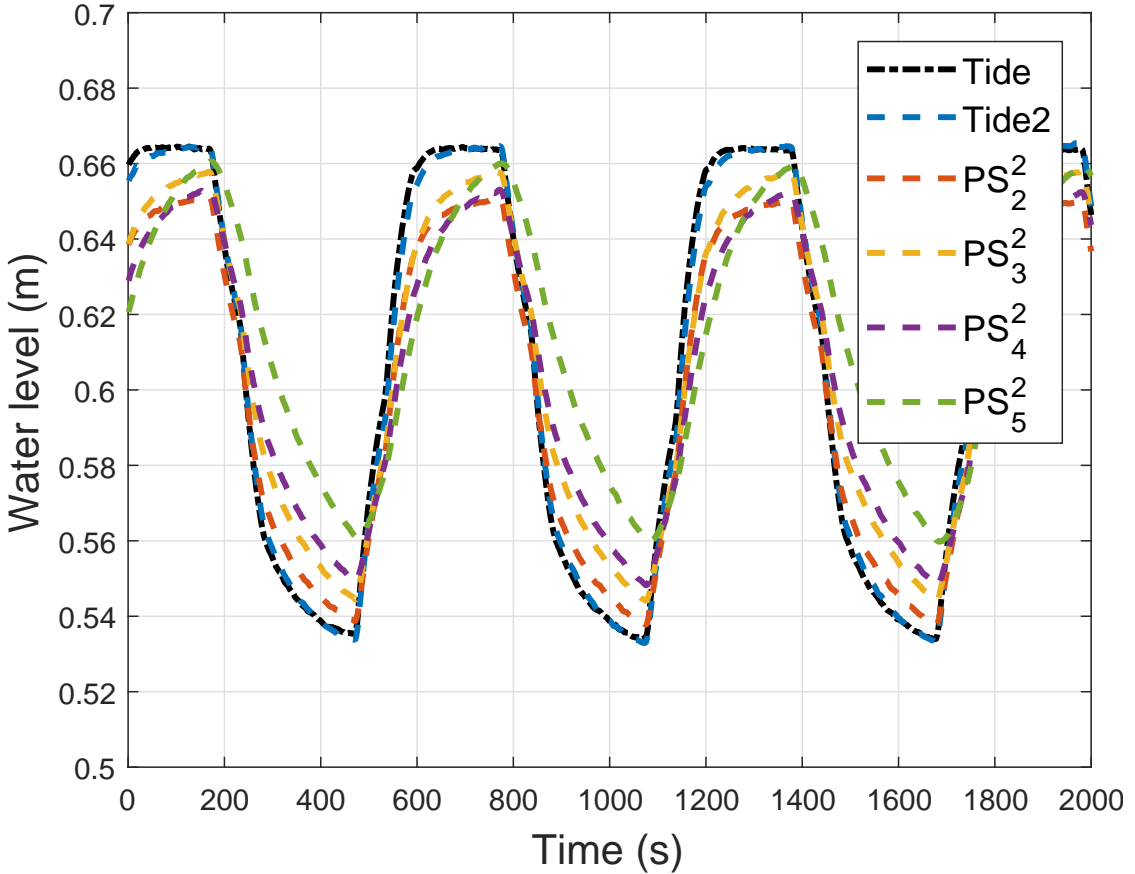


Figure 6.10: CASE-3: Pressure waves of pressure data recorded from time zero s to 8400 s (magnified). Timeperiod of the waves is 600 s

levels all are in well within in  $\pm 2\text{ cm}$  range except the pressure transducer 5 ( $PS_5^3$ ) which is located closer to the inland boundary. However, at time step 16200 s, tidal mean water level itself high for simulation. Hence, pressure sensor readings at other points have deviation more than 2 cm. Freshwater flux at the inland boundary rises the water level at the  $PS_5^3$  to show the higher mean water level.

The amplitude comparisons show that the deviation between simulated and observed are within  $\pm 1\text{ cm}$ , or just more than  $\pm 1\text{ cm}$ . However, the amplitude of the simulated tide itself on the higher side for the time 5400 s which causes the amplitudes at the other locations also deviate more than  $\pm 1\text{ cm}$  from the line indicating observed equal to simulated (the 45-degree line in the middle).  $PS_2^3$  amplitudes deviate more than 1 cm error. It is because  $PS_2^3$  located in the intertidal zone, and the numerical model did not capture the seepage face. Pressure transducer reading cannot be taken continuously since the instruments cannot run a long time due to the overheating issue. Hence, the pressure readings were recorded alternative 30 minutes or 60 minutes time period. The portions without pressure readings were filled up as a continuous cycle of the previously available pressure data for the tide. This padding of tidal wave data may have contributed to the error in amplitudes. There are other reasons like the calibration done in the hydrostatic condition while

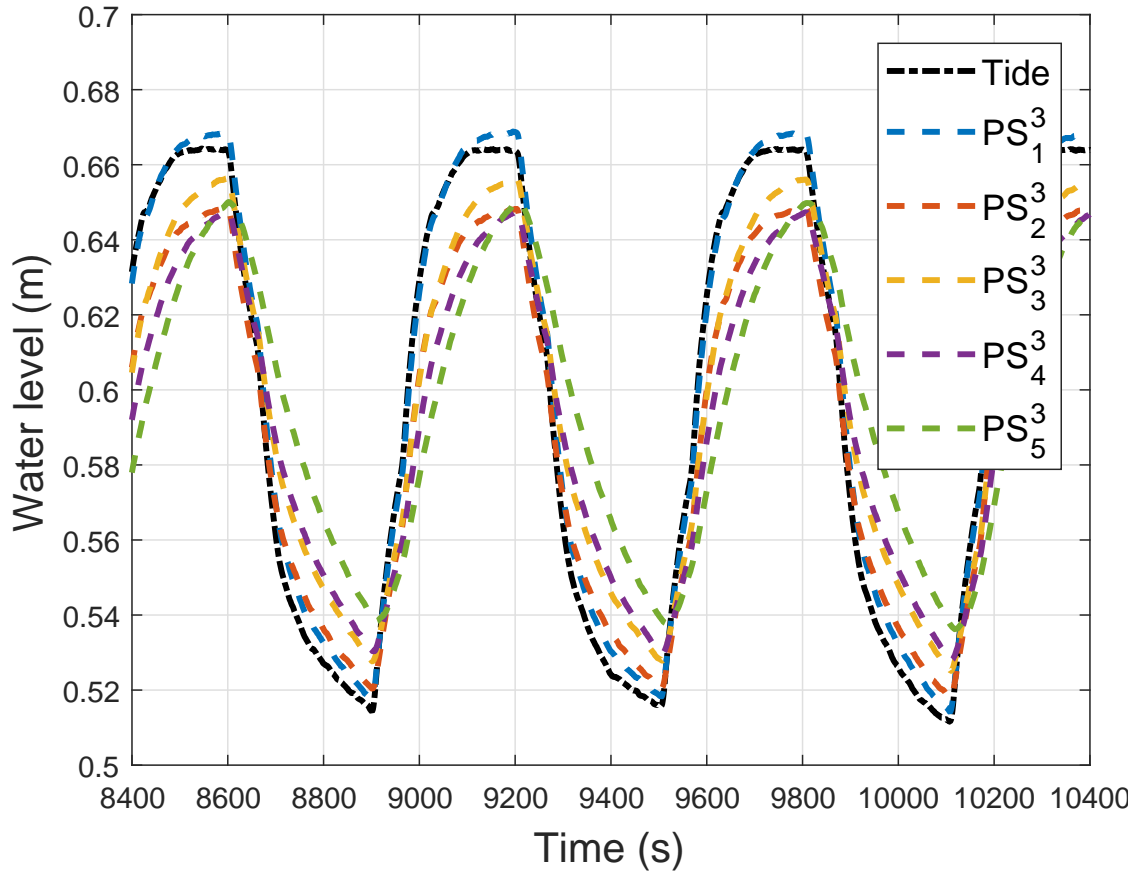
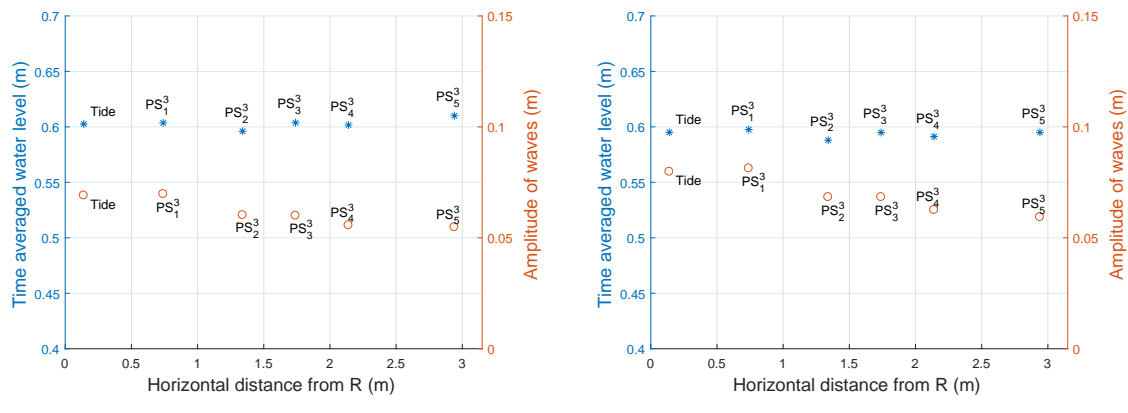


Figure 6.11: CASE-3: Pressure waves of pressure data recorded from time 8400 s to 24000 s (magnified)



(a) Time-averaged water table and amplitudes of CASE-3 from time 0 to time 8400

(b) Time-averaged water table and amplitudes of CASE-3 from time 8400 to time 24000

Figure 6.12: Summary of time-averaged water table, and amplitude of waves recorded for CASE-3

the waves are dynamic, and the minimum pressure transducer accuracy is approximately  $\pm 3.5 \text{ mm}$  in open water. However the instrument accuracy can be poorer inside the porous medium as the porosity in the porous medium is not the same as open water.

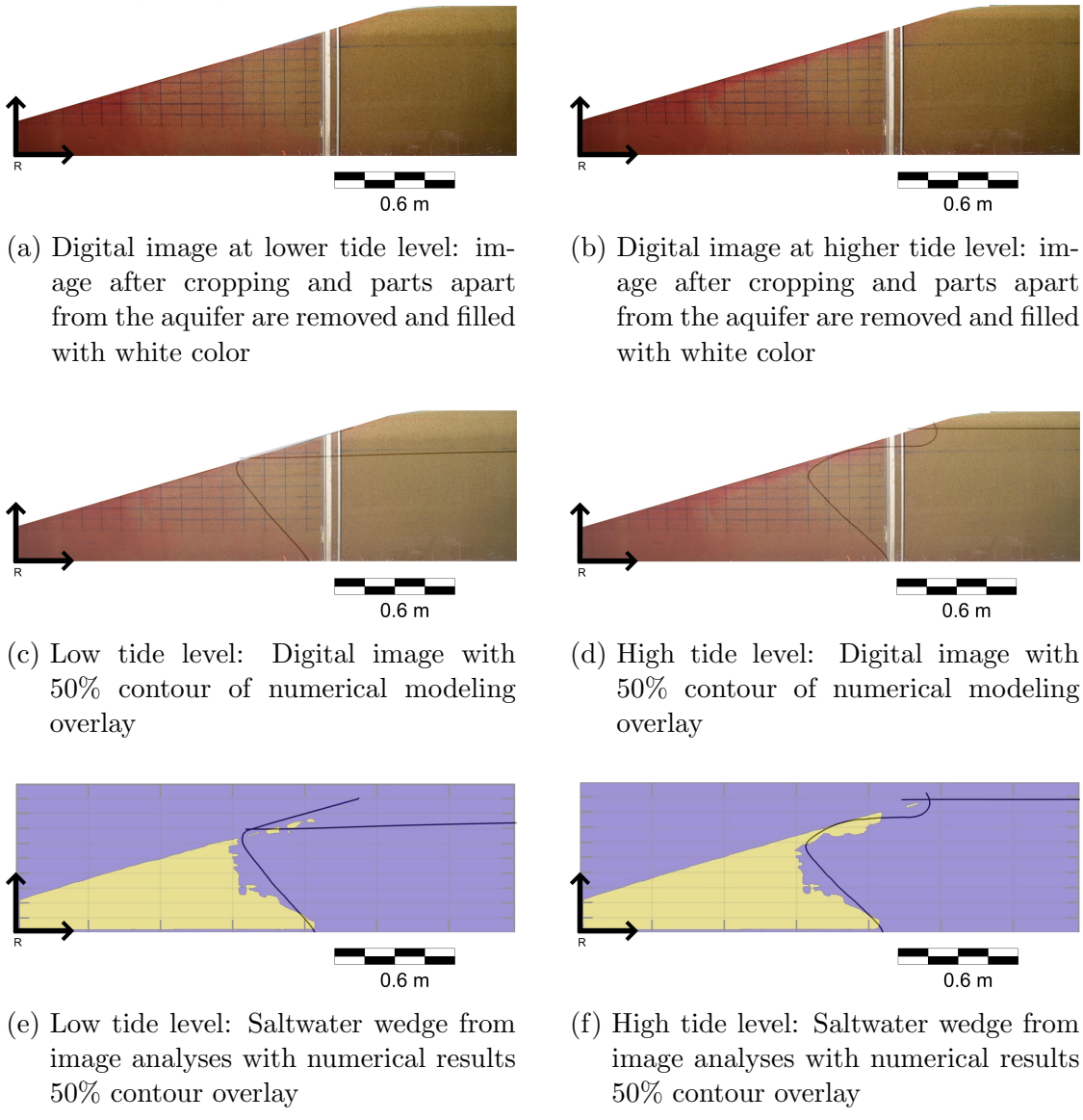


Figure 6.13: ]

CASE-3: Digital image after 2 hours 10 minutes (7800) from experiment start  
 [freshwater flux reduced to  $6.00 \text{ m/d}$  ( $6.944 \times 10^{-5} \text{ m/s}$ )]

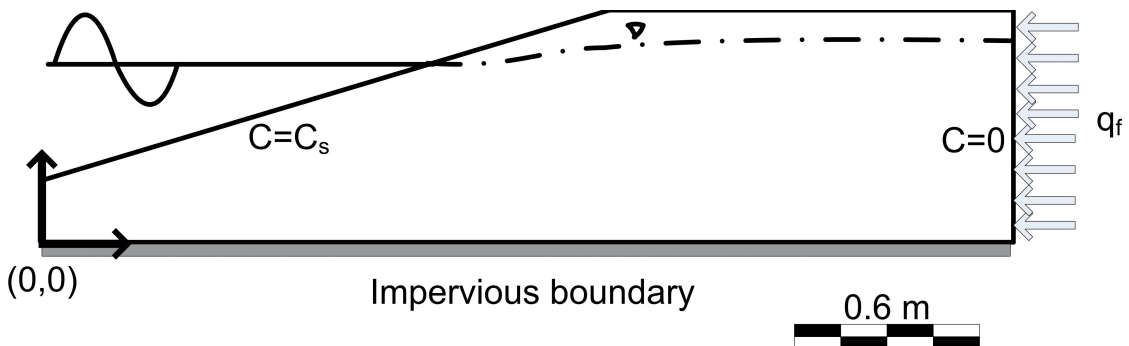


Figure 6.14: CASE-3: Boundary conditions used for FEFLOW simulation

### 6.2.3.2 CASE-4: Coarse Sand with Beach Slope $\pi/6$

Saltwater intrusion experiment of coarse sand with beach slope  $\pi/6$  was done with an aquifer height of  $0.8 \text{ m}$  (Figure 6.5b). This experiment was performed

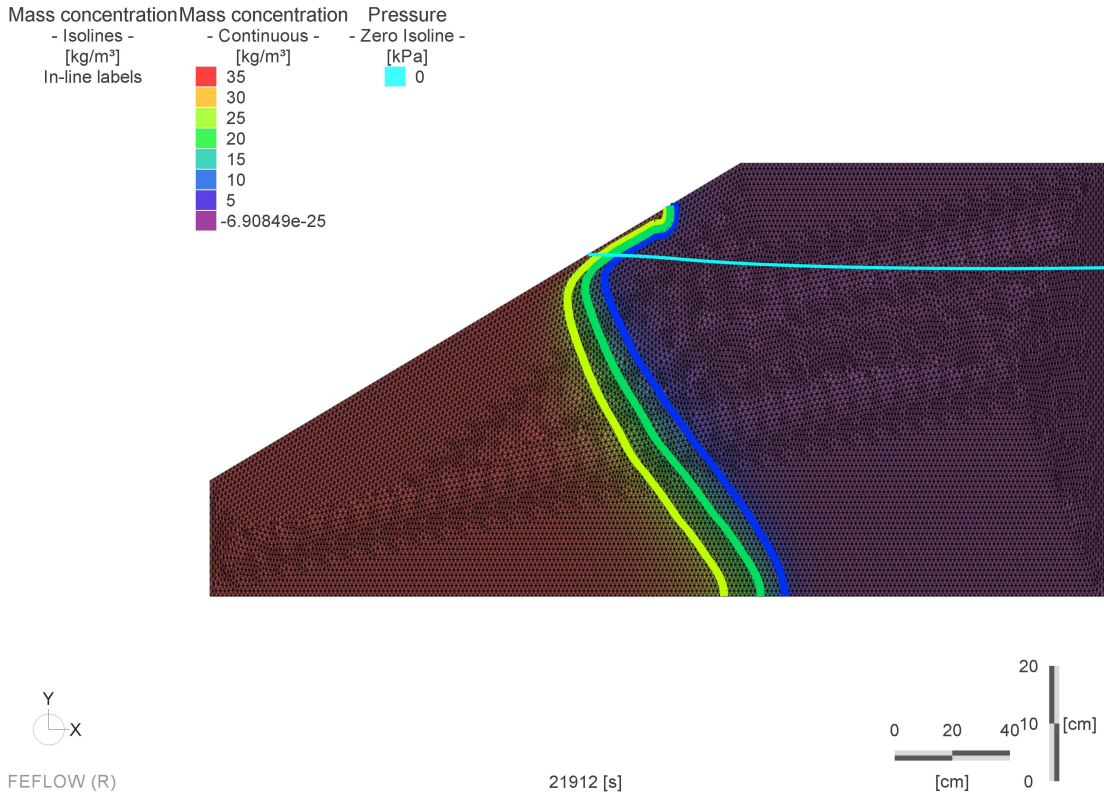


Figure 6.15: CASE-3: FEFLOW model elements with the salt concentration contours at the end of the experiment.

before the CASE-3. Freshwater flux was maintained at  $3.00m/d$  ( $3.472 \times 10^{-5}m/s$ ) for the initial portion of the experiment. The mean water level and the amplitude of the tidal wave were  $59.61\text{ cm}$  and  $11.36\text{ cm}$  respectively (Figure 6.22 and Figure 6.21). The upper saline plume was very large in the vertical direction due to higher amplitude compared to CASE-3. Upper saline plume was always extending approximately between the intertidal zone in the vertical direction (Figure 6.19). However, the toe location of the saltwater wedge was approximately  $40\text{ cm}$  from the origin R. Saltwater contour of  $50\%$  concentration matches well with the saltwater wedge. However, the upper saline plume horizontal zone was not the same as in the experimental digital photograph.

Experimental conditions were maintained for 6 hours ( $21600\text{ s}$ ). The wave conditions were changed to amplitude approximately  $7\text{ cm}$  and mean water level increased to approximately  $61\text{ cm}$ . The toe of the salt wedge moved inland to the range of  $80\text{ cm}$  to  $90\text{ cm}$  due to increased mean water level and the reduced amplitude (Figure 6.20). The upper saline plume areal extent reduced due to the reduction in the intertidal zone, and the freshwater discharge zone moved up correspondingly. The comparison of observed and numerically simulated pressure heads showed that pressure transducer close to the freshwater flux boundary ( $PS_5^4$ ) had higher simulated mean water table (Figure 6.21).  $PS_1^4$  showed a deviation of

Table 6.1: CASE-3: Parameters used for FEFLOW saltwater intrusion modeling

| Parameters                | CASE-3   |
|---------------------------|--|
| Hydraulic conductivity K  | 600 m/d  |
| Freshwater flux, $q_f$    | 6 m/d for time 0 s to 8400 s<br>3 m/d for time 8400 s to 24000 s |
| Density ratio             | 0.025  |
| Specific storage          | 0.0001 1/m   |
| Specific yield            | 0.1  |
| Mass transport porosity   | 0.38<br>Scale parameter 10.00 (1/m)                              |
| van Genuchten parameters  | Slope parameter 2.68<br>Residual saturation 0.10                 |
| Longitudinal dispersivity | 0.1 cm   |
| Transverse dispersivity   | 0.001 cm   |
| Molecular diffustion      | $1 \times 10^{-9} m^2/s$   |
| Initial hydraulic head    | 64 cm  |
| Initial concentration     | 0 kg/m <sup>3</sup>  |
| Tidal period              | 673 s  |
| Tidal amplitude           | 0.0731 m   |
| Tidal mean water level    | 0.5952 m   |

more than 2 cm for time 0 s and 14400 s. This deviation was due to the higher values of the tidal boundary mean water level imposed for these time steps. Moreover,  $PS_1^4$  lied within the intertidal zone. Hence, the numerical model's inability to capture seepage face causes the deviation.

The parameters and boundary conditions used for the experiment and numerical models are given in Table 6.2. The freshwater flux of the experiment was changed to 6 m/d in between 19200 s to 36200 s, and other parts freshwater flux was reduced to 3 m/d. Digital images clearly showed that upper saline plume extent was larger for the lower freshwater flux. This understanding is important for aquifers with seasonal variations in freshwater flux. The image analyses of the digital images gave good results. However, the brown coloured nature of coarse sand made it difficult to differentiate the color of rhodamine dye. The IS sand (Bureau of Indian Standards, 2007) is of more brighter color, and hence it would

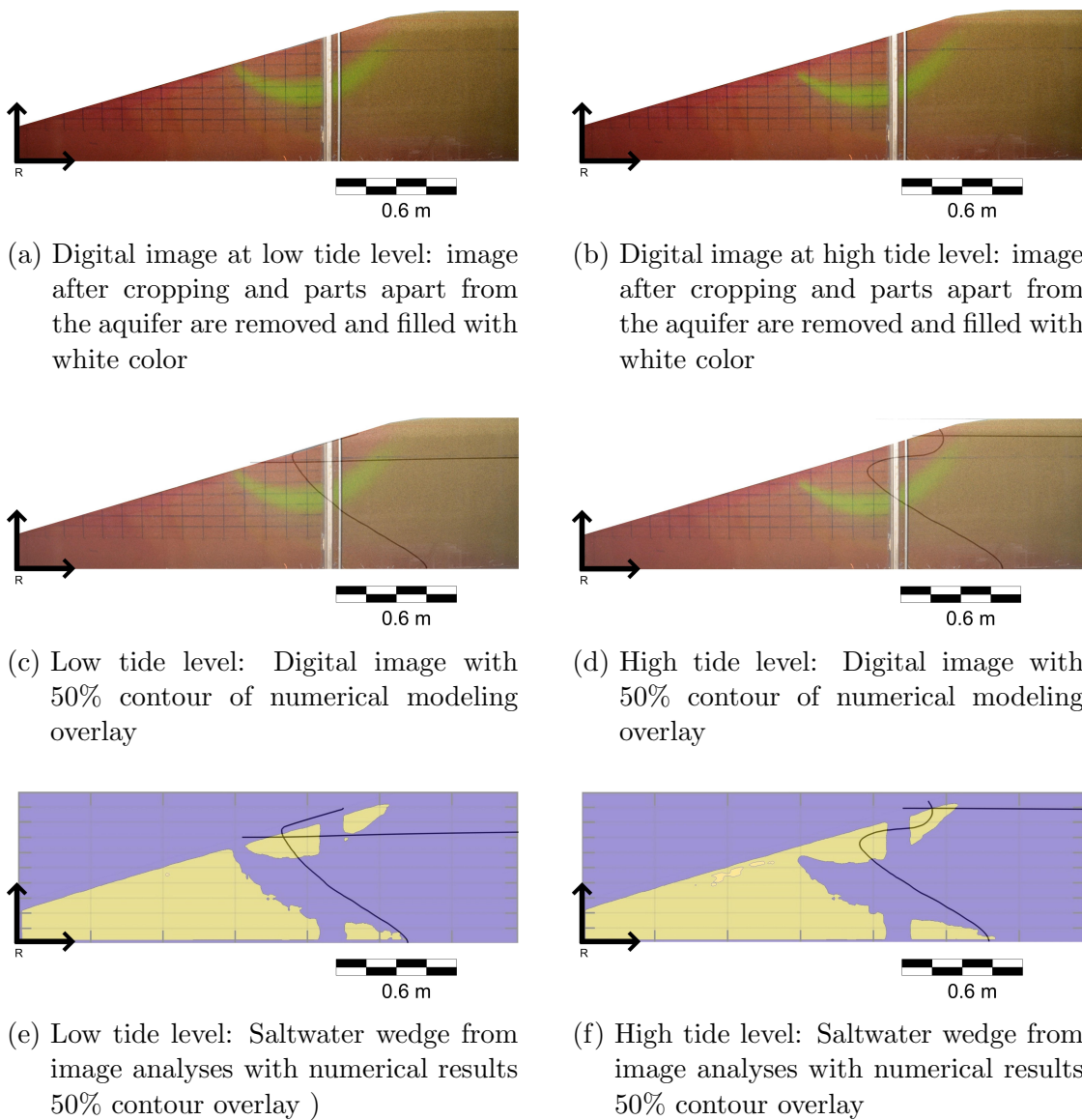


Figure 6.16: ]

CASE-3: Digital image after 6 hours (21600 s) from experiment start [4 hours and 40 minutes or 280 minutes after freshwater flux reduced to  $3.00 \text{ m/d}$  ( $3.472 \times 10^{-5} \text{ m/s}$ )]

be easier to differentiate the zones with the image analyses.

### 6.2.3.3 CASE-5: IS Sand with Beach Slope $\pi/12$

The IS sand Grade - II (Bureau of Indian Standards, 2007) was used to do experiments for different hydraulic conductivities. Moreover, IS sand is pure and very bright white color. This makes it easier for image analysis. CASE-5 experiment for saltwater intrusion was done with IS sand and slope  $\pi/12$  (Figure 6.5c). Coarse sand experiment for the same slope (CASE-3) was done for the aquifer for height  $0.75 \text{ m}$ . However, the IS sand experiment of CASE-5 performed for the aquifer of height  $0.80 \text{ m}$ . The sloping portion extended from zero to  $2.14 \text{ m}$  is higher than sloping portion of CASE-3 ( $1.84 \text{ m}$ ). All pressure transducers of CASE-5 were

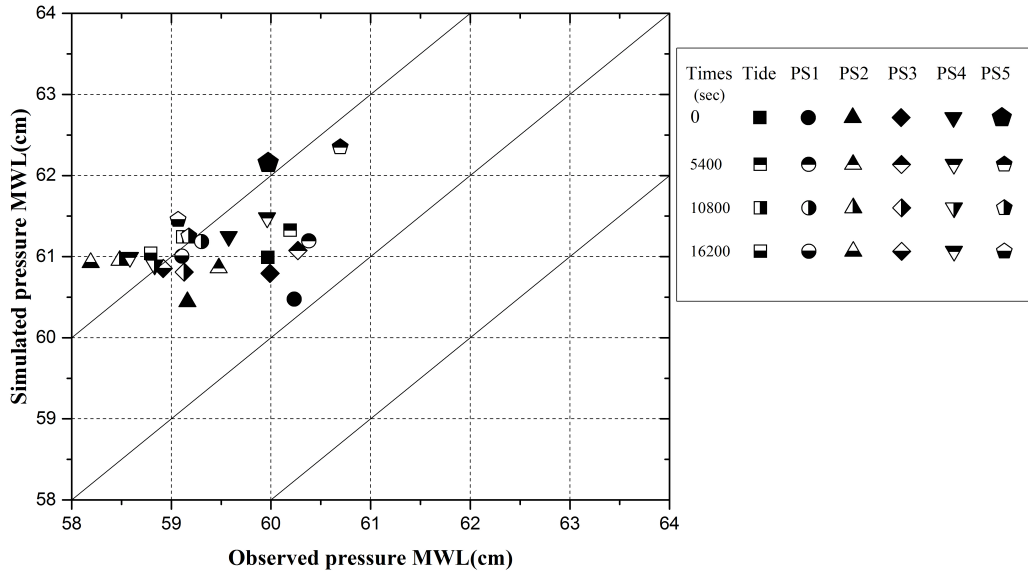


Figure 6.17: CASE-3: Comparison between the time-averaged mean water level of observed and simulated pressure head data with time

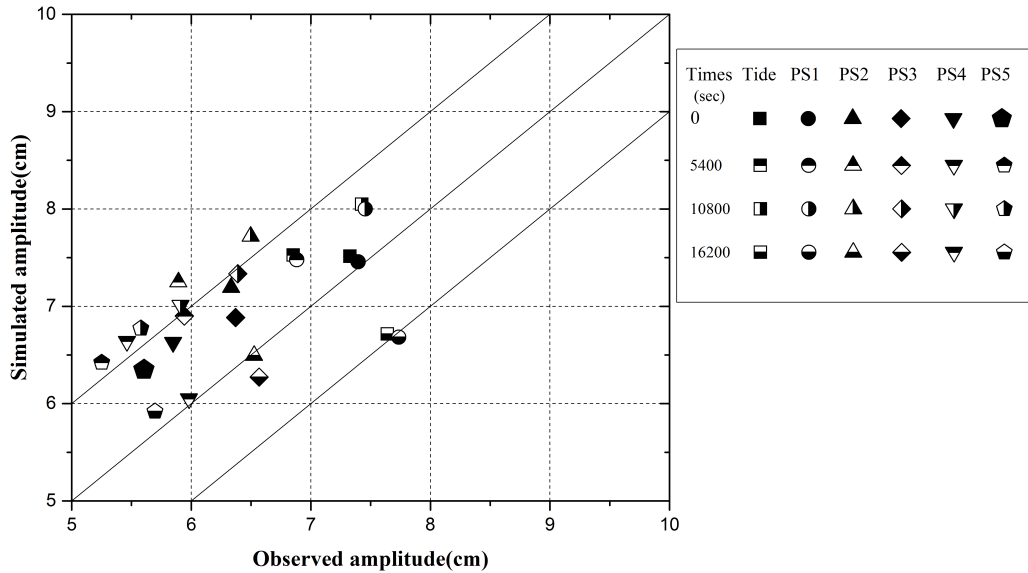


Figure 6.18: CASE-3: Comparison between the amplitudes of observed and simulated pressure head data with time

placed in the region closer to the slope. CASE-3 and CASE-4 experiments had one pressure sensor at the pressure sensor port closest to the freshwater boundary (at 2.14 m from R). Two pressure measurements of  $PS_4^5$  and  $PS_5^5$  are made at the same vertical line near to sea to observe the effects of the vertical hydraulic gradient. The experiment was performed for 12 hours with tidal mean water level was maintained at  $0.57 \pm 0.01$  m throughout (Figure 6.26). The amplitude of the tidal

Table 6.2: CASE-4: Parameters used for FEFLOW saltwater intrusion modeling

| Parameters                | CASE-4   |
|---------------------------|--|
| Hydraulic conductivity K  | 600 m/d<br>3 m/d for time 0 s to 19200 s                               |
| Freshwater flux           | 6 m/d for time 19200 s to 36200 s<br>3 m/d for time 36200 s to 43000 s |
| Density ratio             | 0.025  |
| Specific storage          | 0.0001 1/m   |
| Specific yield            | 0.1  |
| Mass transport porosity   | 0.38<br>Scale parameter 10.00 (1/m)                                    |
| van Genuchten parameters  | Slope parameter 2.68<br>Residual saturation 0.10                       |
| Longitudinal dispersivity | 0.1 cm   |
| Transverse dispersivity   | 0.001 cm   |
| Molecular diffustion      | $1 \times 10^{-9} m^2/s$   |
| Initial hydraulic head    | 64 cm  |
| Initial concentration     | 0 kg/m <sup>3</sup>  |
| Tidal period              | 300 s  |
| Tidal amplitude           | 0.1146 m from 0 s to 21600 s<br>0.0757 m from 21601 s to 43200 s       |
| Tidal mean water level    | 0.5961 m from 0 s to 21600 s<br>0.6112 m from 21601 s to 43200 s       |

wave maintained at  $0.09 \pm 0.01 m$ . Salt concentration was maintained around 35000 mg/l throughout the experiment (Figure 6.25). The points near zero concentration in Figure 6.25 were when CTD-Diver was removed from the experimental setup to verify the concentration data. The parameters and boundary conditions used for the experiment details are provided in Table 6.3.

The hydraulic conductivity of the aquifer was obtained to be  $350 m/d$  ( $4.051 \times 10^{-3} m/s$ ) based on calibration by FEFLOW simulation for different hydraulic conductivity values. The simulated and observed mean water table relation showed that  $PS_3^5$  is an outlier (Figure 6.26). The pressure sensor was located at  $0.31 m$  from

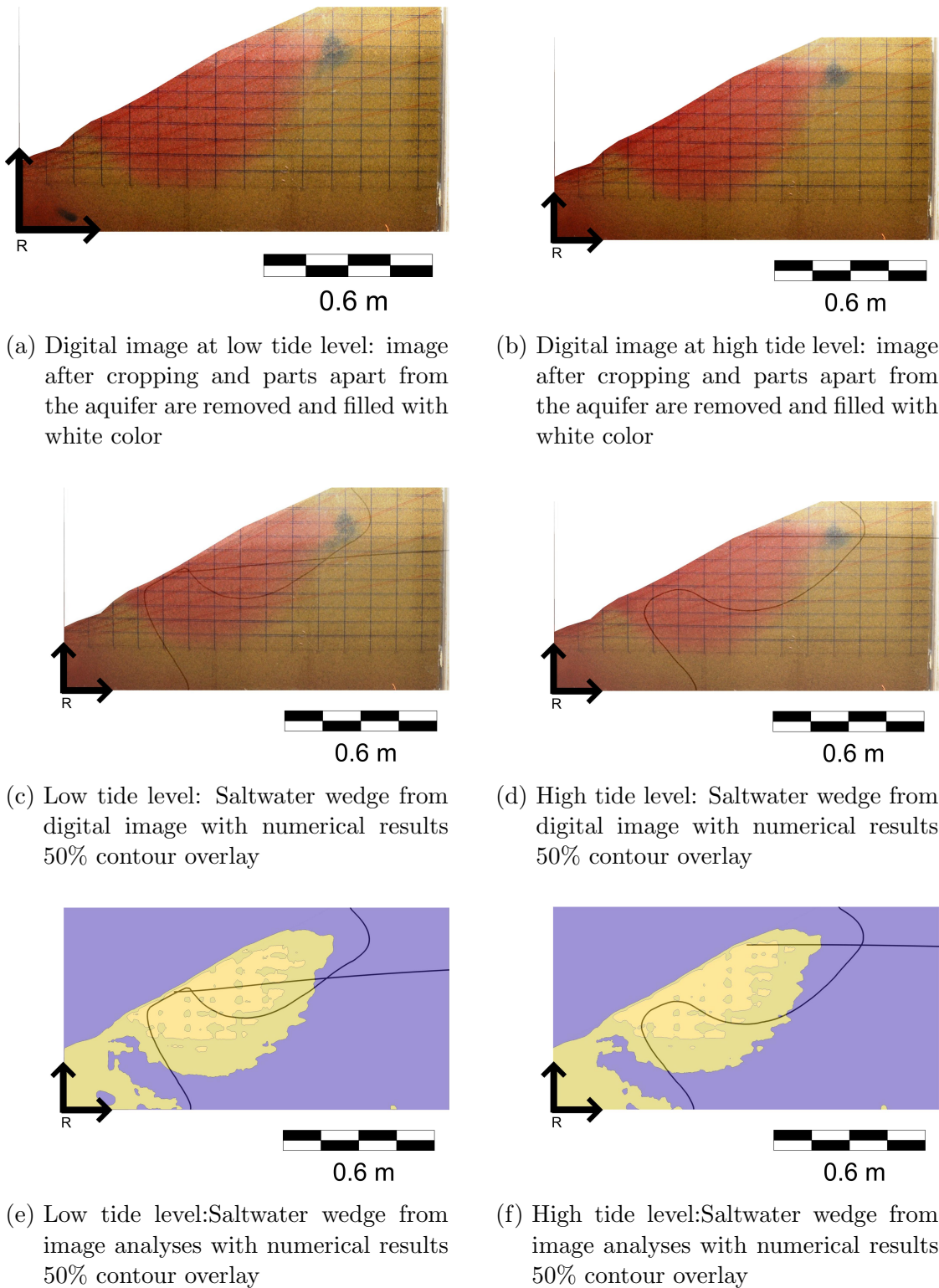


Figure 6.19: ]

CASE-4: Digital image after 1 hours 30 minutes (5400 s) from experiment start  
 [freshwater flux is  $3.00 \text{ m/d}$  ( $3.472 \times 10^{-5} \text{ m/s}$ )]

bottom whereas all other pressure sensors are located at  $0.11 \text{ m}$  from the bottom. Simulated pressure data was showing almost identical mean pressure values while the observed data shows more pressure at  $PS_4^5$  compared to  $PS_3^5$ . The observed pressure values show more vertical gradient upwards. In coarse sand cases (CASE-

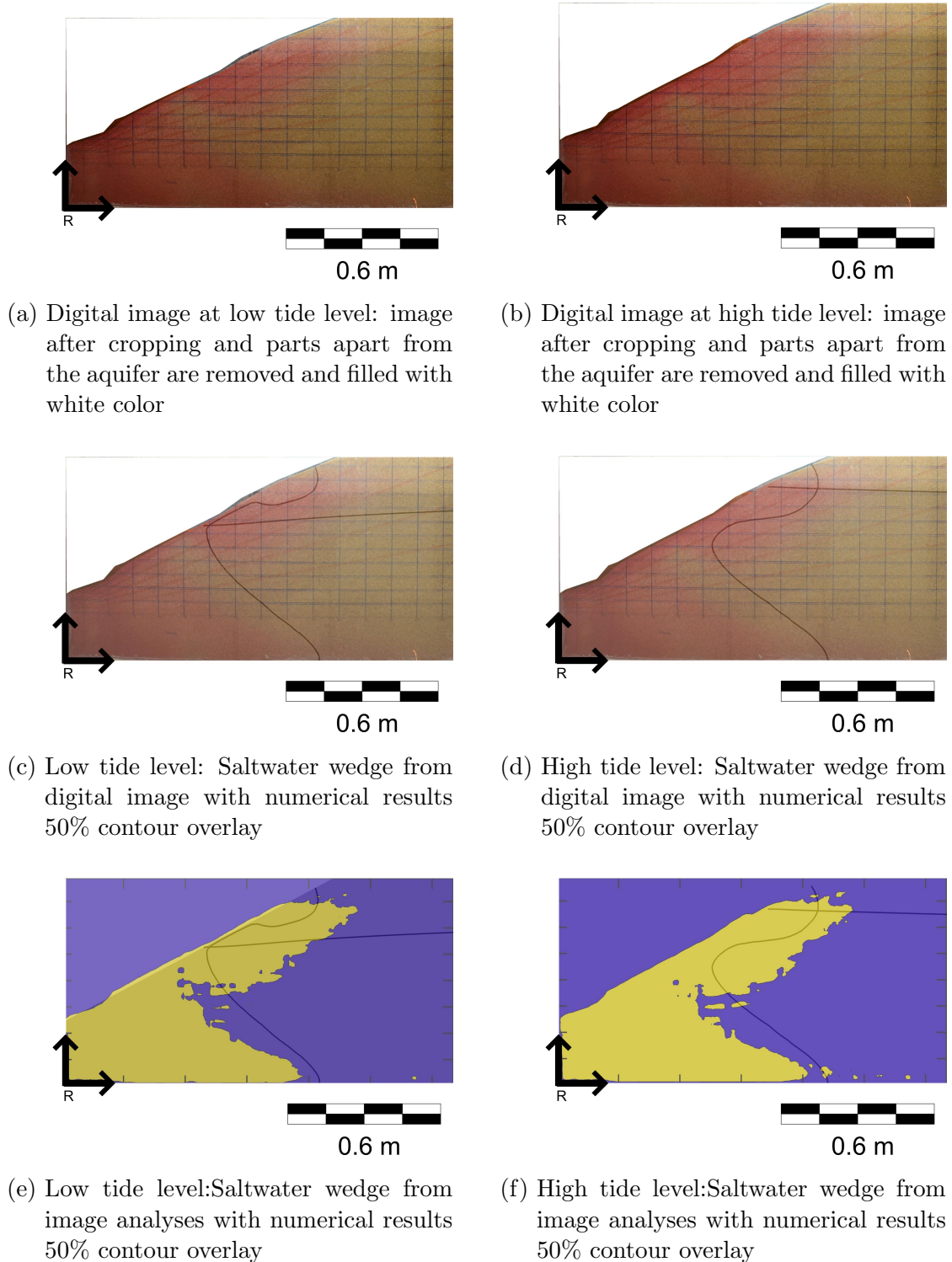


Figure 6.20: ]

CASE-4: Digital image after 12 hours (43200 s) from experiment start [freshwater flux reduced to  $3.00 \text{ m/d}$  ( $3.472 \times 10^{-5} \text{ m/s}$ )]

3 and CASE-4)  $PS_5^3$  and  $PS_5^4$  were outliers. However, in CASE-5 it was not the case. In coarse sand cases ( $PS_5^3$  and  $PS_5^4$ ), the proximity of  $PS_5$  to freshwater boundary resulted in boundary effects to cause outliers. In CASE-5,  $PS_5$  was not in proximity to freshwater boundary. The comparison of observed and simulated

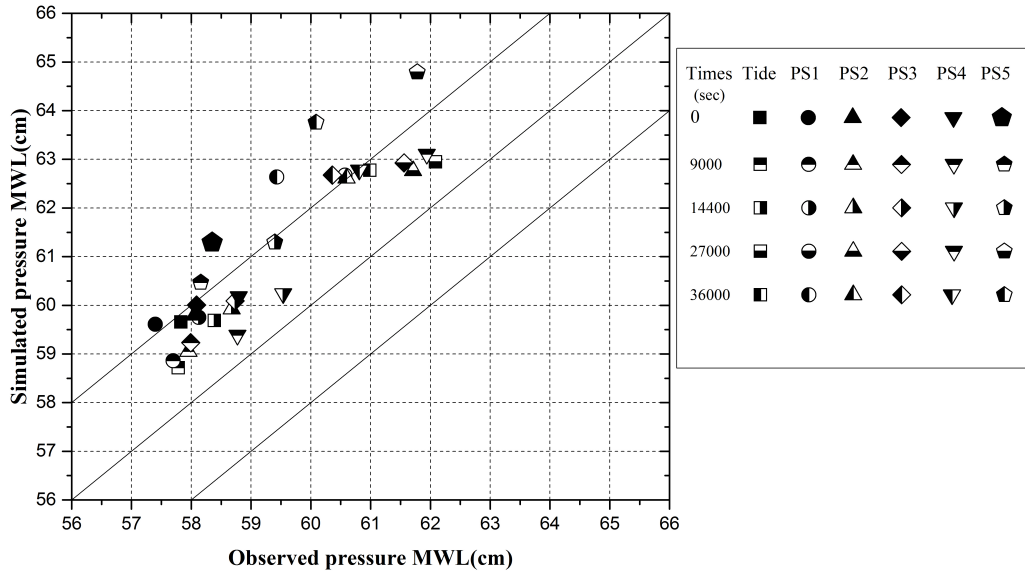


Figure 6.21: CASE-4: Comparison between the time-averaged mean water level of observed and simulated pressure head data with time

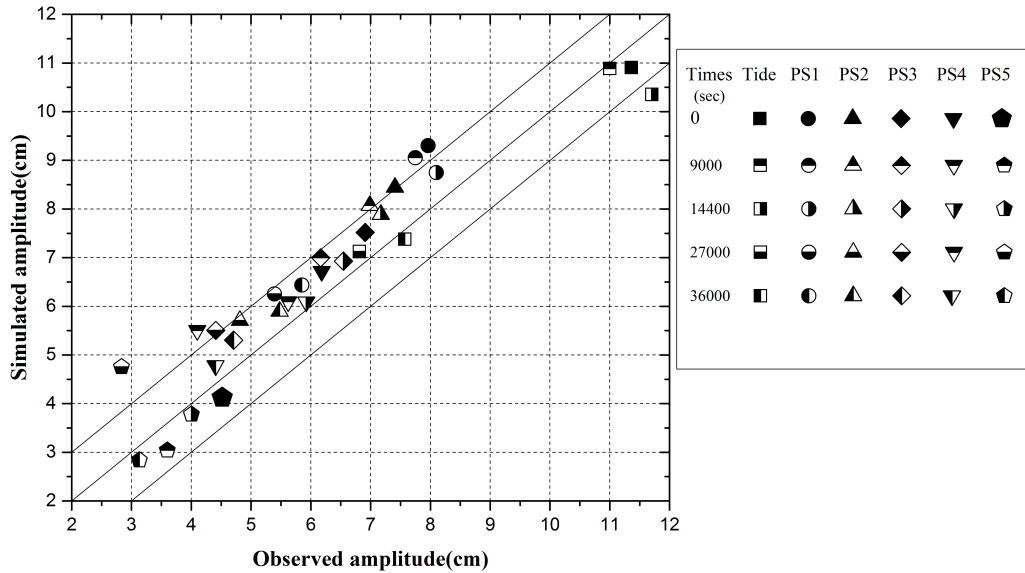


Figure 6.22: CASE-4: Comparison between the amplitudes of observed and simulated pressure head data with time

amplitudes was falling within  $\pm 0.02m$  for all cases except  $PS_5^5$  at time 14400 s. The  $PS_2^5$  located in the seepage face region and the numerical simulation not captured the seepage face condition.  $PS_3^5$  mean water levels in numerical results were always higher than 2 cm error. This pressure sensor was located at 0.31 m from aquifer bottom. The van Genuchten parameters influence the water table fluctuations. In the numerical simulation, van Genuchten parameters were not calibrated for each

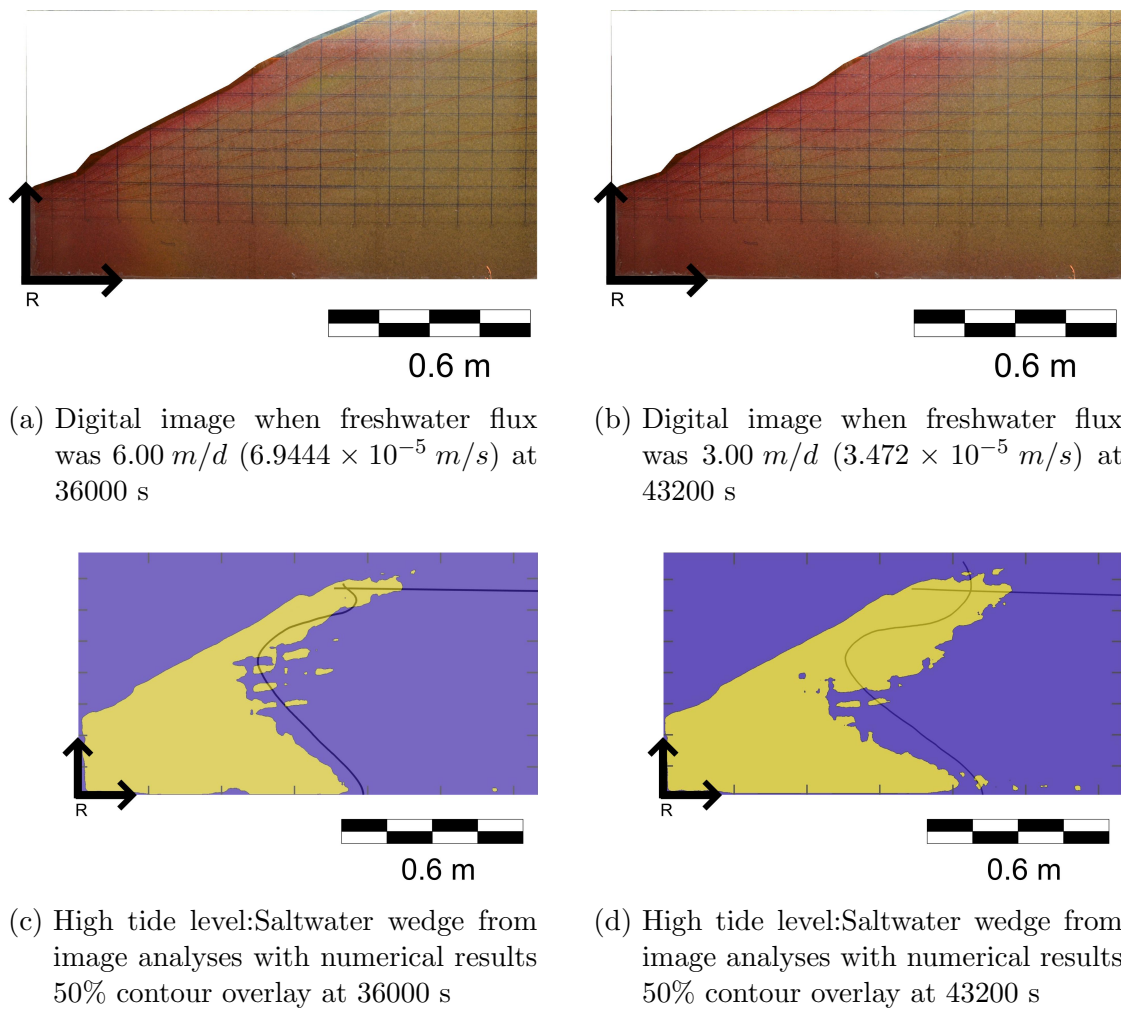


Figure 6.23: CASE-4: Comparison digital image when freshwater flux was  $6.00 \text{ m/d}$  ( $6.944 \times 10^{-5} \text{ m/s}$ ) at 36000 s and freshwater flux was  $3.00 \text{ m/d}$  ( $3.472 \times 10^{-5} \text{ m/s}$ ) at 43200 s

case. This might have been the reason for the deviation for the pressure sensor  $PS_3^5$  located closer to the unsaturated zone. Again, upper saline plume and freshwater discharge zones were prominent. However, numerical modelling has not captured the upper saline plume extent fully.

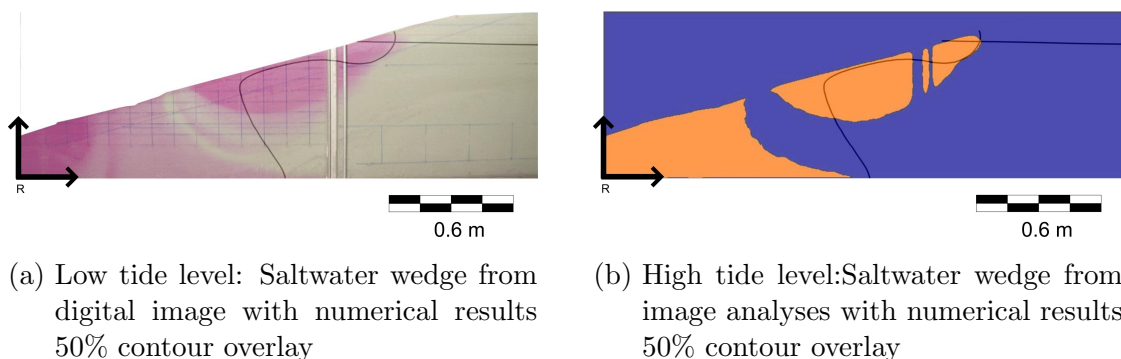


Figure 6.24: ]  
CASE-5: Digital image after 8 hours 30 minutes (30600 s) from experiment start  
[freshwater flux reduced to  $3.00 \text{ m/d}$  ( $3.472 \times 10^{-5} \text{ m/s}$ )]

Table 6.3: CASE-5: Parameters used for FEFLOW saltwater intrusion modeling

| Parameters                | CASE-5   |
|---------------------------|--|
| Hydraulic conductivity K  | 350 m/d  |
| Freshwater flux           | 3 m/d for full experiment                        |
| Density ratio             | 0.025  |
| Specific storage          | 0.0001 1/m                                       |
| Specific yield            | 0.1  |
| Mass transport porosity   | 0.38<br>Scale parameter 10.00 (1/m)              |
| van Genuchten parameters  | Slope parameter 2.68<br>Residual saturation 0.10 |
| Longitudinal dispersivity | 0.1 cm   |
| Transverse dispersivity   | 0.001 cm   |
| Molecular diffusivity     | $1 \times 10^{-9} m^2/s$                         |
| Initial hydraulic head    | 64 cm  |
| Initial concentration     | 0 kg/m <sup>3</sup>                              |
| Tidal period              | 300 s  |
| Tidal amplitude           | 0.0896 m   |
| Tidal mean water level    | 0.5819 m   |

#### 6.2.3.4 CASE-6: IS Sand with Beach Slope $\pi/6$

The experiment of CASE-6 was performed for IS Grade-II sand for beach slope  $\pi/6$ . Aquifer height was 0.80 m and the horizontal extent of the slope was 1.14 m (Figure 6.5d). Pressure transducer locations are the same as CASE-5. The experiment was done for 10 hours, with saltwater concentration maintained at 35000 mg/l. Tidal wave mean water level was  $0.60 \pm 0.01$  m, the amplitude was  $0.07 \pm 0.01$  m and time period of the wave was 300 s. Saltwater toe location after 6 hours from experiment start was approximately at 0.75 m. The FEFLOW simulation parameters are provided in Table 6.4. The comparison plots of observed and simulated water tables of both mean water level and amplitude shows that  $PS_5^6$  is in the outlier zone. Velocity vectors near the seaside boundary within a tidal cycle are shown in Figure 6.32. It was clear that saltwater enters through all regions in contact with the saltwater (Figure 6.32b). However, the water entering in the intertidal zone has movement upwards unlike other parts where the water entered

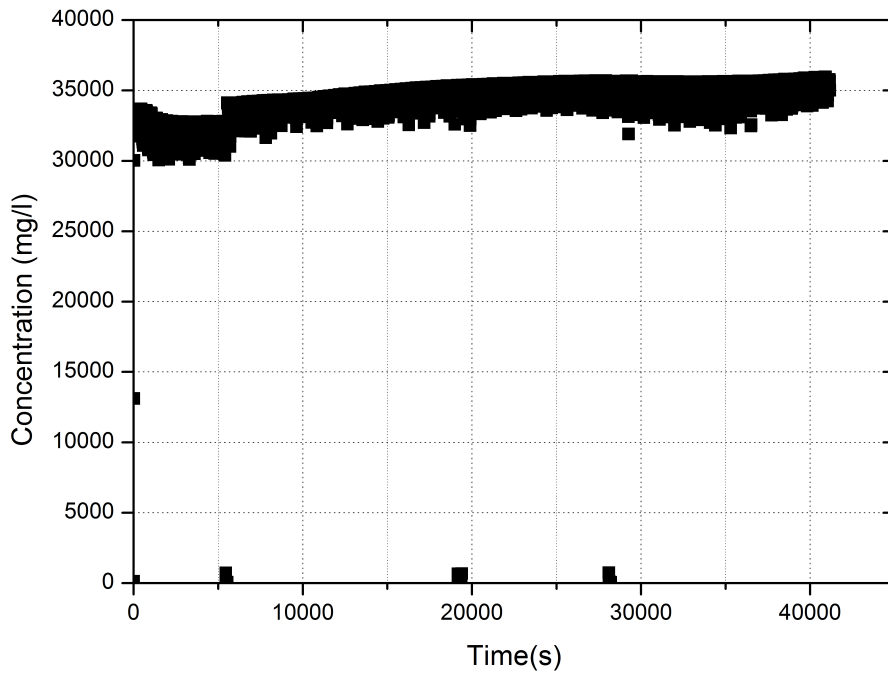


Figure 6.25: CASE-5: Concentration of saltwater recorded in CTD-Diver placed inside the saltwater reservoir. The points near zero concentration are the point when CTD-Diver was removed from the experimental setup to verify the concentration data.

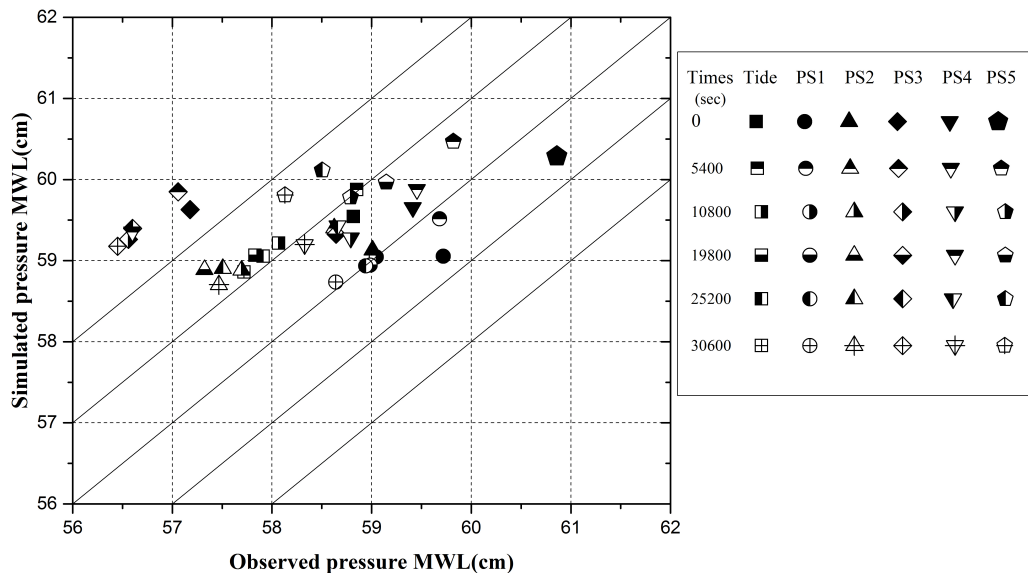


Figure 6.26: CASE-5: Comparison between the time-averaged mean water level of observed and simulated pressure head data with time

in either downwards and then became a horizontal movement in the inland or fully horizontal from the entry itself. Water moved upwards to saturate the unsaturated

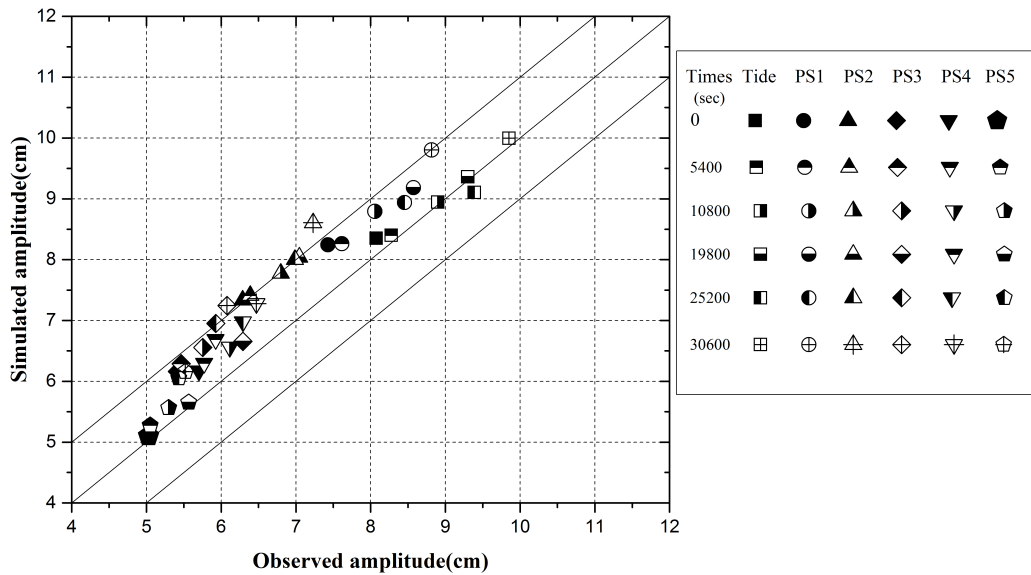


Figure 6.27: CASE-5: Comparison between the observed amplitude and simulated amplitude of pressure head data with time

region above the water table in the rising tide condition. In the falling tide, the saltwater front was pushed towards seawards due to the freshwater discharge towards the sea (from Figure 6.32f). Even when the flow direction shifted towards the sea in the zone above the saltwater wedge, the flow inside the saltwater wedge had small flows in the landward direction. However, the flows inside the saltwater wedge also changed the direction to flow seawards with the falling tide (Figure 6.32g). Meanwhile, the upper saline plume zone was reduced and freshwater discharge zone widened with the falling tide. Even when the tide level started rising flow direction changed only after some lag time (Figure 6.32b).

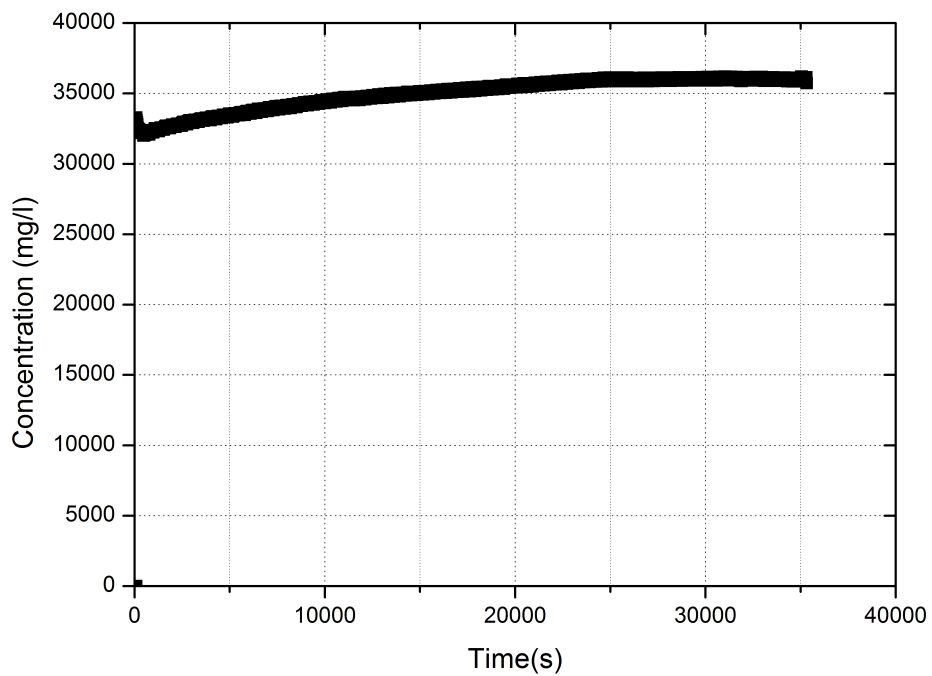


Figure 6.28: CASE-6: Concentration of saltwater recorded in CTD-Diver placed inside the saltwater reservoir.

Table 6.4: CASE-6: Parameters used for FEFLOW saltwater intrusion modeling

| Parameters                | CASE-6   |
|---------------------------|--|
| Hydraulic conductivity K  | 350 m/d  |
| Freshwater flux           | 2.5 m/d for full experiment                      |
| Density ratio             | 0.025  |
| Specific storage          | 0.0001 1/m                                       |
| Specific yield            | 0.1  |
| Mass transport porosity   | 0.38<br>Scale parameter 10.00 (1/m)              |
| van Genuchten parameters  | Slope parameter 2.68<br>Residual saturation 0.10 |
| Longitudinal dispersivity | 0.1 cm   |
| Transverse dispersivity   | 0.001 cm   |
| Molecular diffusion       | $1 \times 10^{-9} m^2/s$                         |
| Initial hydraulic head    | 64 cm  |
| Initial concentration     | 0 $kg/m^3$                                       |
| Tidal period              | 300 s  |
| Tidal amplitude           | 0.0726 m   |
| Tidal mean water level    | 0.5971 m   |

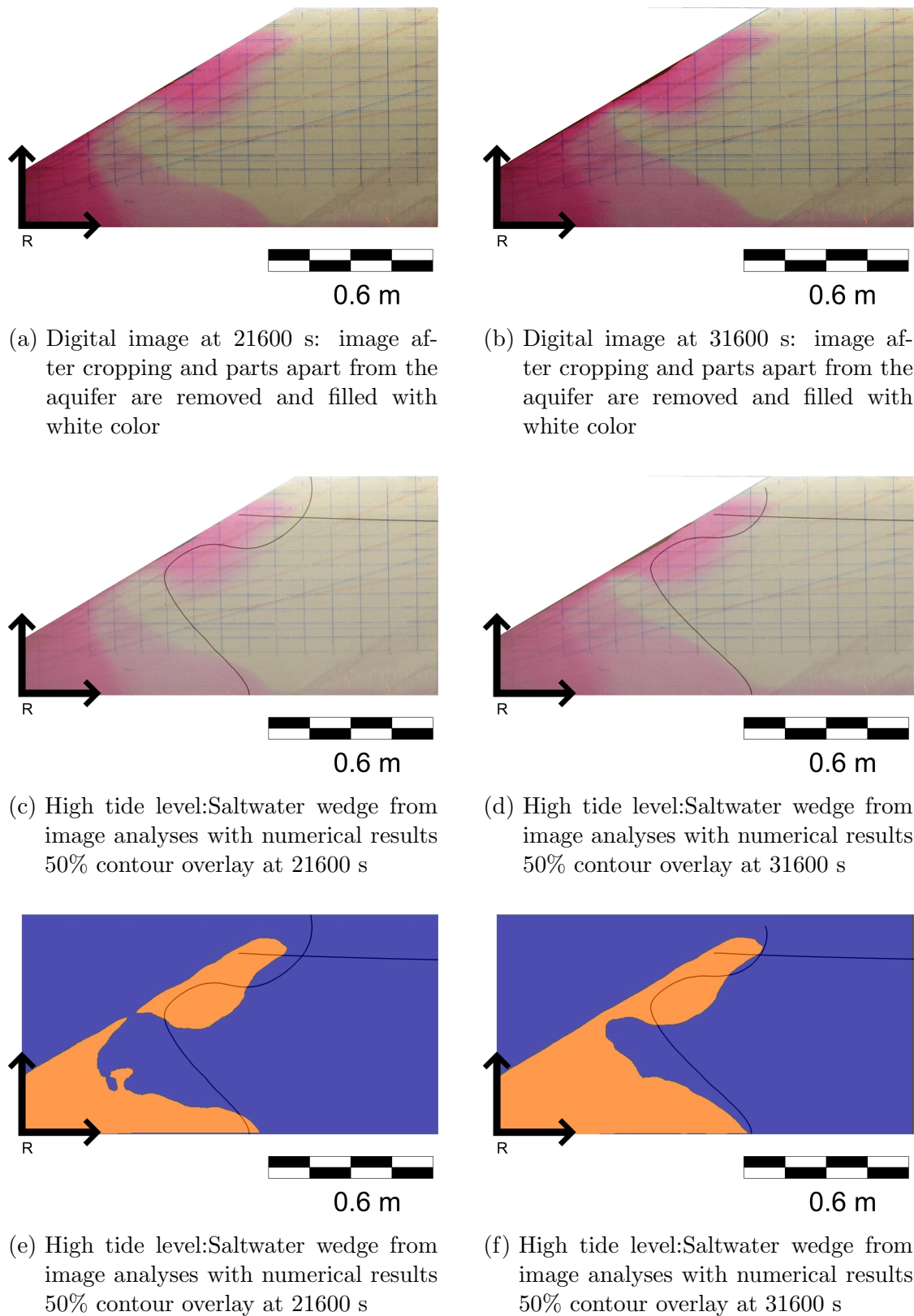


Figure 6.29: CASE-6: Experimental results of freshwater flux  $2.50 \text{ m/d}$  ( $2.894 \times 10^{-5} \text{ m/s}$ ). Images are at 6 hours and 8 hours 45 minutes

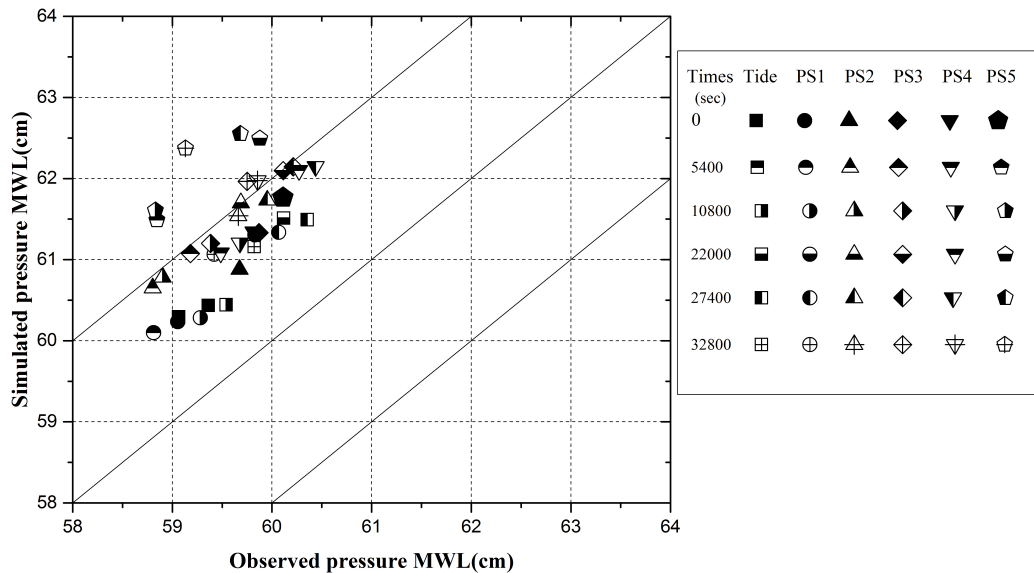


Figure 6.30: CASE-6: Comparison between the time-averaged mean water level of observed and simulated pressure head data with time

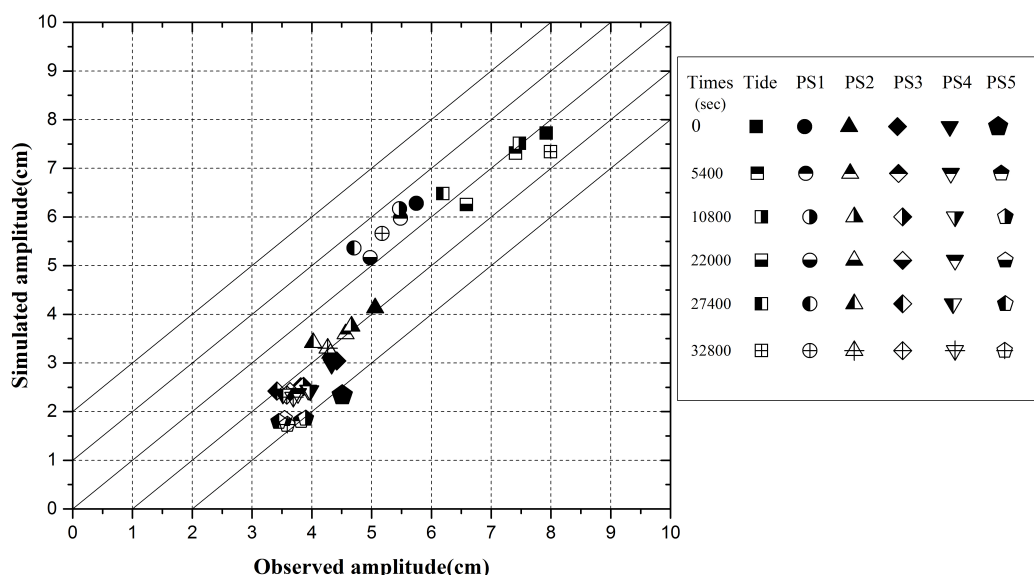


Figure 6.31: CASE-6: Comparison between the time-averaged mean water level of observed and simulated pressure head data with time

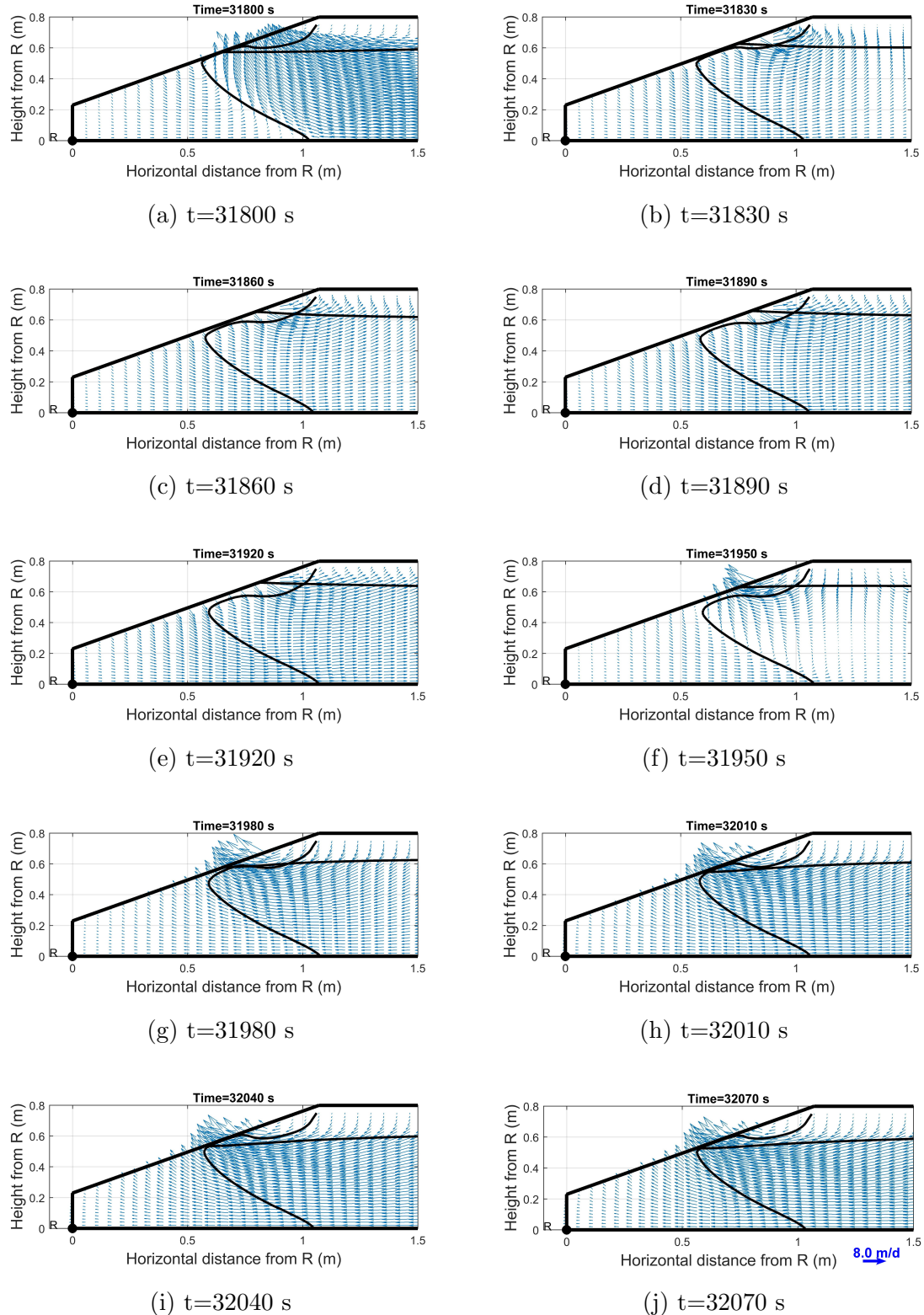


Figure 6.32: CASE-6: Velocity vector plots with in a tidal wave period . Experimental results of freshwater flux  $2.50 \text{ m/d}$  ( $2.894 \times 10^{-5} \text{ m/s}$ ). Images are at 6 hours and 8 hours 45 minutes. Scale of vectors is given at bottom right of Figure 6.32j.

## 6.2.4 Tracer Tests

### 6.2.4.1 Tracer Tests in CASE-3: Coarse Sand with Beach Slope $\pi/12$

Apart from Rhodamine dye used to observe the saltwater intrusion wedge and the upper saline plume, Fluorescein Sodium made by Loba Chemie was used for tracer tests. Tracer tests were done to observe the flow paths of the tracers or contaminants from different locations. The external tracers were injected at different locations through a tube like set up with an opening at the top to inject. The tracer plume movement under tidal conditions was recorded using photographs. Generally, a tracer without salt was injected in the freshwater zone and another tracer with salt concentration approximately equal to saltwater wedge concentration was injected in the saltwater zone. This was to ensure that there was no buoyancy due to density difference plays a role in the tracer movement (density neutral condition).

In CASE-3 experiment, the tracers were injected at 2.20 m in horizontal direction and 0.45 m ( $x_1 = 2.20\text{ m}$  and  $y_1 = 0.45\text{ m}$ ) in vertical axis from the origin R (left bottom corner of the aquifer) at 12600 s from experiment start (Figure 6.33a). This point TP1 ( $x_1 = 2.20\text{ m}$ ,  $y_1 = 0.45\text{ m}$ ) was in freshwater zone. Hence, the tracer solution made of freshwater added with Fluorescein Sodium–no salt added. Total 30 ml ( $3 \times 10^{-5}\text{ m}^3$ ) solution injected in 2 minutes interval at that point. Similarly, a tracer solution of 30 ml with 35000 mg/l salt concentration prepared and injected at two locations inside the saltwater wedge. Second point TP2 was at  $x_2 = 1.30\text{ m}$  and  $y_2 = 0.22\text{ m}$  from the R, which was nearby saltwater and freshwater mixing zone (Figure 6.33f), and third point TP3 was at interior of the saltwater wedge (seaward side from freshwater-saltwater interface) at  $x_3 = 0.60\text{ m}$  and  $y_3 = 0.19\text{ m}$  (Figure 6.33b). The tracers injected at both TP2 and TP3 were 30 ml ( $3 \times 10^{-5}\text{ m}^3$ ) each of 35000 mg/l salt concentration to make them density neutral in their zone. The injections started at 12720 s for point 3( $x_3, y_3$ ) and at 13200 s for point 2( $x_2, y_2$ ). Figure 6.33 and Figure 6.37 shows the digital photographs of tracer movement for each 2 minutes interval. Tracer plume of contaminant injected at point 1 is referred to as TP1, point 2 is referred to as TP2, and point 3 is referred to as TP3 in the following text (Figure 6.33f).

TP1 injected in the freshwater zone increased its spread over time and moved towards seaside boundary over time. However, within the tidal cycle, the plume oscillated up and down and seaward and landward depending on the tidal level (Figure 6.33). Figure 6.33 shows the plume at different tidal levels. The spread of the TP1 plume was increasing with time as the plume disperses while being trans-

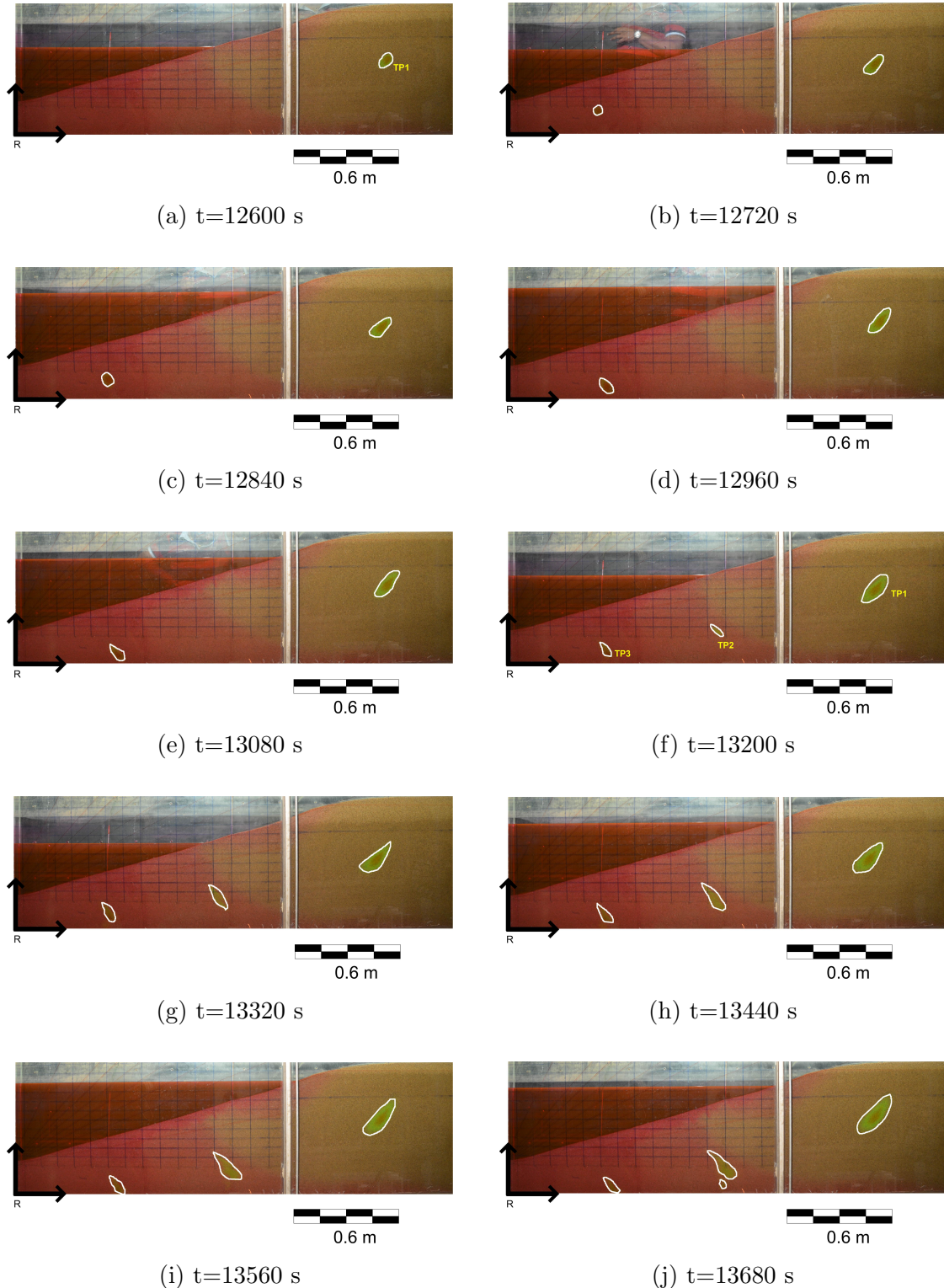


Figure 6.33: CASE-3: Images for tracer injections from time 12600 s. The tracer plume oscillates along with the tidal water level.

ported inside porous media (Figure 6.34). Initially, the plume is of circular shape approximately (Figure 6.33a). The plume shape elongates with time, as contaminant in freshwater elongates in Chang and Clement (2013) (Figure 6.39). However, the initial dispersion happens more downward (vertical) due to tidal oscillation in the present experiment (Figure 6.33). The dispersion direction becomes the fresh-

water tube shape as it moves near the seaside boundary to discharge to sea. In Chang and Clement (2013), the major dispersion happens in near horizontal direction always as the major flow direction is horizontal towards the sea boundary (Figure 6.34). Chang and Clement (2013) performed experiments for constant head without tidal effects. Figure 6.34g, Figure 6.34h, Figure 6.34i, and Figure 6.34j shows the the plume shape changing as it approaches the seaside boundary.

The tracer plume movements were validated qualitatively by using two-dimensional FEFLOW modeling. Richards equation with multi-species transport option was used. In this case, there are two species with salt with density ratio 0.025 (maximum density  $1025\text{kg/m}^3$ ) and the tracer of freshwater density was the second species with density ratio 0.01 (maximum density  $1010\text{kg/m}^3$ ). Dispersivity values for  $1\text{ cm}$  and  $0.01\text{ cm}$  were used for longitudinal dispersivity and transverse dispersivity respectively. Dispersivity values of tracers were of one order above the dispersivity values of saltwater. Other parameters were the same as in saltwater intrusion simulations. Figure 6.36 and Figure 6.39 show the tracer movement simulated with numerical modeling. The movement of tracer showed good match qualitatively with the experimental tracer movement. The calibration of dispersivities and other parameters were very complex process. Hence, the validation is done qualitatively alone.

TP2 tracer initially spreads along the freshwater-saltwater mixing zone and spreads in a direction right angled to the slope of the saltwater boundary (Figure 6.34). The plume moves up and down overtime with the tidal oscillation. However, the tracer moved to salt boundary along with the mixing region and discharges in the seaside boundary just below the freshwater discharge zone (below lower tidal zone). Figure 6.34 shows the TP2 and TP3 movement until 13680 s and the tracer plume boundaries are marked in white manually. Figure 6.37 showed the movement of TP2 and TP3 plumes from 13800 s to 14800 s. After 14160 s the TP2 plume spreads over a large area and making it difficult to delineate. However, it was clear from the images that the plume spread horizontally as well along with the movement towards the seaside boundary.

TP3 plume (Figure 6.33) starts as circular shape and then elongates in near vertical direction. However, TP3 does not move as fast as TP2 and stagnates in the same region with oscillation due to tidal effect. Smaller scale of velocity vectors compared to the freshwater-saltwater interface zone as seen in the velocity vector plots (Figure 6.32) causes the stagnation. TP3 disperses in the same zone over long time and vanishes (Figure 6.34). Hence, a density neutral tracer injected in the interior portion of the aquifer may not discharged in sea as faster as a density

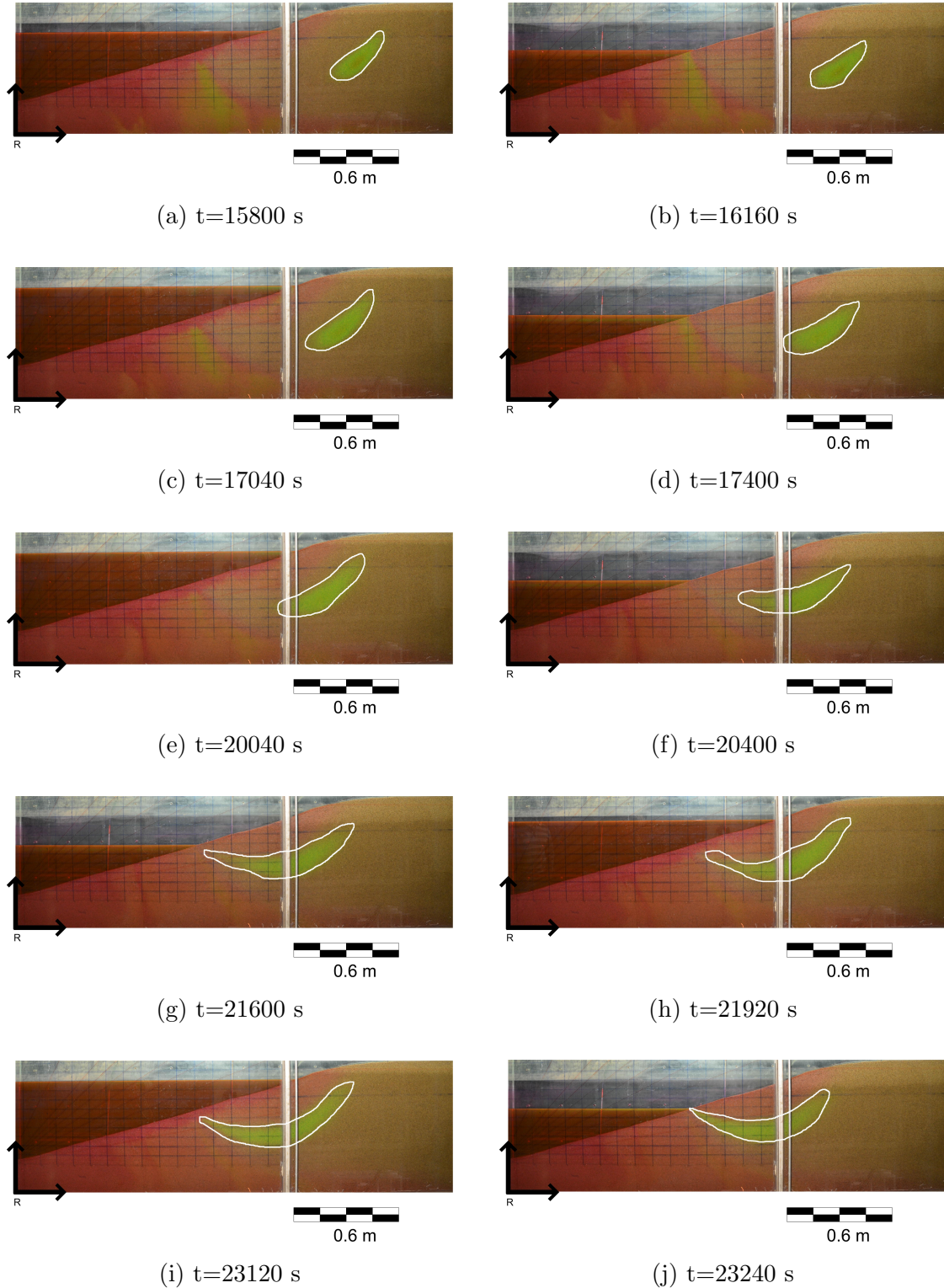


Figure 6.34: CASE-3: Images for tracer injections from time 15800 s till the experiment end. Tracer plume shape changes over time with the spread direction changes

neutral tracer near the freshwater-saltwater interface region. This understanding would help in studying the possible reactions of contaminants leaked inside the saltwater wedge in the coastal aquifers. The contaminant transport of TP2 and TP3 also qualitatively validated using FEFLOW numerical model (Figure 6.38).

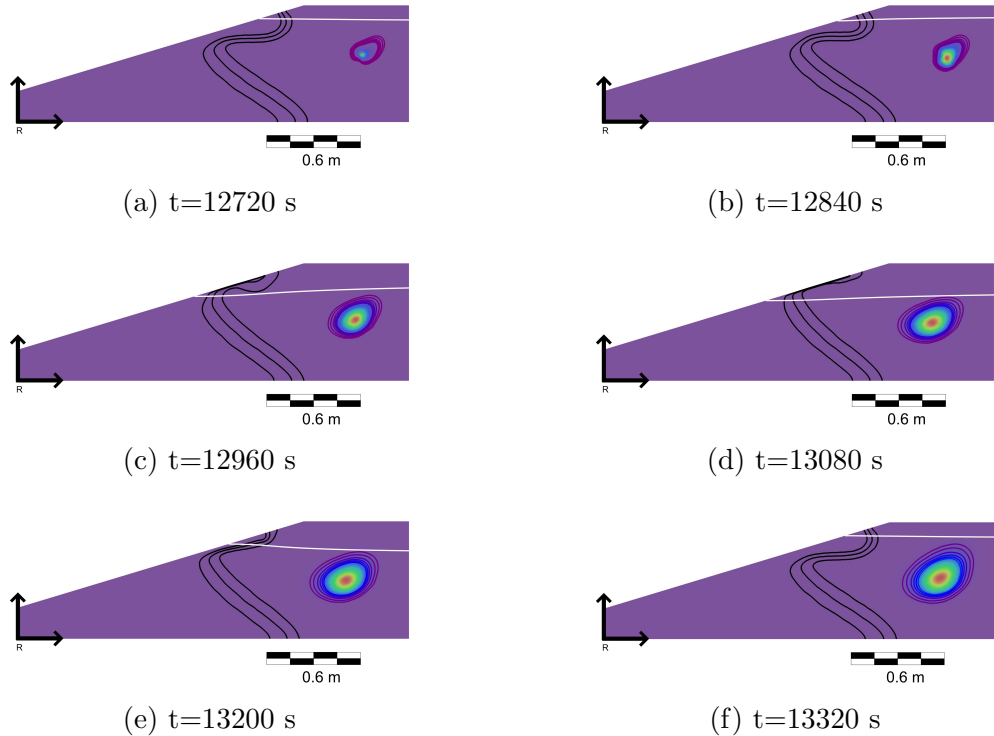


Figure 6.35: CASE-3: Tracer plume movement in 2D FEFLOW modelling of tracer injected in freshwater zone. Trace plume The concentration of the tracer was same as tap water used for the freshwater. The tracer plume oscillations along with the tidal water level within a tidal cycle is shown.

Numerical modeling was done using the same density ratio for this case. Dispersion parameters of the tracer are the same as TP1. The pathways of the tracer movement matches well with the experimental observations. However, the travel times are not matching well with the experimental observations. The complex nature of the parameter uncertainty and seepage boundary may be the possible reasons for such deviations.

#### 6.2.4.2 Tracer Tests in CASE-4: Coarse Sand with Beach Slope $\pi/6$

Tracer tests were done for the aquifer with beach slope  $\pi/6$  (CASE-4) as well. As explained in the CASE-4 results, this experiment was done before CASE-3. An indigo blue colour dye tried as a tracer. However, it could not capture the contaminant movement. After that Fluorescein Sodium tracer was used as a tracer. Figure 6.40a shows the tracer TP4 injected at  $x_4 = 1.5 \text{ m}$  and  $y_4 = 0.57 \text{ m}$  with freshwater density. The tracer plume is spreading over time similar to CASE-3. However the spreading in the vertical direction is not as significant as CASE-3. CASE-4 tidal time period of 300 s was half of the same of CASE-3. Hence, the smaller wave number due to the larger time period of tide for CASE-3 may have caused the more vertical spread compared to CASE-4.

Tracer injected in the saltwater wedge TP5 (Figure 6.41a) with  $35000 \text{ mg/l}$

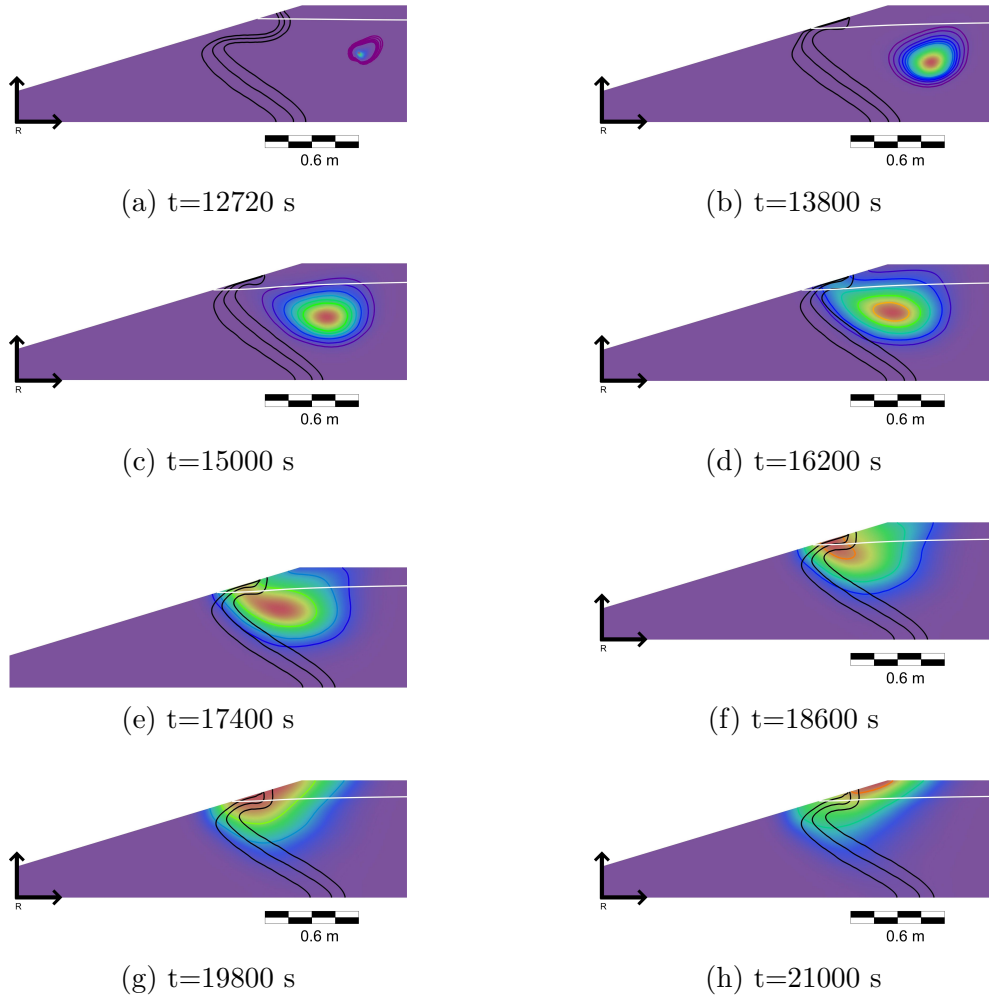


Figure 6.36: CASE-3: Tracer plume movement in 2D FEFLOW modelling of tracer injected in freshwater zone. Trace plume The concentration of the tracer was same as tap water used for the freshwater. Trace plume movement from injection time to end of experiment is shown.

is shown in Figure 6.41. TP4 was injected at 25200 s and TP5 was injected at 29790 s. TP5 was injected at  $x_5 = 0.25\text{ m}$  and  $y_5 = 0.05\text{ m}$ , which was interior (away from the freshwater-saltwater interface) of the saltwater wedge. TP5 tracer oscillated with the tidal wave, but the movement confined within a small region similar to TP3 and vanished over time. TP4 moved towards the seaside boundary and discharged in seaside boundary (Figure 6.42) through freshwater discharge zone(below the upper saline plume).

## 6.3 Summary

Experiments were carried out for saltwater movement in scaled coastal aquifers. Saltwater intrusion experiment procedure was explained in this chapter. In Saltwater intrusion experiments, pressure data for quantitative validation were collected for quantitative validation, digital photographs were recorded for qualitative anal-

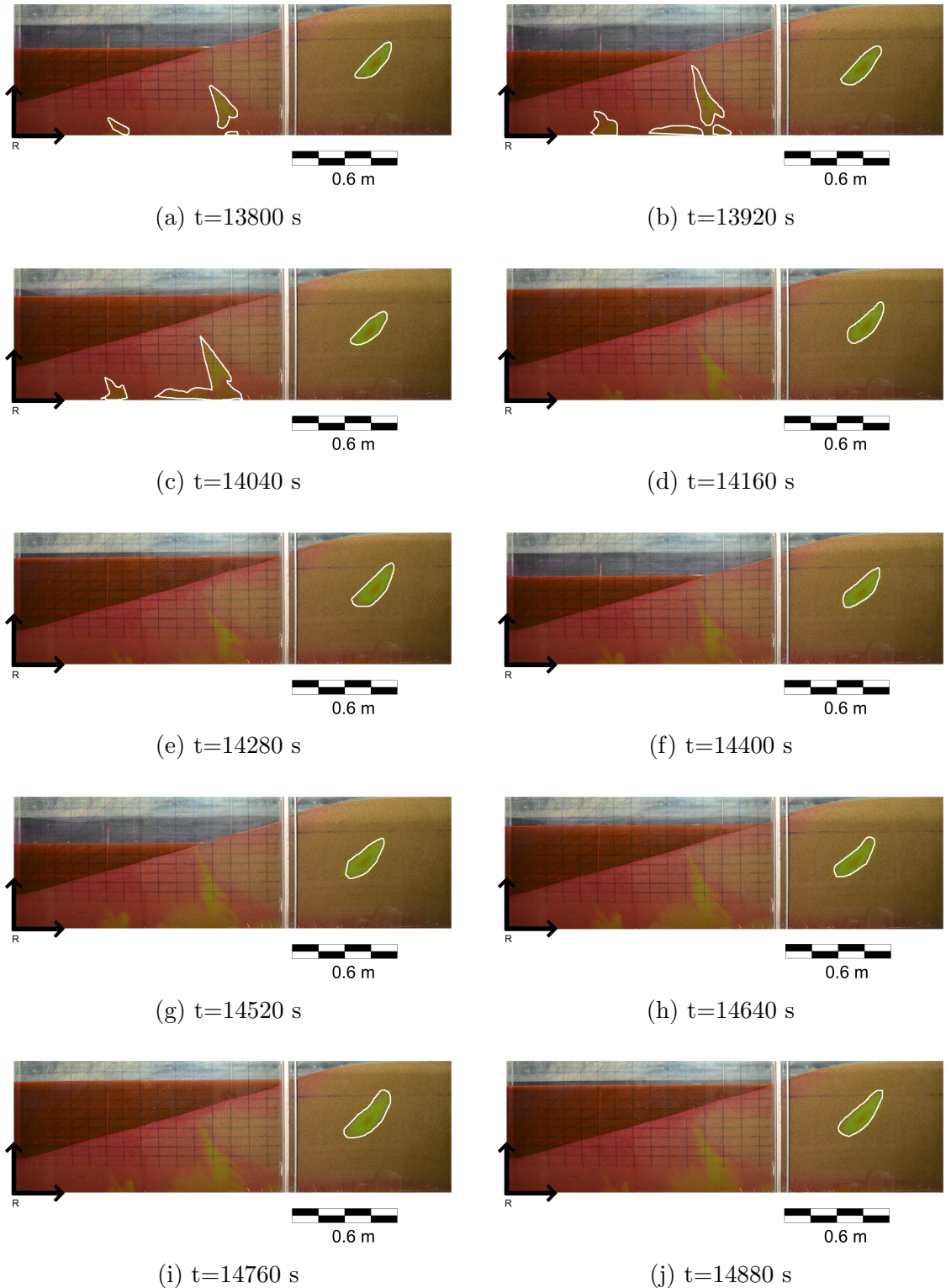


Figure 6.37: CASE-3: Images of racer plumes recorded from time 13800 s to 14880 s.

ysis, and saltwater conductivity data at the saltwater boundary were collected to enforce boundary conditions for the validation by using numerical modeling. Images were analysed through a simplified image analysis technique to obtain the saltwater wedge. Pressure data at the saltwater boundary were used to enforce boundary condition for seaside boundary and the pressure data of pressure trans-

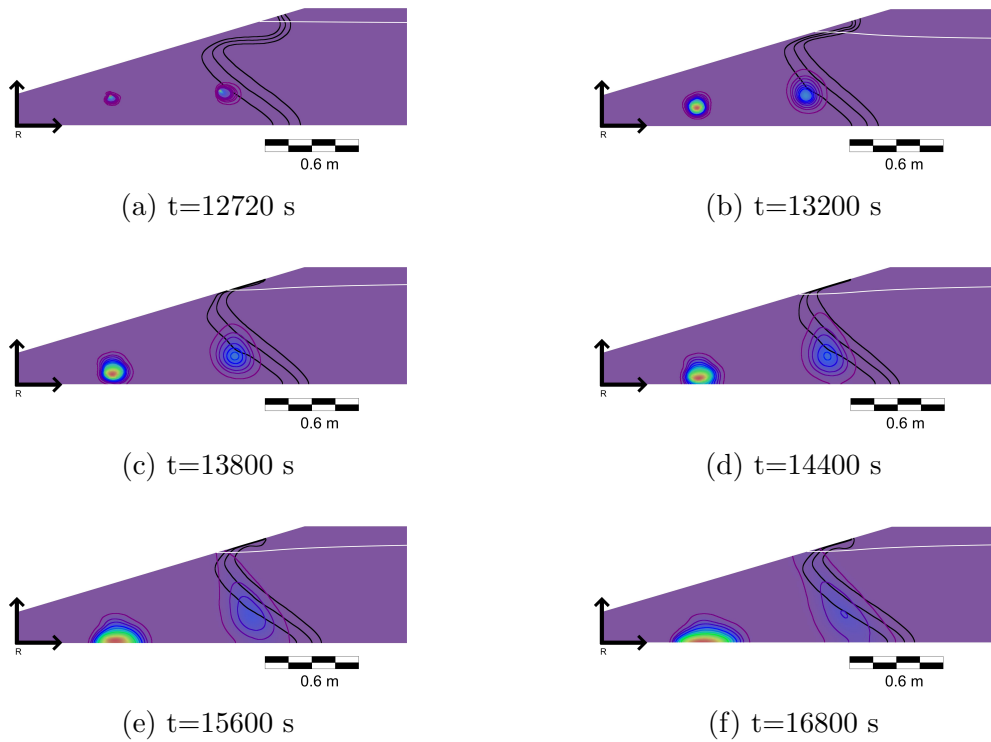


Figure 6.38: CASE-3: Tracer plume movement in 2D FEFLOW modelling of tracer injected inside the saltwater wedge. The concentration of the tracer was 35000 mg/l

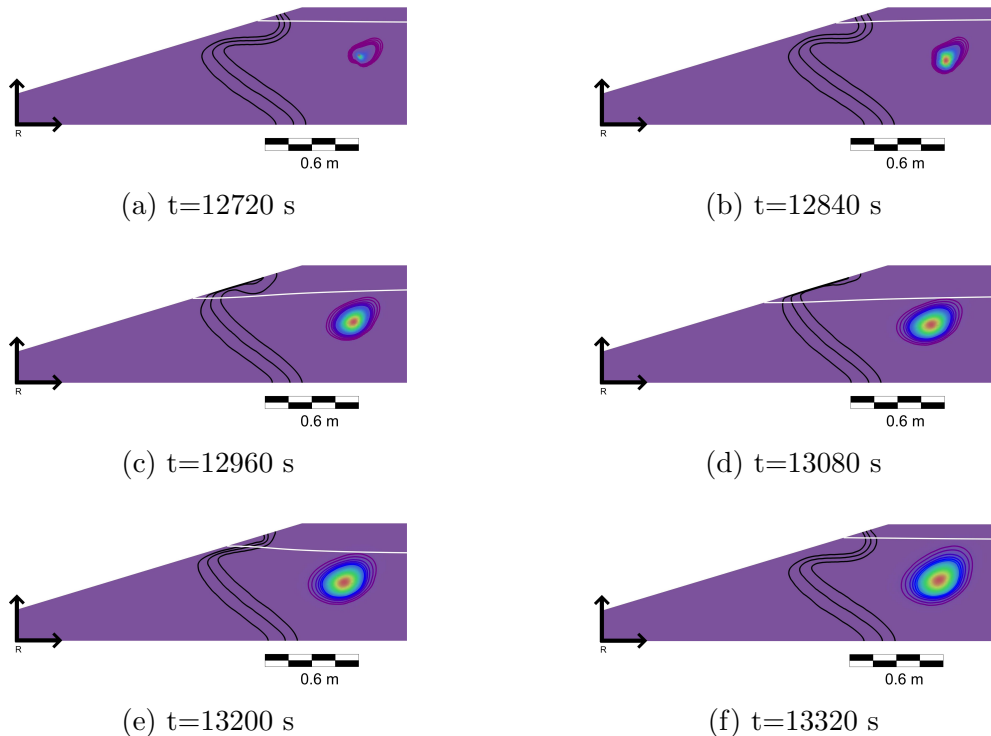


Figure 6.39: CASE-3: Tracer plume movement in 2D FEFLOW modelling of tracer injected in freshwater zone. Trace plume The concentration of the tracer was same as tap water used for the freshwater. The tracer plume oscillations along with the tidal water level within a tidal cycle is shown.

ducers placed at inland regions were used to validate the numerical models. All experiments of  $\pi/12$  and  $\pi/6$  beach slopes for coarse river sand and IS sand shown upper saline plume, saltwater wedge, and freshwater discharge zone. Peclet numbers ( $Pe$ ) is in the order of 5-20 for all FEFLOW numerical simulations. Tracer tests were performed to observe the contaminant pathways of density neutral tracers and their qualitative pathways were validated by using numerical modeling. More studies needed to be done to understand and calibrate the multiple parameters involved in this problem for better understanding of contaminant/nutrient load movement in coastal aquifers.

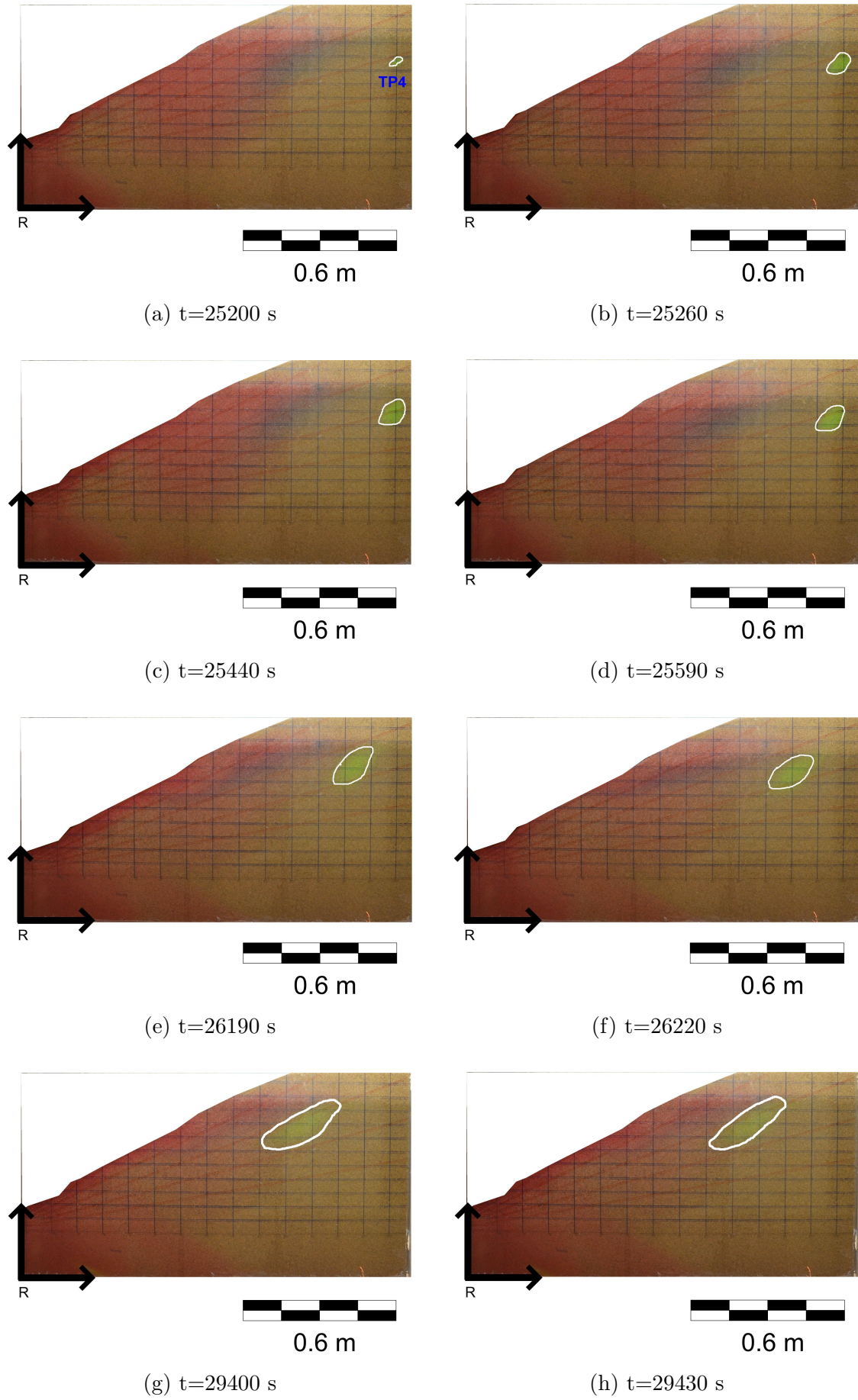


Figure 6.40: CASE-4: Tracer plumes recorded from at different times. Images of the plume injected in the freshwater zone(TP4).

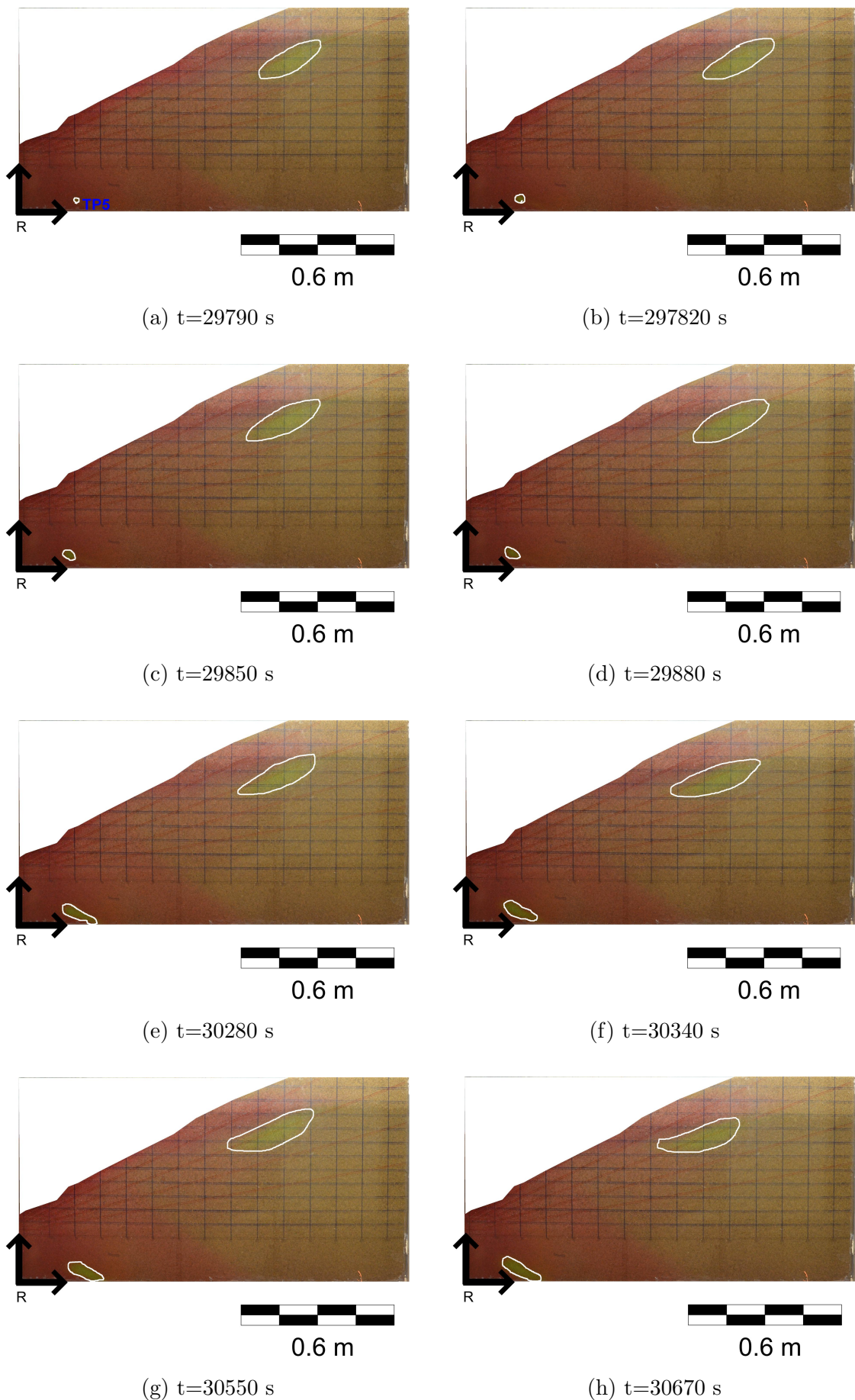


Figure 6.41: CASE-4: Tracer plumes recorded from at different times. Images of the plume injected inside saltwater wedge(TP5).

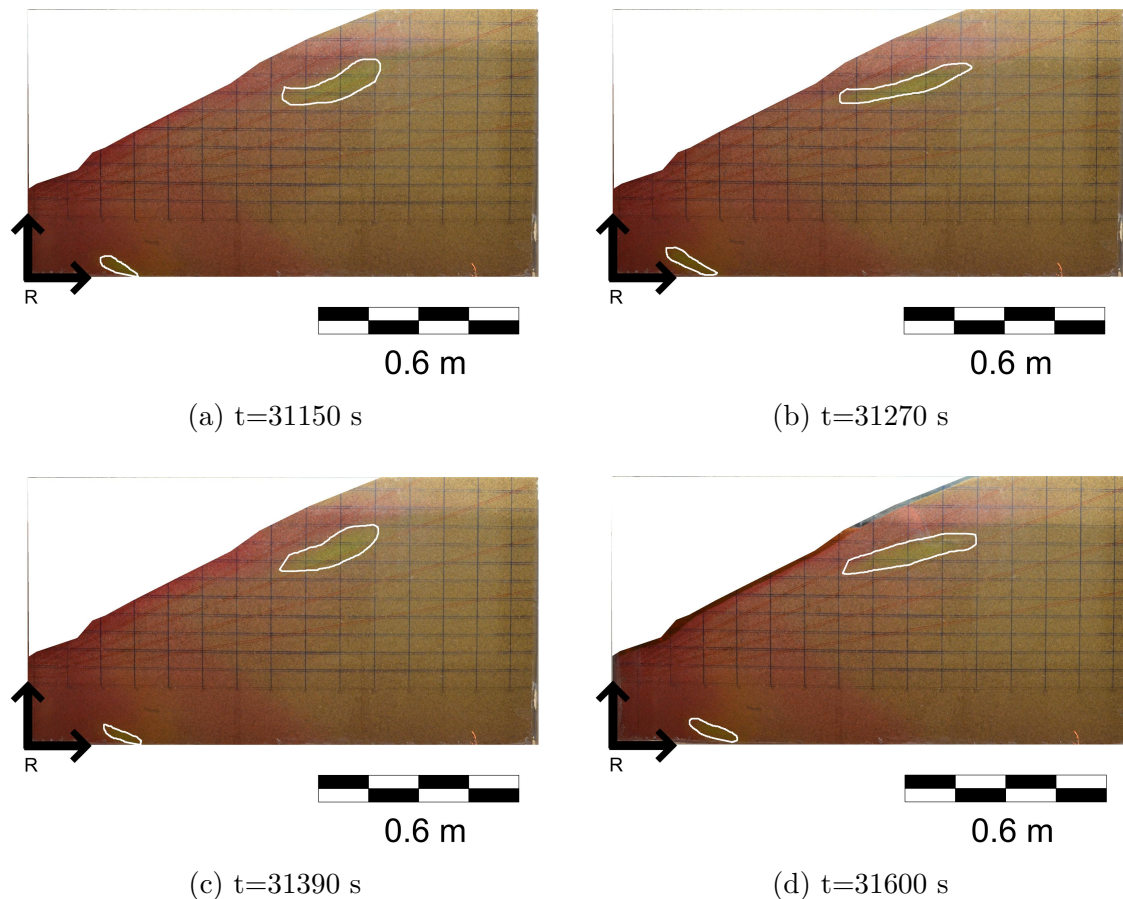


Figure 6.42: CASE-4: Tracer plumes recorded from at different times. Images of the plume injected inside saltwater wedge(TP5).

# Chapter 7

## Conclusions and Future Scope

### 7.1 Overview

The major objective of the thesis is to study the effects of tidal oscillations in coastal aquifers. The study consisted of tidal influence without density effects and tidal influence with density-dependent effects in coastal aquifers. Tidal influence without considering density effects was done by deriving analytical solutions for groundwater waves in response to tides. Analytical solutions were derived using the homotopy perturbation method (HPM). The summary of analytical solutions for groundwater fluctuations are given in Table 7.1. Analytical solutions were validated by comparing with the existing analytical solutions or two-dimension numerical modeling solutions by using FEFLOW model. Experiments were performed to study the tidal influence with and without density effects. The summary of experimental cases are given in Table 7.2. The cases CASE-1 and CASE-2 are freshwater experiments without considering density effects. There were different subcases for different wave time period, frequency, amplitude and mean water level. The cases CASE-3, CASE-4, CASE-5, and CASE-6 are density-dependent flow experiments. Dyes were used along with salt solution to visually study the saltwater intrusion. In CASE-3 and CASE-4, tracer tests of density neutral tracers were performed to study the contaminant pathways. Denisty-dependent experimental results were simulated in FEFLOW model to validate the results. FEFLOW model solution was used to study the velocity vectors at different time periods of tidal wave. Tracer test results were also validated qualitatively with the numerical modeling results.

Table 7.1: Summary of analytical solutions of groundwater fluctuations due to tidal oscillations

| Case                                   | Hydraulic conductivity | Governing Equation               | Virtual Parameters | Secular terms removal                     | Validation  |
|--|------------------------|----------------------------------|--------------------|---|---|
| HPM for vertical beach face            | Isotropic              | Boussinesq equation              | $p$                | Parameter expansion                       | Song et al. (2007)<br>Kong et al. (2011)                                    |
| HPM for sloping beach face             | Isotropic              | Boussinesq equation              | $p_1, p_2$         | Parameter expansion and an auxiliary term | Teo et al. (2003)<br>Kong et al. (2011)<br>2D FEFLOW, Yeh et al. (2010)     |
| HPM for anisotropic aquifer with slope | Anisotropic            | Second-order Boussinesq equation | $p_1, p_2$         | Parameter expansion and an auxiliary term | Teo et al. (2003)<br>Kong et al. (2011)<br>2D FEFLOW, Roberts et al. (2011) |

Table 7.2: Summary of experimental cases

| Case<br>(subcases<br>in bracket) | Density-<br>difference<br>considered | Sand                                 | Slope    | Dye usage&<br>image analysis | Tracers |
|----------------------------------|--------------------------------------|--------------------------------------|----------|------------------------------|---------|
| CASE-1<br>(1A,1B, 1C,1D, 1E)     | No                                   | Coarse sand<br>$d_{50}=1.024$ mm     | $\pi/6$  | No                           | No      |
| CASE-2<br>(2A,2B,2C,2D,2E)       | No                                   | IS Sand Grade II<br>$d_{50}=0.75$ mm | $\pi/12$ | No                           | No      |
| CASE-3                           | Yes                                  | Coarse sand<br>$d_{50}=1.024$ mm     | $\pi/12$ | Yes                          | Yes     |
| CASE-4                           | Yes                                  | Coarse sand<br>$d_{50}=1.024$ mm     | $\pi/6$  | Yes                          | Yes     |
| CASE-5                           | Yes                                  | IS Sand Grade II<br>$d_{50}=0.75$ mm | $\pi/12$ | Yes                          | No      |
| CASE-6                           | Yes                                  | IS Sand Grade II<br>$d_{50}=0.75$ mm | $\pi/6$  | Yes                          | No      |

## 7.2 Conclusions

The following conclusion can be inferred from the present thesis:

- A homotopy perturbation based new analytical solution framework was utilized for tide induced groundwater waves in isotropic/anisotropic unconfined aquifers with sloping/vertical beach face.
  - Group of non-dimensional parameters were identified during the derivation processes.
  - The derived solutions match with existing analytical solutions as well as 2D-FEFLOW solutions.
  - Higher order Boussinesq equation solutions are more accurate.
  - Applicability of the solution depends on the beach slope angle. The derived solution is not applicable for flatter slopes.
- Experiments were carried out for capturing the tide-induced response in scaled coastal aquifers for water-table waves.

- Water-table waves were observed for six different waves in CASE-1 and five different waves in CASE-2. Water-table over height were observed for all experiments (except the point influenced by boundary effects).
- The amplitudes of the waves were attenuating exponentially with increasing distance from the seaside boundary. Similarly, phase difference from the tides of were also increasing with distance from the seaside boundary.
- The amplitudes and time-averaged water table height data were used to calibrate the hydraulic conductivity of the sands.
- Experiments were carried out for saltwater movement in scaled coastal aquifers. Image processing technique was used for analysing the experimental photographs.
  - Image processing technique adopted captures the interface of the dyed saltwater and freshwater interface well.
  - Upper saline plumes were developed in all experimental cases. The extent of the upper saline plume was dependent on the freshwater flux. Time-averaged water table heights recorded at the inland boundary shows as an outlier in comparison with the numerically simulated time-averaged water table heights. This is due to freshwater flux injected at the inland boundary.
  - Velocity vectors obtained from the numerical modelling shows that both freshwater and saltwater breaks their respective zones.
  - Density neutral contaminant flow pathways were observed. The contaminant inside the saltwater wedge closer to the interface travels along the interface region to discharge inside sea. Both freshwater and saltwater contaminants oscillates within tidal cycles in their movement.

### 7.3 Recommendations for Future Works

The present study can be extended to the following to enhance the understanding of tidal influence on coastal aquifers.

- The density-dependent experiments should be done for flatter beach slopes (less than  $10^\circ$ ) and layered aquifer systems. The laboratory setup length scale should be adopted to be bigger to avoid the boundary effects to have effective semi-infinite aquifer system.

- The number of pressure transducers should be increased to have better understanding of vertical flows and efficient mapping of hydraulic conductivities using tomography. Similarly, conductivity probes should be facilitated in the experiment setups to study the density variations. Introduction of tensiometer and soil moisture sensors in the experiments would help in understanding the capillary effects.
- Large scale three-dimensional experiments would help in understanding the influence of pumping wells and recharge wells over salinity distribution.



# Appendix A

## Tidal Dynamics without Density Effects : Experimental Results

### A.1 CASE-2B to CASE-2E: Grade II IS sand with beach slope $\pi/12$

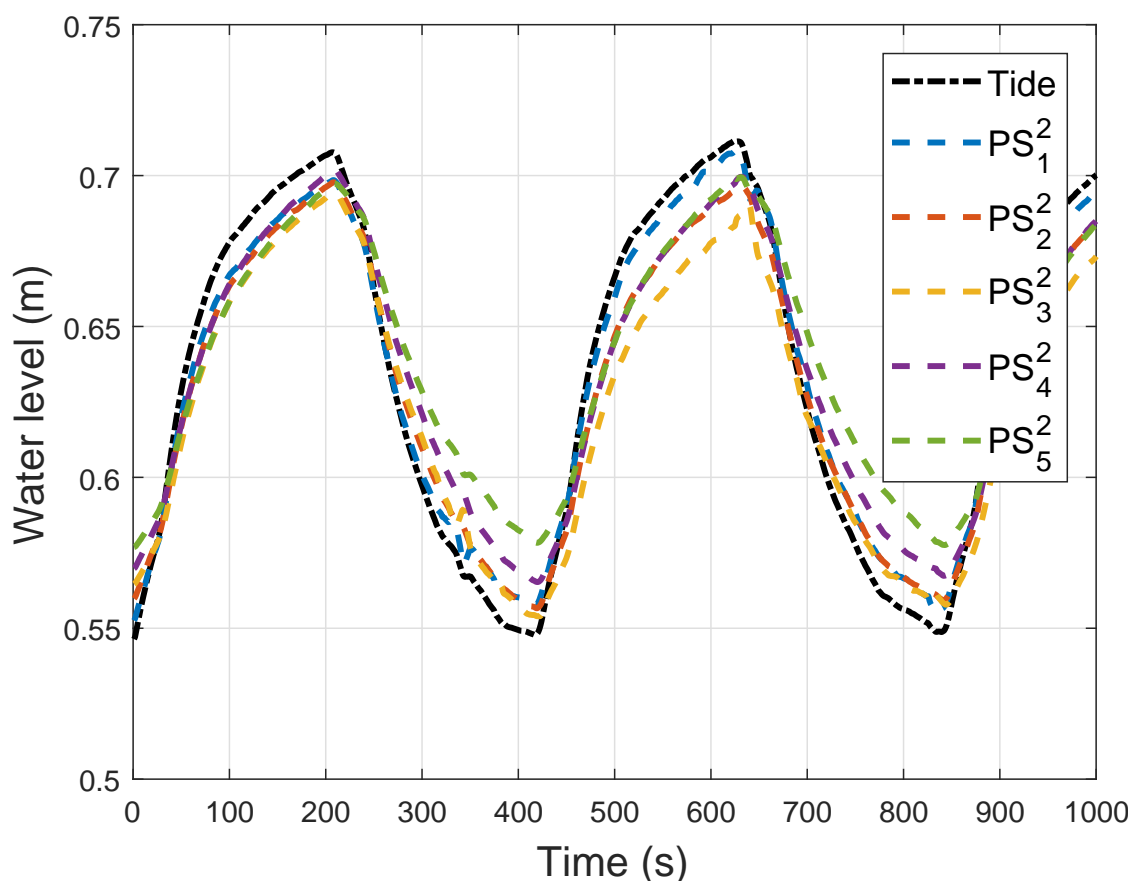
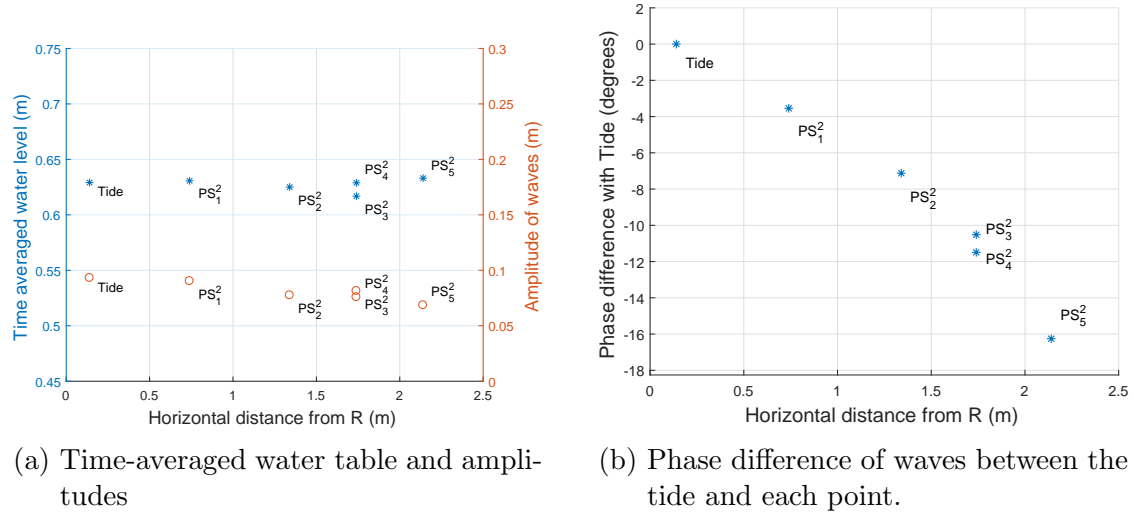


Figure A.1: CASE-2B: Waves recorded by the pressure transducers for the clockwise and anticlockwise times of 181 s, resting period of 30 s and DC motor RPM 161: magnified



(a) Time-averaged water table and amplitudes  
(b) Phase difference of waves between the tide and each point.

Figure A.2: CASE-2B: Time-averages water table, amplitude and phase difference details of waves recorded by the pressure transducers for the clockwise and anticlockwise times of 180 s, resting period of 30 s and DC motor RPM 161.

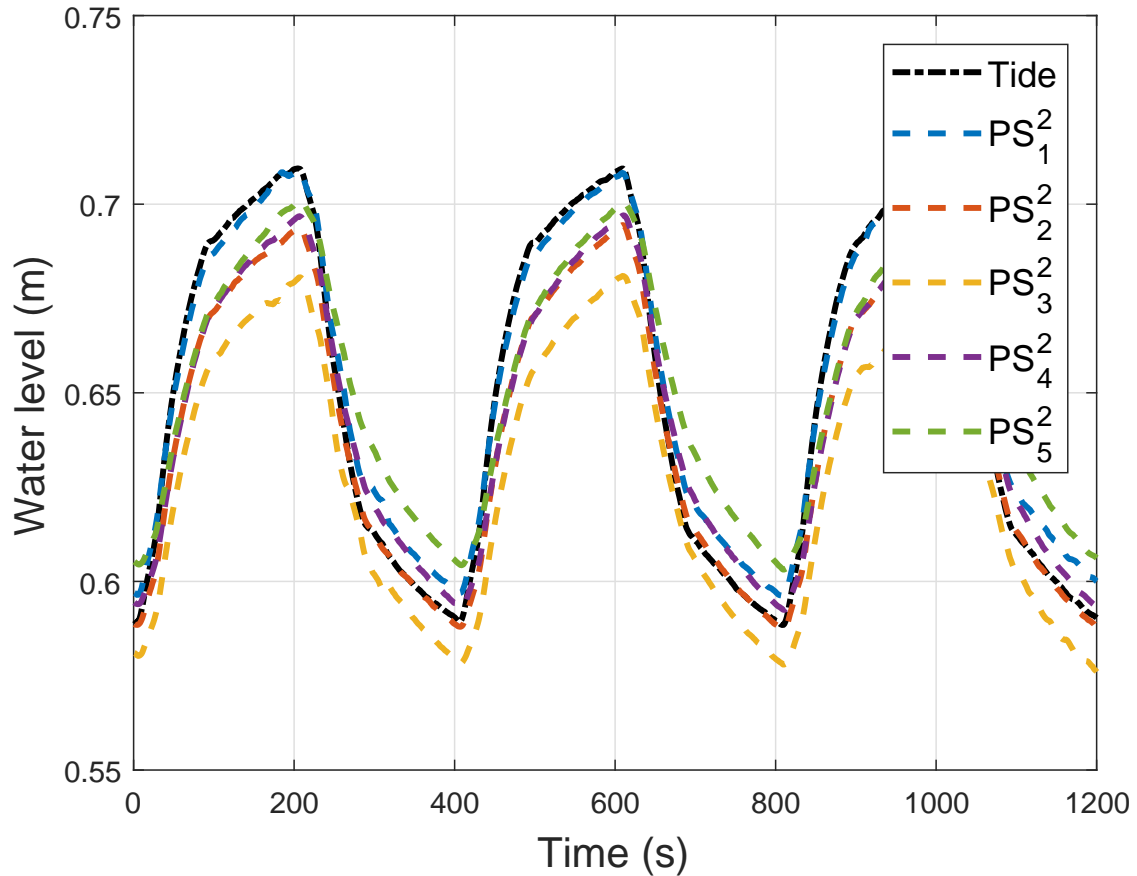


Figure A.3: CASE-2C: Waves recorded by the pressure transducers for the clockwise and anticlockwise times of 180 s, resting period of 20 s and DC motor RPM 161: magnified

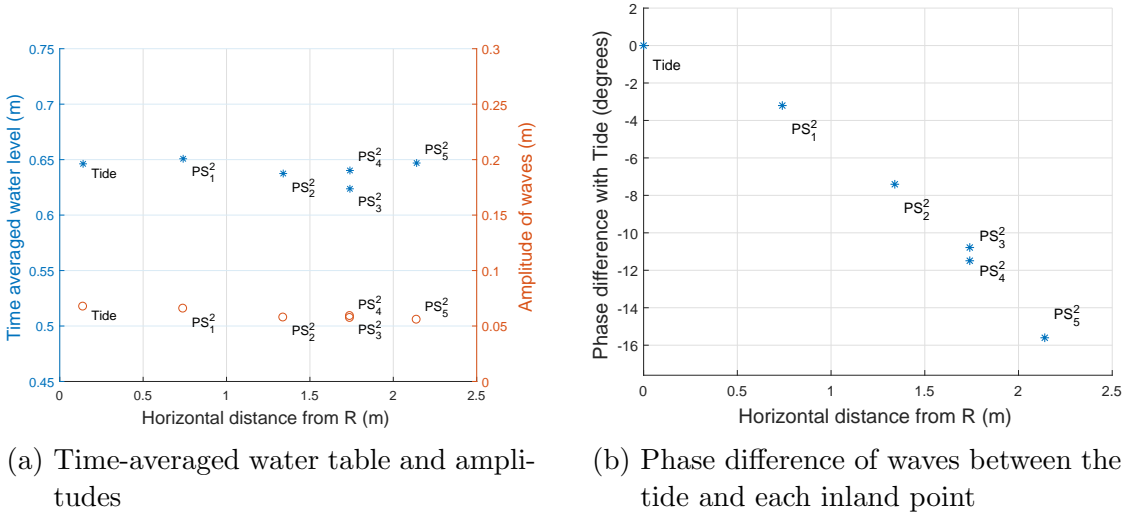


Figure A.4: CASE-2C: Time-averages water table, amplitude and phase difference details of waves recorded by the pressure transducers for the clockwise and anticlockwise times of 180 s, resting period of 20 s and DC motor RPM 161.

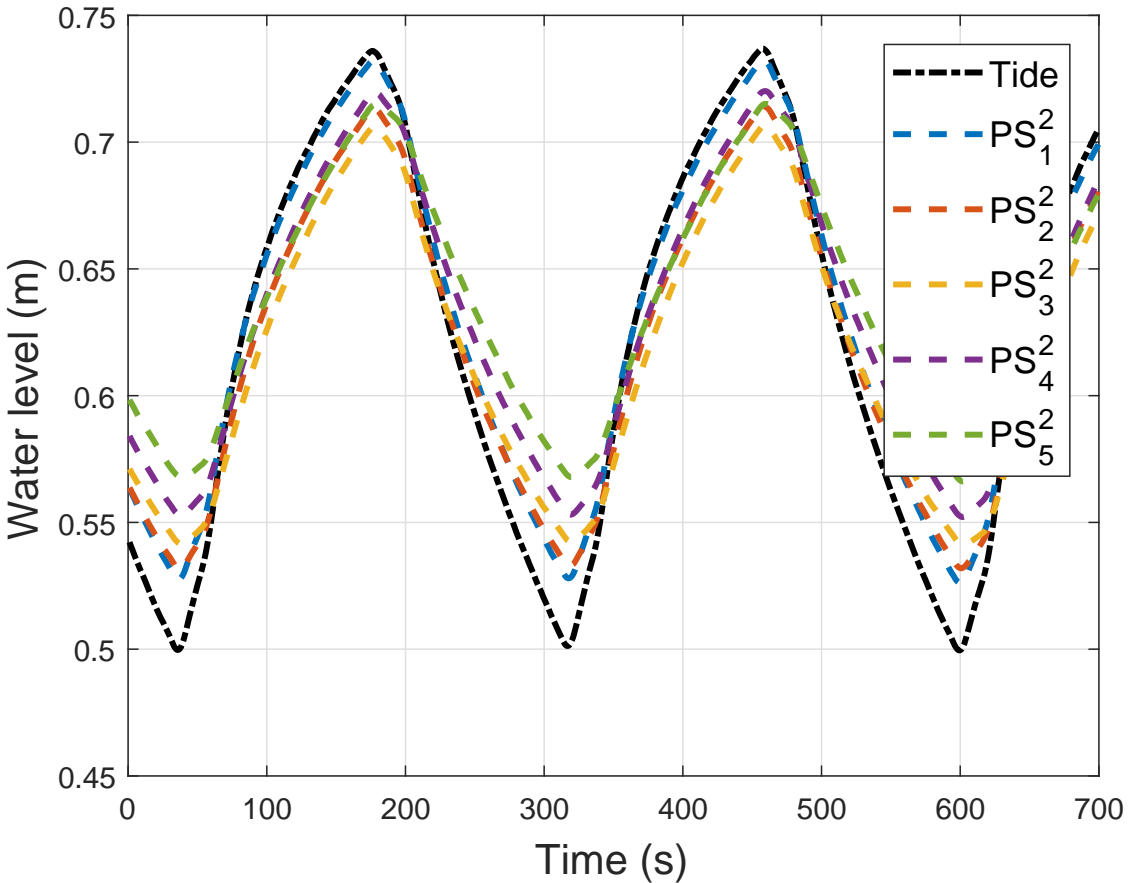
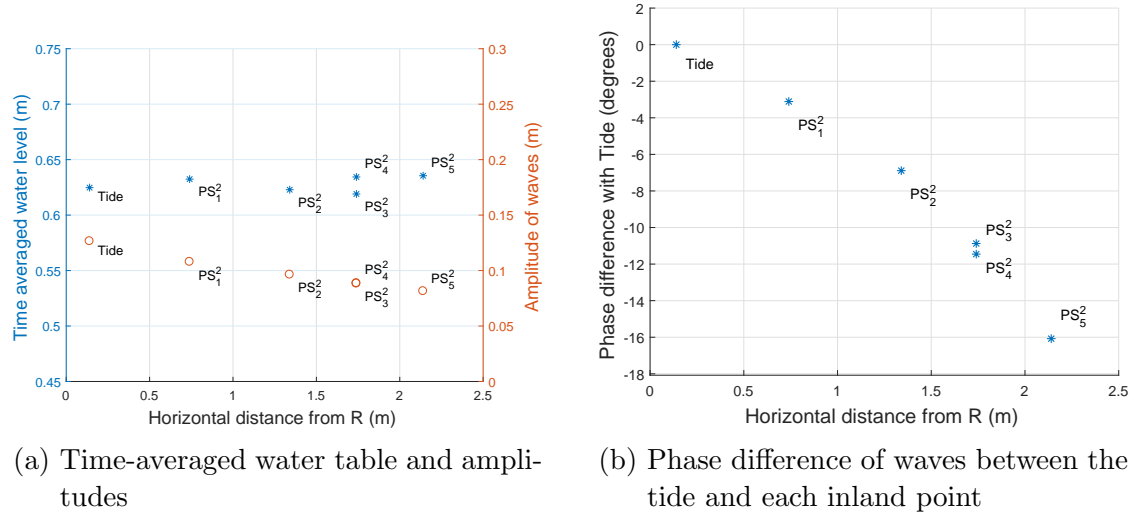


Figure A.5: CASE-2D: Waves recorded by the pressure transducers for the clockwise and anticlockwise times of 120 s, resting period of 20 s and DC motor RPM 161: magnified



(a) Time-averaged water table and amplitudes  
(b) Phase difference of waves between the tide and each inland point

Figure A.6: CASE-2D: Time-averages water table, amplitude and phase difference details of waves recorded by the pressure transducers for the clockwise and anticlockwise times of 120 s, resting period of 20 s and DC motor RPM 161.

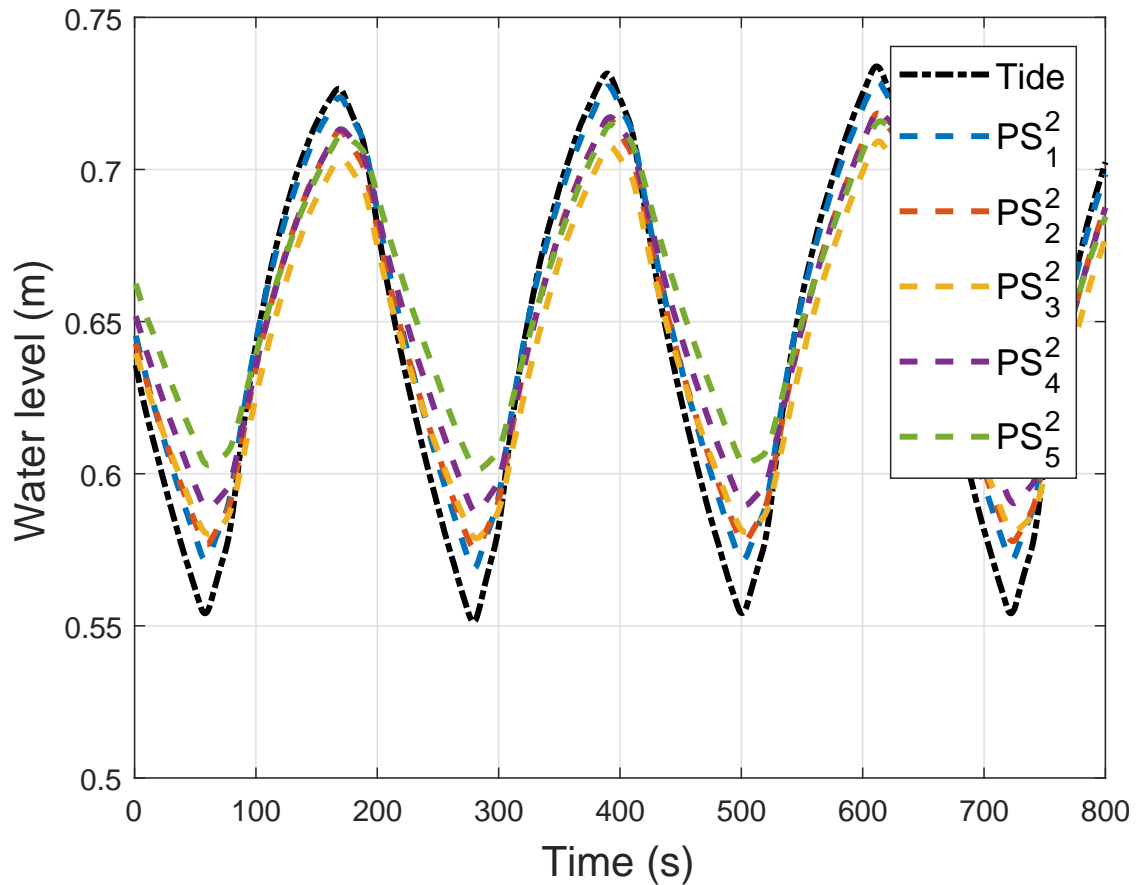
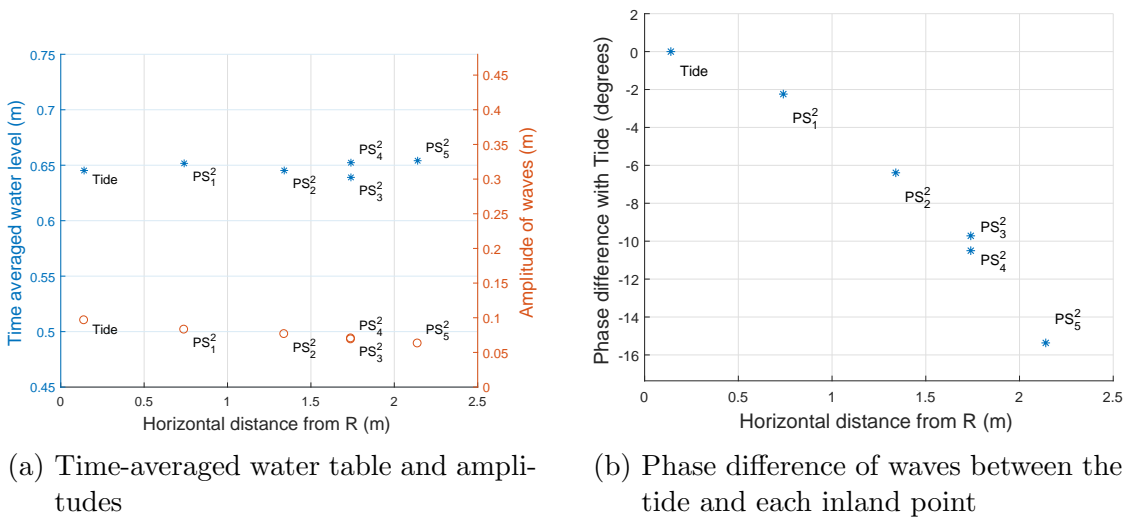


Figure A.7: CASE-2E: Waves recorded by the pressure transducers for the clockwise and anticlockwise times of 90 s, resting period of 20 s and DC motor RPM 161: magnified



(a) Time-averaged water table and amplitudes

(b) Phase difference of waves between the tide and each inland point

Figure A.8: CASE-2E: Time-averages water table, amplitude and phase difference details of waves recorded by the pressure transducers for the clockwise and anticlockwise times of 90 s, resting period of 20 s and DC motor RPM 161.



# References

- Hristo Zhivomirov (2016). UEILogger Data Logger System User Manual. available at: <https://in.mathworks.com/matlabcentral/fileexchange/48025-phase-difference-measurement-with-matlab-implementation> (Dec. 2018).
- United Electronic Industries, Inc. (2012). UEILogger Data Logger System User Manual. available at: <https://www.ueidaq.com/> (Nov. 2018).
- Abarca, E., Carrera, J., Sánchez-Vila, X., and Dentz, M. (2007). Anisotropic dispersive Henry problem. *Advances in Water Resources*, 30(4):913–926.
- Abarca, E. and Clement, T. P. (2009). A novel approach for characterizing the mixing zone of a saltwater wedge. *Geophysical Research Letters*, 36(6):L06402.
- Aeby, P., Forrer, J., Steinmeier, C., and Fluhler, H. (1997). Image Analysis for determination of dye tracer concentrations in sand columns. *Soil Science Society of America Journal*, 35(61):33–35.
- Artiles, W. and Kraenkel, R. A. (2007). An Exact Equation for the Free Surface of a Fluid in a Porous Medium. *SIAM Journal on Applied Mathematics*.
- Asadi-Aghbolaghi, M., Chuang, M. H., and Yeh, H. D. (2012). Groundwater response to tidal fluctuation in a sloping leaky aquifer system. *Applied Mathematical Modelling*, 36(10):4750–4759.
- Ataie-Ashtiani, B., Simmons, C. T., and Werner, A. D. (2014). Influence of boundary condition types on unstable density-dependent flow. *Ground water*, 52(3):378–87.
- Ataie-Ashtiani, B., Volker, R. E., and Lockington, D. A. (1999). Numerical and experimental study of seepage in unconfined aquifers with a periodic boundary condition. *Journal of Hydrology*, 222(1-4):165–184.
- Ataie-Ashtiani, B., Volker, R. E., and Lockington, D. A. (2001). Tidal effects on groundwater dynamics in unconfined aquifers. *Hydrological Processes*, 15(4):655–669.
- Bakker, M. (2006). Analytic solutions for interface flow in combined confined and semi-confined, coastal aquifers. *Advances in Water Resources*, 29(3):417–425.
- Bear, J. and Cheng, A. H. D. (2011). Methods to Derive the Differential Equation of the Free Surface Boundary. *Ground Water*, 49(2):133–143.

- Bear, J., Cheng, A. H.-D., Sorek, S., Ouazar, D., and Herrera, I., editors (1999). *Seawater Intrusion in Coastal Aquifers - Concepts, Methods and Practices*. Kluwer Academic Publishers, 1 edition.
- Bear, J. and Dagan, G. (1964). Some Exact Solutions of interface problems by means of Hodographic Method. *Journal of Geophysical Research*, 69(8):1563–1572.
- Boufadel, C. (2000). A mechanistic study of nonlinear solute transport in a groundwater-surface water system under steady state and transient hydraulic conditions. 36(9):2549–2565.
- Bouzouf, B. and Chen, Z. (2014). A Comparison of Finite Volume Method and Sharp Model For Two Dimensional saltwater intrusion modeling. *Canadian Journal of Civil Engineering*, 41(January):191–196.
- Bouzouf, B., Ouazar, D., Himi, M., and Casas, A. (2001). Integrating hydrogeochemical and geophysical data for testing a finite volume based numerical model for saltwater intrusion. *Transport in Porous Media*, 43:179–194.
- Bureau of Indian Standards, B. (2007). *Indian Standard: Standard Sand for Testing Cement Specification (Second Revision )*, volume 1991. Standards, Bureau of Indian, NEW DELHI 110002, 3.1 edition.
- Burek, P., Satoh, Y., Fischer, G., Kahil, M. T., Scherzer, A., Tramberend, S., Nava, L. F., Wada, Y., Eisner, S., Flörke, M., Hanasaki, N., Magnuszewski, P., Cosgrove, B., and Wiberg, D. (2016). Water Futures and Solution. *Water Futures and Solution: Fast Track Initiative (Final Report)*. IIASA Working Paper. Laxenburg, Austria, International Institute for Applied Systems Analysis (IIASA), (May):1–88.
- Burnett, W. C., Bokuniewicz, H., Moore, W. S., and Taniguchi, M. (2003). Groundwater and pore water inputs to the coastal zone. *Biogeochemistry*, 66:3–33.
- Carsel, R. and Parrish, R. (1988). Developing joint probability distributions of soil water retention characteristics. *Water Resources Research*, 24(5):755–769.
- Cartwright, N., Nielsen, P., and Dunn, S. (2003). Water table waves in an unconfined aquifer: Experiments and modeling. *Water Resources Research*, 39(12):n/a–n/a.
- Cartwright, N., Nielsen, P., and Li, L. (2004). Experimental observations of watertable waves in an unconfined aquifer with a sloping boundary. *Advances in Water Resources*, 27(10):991–1004.
- Castro-Orgaz, O. and Dey, S. (2014). Second-order shallow-flow theory and dupuit approximation for phreatic aquifers. *J. Hydraul. Eng.-ASCE*, 140(9):04014040.
- Castro-Orgaz, O., Giraldez, J. V., and Mateos, L. (2013). Second-order shallow flow equation for anisotropic aquifers. *Journal of Hydrology*, 501:183–185.
- Catania, F., Massabò, M., Valle, M., Bracco, G., and Paladino, O. (2008). Assessment of quantitative imaging of contaminant distributions in porous media. *Experiments in Fluids*, 44(1):167–177.

- Chang, S. W. and Clement, T. P. (2012). Experimental and numerical investigation of saltwater intrusion dynamics in flux-controlled groundwater systems. *Water Resources Research*, 48(9):W09527.
- Chang, S. W. and Clement, T. P. (2013). Laboratory and numerical investigation of transport processes occurring above and within a saltwater wedge. *Journal of contaminant hydrology*, 147:14–24.
- Chang, S. W., Clement, T. P., Simpson, M. J., and Lee, K.-K. (2011). Does sea-level rise have an impact on saltwater intrusion? *Advances in Water Resources*, 34(10):1283–1291.
- Chang, Y. C., Jeng, D. S., and Yeh, H. D. (2010). Tidal propagation in an oceanic island with sloping beaches. *Hydrology and Earth System Sciences*, 7(2008):1407–1430.
- Chen, Y.-J., Chen, G.-Y., Yeh, H.-D., and Jeng, D.-S. (2011). Estimations of tidal characteristics and aquifer parameters via tide-induced head changes in coastal observation wells. *Hydrology and Earth System Sciences*, 15(5):1473–1482.
- Cheng, J., Strobl, R., and Yeh, G. (1998). Modeling of 2D density-dependent flow and transport in the subsurface. *Journal of Hydrologic Engineering*, pages 248–257.
- Cooper, H. (1959). A hypothesis concerning the dynamic balance of fresh water and salt water in a coastal aquifer. *Journal of Geophysical Research*, 64(4):461–467.
- Cooper, H. (1964). Sea water in coastal aquifers. *US geological survey, Water-supply(1613-C)*:84.
- Croucher, A. and O’sullivan, M. (1995). The Henry problem for saltwater intrusion. *Water Resources Research*, 31(7):1809–1814.
- Dagan, G. (1967). Second-Order Theory Of Shallow Free-Surface Flow In Porous Media. *The Quarterly Journal of Mechanics and Applied Mathematics*, 20(4):517–526.
- Dam, J. V. and Sikkema, P. (1982). Approximate solution of the problem of the shape of the interface in a semi-confined aquifer. *Journal of hydrology*, 56:221–237.
- De Jong, G. D. J. (1965). A many valued hodograph in an interface problem. *Water Resources Research*, 1(4):543–555.
- Dentz, M., Tartakovsky, D. M., Abarca, E., Guadagnini, A., Sanchez-Vila, X., and Carrera, J. (2006). Variable-density flow in porous media. *Journal of Fluid Mechanics*, 561:209–235.
- Dhar, A. (2007). *Optimal Management And Monitoring Of Coastal Aquifers And Other Contaminated Aquifers*. PhD thesis, Indian Institute of Technology, Kanpur.
- Diersch, H.-J. and Kolditz, O. (2002). Variable-density flow and transport in porous media: approaches and challenges. *Advances in Water Resources*, 25(8–12):899–944.

- Diersch, H.-J. G. (2009). About the formulation of hydraulic head boundary (potential) conditions for fluid density-dependent groundwater problems. In *FE-FLOW White papers, vol. I*, chapter 7, pages 135–140. DHI-WASY Ltd, Berlin, Germany, 2009 edition.
- Diersch, H.-J. G. (2013). *Feflow -Finite Element Modeling of Flow, Mass and Heat Transport in Porous and Fractured Media*. Springer Science & Business Media, New York.
- Dose, E. J., Stoeckl, L., Houben, G. J., Vacher, H. L., Vassolo, S., Dietrich, J., and Himmelsbach, T. (2014). Experiments and modeling of freshwater lenses in layered aquifers: Steady state interface geometry. *Journal of Hydrology*, 509:621–630.
- Electrolab India (2014). Variable Speed Pump (PP 50VX). available at: <http://www.electrolabindia.com> (Nov. 2018).
- Essaid, H. I. (1990). A multilayered sharp interface model of coupled freshwater and saltwater flow in coastal systems: Model development and application. *Water Resources Research*, 26(7):1431–1454.
- Fakir, Y. and Razack, M. (2003). Hydrodynamic characterization of a Sahelian coastal aquifer using the ocean tide effect (Dridrate Aquifer, Morocco). *Hydrological Sciences Journal*, 48(3):441–454.
- Fenton, J. (1990). Calculating seepage flow with a free surface: Some old methods and some new ones. In *Proc., of the Groundwater and seepage Symposium, Auckland, May 1990*, pages 31–36, Wellington, N.Z. Institution of Professional Engineers.
- Feseker, T. (2007). Numerical studies on saltwater intrusion in a coastal aquifer in northwestern Germany. *Hydrogeology Journal*, 15(2):267–279.
- Frind, E. (1982a). Seawater intrusion in continuous coastal aquifer-aquitard systems. *Advances in water Resources*, 5:89–97.
- Frind, E. (1982b). Simulation of long-term transient density-dependent transport in groundwater. *Advances in Water Resources*, 5:73–88.
- Glover, R. (1959). The pattern of fresh-water flow in a coastal aquifer. *Journal of Geophysical Research*, (4):457–459.
- Goswami, R. R. and Clement, T. P. (2007). Laboratory-scale investigation of saltwater intrusion dynamics. *Water Resources Research*, 43(4):W04418.
- Hamidi, M., Reza, S., and Yazdi, S. (2006). Numerical Modeling of Seawater Intrusion in Coastal Aquifer Using Finite Volume Unstructured Mesh Method. *WSEAS Transactions on Mathematics*, 2006:572–579.
- He, J. H. (1999). Homotopy perturbation technique. *Comput Metho Appl M*, 178:257–262.
- He, J.-H. (2000). A coupling method of a homotopy technique and a perturbation technique for non-linear problems. *International Journal of Non-Linear Mechanics*, 35(1):37 – 43.

- He, J.-H. (2003). Homotopy perturbation method: a new nonlinear analytical technique. *Applied Mathematics and Computation*, 135(1):73 – 79.
- He, J. H. (2012). Homotopy perturbation method with an auxiliary term. *Abstr. Appl. Anal.*, 2012(Jan):1–7.
- He, J. H. (2014). Homotopy perturbation method with two expanding parameters. *Indian Journal of Physics*, 88(2):193–196.
- Held, R., Attinger, S., and Kinzelbach, W. (2005). Homogenization and effective parameters for the Henry problem in heterogeneous formations. *Water resources research*, 41(11):1–14.
- Henry, H. R. (1959). Salt intrusion into fresh-water aquifers. *Journal of Geophysical Research*, 64(11):1911–1919.
- Henry, H. R. (1964). Effects of dispersion on salt encroachment in coastal aquifers. In: Sea Water in Coastal Aquifers. *US geological survey*, Water-supp(1613-C):70–84.
- Hill, M. (1998). Methods and guidelines for effective model calibration: US Geological Survey Water-Resources Investigations Report 98-4005, 90 p. *US Geological Survey, Water Resources Investigations Report 98-4005*, pages 1–98.
- Horn, D. P. (2006). Measurements and modelling of beach groundwater flow in the swash-zone: a review. *Continental Shelf Research*, 26(5):622–652.
- Hsieh, P. C., Hsu, H. T., Liao, C. B., and Chiueh, P. T. (2015). Groundwater response to tidal fluctuation and rainfall in a coastal aquifer. *Journal of Hydrology*, 521:132–140.
- Hubbert, M. (1940). The theory of ground-water motion. *The Journal of Geology*, 48(8):785–944.
- Hunt, B. (1985). Some analytical solutions for seawater intrusion control with recharge wells. *Journal of Hydrology*, 80(1965):9–18.
- Huyakorn, P. and Andersen, P. (1987). Saltwater intrusion in aquifers: Development and testing of a three-dimensional finite element model. *Water Resources Research*, 23(2):293–312.
- Inouchi, K., Kishi, Y., and Kakinuma, T. (1990). The motion of coastal groundwater in response to the tide. *Journal of Hydrology*, 115:165–191.
- Jaeger, S., Ehni, M., Eberhardt, C., Rolle, M., Grathwohl, P., and Gauglitz, G. (2009). Ccd camera image analysis for mapping solute concentrations in saturated porous media. *Analytical and Bioanalytical Chemistry*, 395(6):1867.
- Jeng, D. S., Seymour, B. R., Barry, D. A., Parlange, J. Y., Lockington, D. A., and Li, L. (2005a). Steepness expansion for free surface flows in coastal aquifers. *J. Hydrol.*, 309:85–92.
- Jeng, D. S., Seymour, B. R., Barry, D. a., Parlange, J. Y., Lockington, D. a., and Li, L. (2005b). Steepness expansion for free surface flows in coastal aquifers. *Journal of Hydrology*, 309(2005):85–92.

- Jha, M. K. and Singh, A. (2014). Application of genetic algorithm technique to inverse modeling of tide-aquifer interaction. *Environmental Earth Sciences*, 71(8):3655–3672.
- Jose, S. C. and Cirpka, O. A. (2004). Measurement of mixing-controlled reactive transport in homogeneous porous media and its prediction from conservative tracer test data. *Environmental science & technology*, 38(7):2089–96.
- Jose, S. C., Rahman, M. A., and Cirpka, O. A. (2004). Large-scale sandbox experiment on longitudinal effective dispersion in heterogeneous porous media. *Water Resources Research*, 40(12):W12415.
- Kaleris, V. K. and Ziogas, A. I. (2013). The effect of cutoff walls on saltwater intrusion and groundwater extraction in coastal aquifers. *Journal of Hydrology*, 476:370–383.
- Knight, J. (1981). Steady periodic flow through a rectangular dam. *Water Resources Research*, 17(4):1222–1224.
- Kong, J., Song, Z. Xin, P., and Shen, C. (2011). A new analytical solution for tide-induced groundwater fluctuations in an unconfined aquifer with a sloping beach. *China Ocean Eng.*, 25(3):479–494.
- Koussis, A. D., Mazi, K., and Destouni, G. (2012). Analytical single-potential, sharp-interface solutions for regional seawater intrusion in sloping unconfined coastal aquifers, with pumping and recharge. *Journal of Hydrology*, 416-417:1–11.
- Kuan, W. K., Jin, G., Xin, P., Robinson, C., Gibbes, B., and Li, L. (2012). Tidal influence on seawater intrusion in unconfined coastal aquifers. *Water Resources Research*, 48(2):W02502.
- Lee, C.-h. and Cheng, R. (1974). On seawater encroachment in coastal aquifers. *Water Resources Research*, 10(5).
- Li, H. and Jiao, J. (2013). Quantifying tidal contribution to submarine groundwater discharges: A review. *Chinese Science Bulletin*, 58(25):3053–3059.
- Li, L., Barry, D. A., Stagnitti, F., and Parlange, J. Y. (2000). Groundwater waves in a coastal aquifer: A new governing equation including vertical effects and capillarity. *Water Resour. Res.*, 36(2):411–420.
- Liao, S. (1997). Homotopy analysis method: A new analytical technique for nonlinear problems. *Communications in Nonlinear Science and Numerical Simulation*, 2(2):95 – 100.
- Liao, S. (2004). On the homotopy analysis method for nonlinear problems. *Applied Mathematics and Computation*, 147(2):499 – 513.
- Liao, S. J. (1992). *The proposed homotopy analysis technique for the solution of nonlinear problems*. PhD thesis, Ph. D. Thesis, Shanghai Jiao Tong University.
- Liu, F., Anh, V., Turner, I., Bajracharya, K., Huxley, W., and Su, N. (2006). A finite volume simulation model for saturated-unsaturated flow and application to Gooburrum, Bundaberg, Queensland, Australia. *Applied Mathematical Modelling*, 30(4):352–366.

- Liu, F. and Bhatia, S. (2001). Application of Petrov-Galerkin methods to transient boundary value problems in chemical engineering: adsorption with steep gradients in bidisperse solids. *Chemical Engineering Science*, 56(12):3727–3735.
- Liu, F., Turner, I., and Anh, V. (2002). An unstructured mesh finite volume method for modelling saltwater intrusion into coastal aquifers. *Korean Journal of Computational & Applied Mathematics*, 9(2):391–407.
- Liu, P. L.-F. and Wen, J. (1997). Nonlinear diffusive surface waves in porous media. *J. Fluid Mech.*, 347:119–139.
- Lu, C., Xin, P., Kong, J., Li, L., and Luo, J. (2016). Analytical solutions of seawater intrusion in sloping confined and unconfined coastal aquifers. *Water Resources Research*, 52:6989–7004.
- Luyun, R., Momii, K., and Nakagawa, K. (2009). Laboratory-scale saltwater behavior due to subsurface cutoff wall. *Journal of Hydrology*, 377(3-4):227–236.
- Luyun, R., Momii, K., and Nakagawa, K. (2011). Effects of recharge wells and flow barriers on seawater intrusion. *Ground water*, 49(2):239–49.
- Mantoglou, A. (2003). Pumping management of coastal aquifers using analytical models of saltwater intrusion. *Water Resources Research*, 39(12):1335.
- MOEFCC (2017). Database on Coastal States of India. *Website of Ministry of Environment Forest and Climate Change website*.
- Moore, W. S. (2003). The effect of submarine groundwater discharge on the ocean. *Annual review of marine science*, 2:59–88.
- Munusamy, S. B. and Dhar, A. (2015). Homotopy perturbation method-based analytical solution for tide-induced groundwater fluctuations. *Groundwater*, 54(3):440–447.
- Munusamy, S. B. and Dhar, A. (2016). Homotopy perturbation method-based analytical solution for tide-induced groundwater fluctuations. *Groundwater*, 54(3):440–447.
- Munusamy, S. B. and Dhar, A. (2017). Analytical solution of groundwater waves in unconfined aquifers with sloping boundary. *Sadhana - Academy Proceedings in Engineering Sciences*, 42(9):1–8.
- Nadeem, S. and Hussain, A. (2009). Mhd flow of a viscous fluid on a nonlinear porous shrinking sheet with homotopy analysis method. *Applied Mathematics and Mechanics*, 30(12):1569–1578.
- Nakagawa, K., Momii, K., and Berndtsson, R. (2005). Saltwater intrusion in coastal aquifer – comparison between the CIP and MOC simulation technique. *Environmental Modeling & Assessment*, 10(4):323–329.
- Nielsen, P. (1990). Tidal dynamics of the water table in beaches. *Water Resour. Res.*, 26(9):2127–2134.
- Nielsen, P., Aseervatham, R., and Perrochet, P. (1997). Groundwater waves in aquifers of intermediate depths. *Adv. Water. Resour.*, 20(1):37–43.
- Nielsen, P. and Perrochet, P. (2000). Watertable dynamics under capillary fringes: experiments and modelling. *Advances in Water Resources*, 23(5):503–515.

- Oates, P. M. and Harvey, C. F. (2006). A colorimetric reaction to quantify fluid mixing. *Experiments in Fluids*, 41(5):673–683.
- Oostrom, M. and Dane, J. (1992). Experimental investigation of dense solute plumes in an unconfined aquifer model. *Water Resources Research*, 28(9):2315–2326.
- Oude Essink, G. H. P., Van Baaren, E. S., and De Louw, P. G. B. (2010). Effects of climate change on coastal groundwater systems: A modeling study in the netherlands. *Water Resources Research*, 46(10):n/a–n/a. W00F04.
- Oz, I., Shalev, E., Yechieli, Y., and Gvirtzman, H. (2015). Saltwater circulation patterns within the freshwater–saltwater interface in coastal aquifers: Laboratory experiments and numerical modeling. *Journal of Hydrology*, 530:734–741.
- Parlange, J., Stagnitti, F., Starr, J., and Braddock, R. (1984). Free-surface flow in porous media and periodic solution of the shallow-flow approximation. *Journal of Hydrology*, 70:251–263.
- Philip, J. (1973). Periodic Nonlinear Diffusion: An Integral Relation and its Physical Consequences. *Australian Journal of Physics*, (February):513–520.
- Pinder, G. and Cooper, H. (1970). A numerical technique for calculating the transient position of the saltwater front. *Water Resources Research*, 6(3):875–882.
- Pool, M. and Carrera, J. (2011). A correction factor to account for mixing in Ghyben-Herzberg and critical pumping rate approximations of seawater intrusion in coastal aquifers. *Water Resources Research*, 47(5):W05506.
- Post, V. E. a. (2005). Fresh and saline groundwater interaction in coastal aquifers: Is our technology ready for the problems ahead? *Hydrogeology Journal*, 13(1):120–123.
- Raubenheimer, B., Guza, R. T., and Elgar, S. (1999). Tidal water table fluctuations in a sandy ocean beach. *Water Resources Research*, 35(8):2313.
- Reilly, T. and Goodman, A. (1985). Quantitative analysis of saltwater-freshwater relationships in groundwater systems-A historical perspective. *Journal of Hydrology*, 80:125–159.
- Roberts, M. E., Trefry, M. G., Fowkes, N., Bassom, A. P., and Abbott, P. C. (2011). Water-table response to tidal forcing at sloping beaches. *Journal of Engineering Mathematics*, 69:291–311.
- Robinson, C., Gibbes, B., Carey, H., and Li, L. (2007a). Salt-freshwater dynamics in a subterranean estuary over a spring-neap tidal cycle. *Journal of Geophysical Research*, 112(C9):C09007.
- Robinson, C., Li, L., and Barry, D. (2007b). Effect of tidal forcing on a subterranean estuary. *Advances in Water Resources*, 30(4):851–865.
- Robinson, M. and Gallagher, D. (1999). A model of ground water discharge from an unconfined coastal aquifer. *Groundwater*, 37(I):80–87.

- Röper, T., Greskowiak, J., and Massmann, G. (2015). Instabilities of submarine groundwater discharge under tidal forcing. *LIMNOLOGY and OCEANOGRAPHY*, 60(1):22–28.
- sa Olsson and Grathwohl, P. (2007). Transverse dispersion of non-reactive tracers in porous media: A new nonlinear relationship to predict dispersion coefficients. *Journal of Contaminant Hydrology*, 92(3):149 – 161.
- Schincariol, R. A., Herderick, E. E., and Schwartz, F. W. (1993). On the application of image analysis to determine concentration distributions in laboratory experiments. *Journal of Contaminant Hydrology*, 12(3):197–215.
- Schincariol, R. A. and Schwartz, F. W. (1990). An experimental investigation of variable density flow and mixing in homogeneous and heterogeneous media. *Water Resources Research*, 26(10):2317–2329.
- Schlumberger Water Services (Netherlands) B.V. (2014). Diver Manual Version November 2014. available at: [https://www.swstechnology.com/novametrix/pdfs/equipment/Diver\\_manuals/Diver\\_Product\\_Manual\\_en.pdf](https://www.swstechnology.com/novametrix/pdfs/equipment/Diver_manuals/Diver_Product_Manual_en.pdf) (Nov. 2018).
- Sedláček, M. (2003). Digital measurement of phase difference of lf signals—a comparison of dsp algorithms. In *Proceedings of IMEKO XVII World Congress (CD), Dubrovnik, Croatia*, pages 639–644.
- Segol, G., Pinder, G. F., and Gray, W. G. (1975). A Galerkin-Finite Element Technique for calculating the transient position of the saltwater front. 11(2):343–347.
- Shi, L., Cui, L., Park, N., and Huyakorn, P. S. (2011). Applicability of a sharp-interface model for estimating steady-state salinity at pumping wells-validation against sand tank experiments. *Journal of Contaminant Hydrology*, 124(1-4):35–42.
- Shoemaker, W. (2004). Important observations and parameters for a salt water intrusion model. *Ground water*, 42(6):829–840.
- Si, X.-y., Si, X.-h., Zheng, L.-c., and Zhang, X.-x. (2011). Homotopy analysis solution for micropolar fluid flow through porous channel with expanding or contracting walls of different permeabilities. *Applied Mathematics and Mechanics*, 32(7):859–874.
- Sikkema, P. and Dam, J. V. (1982). Analytical formulae for the shape of the interface in a semi-confined aquifer. *Journal of hydrology*, 56:201–220.
- Simmons, C. T., Fenstemaker, T. R., and Sharp, J. M. (2001). Variable-density groundwater flow and solute transport in heterogeneous porous media: approaches, resolutions and future challenges. *Journal of contaminant hydrology*, 52(1-4):245–75.
- Simpson, M. and Clement, T. (2003). Theoretical analysis of the worthiness of Henry and Elder problems as benchmarks of density-dependent groundwater flow models. *Advances in Water Resources*, 26(1):17–31.

- Simpson, M. J. and Clement, T. P. (2004). Improving the worthiness of the Henry problem as a benchmark for density-dependent groundwater flow models. *Water Resources Research*, 40(1):W01504.
- Slooten, L. J., Carrera, J., Castro, E., and Fernandez-Garcia, D. (2010). A sensitivity analysis of tide-induced head fluctuations in coastal aquifers. *Journal of Hydrology*, 393(3-4):370–380.
- Smith, A. J. (2004). Mixed convection and density-dependent seawater circulation in coastal aquifers. *Water Resources Research*, 40:1–16.
- Smith, S. W. et al. (1997). The scientist and engineer's guide to digital signal processing.
- Song, Z., Li, L., Kong, J., and Zhang, H. (2007). A new analytical solution of tidal water table fluctuations in a coastal unconfined aquifer. *J. Hydrol.*, 340(3–4):256–260.
- Song, Z., Li, L., Nielsen, P., and Lockington, D. (2006). Quantification of tidal watertable overheight in a coastal unconfined aquifer. *Journal of Engineering Mathematics*, 56:437–444.
- Stoeckl, L. and Houben, G. (2012). Flow dynamics and age stratification of freshwater lenses: Experiments and modeling. *Journal of Hydrology*, 458-459:9–15.
- Stoeckl, L., Houben, G. J., and Dose, E. J. (2015). Experiments and modeling of flow processes in freshwater lenses in layered island aquifers : Analysis of age stratification , travel times and interface propagation. *Journal of Hydrology*, 529:159–168.
- Stojsavljevic, J. D., Jeng, D. S., Seymour, B. R., and Pokrajac, D. (2012). Higher Order Analytical Solutions of Water Table Fluctuations in Coastal Aquifers. *Ground Water*, 50(2):301–307.
- Strack, O. (1976). A Single-Potential Solution for Regional Interface Problems in Coastal Aquifers. *Water Resources Research*, 12(6):1165–1174.
- Strack, O. D. (2017). Vertically integrated flow in stratified aquifers. *Journal of Hydrology*, 548:794–800.
- Strack, O. D. and Ausk, B. K. (2015). A formulation for vertically integrated groundwater flow in a stratified coastal aquifer. *Water Resources Research*, 51(8):6756–6775.
- Strack, O. D. L. (1972). Some cases of interface flow towards drains. *Journal of Engineering Mathematics*, 6(2):175–191.
- Teo, H., Jeng, D., Seymour, B., Barry, D., and Li, L. (2003). A new analytical solution for water table fluctuations in coastal aquifers with sloping beaches. *Adv. Water. Resour.*, 26(12):1239–1247.
- UNCED (1992). United Nations Conference on Environment & Development: AGENDA 21. In Nations, U., editor, *United Nations Sustainable Development*, number June, pages 254–266, Rio de Janerio, Brazil. United Nations.

- Van Genuchten, M. T. (1980). A Closed-form Equation for Predicting the Hydraulic Conductivity of Unsaturated Soils1. *Soil Science Society of America Journal*, 44(5):892.
- Volker, R. E., Zhang, Q., and Lockington, D. A. (2002). Numerical modelling of contaminant transport in coastal aquifers. *Mathematics and Computers in Simulation*, 59(1-3):35–44.
- Voss, C. and Souza, W. (1987). Variable density flow and solute transport simulation of regional aquifers containing a narrow freshwater-saltwater transition zone. *Water Resources Research*, 23(10):1851–1866.
- Werner, A. D., Bakker, M., Post, V. E., Vandenbohede, A., Lu, C., Ataie-Ashtiani, B., Simmons, C. T., and Barry, D. (2013). Seawater intrusion processes, investigation and management: Recent advances and future challenges. *Advances in Water Resources*, 51:3–26.
- Werth, C. J., Zhang, C., Brusseau, M. L., Oostrom, M., and Baumann, T. (2010). A review of non-invasive imaging methods and applications in contaminant hydrogeology research. *Journal of Contaminant Hydrology*, 113(1):1 – 24.
- Xu, L. (2007). He's homotopy perturbation method for a boundary layer equation in unbounded domain. *Computers and Mathematics with Applications*, 54:1067–1070.
- Yeh, H. D., Huang, C. S., Chang, Y. C., and Jeng, D. S. (2010). An analytical solution for tidal fluctuations in unconfined aquifers with a vertical beach. *Water Resources Research*, 46(10):1–12.
- Younes, A. and Fahs, M. (2013). A Semi-Analytical Solution for the Reactive Henry Saltwater Intrusion Problem. *Water, Air, & Soil Pollution*, 224(11):1779.
- Zhang, Q., Volker, R. E., and Lockington, D. A. (2002). Experimental investigation of contaminant transport in coastal groundwater. *Advances in Environmental Research*, 6(3):229–237.
- Zhou, Y., Lim, D., Cupola, F., and Cardiff, M. (2016). Aquifer imaging with pressure wavesEvaluation of low-impact characterization through sandbox experiments. *Water Resources Research*, pages 2141–2156.
- Zhu, J., Zheng, L.-c., and Zhang, X.-x. (2009). Analytical solution to stagnation-point flow and heat transfer over a stretching sheet based on homotopy analysis. *Applied Mathematics and Mechanics*, 30(4):463–474.
- Zinn, B., Meigs, L. C., Harvey, C. F., Haggerty, R., Peplinski, W. J., and von Schwerin, C. F. (2004). Experimental visualization of solute transport and mass transfer processes in two-dimensional conductivity fields with connected regions of high conductivity. *Environmental Science & Technology*, 38(14):3916–3926.